Au-Ag BIMETALLIC NANOSTRUCTURES GROWTH AND CHARACTERIZATION ON ULTRA CLEAN SILICON SUBSTRATES

By

ANJAN BHUKTA

(PHYS07201004001)

INSTITUTE OF PHYSICS, BHUBANESWAR, INDIA

A thesis submitted to the

Board of Studies in Physical Sciences

In partial fulfillment of requirements

for the Degree of

DOCTOR OF PHILOSOPHY

of

HOMI BHABHA NATIONAL INSTITUTE

FEBRUARY, 2017

Homi Bhabha National Institute

Recommendations of the Viva Voce Board

As members of the Viva Voce Board, we certify that we have read the dissertation prepared by Mr. Anjan Bhukta entitled "Au-Ag Bimetallic Nanostructures Growth and Characterization on Ultra Clean Silicon Surfaces", and recommend that it may be accepted as fulfilling the dissertation requirement for the Degree of Doctor of Philosophy.

Ajit M. Srivastava **Date:** 9-2-17

Chairman – Prof. Ajit Srivastava

PVSatyam **Date:** 09/02/17

Guide / Convener – Prof. P. V. Satyam

Date: 09/02/17

Member 1 – Prof. T. Som

G. Tripathy **Date:** 09/02/17

Member 2 – Prof. G. Tripathy

Date: 09/02/17

Member 3 – Prof. Dipak Kumar Goswami

Final approval and acceptance of this dissertation is contingent upon the candidate's submission of the final copies of the dissertation to HBNI.

I hereby certify that I have read this dissertation prepared under my direction and recommend that it may be accepted as fulfilling the dissertation requirement.

Date: 09/02/2017

Place: Bhubaneswar

PVSatyam

डॉ. पी.वी. सत्यम / Dr. P.V. Satyam
प्रोफेसर / Professor
भौतिकी संस्थान / Institute of Physics
भुवनेश्वर / Bhubaneswar

Statement By Author

This dissertation has been submitted in partial fulfillment of requirements for an advanced degree at Homi Bhabha National Institute (HBNI) and is deposited in the Library to be made available to borrowers under rules of the HBNI.

Brief quotations from this dissertation are allowable without special permission, provided that accurate acknowledgement of source is made. Requests for permission for extended quotation from or reproduction of this manuscript in whole or in part may be granted by the Competent Authority of HBNI when in his or her judgment the proposed use of the material is in the interests of scholarship. In all other instances, however, permission must be obtained from the author.

A. Bhukta

Anjan Bhukta

Institute Of Physics, Bhubaneswar

Declaration

I, Anjan Bhukta, hereby declare that the investigation presented in the thesis has been carried out by me. The work is original and has not been submitted earlier as a whole or in part for a degree / diploma at this or any other Institution / University.

A. Bhukta

Anjan Bhukta

Institute Of Physics, Bhubaneswar

Acknowledgments

I would like express my deep sense of gratitude to my thesis supervisor Prof. Parlapalli Venkata Satyam for his invaluable guidance and constant encouragement both academically and socially during my Ph. D. His scientific thoughts with complete liberty and incessant drive for betterment have inspired and motivated me to explore many intuitive scientific experiments. During my journey of present degree, I had many valuable discussions with him which have helped me to understand the subject and made me confident to solve the problems.

I sincerely acknowledge all The Directors, IOPB for their extensive supports and helps during the period of my degree.

I wish to thank Prof. S. M. Shivaprasad (JNCASR), Dr. S. K. Dhara (IGCAR) and Prof. D. K. Goswami (IIT Kharagpur) for their valuable advices and supports to carry on experimental investigations. I gratefully acknowledge Dr. B. Satpati (SINP) and Dr. J. Ghatak (JNCASR) for their sincere efforts for accomplishing STEM measurements. I specially thank to Dr. T. Bagarti (IMSc) and Dr. B. Rakshit (IOPB) for their contributions to theoretical modeling which have helped us to understand many experimental outcomes.

I would like to also acknowledge my senior Jatis da for teaching me about MBE operations and thin film deposition techniques. I feel deeply privileged to express my thanks to Dr. Avijit Kumar (Aalto University, Finland) for teaching me about operation of UHV-STM. I feel extremely grateful to Jay da, Ashutosh da and Raghav da who have taught me about TEM specimen preparation techniques and SEM operations. It was a great pleasure for me to work with my other group members Rajib da, Arnab, Puspendu, Paramita and I am thankful for their helps.

I wish to covey my sincere gratitude and thanks to my colleagues and friends Subhadip, Sazim, Shailesh, Oindrila, Manas, Tanmay, Nasrin, Tathamay, Himanshu and Shalik for their immense helps and supports.

I sincerely thank to the scientific staffs in laboratories B. K. Dash, S. R. Mohanty, A. K. Behera, K. C. Patra and other staffs of IBL, for their timely help during experimental works. Name of B. K. Dash is specially mentioned due to his sincere dedication to MBE-STM laboratory and helping me to troubleshoot many instrumental issues.

Finally, I feel privileged to express my sincere gratitude to my parents and family members for their perseverance, love and affection which have strengthened and inspired me to carry on my research work.

TO MY PARENTS

List of Publications

1) * Growth of Ag nanostructures on high-index Si (5 5 12) surfaces under UHV conditions: effect of prior surface treatment before deposition,

   A. Bhukta, P. Guha, A. Ghosh, P. Maiti and P. V. Satyam, *Applied Physics A* **122**, 356 (2016).

2) Coherently Embedded Ag Nanostructures in Si: 3D Imaging and their application to SERS,

   R.R. Juluri, A. Rath, A. Ghosh, **A. Bhukta**, R. Sathyavathi, D. N. Rao, K. Muller, M. Schowalter, T. Grieb, C. Frank, F. Krause, A. Rosenauer and P. V. Satyam, *Scientific Reports* **4,** 4633 (2014) (Nature publishing group).

3) Silver endotaxy in silicon under various ambient conditions and their use as surface enhanced Raman spectroscopy substrates,

   R. R. Juluri, A. Ghosh, **A. Bhukta**, R. Sathyavathi and P. V. Satyam, *Thin Solid Films* **586,** 88 (2015).

4) Photoluminescence study on irradiated yttria stabilized zirconia,

   R. Halder, P. Sengupta, V. Sudarsan, A. Ghosh, A. Ghosh, **A. Bhukta**, G. Sharma, I. Samajdar, G. K. Dey, *Journal Of Nuclear Materials* **456**, 359 (2015).

5) * Ag Induced Bimetallic (Au-Ag) Nanowires on High Index Silicon Substrates**,**

   A. Bhukta, T. Bagarti, P. Guha, B. Satpati, B. Rakshit, P. Maiti and P. V. Satyam *(submitted in Journal Of Applied Physics).*

6) * Effect of Au thickness on AuAg bimetallic growth on reconstructed Si(5 5 12) surfaces,

   A. Bhukta, A. Ghosh, P. Guha, P. Maiti, B. Satpati and P. V. Satyam *(accepted in Applied Physics A).*

7) * Growth of large aspect ratio AuAg bimetallic nanowires on Si(110) substrate,

   A. Bhukta, P. Guha, B. Satpati, P. Maiti and P. V. Satyam *(under review in Applied Surface Science).*

8) * Ag induced shape transition of AuAg bimetallic nanostructures on ultra-clean Si substrates,

   A. Bhukta *et al. (Manuscript in preparation).*

9) Oscillatory amorphization and recrystallization in ion irradiation of Si/Ni/Si and formation of nanoscale η-NiSi**,**

   N. Banu, B. Satpati, **A. Bhukta**, B. N. Dev, *Journal Of Applied Physics* **121**, 045302 (2017).

10) Role of native oxide on Si substrate towards Au catalyzed growth of ZnO nanowires: Transition of growth mode from VLS to VS or vice versa,

    A. Ghosh, P. Guha, **A. Bhukta**, P. V. Satyam, *(Manuscript in preparation)*

11) Real time In-situ XRD study of Endotaxial Growth of Ag Nanostructures in Silicon, P. Guha, R. R. Juluri, A. Ghosh, **A. Bhukta** and P. V. Satyam *(Manuscript in preparation)*

Conference Presentations

1) Study of annealing dependence of MBE grown aligned binary alloy (Au-Ag) nanostructures on Si(5 5 12) substrate,

   A. Bhukta, A. Ghosh, R. R. Juluri, A. Rath, P. V. Satyam,

   International Conference on Electron Microscopy, EMSI, 2013.

2) Growth of Ag nanostructures on high index Si(5 5 12) surfaces under UHV condition : effect of prior surface treatment before deposition,

   A. Bhukta, P. Guha, A. Ghosh, P. Maiti, P. V. Satyam,

   Emerging trends in Advanced Functional Materials (ETAFM), 2016.

3) Study of ion irradiation induced structural changes in a Si/Ni/Si trilayer system,

   N. Banu, **A. Bhukta**, B. Satpati, B. N. Dev,

   International Conference on Electron Microscopy, EMSI, July 8-10, 2015 (Organized by BARC, Mumbai and IIT Bombay, Mumbai).

Synopsis

The thesis reports formation of Au-Ag bimetallic intermixed nanowire on one dimensional template of reconstructed Si surface. The reconstructed high index silicon surfaces (viz. Si (5 5 12)) surface which comprises row-like structures, can be used as template for growing aligned nanowires. By using a sub-monolayers of Ag, prior to Au deposition on reconstructed Si (5 5 12) surface, intermixing of Au and Ag, enhanced aspect ratio of bimetallic Au-Ag nanowires with tunable morphology is systematically studied and presented in this thesis work. Kinetic Monte Carlo simulations based on kinematics of adatoms on an anisotropic template with a solid on solid model in which the relative ratio of binding energies as obtained from the density functional theory (DFT) have been exploited, are in qualitative agreement with experimental data. Focused on reconstructed Si(5 5 12) surface, optimum growth condition for Au-Ag bimetallic intermixed nanowire growth has been reported with systematic variation of different thermodynamic conditions as metal thickness (Au, Ag), growth temperature. Dependence of morphological transformation of Au-Ag bimetallic growth on substrate orientation (hkl) of Si surface has been presented.

Reconstructed Si surfaces are very important for fundamental understanding and technological application of metal growth such that well-ordered and highly good crystalline quality and defect-free nanostructures with desired size, shape and composition could be grown [1-4]. Indeed, in spite of many drawbacks, large amount of abundance and low cost results in that nearly

90% of chip in the electronics and microelectronics are based on Si technology. Au and Ag are the two noble metals, which comprise isoelectronic property. Both metals are belonged to same crystal structure (FCC) and have almost same lattice constant ~ 4.08 Å. However, among them Au is slightly more electronegative and therefore $Au^{\delta-}$-$Ag^{\delta+}$ paring takes place after bond formation. High miscibility (even at room temperature) explores that they can form uniform solid solution at any desired composition ratio (Au:Ag) [5]. Hence, among the different bimetal pairs, Au-Ag bimetallic pair is considered as the ideal candidate for understanding different fundamental phenomena and technological applications for non-linear optics, catalysis, electronics etc. For example, surface plasmonic absorption peak of the Au-Ag bimetallic alloy nanostructure is successfully tuned with systematic variation of Au:Ag concentration ratio [6]. Au-Ag intermixing consequences enhanced catalytic efficiency of the metal nanostructures for oxidation of carbon monoxide [7]. They also have very remarkable catalytic property for hydrogenation of dimethyl oxalate to methyl glycolate [8].

In the Introduction Chapter (Chapter 1), the different aspects of nanotechnology and related issues to various nanostructures are briefly discussed. Focused on the different characteristics of metal nanoparticle, the important technological applications of bimetallic particles have been described. Among the different bimetallic particles, Au-Ag bimetallic particle play an important role and these nanostructures has been considered in this thesis. Following this, the significance of the molecular beam epitaxy (MBE) growth method in comparison with other ‘top down’ and ‘bottom up’ growth approaches has been discussed.

Further, necessity of studying Au-Ag bimetallic growth on reconstructed Si surface is also justified. However, the previous theoretical works in the literature, using DFT and KMC method to understand the different growth aspects of thin film and nanostructures have also been highlighted in this Chapter. Relevance of these two theoretical methods to understand the growth mechanism of Au-Ag bimetallic growth as reported in the present thesis work has been also pointed out.

In Chapter 2, discussion on the different growth modes of thin film growth in MBE method has been presented. Following this, the various experimental techniques that are used to carry out the present thesis work have been reported. In this Chapter, specimen preparation methods of different kinds of growth template *e.g.* reconstructed surface, Hydrofluoric (HF) treated surface have been detailed. For preparing thin film on different kinds of templates, MBE growth method has been briefly discussed. For characterization of growth templates and fabricated thin films, in-situ techniques like reflection high energy electron diffraction (RHEED), scanning tunneling microscopy (STM) is used. Other ex-situ techniques like scanning electron microscopy (SEM), transmission electron microscopy (TEM), scanning transmission electron microscopy (STEM), Rutherford backscattering spectrometry (RBS), X-ray diffraction (XRD) are also utilized. A brief description about the working principle and instrumentation of the aforementioned techniques has been detailed in this Chapter.

In the Chapter 3, the utility of reconstructed Si surfaces in terms of crystalline quality and morphology of the thin film has been discussed. For studying these aspects, Ag growth on reconstructed vicinal Si surface *i.e.* Si(5 5

12) has been worked out. The thesis work is centered around the role of surface and interface conditions for the growth of Au-Ag bimetallic nanostructures on Si surfaces. For this purpose, three types of surface treatments for Si(5 5 12) have been investigated. They are: (i) native oxide covered, (ii) Hydrofluoric acid (HF) treated and (iii) reconstructed. I have found that crystalline quality of the Ag nanostructures becomes polycrystalline, textured and single crystalline for growth on native oxide covered, HF treated and reconstructed Si surface, respectively [9]. Thin films of Ag have been grown in MBE method under UHV conditions. It is known that, HF treatment of native oxide covered Si surface results in partial removal of native oxide on the Si surface. Whereas, to achieve very good crystalline quality of the thin films, reconstructed surface is found to be essential. The morphology on native oxide covered Si surface found to have randomly oriented and irregular shaped nanostructures. On HF treated Si surface, both the oriented and randomly shaped nanostructures are formed. In contrast, on the reconstructed Si(5 5 12) surface, growth of two-fold symmetric and oriented growth of Ag nanostructures has been observed. Followed by the preferential mobility of the adatoms, grown nanostructures are found to be elongated along step edge direction Si$[1\bar{1}0]$ [10-12].

In the subsequent four Chapters (Chapters 4 - 7), discussions about the Au-Ag bimetallic growth on reconstructed Si substrates with systematic variation of relevant thermodynamic conditions to achieve desired morphology and compositions (such as substrate temperature, various annealing conditions, and substrate orientations) have been discussed.

In the Chapter 4, it is reported that, presence of an ultra-thin layer of Ag with sub monolayer thickness on reconstructed Si(5 5 12) surface prior to Au growth at elevated substrate temperature 300 ℃ results in formation of Au-Ag intermixed nanowires [13]. A detailed investigation with varying Ag thickness (Θ_{Ag}) for a fixed Au thickness (Θ_{Au}) and substrate temperature (T_{sub}) 300 ℃, revealed oriented Ag-Au bimetallic nanowire growth taking place for Θ_{Ag} as 0.50-1.00 monolayer (ML). As a result of modification of reconstructed Si(5 5 12) surface with Ag, aspect ratio of the Au-Ag nanostructures starts to increase for $\Theta_{Ag} \geq 0.25$ ML. In the regime of Θ_{Ag} 0.25-0.60 ML, from the fitted curve it is found, mean aspect ratio is rapidly increased with increase of Ag amount. But with Ag coverage above ~ 0.60 ML, the variation of aspect ratio becomes very small. Energy dispersive analysis of X-ray (EDS) mapping from cross section STEM measurements reveals that these nanowires are indeed composed of uniform bimetallic mixture of Ag and Au.

In the next subsection of this chapter (Chapter 4), a detailed theoretical approach to understand the growth mechanism of Au-Ag bimetallic growth on reconstructed Si(5 5 12) surface as mentioned in the preceding subsection is reported. Binding energy calculations of different pairs like Ag-Ag, Ag-Au and Au-Au which play crucial role for Au-Ag bimetallic intermixing, have been carried out considering dimmers on reconstructed Si surface using DFT model. Based on DFT results, the ratio of the binding energy $BE_{Ag\text{-}Ag}$: $BE_{Ag\text{-}Au}$: $BE_{Au\text{-}Au}$ has been used as parameters to carry on KMC simulation. Morphological aspects as found from the KMC simulations, in terms of variation of mean aspect ratio with Θ_{Ag} shows qualitatively good resemblance with the experimental outcomes. KMC simulations also reveal that, uniform Au-Ag bimetallic intermixing takes place throughout individual nanostructures as well. These results emphasize that acting of one-dimensional Ag strips as nucleation center during Au growth, due to strong Au-Ag mixing and anisotropic mobility of adatoms (Au and Ag), performs the decisive role for formation bimetallic Au-Ag intermixed nanowire.

In the Chapter 5, a detailed account of investigation on the optimum thermodynamic condition for growth of one dimensional bimetallic intermixed nanowire has been presented. The study has been carried out on morphological evolution after Au growth on Ag modified Si(5 5 12) surface for systematic variation of Θ_{Au} and T_{sub} [14]. It is shown that nanowire formation takes place at T_{sub} 200-300 ºC regime. At very low temperature, such as, room temperature (RT), Au/Ag thin film is grown. While, at larger temperature 400 ºC influence of Ag is found to be absent. Therefore, at RT mobility of Au and Ag adatoms are not enough for intermixing and formation of nanowires. The RBS measurements for a specimen with Ag growth at RT and subsequent annealing at 400 ºC, show a prominent inter-diffusion of Ag inside the Si substrate. It is hence inferred that due to absence of mobile Ag atoms on the surface during Au growth at 400 °C, Au-Ag intermixing doesn't not take place and role of Ag on Au-Ag morphology is absent.

Following this, growth of Au with varying thickness on Ag:Si(5 5 12) surface (with $\Theta_{Ag} = 0.5$ ML) at substrate temperature 300 °C (during Au growth) has been presented. Mean aspect ratio of the grown nanostructures is gradually increased with enhancement of Au thickness up to ~ 2.2 ML and thereafter reduces. It indicates, preferential accumulation of incoming Au adatoms towards the Ag strips takes place along Si$[1\bar{1}0]$ for low coverage of Au. For further enhancement of Au coverage above 2.2 ML, appreciable accumulation of Au adatoms begins along Si$[66\bar{5}]$ and smaller aspect ratio nanostructures are also grown. Therefore, for large Au coverage, mean aspect ratio of grown nanostructures is gradually decreased.

In the Chapter 6, effect of substrate orientation on the bimetallic growth has been worked out, and in particular on Si (1 1 0) surface. Considering the modification of ultraclean Si(110) surface using 0.50 ML Ag, investigations on morphological aspects using ex-situ SEM for variation of Au thickness and growth temperature has been presented [15]. These measurements show that Au-Ag nanowires are not grown at room temperature. On the other extent, for extremely high growth temperature 400 ºC also, growth of very large aspect ratio nanostructure doesn't take place. Effect of Ag to form extremely high aspect ratio nanostructures becomes very prominent in the temperature range 270-330 ºC. It is noteworthy to mention that, due to influence of sub monolayer Ag a single nanowire has been grown with exceptionally high aspect ratio ~ 45 with length ~731 nm. Morphological evolution of the nanostructures with variation of Θ_{Au} reveals, mean aspect ratio of the nanowires are gradually increased according the enhancement of Au amount up to 3.0 ML and thereafter reduces. It indicates, for increase of Θ_{Au} up to 3.0 ML, preferential accumulation incoming Au atoms takes place along Si$[1\bar{1}0]$ than its perpendicular Si[001] direction. But for Θ_{Au} above

3.0 ML, the effect of one dimensional Ag strips becomes weaker and appreciable coalescence occurs along both directions (*i.e.* Si[$1\bar{1}0$] and Si[001]), which causes reduction of mean aspect ratio.

In the succeeding chapter (Chapter 7), focus has been made to investigate role of orientation of Si surface with different (hkl) plane, on the morphology for Au-Ag bimetallic growth on reconstructed surface [16]. The general aspects of Au-Ag bimetallic growth on variation of the orientation of the substrate have been further explored in this Chapter. On the reconstructed Si(111) surface, due to pre modification of the ultraclean reconstructed Si surface with sub monolayer Ag one dimensional nanowires are not grown. Then these results are compared with the growth on Si(001), Si(110), Si(5 5 12) and Si(553) surfaces. It reveals that for formation of Au-Ag bimetallic one dimensional nanowires, preparation of one dimensional template like reconstructed Si(110) or high index Si surface is essential. Relative enhancement of the mean aspect ratio of the nanostructures due to Ag modification of the reconstructed Si(5 5 12) surface, with respect to ultraclean surface is found ~ 1.68 times. Comparative analysis for other one dimensional surface like Si(110) and Si(553) reveals, magnitude of such relative enhancement is nearly identical.

In the subsequent section, variation of length and width of the nanostructures with its size has been investigated. On ultraclean reconstructed Si(5 5 12) surface, both dimensions (length and width) of the nanostructures are steadily increased with its size. But on Ag:Si(5 5 12) surface, both length and width is gradually increased with size for smaller sized nanostructures. After an intermediate size, although the rapidity of variation length is not modified too much, the rapidity of variation of width is dropped down drastically. Above the intermediate size, width of nanostructures becomes a slowly varying function of its size. Such phenomenon shows quite resemblance with the ‘shape transition’ behavior [17-19]. If the interfacial strain, originated at the metal-semiconductor interface would play a role for such shape transition like behavior, then it should influence the monometallic growth of Au in the same manner. Because, both Au and Ag has similar lattice constant and they belong to FCC structure. So interfacial strain at the two interfaces (Au)/(Si) and (Au-Ag)/(Si) should be similar. The Ag strips which are acting as nucleation center during Au growth comprises one dimensional morphology. In comparison with the length of the Ag strips, widths are constrained and have finite magnitude. Therefore as Au-Ag intermixing takes place, constrained width of the Ag strips compels the resultant width of the bimetallic nanostructure to be restricted. The Au-Ag bimetallic nanowire growth on Si surfaces with the other (hkl) orientations of like (553), (110) and (001) has also been reported in this thesis. From comparative studies, this aspect is established as a general phenomenon on the reconstructed Si surface.

Following the experimental outcomes of Au-Ag bimetallic growth on reconstructed Si surface under various thermodynamic conditions and surface orientation, theoretical approach have been summarized at the end of the present thesis (in Chapter 8).

In conclusion, the thesis has dealt with growth, structural aspects and morphological evolution of Au-Ag bimetallic growth on reconstructed Si surfaces under various growth conditions. Prior to metal growth on Si surfaces, efficacy of reconstructed surface to achieve well-ordered growth and good crystalline quality of nanostructures has been reported, in comparison with native oxide covered and HF-treated surface. On reconstructed Si surfaces for Au-Ag bimetallic growths various conditions are considered as: annealing conditions, thin film thickness and substrate orientation. A complementary KMC model has been proposed which incorporates the inputs from DFT, to explain the experimental outcomes.

References

[1] Y.-W. Mo, D. E. Savage, B. S. Swartzentruber, M. G. Lagally, *Phys. Rev. Lett.* **65,** 1020 (1996).

[2] B. Voigtländer, T. Weber, *Phys. Rev. Lett.* **77,** 3861 (1996).

[3] U. M. Bhatta, J. K. Dash, A. Roy, A. Rath, P. V. Satyam, *J. Phys.: Condens. Matter* **21**, 205403 (2009).

[4] A. Rath, J. K. Dash, R. R. Juluri, A. Rosenauer, P. V. Satyam, *J. Phys. D: Appl. Phys.* **44**, 115301 (2011).

[5] H. Okamoto, T. B. Massalski, *Bull. Alloy Phase Diagra.* **4,** 30 (1983).

[6] M. P. Mallin, C. J. Murphy, *Nano Lett.* **2,** 1235 (2002).

[7] J. H. Liu, A. Q. Wang, Y.S. Chi, H. P. Lin and C. Y. Mou, *J. Phys. Chem. B* **109,** 40 (2005).

[8] J. Zheng, H. Lin, Y. Wang, X. Zheng, X. Duan, Y. Yuan, *J. Catalysis* **297,** 110 (2013).

[9] A. Bhukta, P. Guha, A. Ghosh, P. Maiti, P. V. Satyam, *Appl. Phys. A* **122,** 356 (2016).

[10] A. A. Baski, K. M. Saoud, K. M. Jones, *Appl. Surf. Sci.* **182,** 216 (2001).

[11] A. A. Baski, K. M. Jones, K. M. Saoud, *Ultramicroscopy* **86,** 23 (2001).

[12] J. W. Dickinson, J. C. Moore, A. A. Baski, *Surf. Sci.* **561,** 193 (2004).

[13] *Ag Induced Bimetallic (Au-Ag) Nanowires on High Index Silicon Substrates*, A. Bhukta, T. Bagarti, P. Guha, B. Satpati, P. Maiti, B. Rakshit, P. V. Satyam, *(submitted in J. Appl. Phys.).*

[14] Effect of Au thickness on AuAg bimetallic growth on Reconstructed Si(5 5 12) surfaces, A. Bhukta, A. Ghosh, P. Guha, P. Maiti, B. Satpati and P. V. Satyam *(accepted in Appl. Phys. A)*

[15] Growth of large aspect ratio AuAg bimetallic nanowires on Si(110) substrate, A. Bhukta, P. Guha, B. Satpati, P. Maiti and P. V. Satyam *(under review in Appl. Surf. Sci.).*

[16] *Ag induced shape transition of AuAg bimetallic nanostructures on ultra-clean Si substrates,* A. Bhukta *et al. (Manuscript in preparation).*

[17] R. Batabyal, S. Patra, A. Roy, B. N. Dev, *Appl. Surf. Sci.* **257,** 3248 (2011).

[18] J. C. Mahato, Debolina Das, R. R. Juluri, R. Batabyal, Anupam Roy, P. V. Satyam, B. N. Dev, *Appl. Phys. Lett.* **100,** 263117 (2012).

[19] W.-C. Yang, H. Ade, R. J. Nemanich, *J. Appl. Phys.* **95,** 1572 (2004).

Contents

3 Growth of Ag nanostructures on high-index Si (5 5 12) surfaces under UHV conditions: effect of prior surface treatment before deposition 71

7 Substrate orientation dependence of Au-Ag bimetallic growth on clean Si substrates 172

List of Figures

List of Tables

Chapter 1

Introduction

In the versatile region of science, ‘nanotechnology’ is considered as the special section, where fundamental research and its implementation for technological application is evolved with the particles having at least one dimension less than 100 nm [1- 4]. For example if we consider contraction of height only, nano thin film is formed. While contraction of two dimensions *i.e.* height and width results in formation of nanowire. Similarly, contraction of all the three dimensions *i.e.* height, width and length, consequence formation of nanodot. Since the dimensions of the particles are reached to the near quantum confinement limit, electron energy levels are significantly modified than its bulk value [5, 6]. Very often it causes dramatic alteration of various physical properties, which is the key aspect of modern nanotechnology. As the size of the particle is reduced, fraction of all the atoms on the surface is increased compared to the interior bulk region. This fractional value enormously enhanced when the particle dimension is reduced less than 100 nm. Indeed, increased *‘surface area to volume ratio’* for nano scale particles than the micron scale and bulk, become advantageous for their efficient implementation to numerous surface correlated processes. For example, with gradual decrease of size of the particles, a critical size exists in the nanoscale, which is a crossover between metallic-to-nonmetallic nature. Below the critical size, metallic nature of various metals like Cu, Pd, Au, Ag is switched to non metallic nature. Detailed understanding explores that metallic-to-nonmetallic transition is likely to be common for all the metals [7]. Such interesting phenomenon has been investigated in ambient and also ultra high vacuum (UHV) conditions, with various experimental methods like scanning tunneling spectroscopy (STS), X-ray photoelectron spectroscopy (XPS), ultraviolet photoelectron spectroscopy (UPS) etc. With gradual decrease of the size of the particles, inter-level spacing in spectrum of energy level becomes larger. Plausibly, in the vicinity of quantum size effect, such energy dependent enhanced gap plays the major role for insulating behavior of the metal below its critical size [8]. Several methods like electron microscopy, electron diffraction, XRD have been employed to determine melting point of nanoscale metal particle. Along with these, different properties of metal like crystallographic transformation, change in evaporation rate or change in magnetic susceptibility with variation of annealing temperature also have been monitored to determine melting point of the metal nanoparticles. Extensive studies on various metals like Sn, Bi, Pb, In etc. reveal melting point in nanoscale is smaller than the corresponding bulk value [9]. For any particle, surface atoms are very loosely bonded compared to the interior atoms due to smaller coordination number than the bulk region. Hence, in comparison with bulk dimension enhanced *'surface area to volume ratio'* of the nanoparticles consequences smaller melting point than its bulk value. Further, steady reduction of melting point is also takes place according to the gradual decrease of particle size [10]. Very large fraction of surface atoms also significantly modifies the magnetic property of the nanoparticles. A critical volume exists below which formation of smaller magnetic domains in expense of a larger domain become energetically unfavorable. Generally this critical volume denotes particle dimension as few tenths of nanometer. Below this size magnetic particle comprises many defects like atomic vacancy, unsaturated dangling bonds etc. which are originated from surface disorders. Therefore, in contrast with the interior region of particle, surface magnetization is composed of uncompensated disordered spins which leads to irreversible magnetization [11]. Enhanced fraction of surface atoms, also results in increase of active site for catalysis process [12]. Chemisorption of oxygen with gold is an endothermic process and this noble metal is apparently inert for formation of its oxide or to participate in other oxidation processes. But nano porous gold (NPG) particles, which are prepared by electrochemical dealloying process, show remarkable catalytic efficiency for oxidation of carbon monoxide (CO). Detailed investigation using spherical aberration corrected transmission electron microscopy (TEM) and environmental TEM reveal pronounced formation of steps and kinks on the surface of the NPG particles. These surface defects are ascribed to play the foremost role as active site for superior catalytic performance of NPG particles in oxidation process [13]. When electromagnetic light is incident on metal particle, electric dipole is crated due to partial shift of electrically negative electron cloud and positive core from each other. After removal of external electromagnetic wave, shifted electron cloud is attracted towards the positive core in other direction and shows an oscillatory behavior around the neutral position. However due to presence of damping force, such oscillation is stopped with a decaying variation. Quantization of such coherent oscillation of electron cloud is called *'plasmon'*. Bulk plasmon frequency of the metal particle is smaller than the surface plasmon frequency which is generated due to coherent oscillation of electron at the metal semiconductor interface (*e.g.* metal thin film in air). It is noteworthy that, for metals bulk plasmon frequency lies in ultra violet (UV) range, while surface plasmon lies in visible range of the electromagnetic (EM) spectrum. When the frequency of incident EM wave is matched with plasmon frequency of metal particle, resonance condition occurs. If the size of the metal particle is reduced to a regime comparable or smaller to plasmon frequency, absorption of EM energy by the metal particle is dramatically enhanced due to resonance effect [14]. Such phenomenon is explored for semiconductor nanoparticle in the infrared or mid infrared regime.

In the domain of nanotechnology, bimetallic nanoparticles are considered as a unique group, which has been studied extensively due to its interesting synergic effects. With the conventional size and shape control, bimetallic nanoparticles comprise another extra tuning factor *i.e.* composition. Very often, composition of two different metals, originates many advantageous synergic effects which are not present in their monometallic counterparts. Depending upon the growth conditions and metal-metal interaction, bimetallic nanoparticles are substantially categorized into three distinguishable structures as: (i) heterojunction, (ii) intermixed and (iii) core shell [15]. '*Heterojunction'* structure is formed when a single interface is shared by two monometallic counterparts. In this case, bonding or intermixing among the two different metals takes place only at the common interface. However two different materials could be intermixed and bonded throughout the entire regions of individual nanoparticle. Atomic arrangement of the two different metals takes place in either ordered or random manner, resulting in formation of '*intermixed'* structure. Other type of configuration arises when one type of metal is grown surrounding the other one. It resembles *'core-shell'* structure with bonding among the different metal atoms at the core-shell interfacial region. However in this configuration, multilayer core-shelling with alternating metal layer is also possible. The key physical properties which play detrimental role for structural variation of bimetallic nanoparticles are (i) inter atomic and intra atomic bond strength of the two metals, (ii) bulk surface energy of the individual metals, (iii) atomic size of the two metals, (iv) relative electro-negativity of the monometallic counterparts etc. If the relative strength of inter atomic bond strength is larger than the intra atomic bond strength, two metals generally try to combine with other. While, in the reverse scenario individual metal atoms try to agglomerate among themselves to form monometallic nanoparticle. In the bimetallic nanoparticle, one metallic component with smaller surface energy prefers to segregate towards the surface region to minimize the total surface free energy. Hence in spite of occurrence of uniform bimetallic mixing, enrichment of the surface and interior region with one particular metallic component takes place. When two atoms are brought close together due to repulsion of the electron cloud, *'steric effect'* becomes a decisive factor for resultant bimetallic configuration. It follows the fact that, to minimize the electronic repulsion, metal atoms with smaller size make an effort to be condensed in the core region of the particle. Appreciable difference in electro-negativity among the two different metal atoms causes to transfer of electronic charge towards more electronegative atom. Hence in such cases, alloying is favored due electrostatic hetero metallic bonding.

When multiple metallic components are combined, both the structural and morphological features of the nanostructures differ from their monometallic counterparts. Therefore many advantageous characteristics *e.g.* catalysis, electrocatalysis, nonlinear optics, of the nanostructures are suppressed or enhanced. For example, in hydrogenation process of cycloocta-1,3-diene to cyclooctene, core-shell nanostructure of Au-Pd (with ratio 1:4) perform as a superior catalyst than individual metallic components [16]. For hydrogenation process of nitrobenzene, Ni-Pd catalyst with varying composition ratio (Ni:Pd), has been used. In this case, catalytic performance has been explored as dependent on the Ni:Pd ratio of the nanostructures. For Ni:Pd ratio as 2:3, they comprise best activity which is 3.5 times larger than the typical colloidal Pd catalyst [17]. Based on porous rotating disk and disk-ring electrode technique, catalytic performance of carbon supported Pd-Co bimetallic nanoparticles with different Pd:Co ratio has been examined. Nanoparticles with Pd:Co ratio as 2:1, has been found to comprise best activity in such catalysis process [18]. Plasmonic property of the Ni-Ag clusters with diameter 2.70 nm has been investigated by Gaudry *et al.*

They have found slight blue shift of the wavelength in the absorption spectra with gradual increase of Ni:Ag concentration ratio [19].

In the resourceful domain of bimetallic nanoparticle, Au-Ag binary system has drawn significant attention of the researchers due to its high miscibility and subsequent advantageous physical properties. Au-Ag binary phase diagram reveals homogeneous mixing in the entire window of composition and temperature [20-22]. They are remarkably intermixed due to nearly zero lattice mismatch with face centre crystal (FCC) structure, isoelectronic property and comparable surface free energy. Miscibility among two monometallic counterparts is not influenced by lattice mismatched strain. It is known that the composition of Au-Ag bimetallic nanoparticles significantly influence surface plasmon resonance (SPR) phenomenon, caused by the EM field induced collective oscillation of electron cloud. Tuning of SPR absorption peak in the ultraviolet, visible and infrared region is potentially achievable with controlled variation of composition of Au-Ag binary system [23, 24]. Recently, different pairs of bimetal electrode, such as, Ru-Ta, Pt-Ta, and Au-Ag, have been suggested for continuous tuning of work function of the gate electrode over the desired range of the devices. Work function of the bulk alloy composite of Au-Ag system is followed by quadratic relationship as $\phi = \phi_{\mathrm{Ag}} + 0.91\mathrm{x}^2$, where x is the percentage of Au concentration in the alloy [25]. Specifically for p MOSFET devices, Au-Ag alloy is very suitable as constituent counterpart metals have work function nearly 5.0 eV [26]. Catalytic performance of Au-Ag alloy nanoparticles is significantly better than the counterpart monometallic nanoparticles, for oxidation of carbon monoxide (CO) [27], which is very crucial step to generate CO free hydrogen steam for superior performance of fuel cells at low temperature [28]. Improved catalytic property of Au-Ag bimetallic nanoparticle than the monometallic (Au, Ag) nanoparticle is also observed for hydrogenation of dimethyl oxalate to methyl glycolate at low temperature as 418 Kelvin [29]. Thus, Au-Ag binary system plays the role of an ideal model system, either for fundamental or technologically importance for comprehending miscellaneous tunable physical properties of a bimetal system.

Hence, widespread research works have been devoted, attempting to prepare Au-Ag BMNPs in numerous preparation methods like sol-gel [30], laser ablation [31-33], co-evaporation in physical vapor deposition (PVD) methods etc. But, either proficient exploitation for technological application or theoretical approach for understanding fundamental aspects of growth mechanisms, necessitate extremely organized and controlled morphology of the nanostructures in macroscopic scale.

Among the various *'self-assembly'* processes, molecular beam epitaxy (MBE) under ultra high vacuum (UHV) condition is considered as the most precise technique for preparing contamination free thin film. The word 'epitaxy' come from the Greek literature, where, 'epi' means 'above' and ' taxis' means 'an ordered manner'. In this method, thin film materials are heated above its sublimation temperature for evaporation [34]. Evaporation rate is tuned very accurately and substrate is generally kept at elevated temperature. Low incoming flux rate and appreciable mobility of the evaporating atoms (after reaching on the substrate) consequence formation of thin film with extremely good crystalline quality. This method also provides efficient manipulation of the crystallographic relationship among the thin film and underneath substrate. Hence, MBE method excels over other methods for fabrication of defect free devices like light emitting diode, field effect transistor, laser diode etc. When growth on reconstructed Si surface occurs, controlled morphology and composition of the nanostructures are successfully accomplished by the manipulation of various experimental growth parameters. After removal of native silicon oxide layer (~ 2 nm), unsaturated Si bonds are formed which is energetically unfavorable. To minimize the energy of the system the surface atoms are rearranged and hence 'reconstructed surface' is prepared. It is noteworthy to mention that, achieving desired reconstructed surface over a wide region of the surface is a challenging job. Presence of small amount contamination or irregularity of cleaning procedure, considerably change atomic ordering of the reconstructed surface. For over-layer growth of the thin films on reconstructed Si surface, ad-atoms comprise 4 fold, 3 fold and 2 fold anisotropic mobility for surface orientation (hkl) as (001), (111) and (110) respectively. Vicinal Si surfaces belong to sub category of single crystal Si surfaces, whose surface orientations are largely tilted with respect to stable low index planes. For example, Si(5 5 12) surface is an important vicinal surface for growth of one dimensional nanostructures, which is tilted ~ 30.5° from [001] to [111]. Other important vicinal surfaces are Si(553), Si(557), Si(112) etc. which exhibit stable reconstructed surface [35].

When the vicinal (high index) Si surfaces are reconstructed after removal of top native oxide layers, a one dimensional template for growth of nanostructures is formed. It consists of long range ordering of atomic height step and terrace like structure. After reaching on these templates, ad-atoms attain preferential mobility along the step edge direction. Subsequently, vicinal reconstructed Si surface are proficiently utilized for well-ordered growth of elongated nanostructures along its step edge direction [36-39].

In the present thesis work, we have studied Au-Ag bimetallic growth on reconstructed Si surface. Modification of reconstructed Si surface (Si(5 5 12), S(553), Si(110)) with sub monolayer Ag and then Au growth at elevated growth temperature 300 °C consequence formation of Au-Ag intermixed nanowires. Morphological aspects with variation of thickness of Au and Ag, growth temperature, orientation of the Si surface are also investigated. A kinetic Monte Carlo (KMC) model has been proposed based on the plausible growth mechanism of Au-Ag bimetallic intermixed nanowires. Results of KMC simulation are qualitatively matched with some morphological and structural aspects of our experimental outcomes.

The thesis is organized in the following manner. In Chapter 2, we have briefly discussed about different thin film growth modes which are originated by the interplay of surface-interface energy and lattice strain energy. Here we have also talked about working principle and instrumentation of growth technique and characterization of thin films. In Chapter 3, we have reported about the effect of different type surface treatment on the crystallinity and morphology of the grown

Ag nanostructures on Si(5 5 12) surface. It reveals for preparing well-ordered nanostructures with good crystalline quality, preparation of reconstructed surface is necessary. In the Chapter 4, we have described decisive role of Ag on Au-Ag bimetallic morphology and its composition on reconstructed Si(5 5 12) surface. At optimum coverage of Ag, Au-Ag bimetallic intermixed nanowires are grown. Plausible growth mechanism has been explained in the light of KMC simulation. Subsequently in Chapter 5, growth of Au on Ag modified Si(5 5 12) surface is considered for other experimental conditions *i.e.* varying Au thickness and substrate temperature. Formation of elongated Au-Ag bimetallic nanowires occurs at optimal condition of these two parameters. In the Chapter 6, we report on formation of Au-Ag intermixed nanowires, with extremely high aspect ratio on ultra-clean Si(110) surface. Morphological variation of Au-Ag growth, with varying Au thickness and substrate temperature has been also reported here. Following this, in the Chapter 7 role of crystallographic orientation *i.e.* (hkl) on the Au-Ag morphology has been investigated. From the comparative studies on different one dimensional reconstructed surfaces, general aspects of Au-Ag bimetallic growth has been elucidated. At the end, in Chapter 8, we have summarized entire experimental and theoretical outcomes, as described in the preceding chapters.

References

[1] C. P. Poole, Jr., F. J. Owens, *Introduction to Nanotechnology, Wiley-Interscience, Hoboken, NJ, 2003.*

[2] A. Dowling, et al., *Nanoscience and nanotechnologies: opportunities and uncertainties*, A Report by The Royal Society & The Royal Academy of Engineering, London, July 2004.

[3] G. M. Whitesides, *Small* **1,** 172 (2005).

[4] C. M. Lieber, *MRS Bulletin* **28,** 486 (2003).

[5] Y. Volokitin, J. Sinzig, L. J. De Jongh, G. Schmid, M. N. Vargaftik , I. I. Moiseevi, *Nature* **384,** 621 (1996).

[6] P. J. Feibelmen, *Phys. Rev. B* **27**, 1991 (1983).

[7] C. P. Vinod, G. U. Kulkarni, C. N. R. Rao, *Chem. Phys. Lett.* **289,** 329 (1998).

[8] H. N. Aiyer, V. Vijayakrishnan, G. N. Subbanna, C. N. R. Rao, *Surf. Sci.* **313,** 392 (1994).

[9] M. Takagi, *J. Phys. Soc. Jpn.* **9,** 359 (1954).

[10] Ph. Buffat, J-P. Borel, *Phys. Rev. A*, **13,** 2287 (1976).

[11] B. Issa, I. M. Obaidat, B. A. Albiss, Y. Haik, *Int. J. Mol. Sci.* **14,** 21266 (2013).

[12] R. M. Mohamed, D. L. McKinney, W. M. Sigmund, *Mater. Sci. Eng. R* **73,** 1 (2012).

[13] T. Fujita, P. Guan, K. McKenna, X. Lang, A. Hirata, L. Zhang, T. Tokunaga, S. Arai, Y. Yamamoto, N. Tanaka, Y. Ishikawa, N. Asao, Y. Yamamoto, J. Erlebacher, M. Chen

Nat. Mater. **11,** 775 (2012).

[14] P. K. Jain, X. Huang, I. H. El-Sayed, M. A. El-Sayed, *Plasmonics* **2**, 107 (2007).

[15] R. Ferrando, J. Jellinek, R. L. Johnston, *Chem. Rev.* **108,** 846 (2008).

[16] L. A. Pretzer , H. J. Song , Y. Fang , Z. Zhao , N. Guo , T. Wu, I. Arslan , J. T. Miller , M. S. Wong, *J. Catal.* **298,** 206 (2013).

[17] P. Lu , T. Teranishi , K. Asakura , M. Miyake, N. Toshima, *J. Phys. Chem.* B **103,** 9673 (1999).

[18] W. Wang , D. Zheng , C. Du, Z. Zou, X. Zhang, B. Xia, H. Yang , D. L. Akins , *J. Power Sources* **167,** 243 (2007).

[19] M. Gaudry, E. Cottancin, M. Pellarin, J. Lerme´, L. Arnaud, J. R. Huntzinger, J. L. Vialle, M. Broyer, *Phys. Rev. B* **67**, 155409 (2003).

[20] H. Okamoto and T. B. Massalski, *Bull. Alloy Phase Diagr.* **4**, 30 (1983).

[21] W. C. Mallard, A. B. Gardner, R. F. Bass, L. M. Slifkin, *Phys. Rev.* **129**, 617 (1963).

[22] J. L. White, R. L. Orr, R. Hultgren, *Acta Metall.* **5**, 747 (1957).

[23]D. –H. Chen, *J. Mater. Chem.* **12**, 1557 (2002).

[24] M. P. Mallin and C. J. Murphy, *Nano Lett.* **2**, 1235 (2002).

[25] S. C. Fain, Jr.* and J. M. Mcoavid, *Phys. Rev. B,* **9,** 5099 (1974).

[26] H. R. Gong, *Solid State Commun.* **149,** 2143 (2009).

[27] J. H. Liu, A. Q. Wang, Y. S. Chi, H. P. Lin, C. Y. Mou, *J. Phys. Chem. B* **109**, 40 (2005).

[28] J. N. Armor, *Appl. Catal., A*, **176,** 159(1999).

[29] J. Zheng, *J. Catal.*, **297,** 110(2013).

[30] S. Pal, G. De, *Chem. Mater.*, **17,** 6161 (2005).

[31] G. Compagnini, E. Messina, O. Puglisi, V. Nicolosi, *Appl. Surf. Sci.*, **254**, 1007 (2007).

[32] G. Compagnini, E. Messina, O. Puglisi, R. S. Cataliotti, V. Nicolosi, *Chem. Phys. Lett.* **457,** 386 (2008).

[33] P. Sangpour, O. Akhavan, A. Z. Moshfegh, *Appl. Surf. Sci.***253**, 7438 (2007).

[34] J. R. Arthur, *Surf. Sci*. **500,** 189 (2002).

[35] A. A. Baski, S. C. Erwin , L. J. Whitman, *Surf. Sci.,* **392,** 69 (1997).

[36] B. Z. Liu, J. Nogami, *Nanotechnology* **14,** 873 (2003).

[37] J. N. Crain, J. L. McChesney, F. Zheng, M. C. Gallagher, P. C. Snijders, M. Bissen, C. Gundelach, S. C. Erwin, F. J. Himpsel, *Phys. Rev. B* **69,** 125401 (2004).

[38] H. H. Song, K. M. Jones, A. A. Baski, *J. Vac. Sci. Technol. A* **17**, 1696 (1999).

[39] J. N. Crain, J. L. McChesney, F. Zheng, M. C. Gallagher, P. C. Snijders, M. Bissen, C. Gundelach, S. C. Erwin, F. J. Himpsel, *Physical Review B* **69,** 125401 (2004).

Chapter 2

Epitaxial growth of self-assembled nanostructures and different characterization techniques

2.1 Introduction

In this following chapter, we have discussed in detail about the different experimental techniques for understanding the various aspects of present thesis work as I have mentioned in the 'synopsis' section. At the beginning, we have discussed in detail about the methods for preparing the different kinds of template for the thin film growth. Following this discussion, method for preparing thin film and nanostructures has been described. At the end of this chapter, we have talked about the numerous in-situ and ex-situ characterization techniques to investigate the growth template and structural and morphological aspects of grown thin film and nanostructures.

2.2 Self-assembly process of growth of nanostructures

For fabrication of nanoparticles, a large number of techniques have been employed by the researchers in the different domains of modern research like physical science, chemistry, biology etc. Based on the growth strategies, these techniques could be classified into two kinds of methodology: (i) top-down and (ii) bottom-up [1].

In the 'top-down' approach, materials are gradually removed from its bulk sizes, until it reaches to nanoscale using different physical processes like cutting, slicing, milling etc. To achieve well-ordered array of nanostructures, along with the conventional lithography, other kind of lithography techniques are also used like photolithography, e-beam lithography, scanning lithography. In micro fabrication process, to achieve large scale production of nanostructures, 'top down' approach is routinely used. But major drawbacks like crystallographic structural damage, surface defect, internal stress in the fabricated nanostructures in this approach limits its applicability.

In contrast, 'bottom-up' approach is followed by adding of atoms, molecules or atomic clusters to achieve larger structure in nanoscale. Different techniques like sol-gel synthesis, chemical vapor deposition (CVD), physical vapor deposition (PVD), are categorized in this approach. In this approach, much smaller structure than the physical and instrumental limit of lithography is achieved. But in this approach, size, shape, patterning of the nanoparticles, become very complex due to trace amount impurity or small variation in growth condition. Self-assembling process of the atoms is remarkably influenced by the presence of catalyst, seed etc.

2.3 Growth Modes

Depending upon the nature of material of the thin film and the substrate MBE growth is classified as (a) homoepitaxy and (b) heteroepitaxy. In case of 'homoepitaxy' both the material are same (*e.g.* Si on Si(001)). In the reverse case where the materials are different from each other like Ge growth Si (or Au growth on Si), is considered as heteroepitaxial growth. Based on the thermodynamics conditions and the structural property of the materials, variety of growth mechanism takes place. From the name of the inventors, the different growth mode of the thin film on the various substrate are classified as FM (Frank-van-der Merwe) [2], VW (Volmer-Weber) [3] and SK (Stranski-Krastanov) [4] (Fig. 2.1).

a) FM or Layer-by-layer

In FM growth mode, the thin film grows as layer by layer manner. It indicates, new layer of the film starts to take place after the formation of the previous layer. In this case one layer first terminates or covers the substrate fully and thereafter the new layer starts to take place (Fig. 2.1(a)).

b) VW or Island

In this case, immediately from the beginning of thin film growth three dimensional (3D) islands are formed. As the growth continues, new ad-atoms are reached to the substrate, the 3D islands grow in volume and the new small islands also start to form (Fig. 2.1(c)).

c) SK or Layer-plus-island

In the mode 'SK' the growth phenomenon is intermediate among the above mentioned two modes. In particular, at the beginning, a two dimensional layer of thin film is formed. As the incoming of the evaporant atoms is continued, after a certain thickness, the incoming materials try to form 3D islands on the top of previously grown two dimensional (2D) layer (Fig. 2.1(b)).

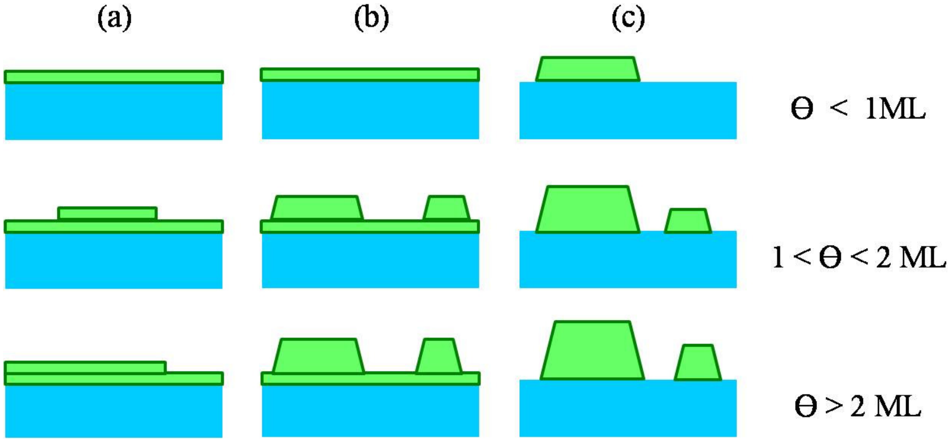

Figure 2.1 Schematic presentation of various types of growth modes: a) FM (layer-by-layer), b) SK (layer-plus-island) and c) VW (island). 'ϴ' indicates coverage of the thin film [5].

These three kinds of distinguishable growth modes are explained in the light of thermodynamic equilibrium conditions of the surface energies. Force required to create unit surface area for thin film, substrate and thin film-substrate interface is considered as thin film surface energy (σ_f), substrate free energy (σ_s) and interface energy (σ_i) respectively. Due to interaction of these three vector quantities most probable equilibrium condition is reached as [5]:

$$\sigma_s = \sigma_i + \sigma_f \cos\phi \tag{2.1}$$

It follows that, layer by layer growth takes place when $\Delta\sigma = \sigma_s - \sigma_f - \sigma_i > 0$. In this consideration, the lattice mismatched strain energy is absorbed in the σ_i term. In principle, magnitude of the different terms in the eqn. 2.1 is varied with change in thickness of the thin film, which requires a better presentation as [5]:

$$\sigma_s(n) = \sigma_i(n) + \sigma_f \cos\phi \tag{2.2}$$

for n^th layer from the beginning.

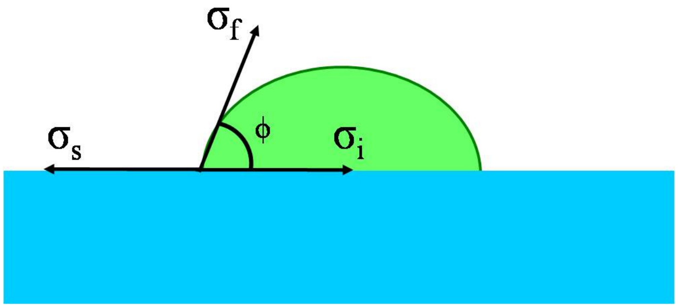

Figure 2.2 Schematic presentation to show relationship among 'surface energy' parameters for growth of island on the substrate. σ_s, σ_f, and σ_i is the surface energy of substrate, thin film and thin film/ substrate interface respectively [5].

When for all values of 'n' the thermodynamic condition of eqn. 2.2 is satisfied, layer by layer growth takes place. In case of homo-epitaxial growth the strain contribution in term σ_i becomes zero and the ideal condition of the 'layer by layer' growth is satisfied. The thickness dependency like strain energy, chemical interaction of the σ_i term, is gradually developed in other kinds of growth modes, and the different equilibrium condition is achieved like $\Delta\sigma < 0$. This condition is satisfied at the beginning of the thin film growth for VW growth mode. But for SK growth mode initially $\Delta\sigma$ remains zero and as growth is continued, after a certain thickness $n = n^*$, $\Delta\sigma < 0$ is attained.

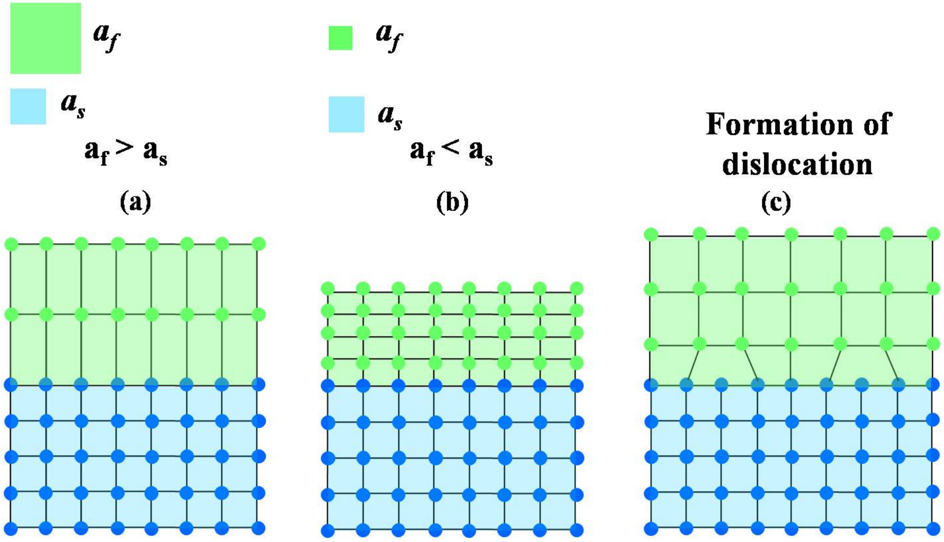

Figure 2.3 Influence of strain due to lattice mismatch between substrate and thin film in hetero-epitaxial growth. 'a_f' and 'a_s' represents lattice constant of thin film and substrate respectively. Effect on lattice structures by strained pseudomorphic growth fora) $a_f > a_s$ and b) $a_f < a_s$. c) Formation of dislocation due to relax of strained energy [6].

From the schematic diagram (Fig. 2.4), we find that if the strain misfit (η) is zero and the interaction parameter (W) is very large, the thermodynamics condition for

FM growth mode is reached. While for very large misfit (η), always VW growth occurs. In the region with small η and appreciable W, the intermediate growth condition between FM and VW takes place. This region in the diagram (as marked) denotes the layer plus island growth in the MBE process [7].

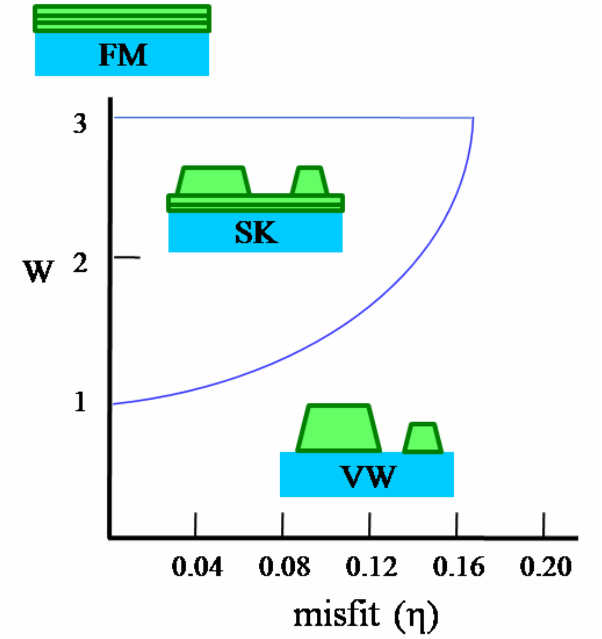

Figure 2.4 Schematic presentation to explore dependence of equilibrium growth modes on misfit (η) and strength of film-substrate interaction (W). FM growth takes place for η = 0.0 and W > 1. Other two growth modes (SK and VW) occur depending upon the relative strength of these two parameters. A representative solid line is drawn which distinguishes these two growth modes.

2.4 Molecular Beam Epitaxy (MBE)

In the MBE chamber the base pressure is routinely maintained ~ 2.0×10^{-10} mbar and it rises to ~ 1.0×10^{-9} mbar during the growth of thin film. Followed by the baking at ~ 130 °C for 24-30 hours, we use four types of pumps stepwise to achieve UHV inside the chamber. In the baking process, whole chamber is heated at ~ 130 °C which is much larger than the vaporization temperature of water molecule and many organic impurities. During 'baking' process, chamber is also simultaneously evacuated by turbo pump which is backed by the diapharm pump. Therefore all the vaporized impurity particles from the chamber wall, manipulator and the interior region of the chamber are pumped out to the atmosphere. At the end of this step, a typical vacuum level is achieved 1.0×10^{-8} mbar. Further higher level of vacuum is attained by the employment of ion pump. Due to application of very high bias voltage (typically kilovolt) all the impurity with ionic bond are ionized and attracted towards the electrode of opposite bias. Kinetic energy of the ions becomes sufficient to be buried to a depth nearly 10 atomic layers, inside the electrode after reaching there. In such a way, UHV in the range ~ 1.0×10^{-10} mbar could be achieved. Along with these pumps, in our set up Titanium sublimation pump (TSP) is also used to achieve better vacuum level. With passing a very current (~ 50 Amp), through the filament of TSP (filament is made of Ti-Mo alloy), they are heated up so much that titanium particles are come out. Then they form a getting layer of Ti inside the chamber wall. Such Ti atoms are very reactive and they form very stable, nonvolatile compound of Ti after reacting with residual molecules. Utilization of TSP, leads to efficient pumping of H_2, O_2, N_2

etc. and UHV level ~ 5.0×10^{-11} mbar could be reached. However, some residual elements like methane, 'inert gases' can't be pumped out by the employment of TSP.

Necessity of vacuum?

In the Table 2.1 we have summarized the variation of various parameters like (i) particle density (n), (ii) molecular incidence rate (φ), (iii) mean free path (λ) and (iv) time for formation of one atomic layer of residual gas (τ), in accordance with variation of base pressure (P).

Table 2.1: Evolution of various vacuum parameters, in accordance with variation of base pressure of the chamber.

P (Torr)	**n (molecules/cm^3)**	**φ (molecule/cm^2.s)**	**λ (cm)**	**τ (sec)**
760	2.49×10^{19}	2.88×10^{23}	6.7×10^{-6}	2.9×10^{-9}
1	3.25×10^{16}	3.77×10^{20}	5.1×10^{-3}	2.2×10^{-6}
10^{-3}	3.25×10^{13}	3.77×10^{17}	5.1	2.2×10^{-3}
10^{-6}	3.25×10^{10}	3.77×10^{14}	5.1×10^{3}	2.2
10^{-9}	**3.25×10^{7}**	**3.77×10^{11}**	**5.1×10^{6}**	**2.2×10^{3}**
10^{-12}	3.25×10^{4}	3.77×10^{8}	5.1×10^{9}	2.2×10^{6}
10^{-15}	3.25×10	3.77×10^{5}	5.1×10^{12}	2.2×10^{9}

Clearly, in UHV, particle density is reduced significantly compared to ambient condition. For a base pressure 1.0×10^{-10} mbar, the partial pressure of oxygen becomes ~ 1.0×10^{-12} mbar. The partial pressure of other elements like CO, H_2, N_2, H_2O also comes down in this range. After achieving UHV inside the chamber, the mean free path of the particles becomes several kilometers which is extremely large with respect to the dimension of the chamber. Large mean free path depicts appreciable reduction of collision probability among the residual gas molecules. Therefore thin film growth takes place very smoothly and with minute amount of impurity. In UHV regime, rate of formation of residual gas layer inside the chamber wall becomes very small. Therefore, after removal of top native silicon oxide layer clean Si surface is restrained for re-oxidation for ~ 12 hours in UHV. It becomes helpful, to carry out different in-situ characterizations like RHEED, STM on reconstructed surface before appreciable re-oxidation. Indeed, controlling of impurity level at its extremely low value is also essential because it significantly influences the surface atomic arrangement of the reconstructed surface.

In the field of thin film deposition, molecular beam epitaxy (MBE) is considered as one of the most delegate and refined technique for preparing defect free, contamination free thin film with extremely high crystalline quality [8] (schematically shown in Fig. 2.5). When the grown thin films are further processed for device application, based on transport properties, or optical properties, the interfacial defects drastically degrade the device quality. For preparing any metal semiconductor device like Ag/Si, formation of defect free single crystalline thin film is very essential. Amorphous or polycrystalline thin film with interfacial defect causes unavoidable dissipation of heat. Indeed the word ‘epitaxy’ comes from the literature of Greek language. ‘Epi’ means above and ‘taxis’ means a well-established relationship with the substrate. Grown thin film in this process conquers a very well ordered profound relationship with underneath substrate. In this method, incoming flux rate is maintained very small and the usually substrate is kept at elevated temperature than the room temperature.

As mentioned in the previous section, when the base pressure in the chamber reaches to the UHV regime, collision of the evaporant atoms (or molecules) with residual molecules becomes very insignificant. So, incoming flux of the evaporant atoms reaches to the template without any adequate disruption and form the thin film. Flux rate is reduced to very low value and finely controlled such that evaporant atoms sit on the nucleation centre on the substrate uniformly with a very high precision within the molecular beam size. Due to keeping the substrate temperature high, the evaporant atoms after reaching the substrate gains enough kinetic energy to migrate on the substrate and follow the atomic ordering of the surface atoms. If we either increase the flux rate or decrease the substrate temperature, after reaching on the substrate agglomeration among evaporant atoms takes place. In this case, crystalline quality of the thin film is degraded and instead of getting a single crystalline thin film, we generally get polycrystalline or amorphous thin film. For example, we have prepared Ag nanostructures on reconstructed Si(5 5 12) substrate with good crystalline quality at substrate temperature 400 °C and flux rate 0.4 nm/minute (Chapter 3). However, according to the requirements of achieving the degree of crystalline quality and other aspects, growth parameters are manipulated.

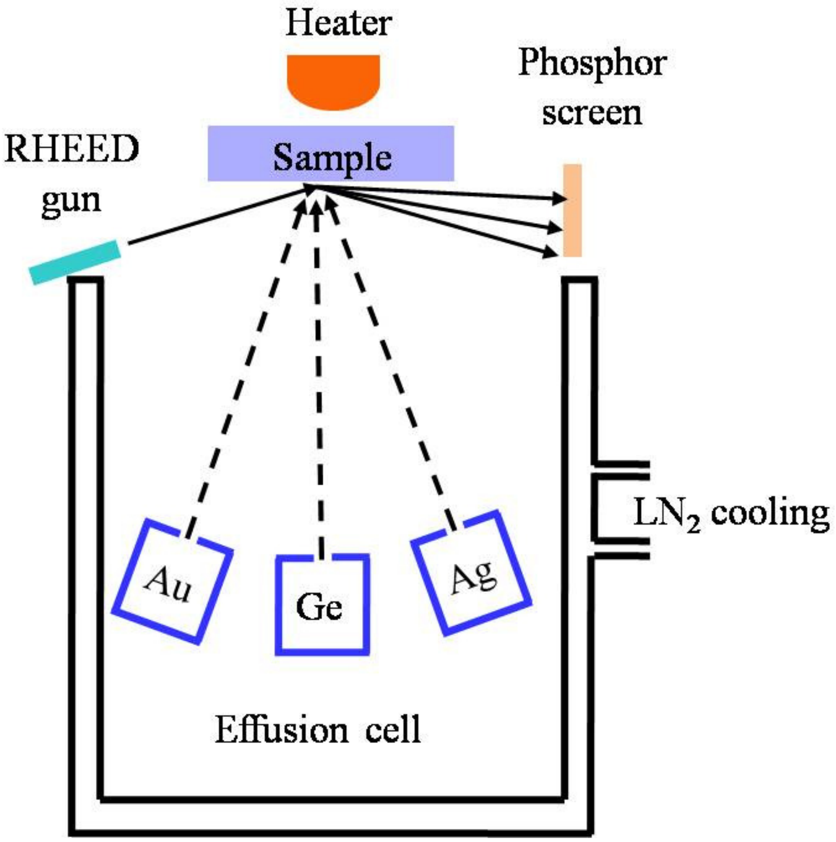

Figure 2.5 Schematic sketch of MBE set up depicting its main facilities effusion cell, substrate heater, LN_2 cooling and RHEED system (including electron gun, phosphor screen).

To carry out the growths of thin film which are presented in the present thesis work, we have employed a custom-build MBE set up (Omicron Vacuumphysik GmbH) (Fig. 2.6) [9]. Along with the MBE growth chamber a small load-lock chamber is attached for initial sample mounting and this chamber is pumped down using turbo pump which is backed by a diapharm pump. Then the sample is mounted on the manipulator (inside the MBE chamber) using a sample transfer mechanism with magnetically couple sample transfer rod. This manipulator comprises Z-translation (vertical) and X-, Y- translation facilities (horizontal). Along these, it can be rotated 0-360° azimuthally about the vertical direction (Z axis). Sample is cleaned using direct current (DC) heating and Ar ion sputtering methods. Using DC heating, we can increase the substrate temperature ~ 1200 °C. Manipulator is also comprised with another heating facility *i.e.* resistive heating, which allows controlling the substrate temperature by radiation of heat from a heater at backside of the sample. Utilizing the resistive heating facility, substrate temperature could be raised up to ~ 800 °C. Substrate temperature is measured using an external optical pyrometer and a type K thermocouple which is attached at the backside of the manipulator. For evaporation of thin film materials, Knudsen cell (K Cell) and e-beam evaporators are used. Out of four K cells, one (SEZ-40) has the facility to reach temperature up to ~ 1400 °C which is used for evaporation of Ag. Another two K cells (MTEZ) are used for evaporation of Au and Ge which have the facility to achieve temperature 1700 °C. Using other K cell (HTEZ), we can raise the temperature of source up to 1900 °C, which is employed for growth of MoO_3. For the growth of Si material, we use the e beam evaporator (EVC 300). Source temperature is generally measured utilizing a type C thermocouple which is placed below of crucible (with a gap ~ 1 cm), inside the K cells. Flux rate is finely maintained by means of control of source temperature using PID controller. Thickness of the grown thin films is determined with the help of a quartz crystal microbalance which has been calibrated by Rutherford backscattering spectrometry (RBS) at different flux rate. MBE growth chamber is also equipped with in-situ RHEED and VTSTM set up. For carrying out in-situ STM measurements, samples are transferred from MBE to STM chamber using the sample transfer mechanism using magnetically transfer rod. In the VTSTM chamber the base pressure is maintained ~ 2.0 × 10^{-10} mbar and substrate temperature is manipulated in the range 25-1400 °K.

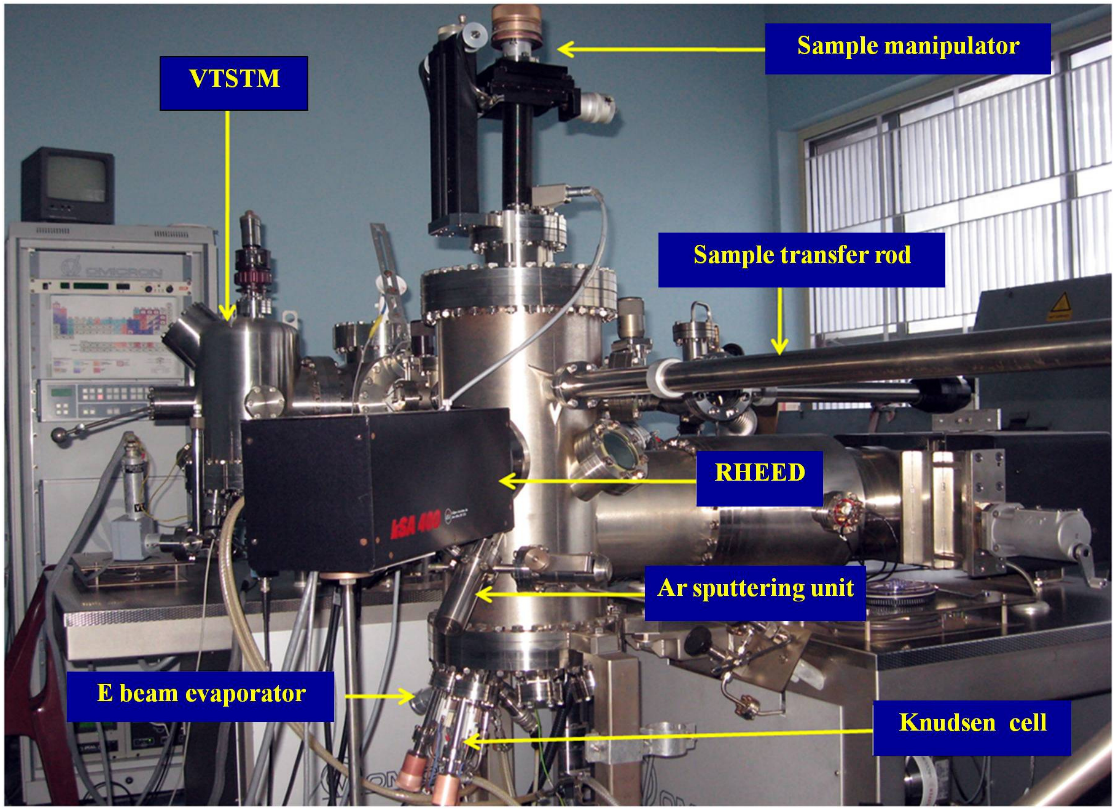

Figure 2.6 A custom designed compact MBE system with chamber diameter 250 mm, coupled with a variable temperature STM in Institute of Physics, Bhubaneswar.

2.5 Preparation of Growth Template

In the present thesis work we have considered growth of Au and Ag on the Si surface with various (hkl) orientations. A protective native oxide layer is immediately formed due to keeping Si wafer in ambient condition followed by its fabrication. Oxide concentration in this layer is gradually increased as we go from the top surface towards the bulk region of Si. It has typical width 2-5 nm and is amorphous in nature. It also contains some other compounds of Si like SiH_4, SiH_2 etc. Presence of this oxide layer works as barrier for any substantial influence of the substrate on the thin film growth above it. In some experiments, we have also used such native oxide covered surface. Depending on the cleaning procedure of this native oxide layer we classify the template in two types: (a) Reconstructed and (b) HF treated substrate.

2.5.1 Reconstructed Substrate

First we cut the commercially available Si wafer with size 3 mm × 8 mm according the suitable size in our MBE set up. Then it is ultrasonicated in methanol solution for ~ 5 minutes to remove different physically absorbed organic contamination and dust due to keeping in air. Thereafter it is brought inside the UHV chamber and degassed for 12-15 hours at 600°C. For degassing at elevated temperature we have used DC heating method, under ultra high vacuum (UHV) condition. In this method, a DC current (I) is passed through the sample and it is heated due to '*Joule's law of heating*' with power $P = I^2R$. Where, R is the resistance of the sample. Then it is treated a flash heating (very fast heating rate) at 1200 °C for one minute. Thereafter it is cooled down to 700 °C and kept for ~ 5 minutes. Due to heating at 1200 °C, native silicon oxide layer is removed and also many surface disordering of the top layer atoms also takes place. Post annealing at 700 °C after the flashing treatment results in the improvement of the crystalline disorder. Then it is brought to desired substrate temperature with extremely slow cooling rate. This procedure with the successive steps as mentioned above repeatedly carried out for achieve improved clean surface. Due to removal of the native oxide layer, surface atoms comprise unsaturated dangling bonds. Depending upon the (hkl) orientation of the single crystal substrate no of unsaturated dangling bonds per surface atoms varied. Formation of such dangling bonds is energetically not favorable and it brings the system to a higher energy level. To minimize the total energy of the system the dangling bonds form dimer and surface also absorbs some adatoms which are formed during removal of oxide layer and they rearrange themselves. After stabilization, rearrangements of the surface atoms become different than its bulk state. This phenomenon is called 'reconstruction'. Atomic arrangement of the reconstructed surface depends on many factors like (hkl) orientation of the substrate, cleaning procedure, contamination etc. For example reconstructed low index Si(111) surface shows '7 × 7' unit cell [10], while vicinal Si surfaces show step and terrace like structure, with atomic height step after reconstruction. On reconstructed vicinal Si surfaces, atomic rows are oriented along atomic step edge direction [11, 12]. To achieve reproducible reconstruction with very long range ordering, flashing conditions like annealing and cooling rate at high temperature range (600-1200 °C) is very crucial and challenging. Annealing at high temperature ~ 1200 °C, very often result in formation of granular shaped Silicon carbide (SiC) particles which is extremely undesirable for device fabrication and understanding various growth phenomena. Along with this, segregation of the dopant atoms towards the surface of the Si substrate is also takes place due to annealing at high temperature ~ 1200 °C.

2.5.2 HF treated Substrate

We have also cleaned the native oxide layer using water solution of hydrofluoric (HF) acid. First the wafer is cut to desired shape as mentioned above and its physically absorbed organic contamination and dust are removed using ultrasonication in organic solvent methanol. *'Piranha solution'* is prepared by mixing of concentrated H_2SO_4 and 50% H_2O_2 solution in 3:1 ratio [13].

After ultrasonication, it is brought to piranha solution for ~ 5 minutes and followed by rinsing for 10 minutes in de-ionized (DI) water. Then it is dipped inside 2% water solution of HF acid to remove the native silicon oxide layer. Followed by HF treatment, it is thoroughly rinsed in DI water for 5 minutes. Within 15 minutes, HF treated surface is brought to low vacuum (LV) in the load lock chamber. After keeping it in load lock chamber for ~ 2 hours, it is transferred inside the MBE chamber to carry out further experiments.

The native silicon oxide layer is removed by the formation of water soluble SiF_4 compound during etching process. Due to very robust corrosive nature of the etching of HF, slight variation of its concentration and etching time result in drastic change in the roughness of the template. As the different steps of the cleaning process is carried out in air and the HF treated substrate is kept inside the LV and HV ambience for prolonged time, very often appreciable re-oxidation takes place. In Si based technology for device preparation and nanofabrication process, etching of native silicon oxide layer is routinely carried out by HF treatment.

2.6 Characterization techniques

2.6.1 Reflection High Energy Electron Diffraction (RHEED)

RHEED is a surface sensitive technique, based on the electron diffraction in the reflection geometry, to investigate arrangements of surface atoms on crystalline substrate and monitor the thin film growth on it. This technique is routinely used in MBE method to understand the surface roughness, range of atomic scale ordering, surface defects (like steps and terrace) of the growth template. With in-situ facility, RHEED is also used to monitor different growth mode (FM, SK or VW) and thickness measurement. This technique also enumerate the crystalline quality of the thin film and the crystallographic relationship (epitaxial or non epitaxial) with the underneath substrate. When the coherent electron beam is incident on a surface having ordered array of the surface atoms and therefore is reflected the emergent electron beam comprises well defined phase relationship among the electrons. We have shown schematically this process in Fig. 2.7. If the in plane distance among the two successive scatters is ‘d’ and the incident electron beam and the reflected electron beam make angle respectively Θ_1 and Θ_2 with the surface, the path difference (Δ) in between two consecutive reflected electron beam becomes $d\times(\cos\Theta_1 - \cos\Theta_2)$.

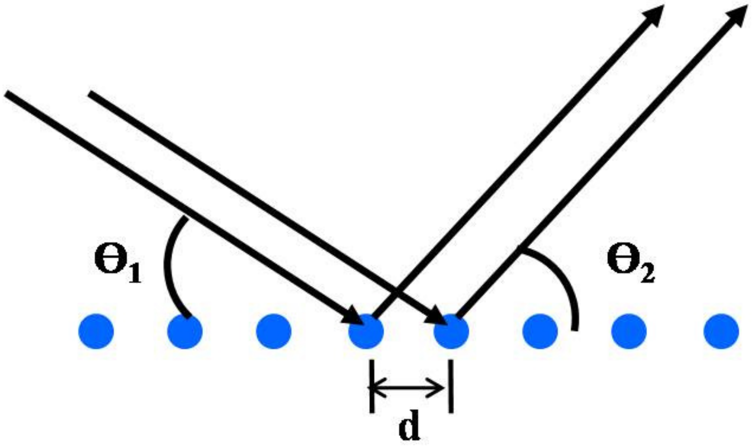

Fig.2.7 Diagram to show path difference in the reflected electron beam from two consecutive atoms in a one-dimensional chain.

Therefore if the path difference Δ becomes an integral multiple of the de Broglie wavelength of the electron (λ) such that $\Delta = n\lambda$, the constructive interference takes place. Therefore on the fluorescent screen (as shown in Fig. 2.8), constructive diffraction spot with different values of n = 1, 2, 3 are generated. Long range ordering of the surface atoms results in formation of well defined diffraction spots and high contrast. For n = 0, an intense bright spot is observed on the screen which indicates the specular reflection of the incident electron beam. As the inter-scattering element distance (d) on the plane is changed, distance of the diffraction spots from direct beam spot is varied for higher values of ‘n’ *i.e.* n = 1, 2, 3 etc.

We have shown the formation of ewald sphere when electron beam is incident on the surface in RHEED method (Fig. 2.8). In respect to the spacing (~3 Å), between the successive scatterers on the surface, radius of the ewald sphere become very large due to using a high energy (~ 20 keV) of electron. Due to incidence of electron in nearly tangential condition, only few top atomic layers of the substrate participate in the interaction process with the electron. Comparing this distance from the top of the surface (Δz), in other two direction length for electronic interaction process (Δx and Δy) becomes infinitely large. Therefore, reciprocal space for this substrate comprises of reciprocal rods only. Such reciprocal rods are finite in the two directions (X and Y) along the substrate plane and infinite along the vertical direction of the substrate [14]. When these reciprocal rods intersect the ewald sphere, it gives rise to formation of constructive diffraction (Fig. 2.8). Due infinite dimension of the reciprocal rods in z direction, compared to other two directions, constructive diffraction results in streaky nature on the screen. As the thin film growth takes place and the 3D islands are formed, electron beam transmits through the nanostructures. Then the dimensions Δx, Δy and Δz along three orthogonal directions become finite. Consecutively in the reciprocal space, instead of formation of infinite reciprocal rods, a set of spots is generated. Hence the streaky pattern of the RHEED, becomes spotty in nature after formation of the 3D nanostructures.

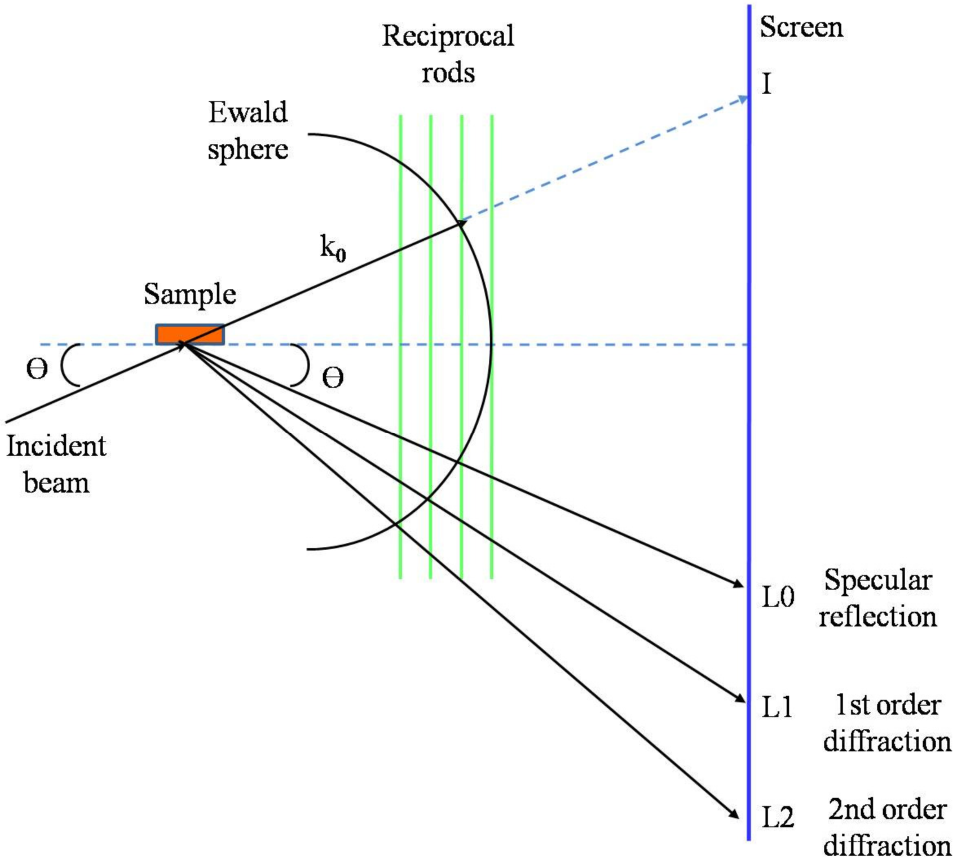

Figure 2.8 Ewald sphere construction during diffraction of electron in RHEED method.

As the electron beam is incident on the surface in a grazing condition with angle of incidence 1-3°, the vertical component of the electron beam (towards the substrate), in comparison with the horizontal component, becomes very small. It follows that only few planes of the substrate, contribute in the interaction process of the electron with the substrate and therefore it is considered as very delegate surface sensitive technique. When the three dimensional nanostructures are formed on the surface as a result of thin film growth, electron beams are transmitted and the diffraction takes place among the different planes of the nanostructures. Indeed, this phenomenon becomes similar as the transmission electron diffraction (TED) in the TEM method [15]. Schematically we have shown such diffraction process in Fig. 2.9. However, inappropriate sample preparation method and presence of appreciable amount of contamination also gives rise to transmitted electron diffraction.

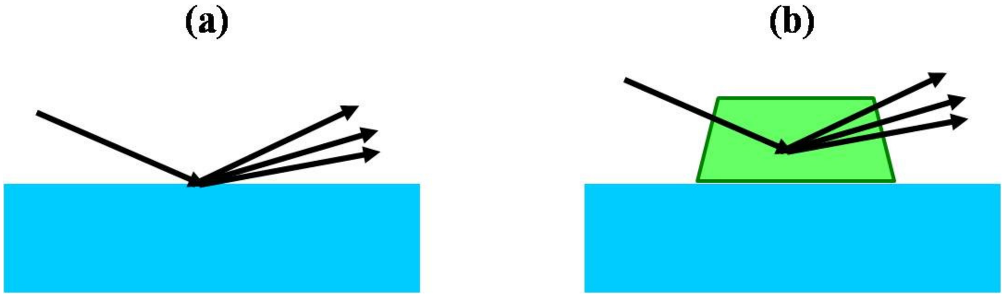

Figure 2.9 Schematic of electron diffraction in RHEED method due to a) reflection from the surface and b) transmission through the crystalline three dimensional islands.

In our laboratory, we have performed in-situ RHEED measurements for growth of Ge thin film on reconstructed Si(111) surface using electron beam with energy 17.2 keV and angle of incidence 2° (Fig. 2.10). In the 2.10 (a), we have shown a RHEED pattern on the reconstructed Si(111) substrate along azimuthal direction

Si[11$\bar{2}$] which comprises the '7 × 7' reconstruction. Such diffraction pattern is transformed to TED pattern when we have grown Ge on it (Fig. 2.10 (b)). Grown thin film is found to have epitaxial relationship with the underneath substrate.

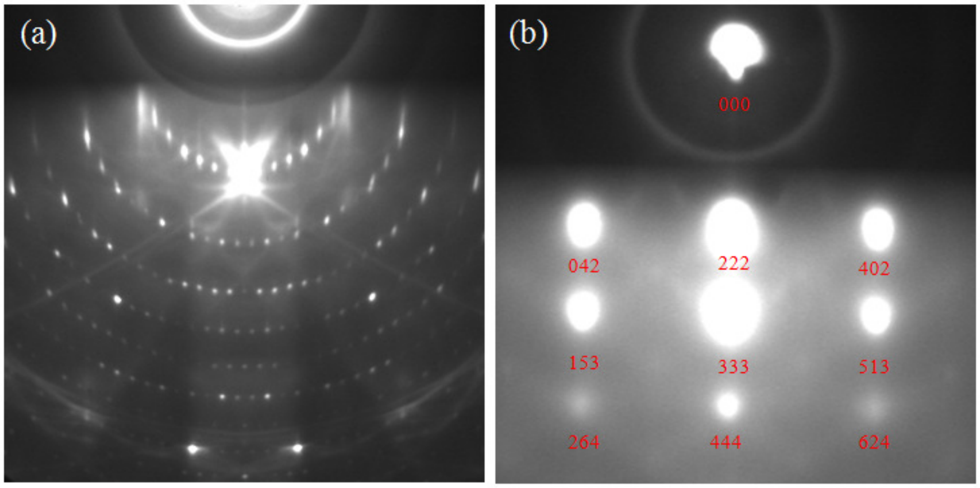

Figure 2.10 RHEED pattern along azimuthal direction Si[11$\bar{2}$] of a) reconstructed Si(111) surface and b) after the growth of Ge on reconstructed Si(111) surface.

2.6.2 Scanning Tunneling Microscopy (STM)

Scanning tunneling microscopy is the one of most powerful tool which allows the researchers to image and study different electronic properties in atomic scale for the metallic, semiconductor or thin insulator surfaces. Beside its utilization in UHV condition, it is successfully used in water, in other liquids, air and other gas ambience.

When the tip is brought to the surface very close with a typical gap less than 1.0 nm, wave functions of the tip atom and surface start to overlap. In this condition, if an electrostatic bias voltage is applied between the tip and the surface, quantum mechanical tunneling of the electrons takes place (Fig. 2.11). Depending on the polarity of bias voltage, electrons tunnel from the tip to the surface or vice versa. The magnitude of the tunneling current depends on the various factors like tip to surface distance, magnitude of the bias voltage, local density of states of the tip atom and sample atom. Dependence of tunneling current on these parameters for small bias voltage could be represented as:

$$j = \frac{D(V)V}{d} \exp\left(-A\sqrt{\phi} d\right) \qquad (2.3)$$

'D(V)' and 'V' is electron density of state and bias voltage respectively. 'A' is a constant, 'ϕ' is effective barrier height at the tip sample junction and 'd' is the tip-sample distance. It indicates that, small variation of the tip to sample distance by 1 nm results in the variation of the tunneling current by a factor 2. Therefore this technique is highly sensitive for height variation with resolution 0.01 nm. During scanning with an atomically sharp tip, 90% of the total current is passed from the last atom of the tip to local surface atom and it causes the horizontal resolution 0.1 nm.

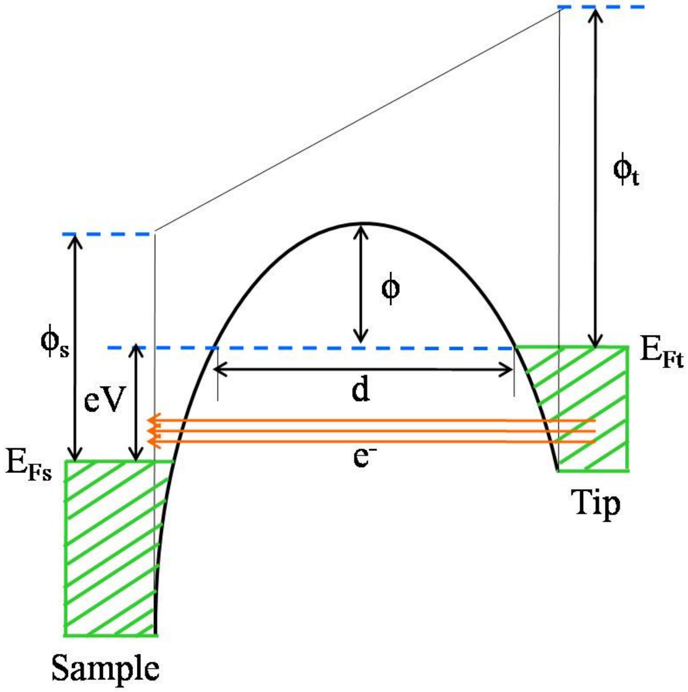

Fig. 2.11 Energy diagram after reaching of tunneling condition between tip and sample. Work function and Fermi level of the sample is denoted by ϕ_s and E_{Fs} respectively. Similarly, for tip, work function and Fermi level is denoted by ϕ_t and E_{Fs} respectively. An external electrostatic positive bias voltage 'V' is applied to the sample and consequent tunneling of electrons from tip to sample is shown as orange colored arrow line.

STM tip is generally prepared using wires of different metals like W, Au, Pt-Ir, Rh-Ir etc. by electrochemical etching or mechanical cutting. After these ex-situ processes, in-situ field emission, annealing are also performed to improve the tip quality. Sometimes, 'soft crash' of the tip on the surface also results in formation of good quality tip. Piezoelectric ceramics are used as electromechanical transducer in the scanner, which is attached with the tip. Bias voltages are provided to the scanner by the external electrodes for the movement in ±X, ±Y and ±Z directions (Fig. 2.12). Application of alternating voltage in the X and Y electrodes causes the scanner to bend back and forth in X and Y direction horizontally. Similarly, voltage is applied in the Z electrode to control the vertical motion of the scanner. During scanning process typically linear motion of tip from a fraction of Angstrom to few micrometers takes place by the conversion of electrode voltage 1 mV to 1 kV.

Modes of operation

After choosing a frame, tunneling current is acquired at each individual data point and therefore transformed to image using the electronics. Depending upon the electronic configurations, imaging by STM could be classified in two different modes: a) constant current and b) constant height. Two kind of imaging modes have been shown in Fig. 2.13.

Constant current mode

In this mode, tip is scanned over the surface by maintaining constant current and voltage (Fig. 2.13(a)). During scanning, roughness of the surface causes fluctuation of tunneling current for invariant bias voltage. But the tunneling current is again brought back to initial value (set point value), by applying feedback voltage (V_Z) to the Z electrode. Amount of V_Z which fed to the Z-piezoelectric driver by the feedback circuit, is determined by the amount of fluctuation in tunneling current. Further signal V_Z is acquired at each data point and processed for image formation. Image processing for an electronically homogeneous system depicts, height profile of the scanned area is evolved accordingly with V_Z. But in real situations, variation of V_Z also depends on the other parameter *i.e.* local work function on the sample surface. Therefore imaging in this mode is actually explores a constant current surface according to the experimental conditions. Although this method is extensively used for imaging, scan speed and data acquisition takes place slowly because of finite response time in feedback system.

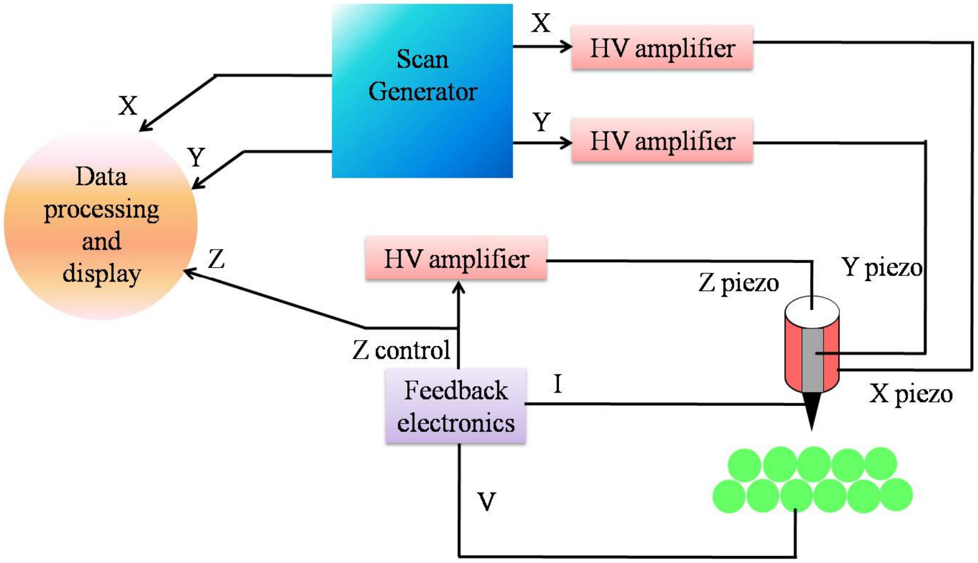

Figure 2.12 Schematic presentation to illustrate different section of STM set up.

Constant height mode

In this mode, the feedback circuit is switched off and feedback voltage to the Z piezo electric driver (V_Z) doesn't influence the scanning of the tip (Fig. 2.13(b)). During scanning, evolution of height profile of the surface consequences variation of tunneling current for fixed sample bias voltage. Therefore, such variation of current is processed for image formation. In contrast with constant current imaging, this method is not influenced by the finite response time of the feedback signal. Hence, it enables to investigate dynamical process like surface diffusion by fast imaging. However, to image in this method, formation of smooth surface is required to avoid 'tip crash', which constrains its applicability.

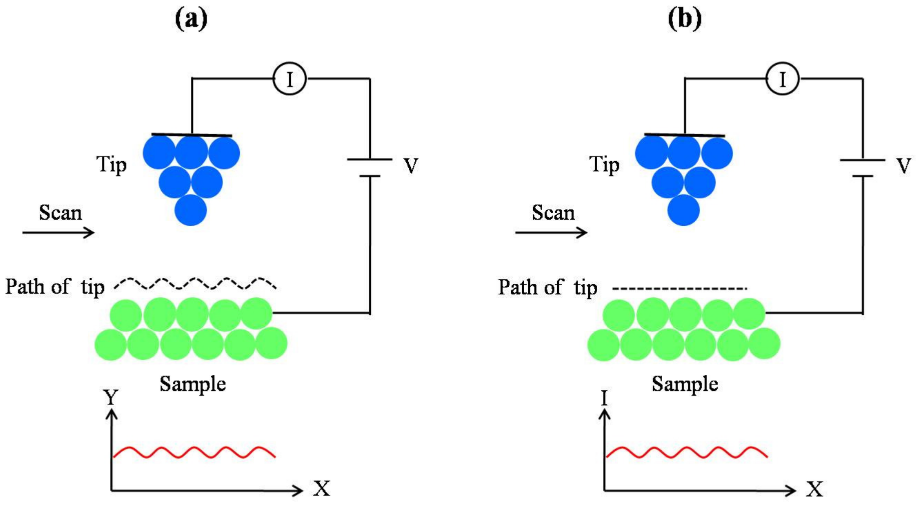

Figure 2.13 STM measurements are performed in two different modes as schematically shown in a) constant current mode and b) constant height mode [16].

Scanning tunneling spectroscopy (STS)

Within small range of bias voltage (milivolt), tunneling current for the metal surface is varied linearly with applied voltage. However if bias voltage is increased to the order of voltage, ohmic relationship among the tunneling current and applied bias is not obeyed (particularly for the semiconductors). Fig. 2.14 shows the simplified one dimensional energy diagram at temperature zero Kelvin based on sample–tip interaction. If the bias voltage is not provided to sample, the

Fermi level of the sample and tip are not influenced and equilibrium condition is established (as shown in Fig. 2.14(b)). As the sample is positively biased with voltage V with respect to tip, its Fermi level (of the sample) is reduced by amount $|eV|$ from the equilibrium condition. Hence a finite tunneling current is originated due to tunneling of electrons from the occupied state of tip to unoccupied state sample (Fig. 2.14(c)). If the sample is negatively biased, then the reverse scenario arises and electrons tunnel from occupied state of sample to unoccupied state of the tip. For a particular tunneling event, magnitude of tunneling current (I) depends on the density of state (DOS) of the sample (n_s) and tip (n_t), corresponding to their energy levels. It also depends on the bias dependent transmission coefficient (T) of tunneling current. Indeed, such dependence could be expressed as:

$$I \sim \int_0^{eV} n_t(\pm eV \mp E) n_s(E) T(E, eV) dE \tag{2.4}$$

Here, energy (E) is measured with respect to Fermi level.

In the Fig. 2.15, we have shown STM image of reconstructed Si(111) surface at RT as obtained by us in our laboratory. We have also carried out STM measurements on highly oriented pyrolytic graphite (HOPG) substrate at RT and the images are shown in Fig. 2.16 (a). Following the imaging, I-V spectroscopy has been also done for a constant tip to sample distance (Fig. 2.16 (b)) at different regions of the sample.

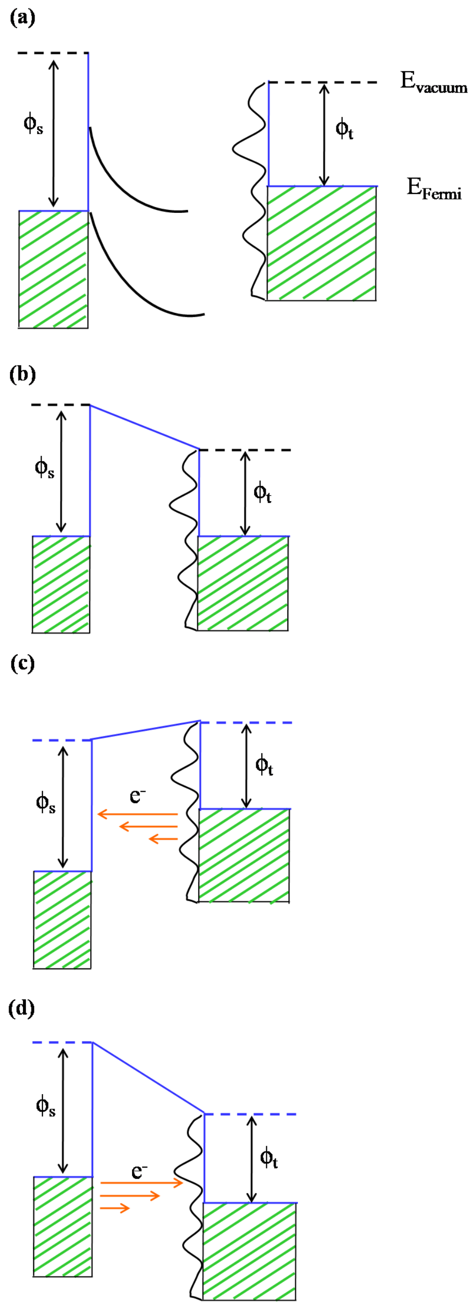

Figure 2.14 Schematic presentation of energy level diagram of sample and tip a) independent of sample and tip with large gap among them, b) equilibrium condition among sample and tip due to small vacuum gap among them, c) sample is positively biased and d) sample is negatively biased. In Fig. 2.14 (c) and (d), orange colored arrow line indicate the tunneling of electrons [16].

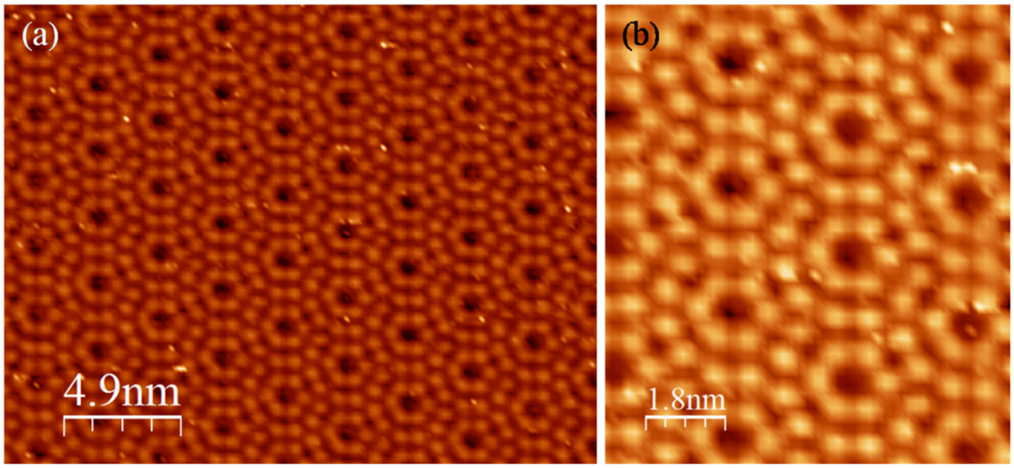

Fig. 2.15 a) and b) STM topographic image at room temperature of reconstructed Si(111) surface with sample bias +2.0 V and tunneling current 0.20 nA.

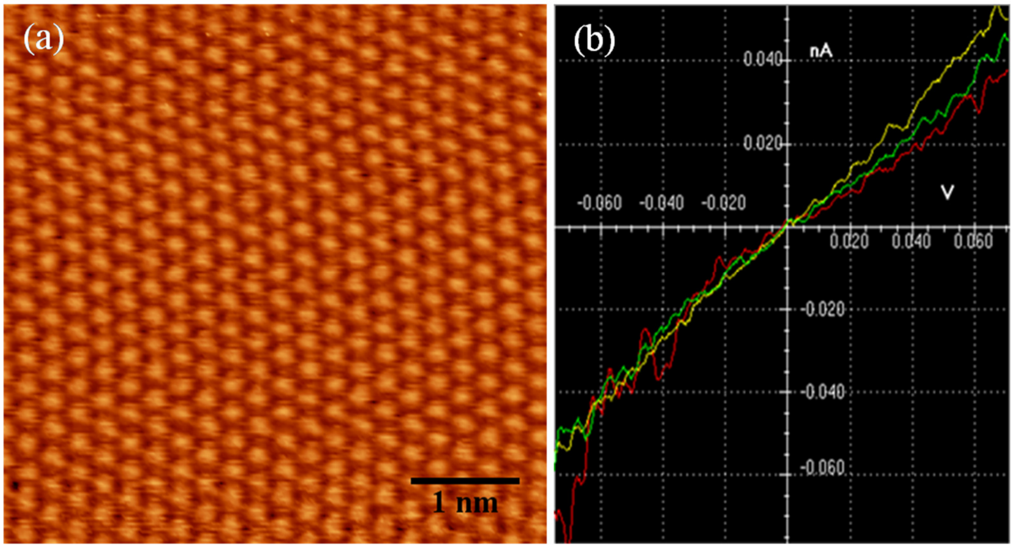

Fig. 2.16 STM measurement at room temperature on HOPG substrate a) topographic image with sample bias +0.4 V and tunneling current 0.50 nA b) I-V spectroscopy on various regions of the substrate.

2.6.3 Transmission Electron Microscopy (TEM)

Among the various microscopy techniques, TEM is an important technique where very high energy electron beam interacts with the material by passing through the ultra thin region. Owing to the fact that, using optical microscopes resolution in submicron length scale is not achievable, possibility of using electron for imaging has been proposed by Knoll and Ruska [17]. They have build up the concept of electron lenses based on the wave nature of the electrons, in analogous to the optical lenses. In reality, for very high energy (200 keV) electron, its de Broglie wave length becomes so small that single atomic column could be resolved. In addition with capability of extremely high resolution, TEM method is successfully used in the diverse field of nanotechnology with its other associated accessories like EDS, STEM etc.

In TEM method, specimen is thinned so much (< 100 nm) that high energy (200 keV) electron could pass through the specimen. As the electron beam interacts with specimen material, many secondary signals are generated (Fig. 2.17). The primary beam which is transmitting through the sample is used for imaging, while other secondary signals are used for different analytical studies. For the primary beam, if the thickness of the thin film or atomic number (Z) is larger, then scattering is more therefore resultant image comprises darker contrast. Scattering becomes less when thickness or the atomic number (Z) becomes less and consequences brighter contrast. It is called '*mass-thickness*' contrast. Electron diffraction condition is modified if crystal orientation is varied among the different grains of the thin films or formation of defects within the individual grain. Near the region of defect such as dislocation, electron beams are strongly diffracted and originates darker contrast. Such dependency of diffraction on the crystallinity of the thin films, results in generation of contrast in the image and it is called *'diffraction contrast'*.

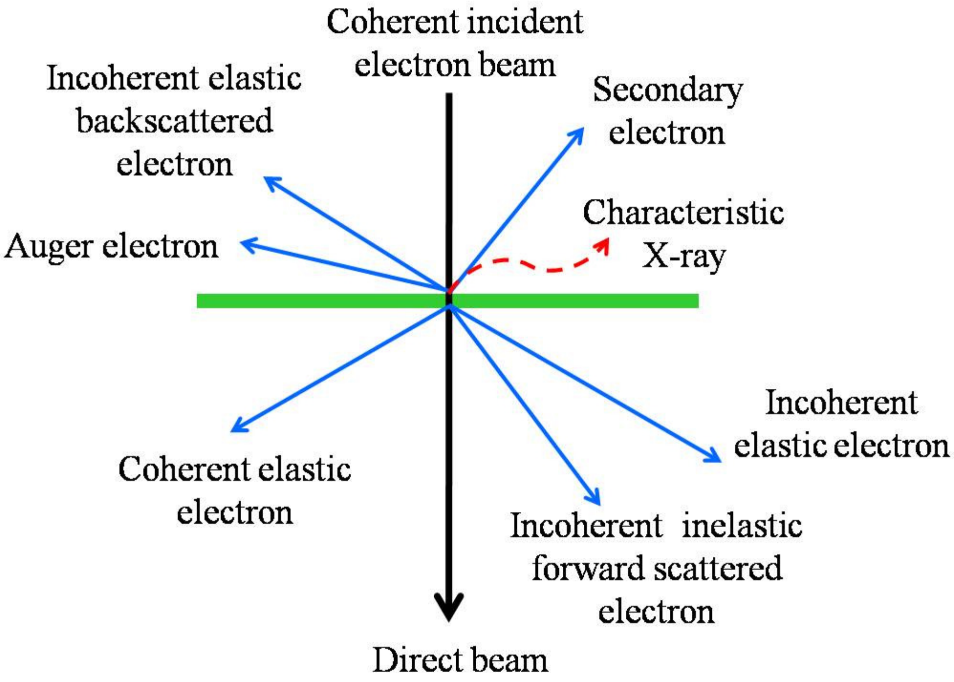

Figure 2.17 Schematic presentations of different processes and generation of many secondary signals along with the direct beam, due to electrons-solid interaction.

Schematically, we have shown the mechanisms of formation of image and diffraction pattern by the elastically scattered electron from the ultrathin regions of the specimen in Fig. 2.18. After emission from the source, electrons are focused by the electrostatic lens made in the shape of 'wehnelt cup' to converge maximum no of electrons on the specimen (Fig. 2.18(a)). In the case of a very thin specimen, elastically scattered electrons comprise coherent relationship among themselves. They form image and diffraction pattern in the image plane and back focal plane of the objective lens, respectively. Diffraction pattern is generated due to the fast Fourier transformation (FFT) of the electron waves at the back focal plane of the objective lens. While another FFT of those electron wave at the back focal plane of the objective lens results in formation of high resolution lattice image (Fig. 2.18 (b) and (c)).

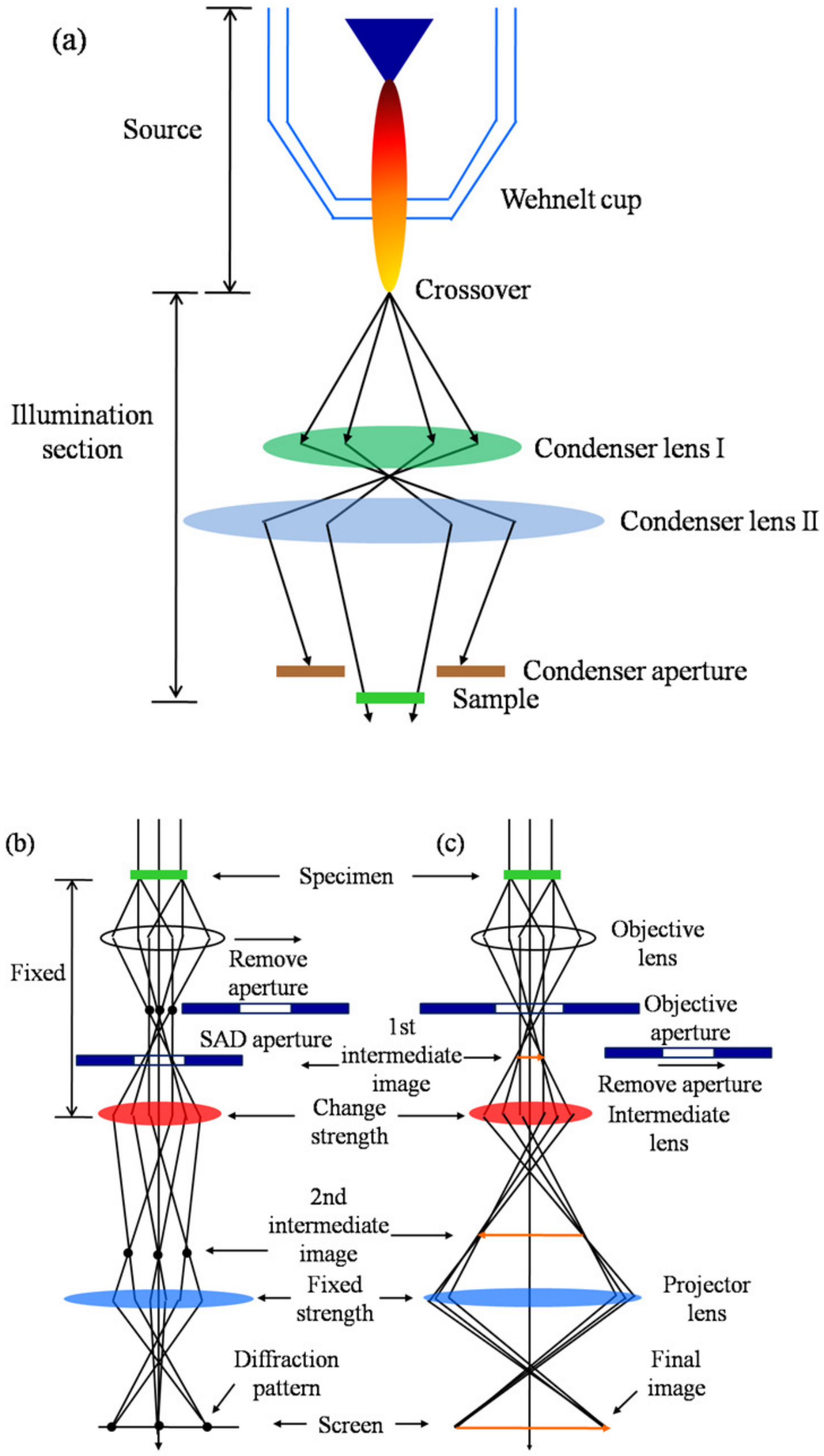

Figure 2.18 A schematic diagram to show the different part of TEM as a) filament and illumination, b) diffraction formation and c) image formation [18].

Instrumentation

Generally a TEM set up could be divided into three distinguishable segments: (i) illumination system (ii) objective lens/stage and (iii) imaging system (Fig. 2.18). 'Illumination system' consists of electron guns either thermionic (W, LaB_6) or field emission in nature. For carrying out the operation in TEM, type of electron gun is chosen based on the different parameters like work function of electron source material, operating temperature, life time, cost etc. Illumination system also includes the only electrostatic lens (in the shape of 'wehnelt cup' in Fig. 2.18(a)), which plays the role to converge maximum fraction of the emergent electron beam from the source. Followed by the 'objective lens/ stage' section, after the interaction of the electron beam with the specimen, objective lens form image or SAED pattern. Indeed this section is the most crucial part of the TEM because performance of the objective lens determines the resolution of the resultant image. Then in the next section 'imaging system', generated image or SAED pattern is magnified by the different intermediate lenses. After that, projector lens plays the role to project the image to the CCD/TV camera which is coupled with the computer to acquire the data. To carry out the TEM measurements, we have utilized a JEOL-2010 set up, operating at 200 keV (Fig. 2.19) [9]. The objective lens consists of ultra high resolution pole piece (UHR-URP22) with spherical aberration coefficient 0.50 mm. Indeed it is capable of reaching point-to-point resolution 0.19 nm. Image is acquired in frame size 4008×2672 pixels using a charge coupled device with time resolution 40 ms.

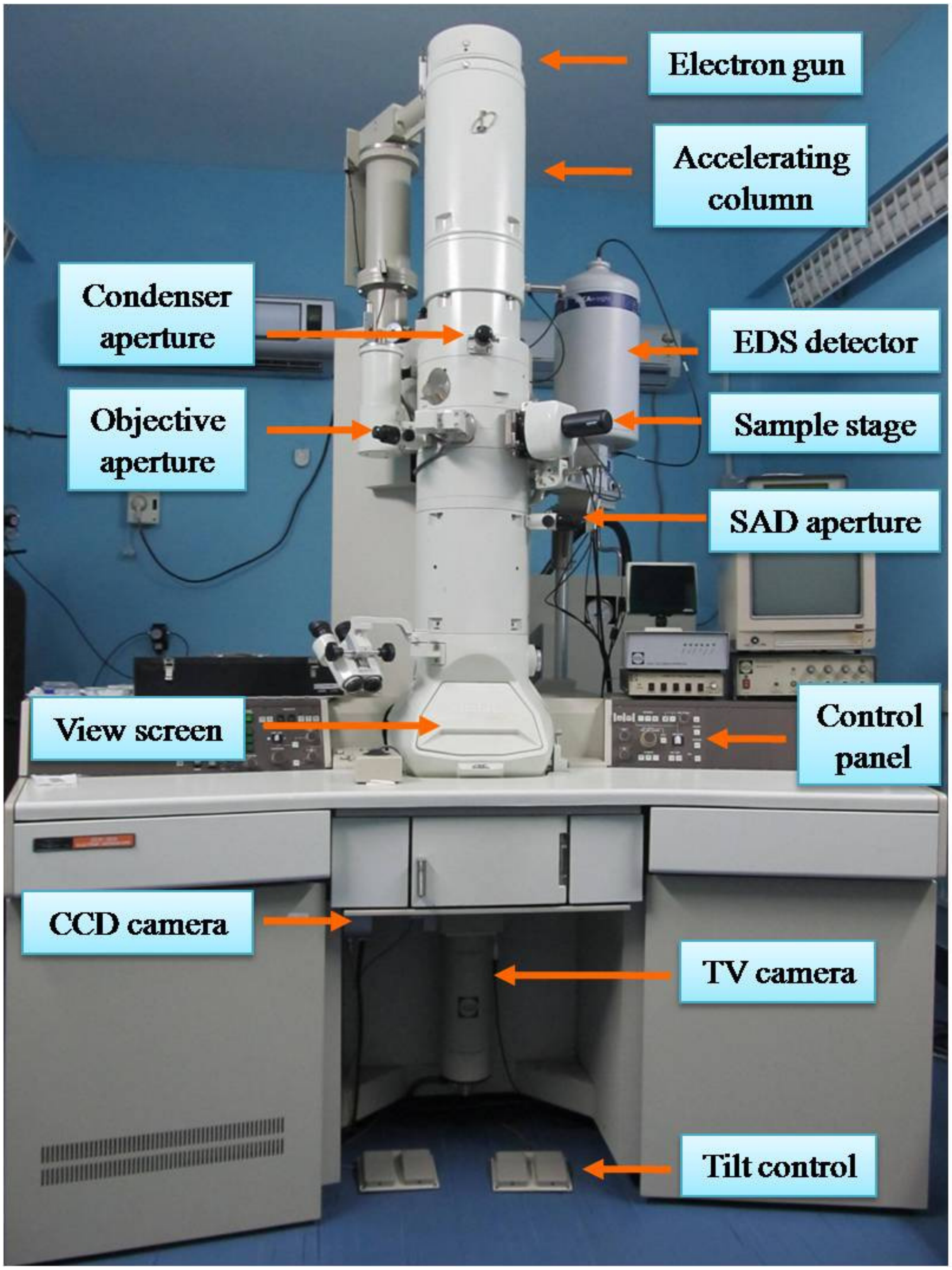

Fig. 2.19 200 keV JEOL HRTEM facility in Institute of Physics, Bhubaneswar.

Image Analysis

From the SAD pattern, the d-spacing *i.e.* spacing between two consecutive planes is measured in the following procedure. When electron beam is transmitted through the specimen, majority of the electron reach to the screen without any scattering and they create a highly intense spot. Apart from that, a number of electrons are scattered at an angle 2ϴ with respect to the direct beam, by the atomic plane of the crystalline grains (Fig. 2.20). Among the elastically scattering electrons, the constructive diffraction condition is satisfied if it follows:

$$\lambda/\mathrm{d} = 2\sin\Theta \sim 2\Theta \qquad (2.5)$$

Where, 'λ' is de Broglie wavelength of electron and 'd' is spacing between successive plane of the crystallite.

According to the geometrical set up another condition is also satisfied as

$$\mathrm{R}/\mathrm{L} = \tan 2\Theta \sim 2\Theta \qquad (2.6)$$

Where, 'R' is the distance of the corresponding diffraction spot from direct beam spot and 'L' is the distance between specimen and viewing screen (camera length).

Therefore these two equations imply that:

$$\mathrm{Rd} = \lambda\mathrm{L} \qquad (2.7)$$

'λL' is known as the 'camera constant' and it is specified during a set of experimental measurements. Hence, by measuring the distance 'R' we can come across the corresponding *'d-spacing'* value of the crystal plane.

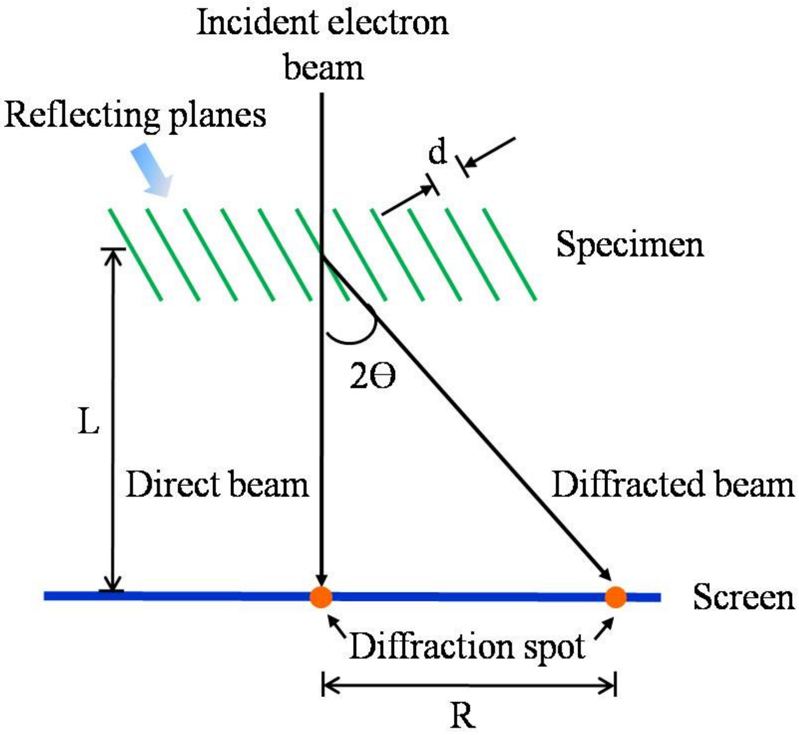

Figure 2.20 Schematic presentation of formation of diffraction pattern in TEM method [18].

For a polycrystalline material, transmitted electron diffraction results in formation of concentric rings on the screen. If the material is composed textured grain, the diffraction pattern becomes streaky in nature. In these two cases, ‘R’ is indicated as the radius of the diffraction rings or arc. Following the same procedure, ‘R’ is measured and the corresponding ‘d’ spacing is found. From a high resolution image, *‘d-spacing’* is measured by drawing several line profile, perpendicular to the crystalline plane and averaging them.

Specimen preparation

For investigation of the crystallinity and structural aspects of the material using TEM with typical electron energy ~ 200 keV, the thickness of the specimen should be less than 100 nm to achieve the adequate electron transparency. Generally samples are in two forms: (i) chemical powder and (ii) self supporting *e.g.* Au thin film on Si(111) substrate. If the sample is in chemical powder form, it is dissolved in solvents and then dropped on carbon coated cupper grid. Following this step, it is allowed to dry for sufficient time and becomes ready for TEM measurements. Complicacy arises for preparing as specimen from other kind of sample. It becomes very challenging job to prepare electron transparent region from the self supporting sample.

Planar specimen

If the some aspects from the top surface of the sample have to be studied, *'planar specimen'* is prepared. While if the interfacial aspects have to be studied, *'cross sectional specimen'* is prepared. However for preparation of the specimens, components of the sample should withstand its chemical and structural identity during the two robust processes: mechanical thinning and ion milling. Normally TEM specimens are shaped as circular disc with diameter 3.0 mm (Fig. 2.21). A circular disc is cut from the sample using an ultrasonic disc cutter. In this ultrasonic disc cutter, a cylindrical shaped, hollow metal rod is vibrated with ultrasonic frequency. The vibrating metal rod force to vibrate silicon carbide (SiC) material on top of the sample and consequences erosion of material in desired size and shape. After formation of such disc shaped sample, it is gradually polished using different size emery paper. This step is continued up to reduction of thickness to 100 micron. To overcome the possibility of damaging of the sample while handling the sample, maintenance of the peripheral thickness ~ 100 micron is essential. In the next step, keeping the thickness ~ 100 micron at the periphery of the sample, a dimple is created at its middle region, using 'dimple grinder'.

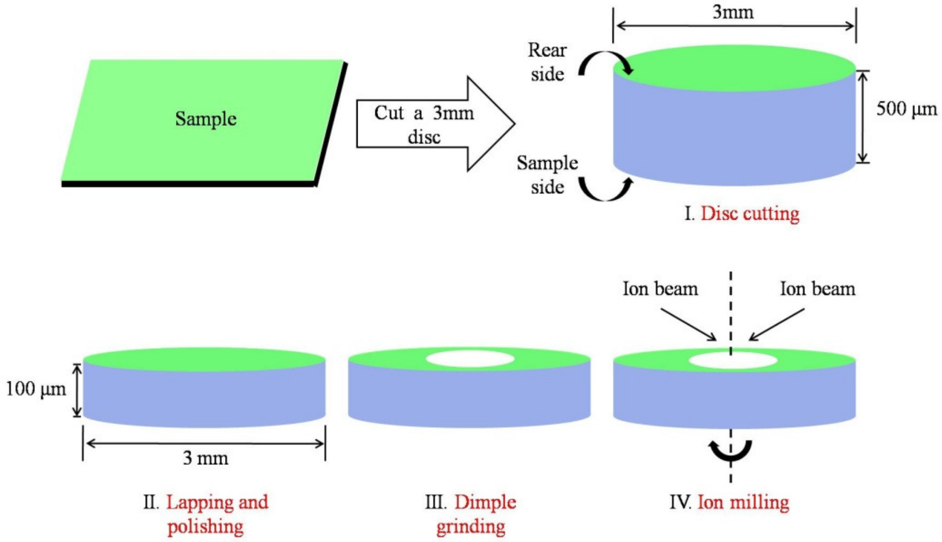

Figure 2.21 A schematic diagram to illustrate different steps of preparing 'planar specimen' for further TEM measurement.

Thereafter an ion milling process takes place by 3 keV Ar ions to make the central region of the sample much thinner. Finally at the end of this step, an electron transparent region is prepared at the central region of the sample and the specimen is used for further TEM measurement. It is noteworthy to note that, above mentioned steps such as lapping, dimpling, ion milling for preparing the 'planar specimen' is performed from the rear side of the sample.

Cross sectional specimen

In the first step of preparing a *'cross section specimen'*, a slice is cut from the sample with width 2.50 mm (Fig. 2.22). In the first step of preparing a 'cross section specimen', a slice is cut from the sample with width 2.50 mm. Then, another dummy slice with equal width is stuck at the front side of the sample using epoxy glue.

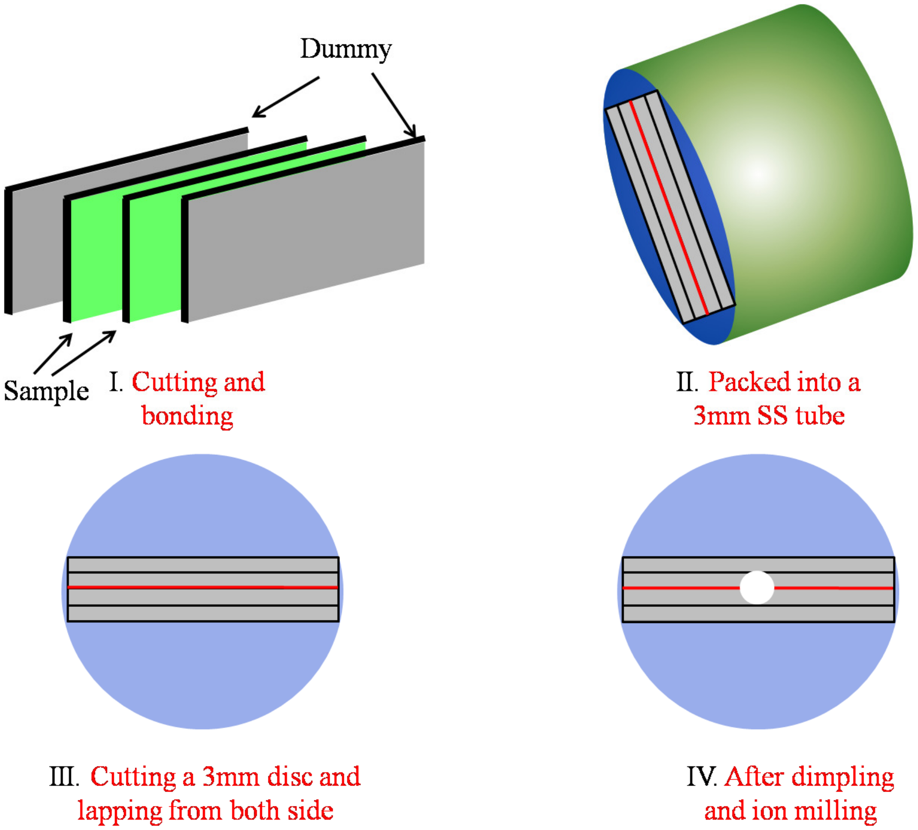

Figure 2.22 A schematic diagram to illustrate different steps of preparing 'cross-sectional specimen' for further TEM measurement.

For example, if we are preparing *'cross section specimen'* of a sample with Au thin film grown on Si substrate, we choose another Si substrate with dimensions equal to the sample as a dummy slice. Thereafter another two dummy slices are stuck at the back side of the sample and the dummy slice attached with sample. Now, the combined stack of sample and slices is inserted in a SS tube with diameter 3.0 mm. After insertion, the tube is sliced into smaller sizes and further steps for specimen preparation are followed. All the further steps are similar as preparation of 'planar' specimen' like lapping, dimpling and low energy ion milling.

2.6.4 Scanning Transmission Electron Microscopy (STEM)

In the category of transmission electron microscopy (TEM), STEM is an extremely useful characterization technique to investigate different aspects of modern science. It comprises of analytical ability for elemental composition and electronic structures in the atomic resolution limit. High energy electrons is sharply focused on the specimen to sub nanometer diameter and scanned in raster fashion over the desired region. After incidence, electrons interact with the specimen material and subsequently numerous signals are collected by the detector for further analysis. Hence, the mechanism of image formation in STEM is quite different from the conventional TEM method.

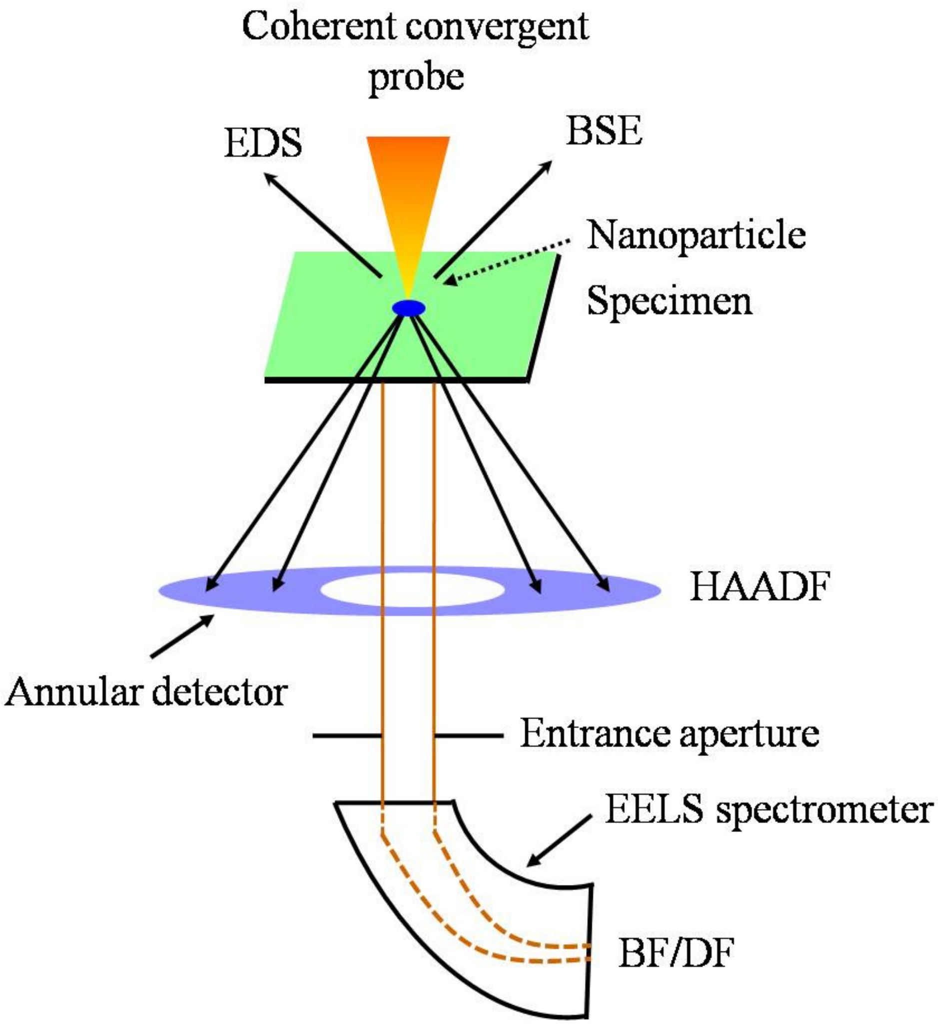

Figure 2.23 Schematic diagram to show various kinds of detector which are used during STEM measurements.

Utilizing a set of condenser lens and an objective lens, electron beam is focused on the specimen. The maximum angle of illumination which is included in the incident probe, is restricted by acting of an objective aperture. Focused beam of electron is scanned over the sample by a set of scan coils and local information is accumulated by the several kinds of detector. Bright field detector is placed to intercept the transmitted electron beam and an annular dark field (ADF) detector is placed surrounding the transmitted beam (Fig. 2.23). Indeed ADF detector is utilized to collect the generated signals which are scattered with angle larger than 30 mrad. Following the Rutherford backscattering by unscreened coulomb potential, the intensity of signals which reach to the ADF detector, is influenced by the atomic number (Z) as ~ Z^2. However due to the screening effect of the core electrons, the backscattered intensity is followed as ~ $Z^{1.7}$. Hence STEM images are interpreted by the 'Z contrast' which indicates element with higher Z value has the brighter contrast and vice versa. The transmitted electron beam emerging from the specimen is passed through the central hole of the ring shaped ADF detector. This signal is acquired by the bright field detector and generally used to generate bright field image similar as conventional TEM technique. Addition of an electron spectrometer in STEM makes it possible to carry out elemental identification, determination of electronic structure, chemical bonding using electron energy loss spectroscopy (EELS) method.

EDX

Along with these facilities, an X-ray spectrometer is used for compositional analysis with resolution in sub-nm range. Due to extremely high kinetic energy of the incident electron in STEM, the strongly bound electrons in the inner orbital of the target atoms are knocked out. To fill up this vacancy, electron jumps from outer orbital to inner orbital. Subsequently, in this process a photon is generated with energy equal to the energy difference among the corresponding two orbitals. If the atomic mass of the target is high enough, then emitted photons are comprised of energy in the X-ray regime. The energy of the emitted photons is the characteristic of the specific target material which enables us to identify the elements in the specimen. In general, EDX measurements are carried out in STEM, using detectors of type Si(Li), SDD (silicon drifted detector) with energy resolution ~ 135 eV.

2.6.5 Scanning Electron Microscopy (SEM)

Scanning electron microscopy (SEM) is an essential technique to investigate the morphology of any system by scanning of a focused high energy electron beam. In addition, compositional aspects also are studied using this technique. Generally two kinds of electron sources are used *i.e.* thermionic or field emission. In case of thermionic sources, metal sources are heated up enough such that electrons can overcome the barrier of work function and are emitted. Due to extremely high melting point and low vapor pressure of tungsten it is electrically heated to very high temperature and considered as a suitable cathode for the thermo ionic emission. Beside, lanthanum hexaboraide (LaB_6) is also used alternatively for electron emission in this process. Compared to thermionic emission, other type of source becomes more useful in SEM to achieve smaller sized coherent beam spot, higher current density and better signal to noise ratio. In this process, metal cathode with sharp tip is negatively biased with voltage difference several kilovolt with respect to corresponding anode. Therefore at the apex of the tip, very high electric field is generated such that electrons are pulled out overcoming its surrounding barrier. Among the emitters, they could be *'cold-cathode type'* which comprises generally tungsten tip with tip radius ~ 100 nm. In other type of emitter *i.e.* '*Schottky type'*, thermo ionic emission is enhanced by the lowering the surface barrier, in presence of external electric field. Generally this type of emitter is fabricated considering a sharp tungsten tip and then putting a layer of zirconium oxide which has very high electrical conductivity at high temperature.

After emergence of the electron beam from the source with energy 0.20-40 keV, it is focused by the condenser lens to beam size typically 0.4-5.0 nm. Then the beam is passed through a pair of solenoid coils or deflecting plates which are arranged orthogonally to each other. It results in scanning of the focused electron beam in raster fashion in orthogonal X and Y direction over a rectangular region of the sample. Magnification in this method is determined by the ratio of dimension of the display device (A_1) to the dimension of 'raster area' on the sample (A_2), *i.e.* A_1:A_2. As the dimension of A_1 could be considered unchanged, smaller the dimension of A_2 implies larger the magnification and vice versa. When electron beam is incident on the sample, electrons interact with the sample material via repeated random scattering and absorption within a teardrop shaped region within the material. Depending upon the energy of incident beam energy, these interaction processes generate numerous kinds of signals like (i) backscattering electrons by elastic scattering, (ii) secondary electrons by inelastic scattering and (iii) electromagnetic radiation due to inelastic scattering.

Backscattering electrons are produced due to the reflection or backscattering of the incident electrons from the target atoms and comprised of very high energy in comparison with generated secondary electrons in inelastic process. In accordance with increase of atomic mass of target, energy of the backscattered energy is increased and vice versa. Hence such signals are very useful to understand compositional analysis, based on the capability of distinguishing of different atomic mass value within a specified region.

Other kind of signal is also generated due to formation of secondary electrons by inelastic scattering process. These electrons are generally come out from the K shell of the target atoms and comprise very low energy as < 50 eV. Intensity in the image depends on the amount of secondary electrons which are reached to the detector. Instead of falling normally on a surface, if the beam is fallen with some tilt, the escape distance of the electrons is decreased. Therefore amount of generated secondary electron become more at the edges and steeper region of the sample than its complementary flat region. Based on this fact, this signal is successfully implemented for analysis of surface topography of the specimen.

Electromagnetic radiation is obtained by the generation of two kinds of signal: (i) *Cathodoluminescence* and (ii) *X-ray*.

Cathodoluminescence (CL) takes place, due to emission of light when the electron in atom goes to higher energy state due to interaction with beam electron and comes down to lower energy state. The emitted light with various wavelengths are collected by the CL detector and further analyzed.

In the other scenario, electrons in the target atoms are knocked out from the inner energy shell by the incident high energy electron beam. If such vacancy is filled up by the coming down of the electrons from the outer energy shell, it causes electromagnetic radiation. Such radiation reveals the characteristics of the target atom and has energy equal to the energy level difference of the corresponding inner shell and outer shell. If the SEM is equipped the energy dispersive X-ray spectrometer, characteristic X rays are analyzed for detection and quantitative information of the target material.

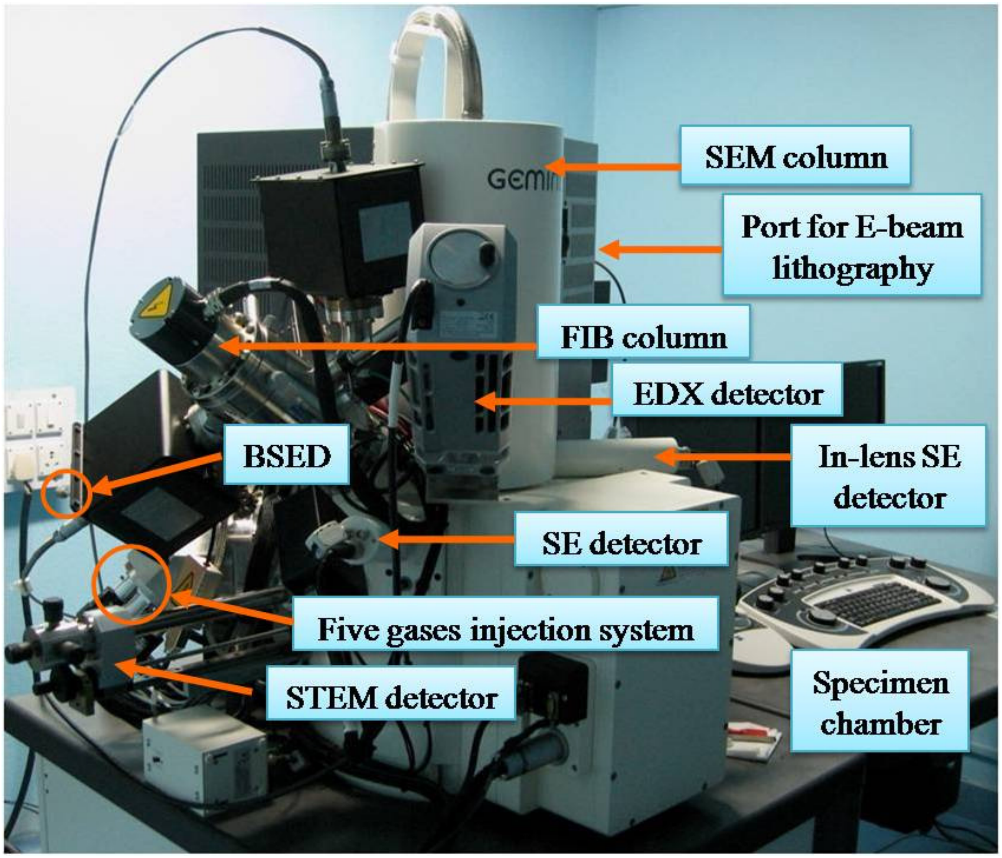

Figure 2.24 FEGSEM (Carl Zeiss, Neon 40) facility in Institute of Physics, Bhubaneswar.

To carry out SEM measurements, we have used a FEGSEM set up at IOP, Bhubaneswar (Fig. 2.24). It comprises facilities of accelerating voltage of electron source 0.1-30 keV and probe current 4 pA- 20 nA. In this set up, resolution is 1.1 nm for using 20 keV energy and 2.5 nm for using 1 keV energy of the electron beam.

2.6.6 Rutherford Backscattering Spectroscopy (RBS)

In material science among the different analytical methods for investigating structural and compositional aspects, Rutherford backscattering spectrometry (RBS) is an important method which deals with the analysis of backscattered energy of high energy charged particles *e.g.* proton or alpha.

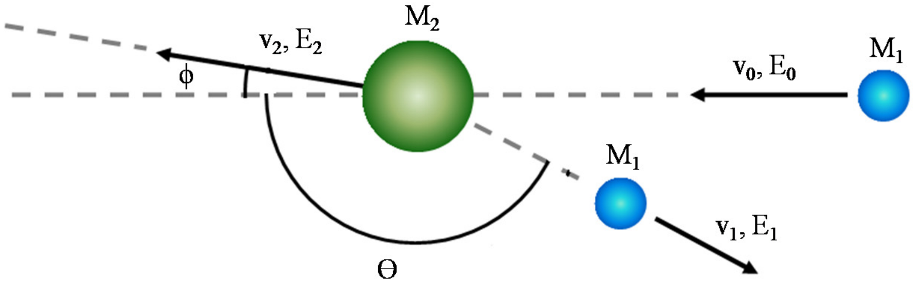

Figure 2.25 Schematic diagram of collision of incident probe atom (*e.g.* proton, alpha) with target atom. M_1 and M_2 denote the mass of probe atom and target atom respectively. v_0 (with kinetic energy E_0) and v_1 (with kinetic energy E_1) represent the velocity of probe atom before and after the collision with the target atom respectively. Target atom which has the initially zero velocity, achieves velocity v_2 (with kinetic energy E_2) followed by the collision. ϕ and Θ denotes exit angle and backscattered angle respectively.

Kinematic factor

After incidence of charged particles, due to energy transfer by collision with target atoms, its initial energy is changed. The ratio of backscattered energy to the incident energy is defined as the kinematic factor.

It follows

$$E_1 = k \times E_0 \tag{2.8}$$

'E_1' and 'E_0' is backscattered and incident energy of the charged particles and 'k' is the corresponding kinematic factor.

Considering incident energy (E_0) much larger than the binding energy but smaller than the required energy for nuclear reactions and resonances, the kinematic factor is found to follow the relationship:

$$k = \left[\frac{(M_1 \cos \theta + (M_2^2 - M_1^2 \sin^2 \theta)^{1/2}}{M_1 + M_2}\right]^2 \tag{2.9}$$

'M_1'and 'M_2' are the mass of incident particle and target atom respectively. 'Θ' is considered as the backscattered angle. This above mentioned relationship of kinematic factor with the atomic masses and the backscattered angle is obtained from the consideration of kinematics of elastic collision where momentum and energy are conserved (Fig. 2.25).

Thickness Analysis

The relative number of backscattered charged particle which are emerged through a solid angle dΩ is called as *'differential cross section'* $(\frac{d\sigma}{d\Omega})$. It is related to the average scattering cross section (σ) as following manner:

$$\sigma = \frac{1}{\Omega}\int \frac{d\sigma}{d\Omega}\, d\Omega \qquad (2.10)$$

The differential cross section for collision of two atoms based on the Rutherford's formula is obtained as:

$$\frac{d\sigma}{d\Omega} = \left[\frac{Z_1 Z_2 e^2}{4E_0}\right]^2 \times \left(\frac{4}{\sin^4\theta}\right) \times \frac{\left[\left[1-\left(\frac{M_1}{M_2}\sin\theta\right)^2\right]^{1/2} + \cos\theta\right]^2}{\left[1-\left(\frac{M_1}{M_2}\sin\theta\right)^2\right]^{1/2}} \qquad (2.11)$$

When the beam of charged particles is incident on the target normally and thereafter is backscattered, no of detected particles is given by in terms height of the yield as:

$$H_i = \sigma(E_i)\Omega Q N.dt \qquad (2.12)$$

Here, total thickness of the thin film is given by t = i×dt. 'i' is the number of equally smallest slabs with its magnitude of width 'dt'. *'Atomic density'* and *'no of incident particles'* is denoted by 'N' and 'Q' respectively. 'Ω' represents the *'solid angle of detection'*. The total number of detected backscattered particle is measured by adding up all H_i *i.e.* $\sum_i Hi$ values for varying 'i' (Fig. 2.26).

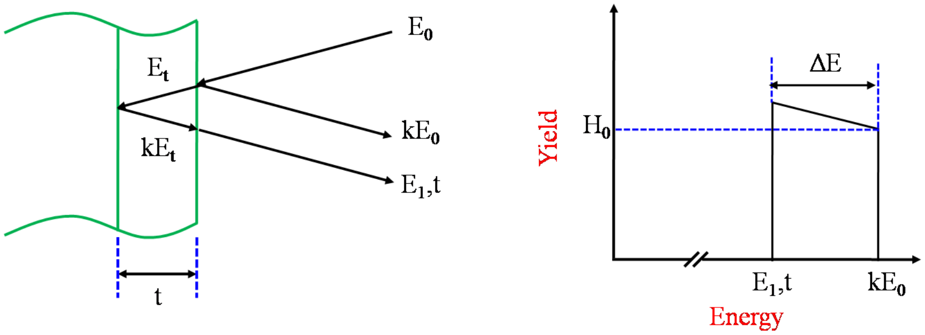

Figure 2.26 Schematic presentation of formation of RBS spectrum for a thin film.

Thickness of the thin film and the kinematic factor in this process is denoted by ‘t’ and ‘k’ respectively. ‘E_0’, ‘kE_0’indicate the incident kinetic energy of the probe atom and backscattered energy from the top surface of the thin film, respectively. ‘E_t’ and ‘kE_t’ denote the incident energy and backscattered energy of the probe atom at a layer which is inside of the thin film with a distance ‘t’ from the top surface. $E_{1,t}$ is the energy of the probe atom during exit from the thin film, followed by the back scattering from a layer which is at a distance ‘t’ interior from the top surface. H_0 is the backscattered energy of the probe atom, which corresponds the backscattered energy kE_0 and ΔE represents as $kE_0 - E_{1,t}$.

Instrumentation

The working principle of the RBS method could be described by three distinguishable sections: (i) accelerator, (ii) target chamber and (iii) energy analyzer.

At the beginning, according to the requirement, either proton or alpha particles are produced using the ionization process. Thereafter they are accelerated to achieve very high kinetic energy 1-3 MeV. As the beam of charged particles is passed through the mass analyzer, the desired isotope is selected before entering in the target chamber. Beam is well collimated before falling on the target sample. The sample is connected with a ‘current integrator’ which gives account of total amount of incident charged particle. A surface barrier detector is kept at a very high scattering angle 160° or above, such that appreciable amount of charged particles will be detected. The voltage pulse which is sensed by detector is consecutively transferred to preamplifier, amplifier and finally to multi channel analyzer (MCA). Then the signal from MCA is communicated to the external computer where we find RBS spectrum for further analysis.

We have carried out RBS measurements using the 45° beam line of 3 MV tandem Pelletron accelerator (9SDH2, NEC, USA) in IOP, Bhubaneswar [19]. Most of the experiments have been done using beam of helium ion with energy 2 MeV. For some other case, we have also utilized beam with energy 1 MeV. Based on the experimental observations, compositional aspects of the thin film growth on Si substrates (viz. Au/Si, Ag/Si or Au-Ag/Si) have been investigated using SIMNRA software package [20].

References

[1] D. Mijatovic, J. C. T. Eijkel, A. van den Berg, *Lab Chip* **5**, 492 (2005).

[2] F. C. Frank, J. H. vander Merwe, *Proc. Roy. Soc. London A* **198***,* 205 (1949).

[3] M. Volmer, A. Weber, *Z. Phys. Chem.* **119**, 277 (1926).

[4] I. N. Stranski, Von L. Krastanow, *Akad. Wiss. Lit. Mainz Math. -Natur. Kl. IIb* **146**, 797 (1939).

[5] K. Oura, V. G. Lifshits, A. A. Saranin, A. V. Zotov, M. Katayama, *Surface Science - An Introduction (Springer-verlag, 2003).*

[6] Ph. D. Thesis, Utkal University, February, 2010 by Kuntala Bhattacharjee.

[7] Marcia H. Grabow, George H. Gilmer, *Surf. Sci.* **194,** 333 (1988).

[8] J. R. Arthur, *Surf. Sci.* **500**, 189 (2002).

[9] D. K. Goswami, B. Satpati, P. V. Satyam, B. N. Dev, *Curr. Sci. (India)* **84**, 903 (2003).

[10] G. Binnig, H. Rohrer, Ch. Gerber, E. Weibel. *Phys. Rev. Lett*. **50**, 120 (1983).

[11] A. A. Baski, K. M. Saoud, K. M. Jones, *Appl. Surf. Sci.* **182**, 216 (2001).

[12] S. Hara, M. Yoshimura, K. Ueda, *Jpn. J. Appl. Phys.* **47**, 6102 (2008).

[13] C. W. Jones, *Applications of Hydrogen Peroxide and Derivatives*, Royal Society of Chemistry, Cambridge UK, 1999.

[14] J. E. Mahan, K. M. Geib, G. Y. Robinson and Robert G. Long, *J. Vac. Sci. Technol. A* **8**, 3692 (1990).

[15] A. Bhukta, P. Guha, A. Ghosh, P. Maiti, P. V. Satyam *Appl. Phys. A* **122**, 356 (2016).

[16] R. Wiesendanger, Scanning Probe *Microscopy and Spectroscopy: Methods and applications, (Cambridge University Press, 1994).*

[17] M. Knoll, E. Ruska *Z. Physik.* **78,** 318 (1932).

[18] D. B. Williams, C. Barry Carter *Transmission Electron Microscopy,* Vol. I-IV (Plenum Press, New York, 1996).

[19] K. Sekar, G. Kuri, P. V. Satyam, B. Sundaravel, D. P. Mahapatra, B. N. Dev *Indian J. Phys.* **684**, 1 (1994).

[20] M. Mayer, *Nucl. Instr. Meth. Phys. Res. B* **194**, 177 (2002).

Chapter 3

Growth of Ag nanostructures on high-index Si (5 5 12) surfaces under UHV conditions: effect of prior surface treatment before deposition

3.1 Introduction

High-index (vicinal) Si surfaces are misoriented by a mis-cut or vicinal angle from the low-index Si[001] or Si[111] surfaces. Formation of alternating terraces and atomic steps on reconstructed high-index (vicinal) Si surfaces consequences anisotropic mobility of ad-atoms and such templates have been exploited for growth of one dimensional (1D) metal nanostructures [1-7]. Vicinal Si(5 5 12) surface which shows large (5.35 nm × 0.77 nm), single domain, stable unit cell upon reconstruction [1] has been successfully employed for growth of noble metals (Au, Ag) nanowires with ultra-thin layers [2, 9, 10]. Preparation of reconstructed Si surfaces is performed by removal of native silicon oxide layer with flash heating at high temperature under UHV conditions. Hence, an attempt for comparative study on growth of nanostructures on vicinal Si surfaces (*e.g.* Si(5 5 12)) with and without reconstruction would be helpful for possible use of high-index Si surfaces at ambient conditions. In this chapter, we discuss about the growth of Ag nanostructures on three kinds of surfaces of Si(5 5 12): (i) a native oxide covered surface, (ii) a hydrofluoric (HF) acid treated surface and (iii) a reconstructed surface after removal of native oxide under UHV conditions. Depositions of Ag have been carried out in molecular beam epitaxy (MBE) system and thereafter crystalline quality and orientation relationship with substrate have been characterized by in-situ RHEED and TEM measurements. Morphology of the grown nanostructures has been studied by SEM and TEM methods. All the depositions have been carried out under UHV conditions using a molecular beam epitaxy (MBE) system. When over-layer thin film is grown of native oxide covered Si surfaces, presence of interfacial oxide layer acts as a barrier for inter-diffusion of over-layer metal thin film. While, passivation of the clean surface with bromine or hydrogen molecules is done followed by the removal of native oxide layer, inter-diffusion of metal overlayer shows quite similar behaviour as the UHV conditions. For example, for growth of Cu on clean Si(001) surface in UHV conditions and H- passivated (or Br- passivated) Si(001) surface at HV conditions explore inter-diffusion of Cu inside Si matrix at much lower temperature than native oxide covered Si(001) surface [11, 12]. In earlier work, epitaxial growth of Ag on hydrogen passivated Si(001) and Si(111) surfaces have been observed R. Naik *et al.* [13]. To best of our knowledge, no reports exist for similar studies for high index Si substrates. In contrast with native oxide covered Si surfaces, for Ag deposition re-oxidized layer on low index Si(001), Si(110) and Si(111) surfaces, partially oriented growths have been observed [15-17]. Ag/SiOx templates have been successfully implemented for enhancement of infrared absorption coefficient of some bio-molecules [18] and catalytic behaviors [19]. Recently, due to embedded nature inside of Si matrix and well-defined shapes endotaxially grown Ag nanostructures have been explored as robust surface enhanced Raman spectroscopy (SERS) substrate [20, 21].

3.2 Experimental Methods

Growth of Ag nanostructures is carried out under UHV conditions inside MBE chamber (Omicron Vacuumphysik GmbH) through a deposition of a 3.0 nm thick Ag thin films. Base pressure inside the MBE chamber is better than 3.0×10^{-10} mbar and it rises to ~ 1.0×10^{-9} mbar during deposition [22]. Ag is grown by thermal evaporation method from pyrolytic boron nitride(PBN) crucible with a typical flux rate of ~ 0.6 nm/minute and while keeping the substrate at 400 °C. Thickness is measured using quartz microbalance (that is pre-calibrated using Rutherford backscattering spectrometry (RBS)) technique. Substrate temperature is measured using a Type K thermocouple. As the film thickness is small and deposition done at elevated substrate temperatures, layer-by-layer growth of Ag is not expected on the silicon surfaces. This results in nanostructured growth of Ag.

Ag nanostructures are grown on commercially procured n-type Si(5 5 12) (resistivity ≈ 1-20 Ω-cm) at three different conditions of substrate surfaces:

(i) native oxide covered (here after known as Sample A)

(ii) HF-treated (Sample B)

(iii) reconstructed surface (Sample C). (Schematically are shown in Fig. 3.1)

HF acid treated surface (Sample B) is prepared in three steps. a) Si wafer is treated in Piranha solution for 10 minutes and then stirred in de-ionized (DI) water. Piranha solution is prepared by mixing of concentrated H_2SO_4 and 20% H_2O_2, with volume ratio of 3:1 [23] b) Then, it is dipped in 2% water solution of HF for 2 minutes and stirred in DI water for 10 minutes to remove native oxide layer, c) Following this, it is kept in air for 15 minutes before bringing into the load-lock chamber attached with MBE growth chamber [22]. Subsequently, it is kept inside load lock chamber for ~3 hours, in high vacuum (HV) and then brought inside the MBE chamber. Prior to Ag deposition, HF etched Si(5 5 12) substrate is possibly, partially re-oxidized due to keeping in air and HV [15-17]. Further, RHEED on two more samples (Sample D: Ag grown on HF-treated while keeping the substrate at room temperature and Sample E: Ag grown on HF-treated while keeping the substrate at 600 °C) have been done to understand the temperature effect on the crystalline structure of Ag nanostructures.

Reconstructed substrate (Sample C) is prepared by using direct current (DC) heating method in UHV conditions. First, the samples (*i.e.*, Si(5 5 12) surfaces) are degassed at 600 °C for ~ 12 hours. Then, they are flashed at ~ 1250 °C for few minutes to remove native oxide layer. In-situ RHEED is done with electron incident energy 17.2 keV and incidence angle ~ 2°. Scanning tunneling microscopy (STM) measurements have been performed under UHV conditions, using Omicron variable temperature scanning tunneling microscope, attached with MBE chamber [22]. STM topographic images of HF treated Si(5 5 12) surface have been taken at room temperature (RT) with sample bias at +3.0 V, tunneling current 0.5 nA and scan speed 400 nm/sec. Similarly, STM topographic images of reconstructed Si(5 5 12) surface have been acquired at RT, with sample bias +2.0 V, tunneling current 0.2 nA and scan speed 80 nm/sec. Preparation of TEM specimen has been carried out by mechanical thinning and then followed by low energy Ar^+ milling. HRTEM (planar and cross section) studies have been done using JEOL-2010 operating with 200 keV electrons (URP pole piece). It should be noted that the HRTEM measurements have been carried out at high vacuum conditions in TEM specimen stage and hence no surface- reconstruction effects can be seen.

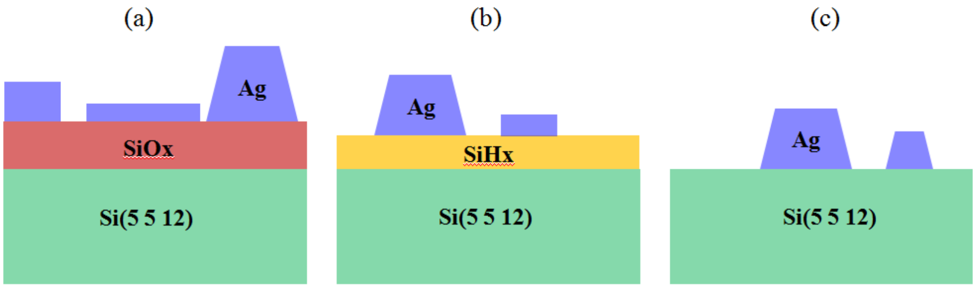

Figure 3.1 Schematic presentation of Ag growth on Si(5 5 12) surfaces with different kinds of prior surface treatment: a) native oxide covered, b) HF-treated c) reconstructed.

3.3 Description of vicinal Si(5 5 12) surface

Fig. 3.3 depicts high resolution cross-sectional TEM (XTEM) image of Si (5 5 12) (Sample C: Ag nanostructures grown on reconstructed Si surface). Here, we note that after Ag growth on reconstructed surface inside MBE chamber, Sample C has been exposed to ambient condition and ex-situ TEM measurements are carried out with JEOL 2010 UHR (consisting of ultra high resolution pole piece with a C_s of 0.5 mm) system with 200 keV electrons.

In this case, we have observed 3D nanostructures, partially covered on the Si surface (see the next subsection of this chapter). This high resolution XTEM lattice image (Fig. 3.3) has been acquired on a region without 3D nanostructures of Sample C, along zone axis Si$[1\bar{1}0]$ (corresponding SAD pattern in Fig. 3.2). While the XTEM specimen is prepared using mechanical polishing followed by ion milling, the Ag nanostructures have been sputtered out during the thinning process. Efforts are being made to prepare these TEM specimen with FIB - lamella preparation to see the interface of Ag and Si(5 5 12). Due to a technical problem in our FIB system, we are unable to make this site specific specimen at this juncture. The lattice image shows that, the surface is made of atomic scale facets with varying width.

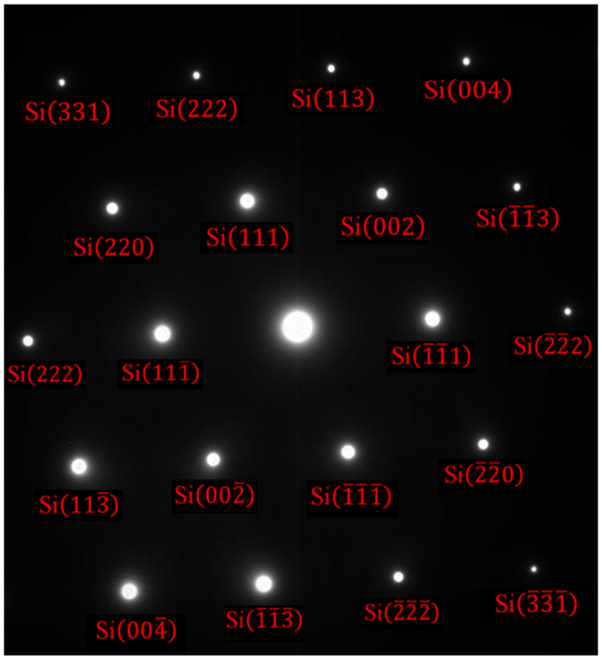

Figure 3.2 SAD pattern from Si(5 5 12) substrate along zone axis Si[$1\bar{1}0$].

Details of analysis to determine orientations of facet planes

These facets are made of two stable low index planes of Si *i.e.* (001) and (111). To determine orientations of different facet planes, we follow the previously reported work of A. A. Baski *et al.* [27]. Let us consider a parallelogram A1B1C1D1 as shown in Fig. 3.3 (HRTEM). Here, A1C1 indicates the resultant facetted plane, formed by two adjacent planes A1B1 and B1C1. Orientation and dimension of the four sides of this parallelogram are determined using SAD pattern and HR XTEM imaging methods.

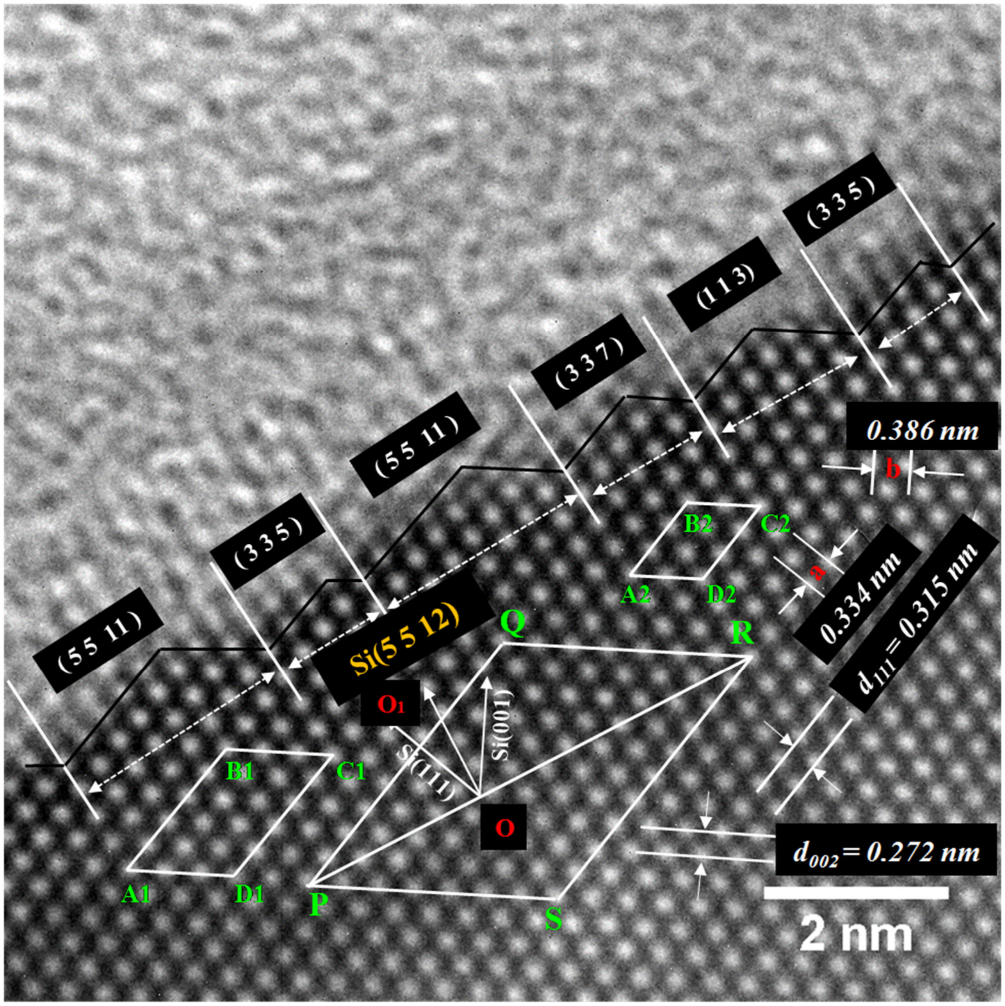

Figure 3.3 Bright field High resolution cross-sectional TEM image of a region without 3D nanostructures of Sample C.

With respect to those observations, we have determined the orientation of the different facetted planes (Fig. 3.3) as given below. A1B1 and A1C1 indicates Si(111) and Si(001) planes, respectively. Further, we have considered sub units '*a*' (≈ 0.334 nm) along (111) and '*b*' (≈ 0.386 nm) along (001) as marked in Fig. 3.3. Dimension of A1B1 and A1C1 is found 5×a and 3×b, respectively. The angle between A1C1 plane and (111) and (001) plane have been found to be 21.8° and

32.6°, respectively. Corresponding to the parallelogram (A1B1C1D1) has been shown in Fig. 3.4 (schematic figure of Si crystal observing along Si[$1\bar{1}0$]) also [27]. From the comparison of $A_1B_1C_1D_1$ with A1B1C1D1 (from Fig. 3.3 and 3.4), we have found that A1C1 denotes Si(5 5 11) plane.

Next, we have considered another parallelogram, A2B2C2D2 as shown in Fig. 3.3. Observed angle between A2C2 with (111) and (001) has been found to be 23.4° and 31.0°, respectively. In this case dimension of A2B2 and B2C2 is 3×a and 2×b, respectively. Corresponding parallelogram $A_2B_2C_2D_2$ in Fig. 3.4 reveals that, A2C2 indicates this to be Si(3 3 7) plane. Following the same procedure, we have determined other facetted planes (viz. (335), (113)).

We have followed the same procedure to find out orientation of Si(5 5 12). We have considered a parallelogram PQRS as shown in Fig. 3.3 (and corresponding in Fig. 3.4). PQ (along (111)) and QR (along (001)) has dimension 10×a units and 7×b units, respectively. Approximately, angle between PR plane and Si(001), Si(111) is 30.3°, 23.9°, respectively. It indicates resultant plane PR represents Si(5 5 12) as shown in Fig. 3.3.

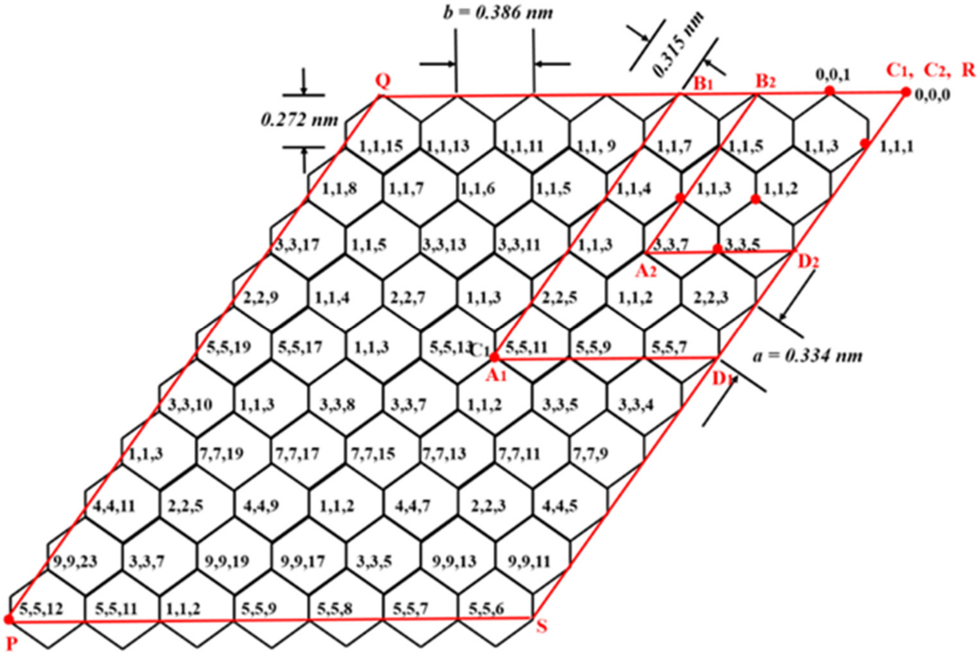

Figure 3.4 Schematic of Si crystal lattice observing along Si$[1\bar{1}0]$ [26].

3.4 Results and discussions

3.4.1 Pretreatment effect on growth template

Fig. 3.5 (a) shows a topographic STM image of HF treated Si(5 5 12) (Sample B) surface prior to Ag growth. After etching out the native oxide layer using HF, surface becomes atomically rough (rms roughness ≈ 0.255 nm) as revealed from the line scan (Fig. 3.5 (b)). The reconstruction of Si(5 5 12) surface is understood via the UHV-STM measurements. Ordered atomic rows along Si$[1\bar{1}0]$ and a periodicity of 5.17±0.67 nm along Si$[66\bar{5}]$ is observed (Fig. 3.5 (c)-(d)). Three sub units of the unit cell (337), (225) and (337) are also observed as D1(1.50±0.30 nm), D2(2.17±0.66 nm) and D3(1.50±0.89 nm). These values are in agreement with earlier works [1].

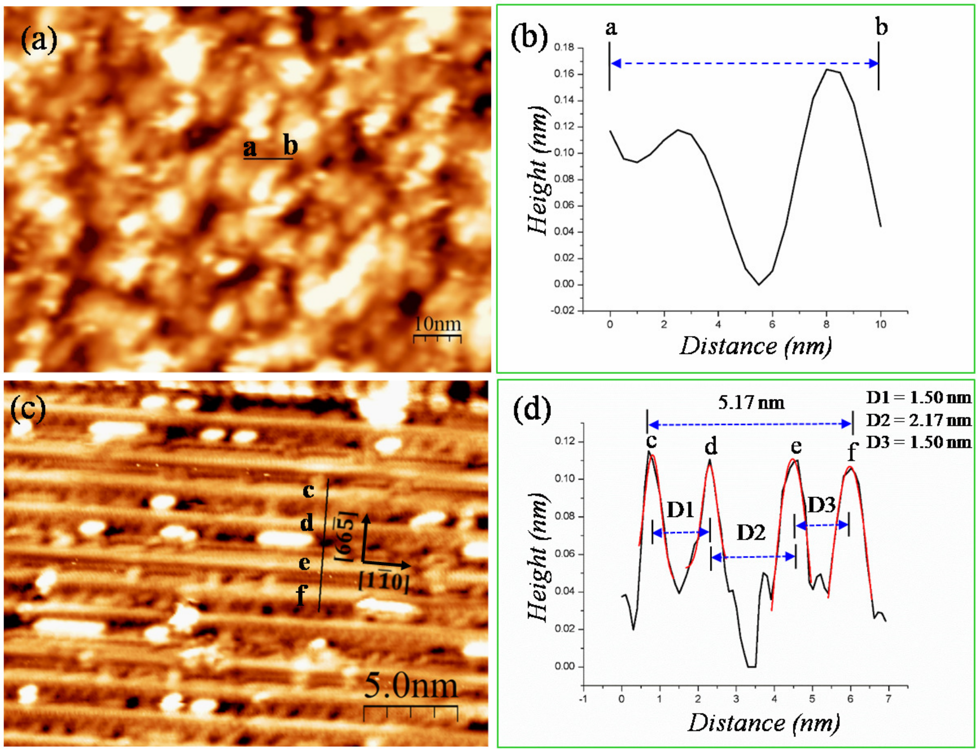

Figure 3.5 a) STM topographic image of HF-treated Si(5 5 12) surface taken at room temperature with sample bias +3.0 V, tunneling current 0.5 nA and scan speed 400 nm/sec b) line profile of a selected region as marked in Fig. 3.5(a). c) STM topographic image of reconstructed Si(5 5 12) surface taken at room temperature with sample bias +2.0 V , tunneling current 0.2 nA and scan speed 80 nm/sec. d) line profile along Si$[66\bar{5}]$ over a unit cell as marked in Fig. 3.5(c). Periodicity of 5.17±0.67 nm along Si$[66\bar{5}]$ is observed. D1(1.50±0.30 nm), D2(2.17±0.66 nm) and D3(1.50±0.89 nm) denotes (337), (225) and (337) sub unit respectively.

Prior to the deposition of Ag nanostructures, the RHEED has been primarily employed to check the crystalline structure of the surface of Si(5 5 12) as shown in Fig. 3.6: (i) on native oxide (Fig. 3.6(a)) (ii) on HF treated (Fig. 3.6 (b)) and (iii) on reconstructed (Fig. 3.6 (c)). In case of native oxide covered Si(5 5 12) substrate (Fig. 3.6(a)), only a bright spot (marked as O`) corresponding to specular reflection of incident electron beam has been observed. No other diffraction spots are observed, indicating amorphous nature of the native oxide layer. For reconstructed substrate (Fig. 3.6(c)), it shows two fold periodicity along Si$[1\bar{1}0]$ direction with beam incidence along Si$[66\bar{5}]$ [24]. For HF treated substrate, incidence direction of the electron beam is aligned to Si$[66\bar{5}]$ by observing the arrangement of the Kikuchi lines. In this case (inset of Fig. 3.6(b)), formation of symmetrically arranged diffraction spots (marked as a,..,d) about this direction is observed. Orientation of these spots is similar as the characteristic spots (marked as a`,..,d`) of reconstructed substrate (inset of Fig. 3.6 (c)). These diffraction spots are expected to originate due to electron beam interaction with the Si atoms within a few top layers of the substrate, after removal of native oxide layer. However, long range ordering of the surface atoms, like reconstructed substrate (Fig. 3.6 (c)), is absent. Further, substrate temperature is increased up to 600 °C under UHV.

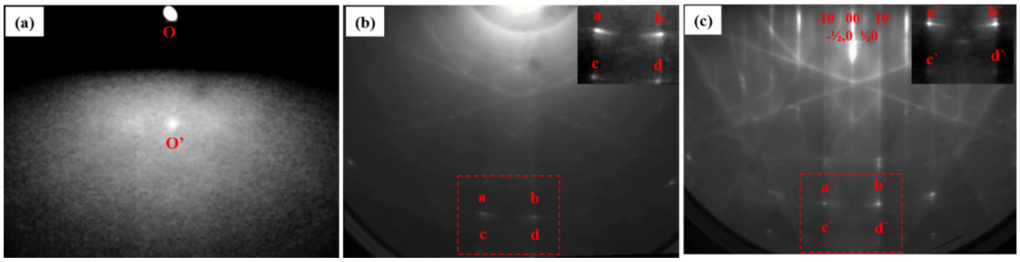

Figure 3.6 RHEED pattern of Si(5 5 12) substrate a) native oxide covered , b) HF treated, along azimuthal direction Si[$66\bar{5}$] and c) reconstructed along azimuthal direction Si[$66\bar{5}$].

3.4.2 Morphological and structural aspects of grown nanostructures

In the following, we discuss about the morphology and crystalline quality of Ag nanostructures on high index Si surfaces using RHEED and TEM. In order to understand the role of interfacial layer on the crystalline quality of the Ag nanostructures, three samples A, B and C are used (details of Samples A, B and C are given in the *'experimental method'* section). All the samples have been post annealed at growth temperature (400 °C) for further 60 minutes. For the Sample A, RHEED pattern shows formation of concentric and broad Debye-Scherer rings, arising from randomly oriented 3D Ag nanostructures (as shown in Fig. 3.7(a)). This confirms the polycrystalline nature of the Ag nanostructures grown on native oxide layer. These rings correspond to diffraction from set of planes Ag{311}, Ag{331} and Ag{442}. For other two samples (Sample B and C), RHEED patterns show absence of Debye Scherrer rings and formation of well-ordered diffraction spots as an indication of transmission electron diffraction (TED) through the crystalline 3D islands (Fig. 3.7(b), 3.7(c)). RHEED studies along zone axis Ag[$11\bar{1}$], reveal for both samples, orientation relationships of Ag growth directions of different Ag(hkl) planes are similar to both the samples B and C (as shown in the inset of Fig. 3.7(b) and Fig. 3.7(c)). It is interesting note the difference between the RHEED for Ag on native-oxide covered (Sample A, Fig. 3.7(a)) and Ag on HF-treated (Sample B, Fig. 3.7(b)) as no polycrystalline rings are seen for the HF treated substrate. From these data, we can infer that the Ag nanostructure growth on HF treated and on reconstructed substrate are single crystalline in nature. This could be possible due to the hydrogen passivation of many of the dangling bonds soon after the HF - treatment.

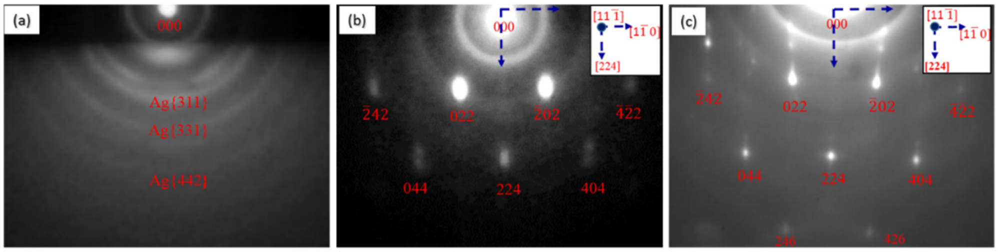

Figure 3.7 RHEED pattern after 3 nm Ag deposition on Si(5 5 12), at substrate temperature 400 °C with substrate a) native oxide covered (Sample A) b) HF treated (Sample B) c) reconstructed (Sample C).

The RHEED method is more sensitive to the in-plane growth of the thin films (or nanostructures) and less sensitive to overall crystalline quality of thicker structures. To understand the crystalline orientation relationship with the substrate, the transmission electron microscopy measurements in the planar specimen geometry are carried out and wherein selected area diffraction (SAD) is used. We now discuss the TEM results (both the planar and cross-section views) obtained from these Samples (A, B and C). The planar TEM bright field images are shown in Fig 3.8 (b), 3.8 (d) and 3.8 (f) for Samples (A), (B) and (C), respectively. The bright field (BF) image of Sample A (shown in Fig. 3.8 (b)), depicts more circular shaped particles with diameter varying between 8-34 nm. Being Si(5 5 12) a forbidden plane for constructive diffraction for Diamond cubic crystal, we have performed selected area electron diffraction (SAD) analysis along zone axis Si[224], which is tilted by 4.76° from substrate orientation [25]. From the corresponding selected area electron diffraction (SAD) for Sample A (shown in Fig. 3.8 (a)), polycrystalline nature of the Ag nanostructures is quite evident with observation of Debye-Scherrer rings due to diffraction from {111}, {002}, {112}, {220} and {311} planes of Ag. Diffraction spots corresponding substrate silicon are also seen from the SAD pattern in Fig. 3.8 (a). The BF micrograph for Sample B (HF treated) is shown in Fig. 3.8 (d). Though the particle size for bigger particles is ~ 40 nm, much smaller particles are also seen around the bigger particles. The corresponding SAD pattern is shown in Fig. 3.8 (c). Interestingly, although the specimen has been passivated with Hydrogen and expected to be partially re-oxidized, streaking of the diffraction spots is evident which represents basically the texturing of the nanostructures. This texturing has been observed to corresponding planes of Ag{111}, Ag{311} and Ag{220}. It should be noted that, SAD pattern shows corresponding diffraction spots from Si substrate as well. In-plane texturing takes place according to the orientations Ag{220}∥Si($2\bar{2}0$), Ag{111}∥Si($11\bar{1}$), Ag{311}∥Si($\bar{1}3\bar{1}$) with Ag[224]∥Si[224]. Ag nanostructures also grow following the orientation of equivalent planes of ($2\bar{2}0$), ($11\bar{1}$) and ($\bar{1}3\bar{1}$) of the substrate. As a result, diffraction pattern shows texturization (meaning many crystalline orientation are in similar direction, representing high degree of orientation) for Ag{220} as Ag{220}∥Si($20\bar{2}$), Ag{220}∥Si($02\bar{2}$) and for other {hkl} planes of Ag crystallites as well. It is important note that for other {hkl} planes of Ag, such as, {002} and {112}, corresponding Debye-Scherrer rings are seen. This is more evident from the inset of Fig. 3.8 (c) and Fig. 3.8 (e). This confirms partial crystalline structure of the Ag nanostructures on HF treated substrate. Interestingly, some of the nanostructures are seen in rectangular shape (which shows aligned structures with substrate) on Sample B (Fig. 3.8 (d)). In some regions, morphology for Ag films on HF treated substrate (Sample B) is similar to Sample A and in other regions it is similar to Sample C. From the bright field image (Fig. 3.8 (f)) of Sample C (Ag film grown on reconstructed Si(5 5 12) surface), the Ag nanostructures found to be much larger and ordered. The corresponding SAD pattern shown in Fig. 3.8 (e) clearly displays that the Ag nanostructures are epitaxial in nature as diffraction from similar planes is seen for both the over film (Ag nanostructures and substrate silicon) (Inset of Fig. 3.8 (e)). As expected, the observed orientation relationships of Ag nanostructures with substrate (Samples A, B, C) from RHEED (Fig. 3.7 (a), (b) and (c)) and SAD (Fig. 3.8 (a), (c) and (e)) pattern are consistent with each other.

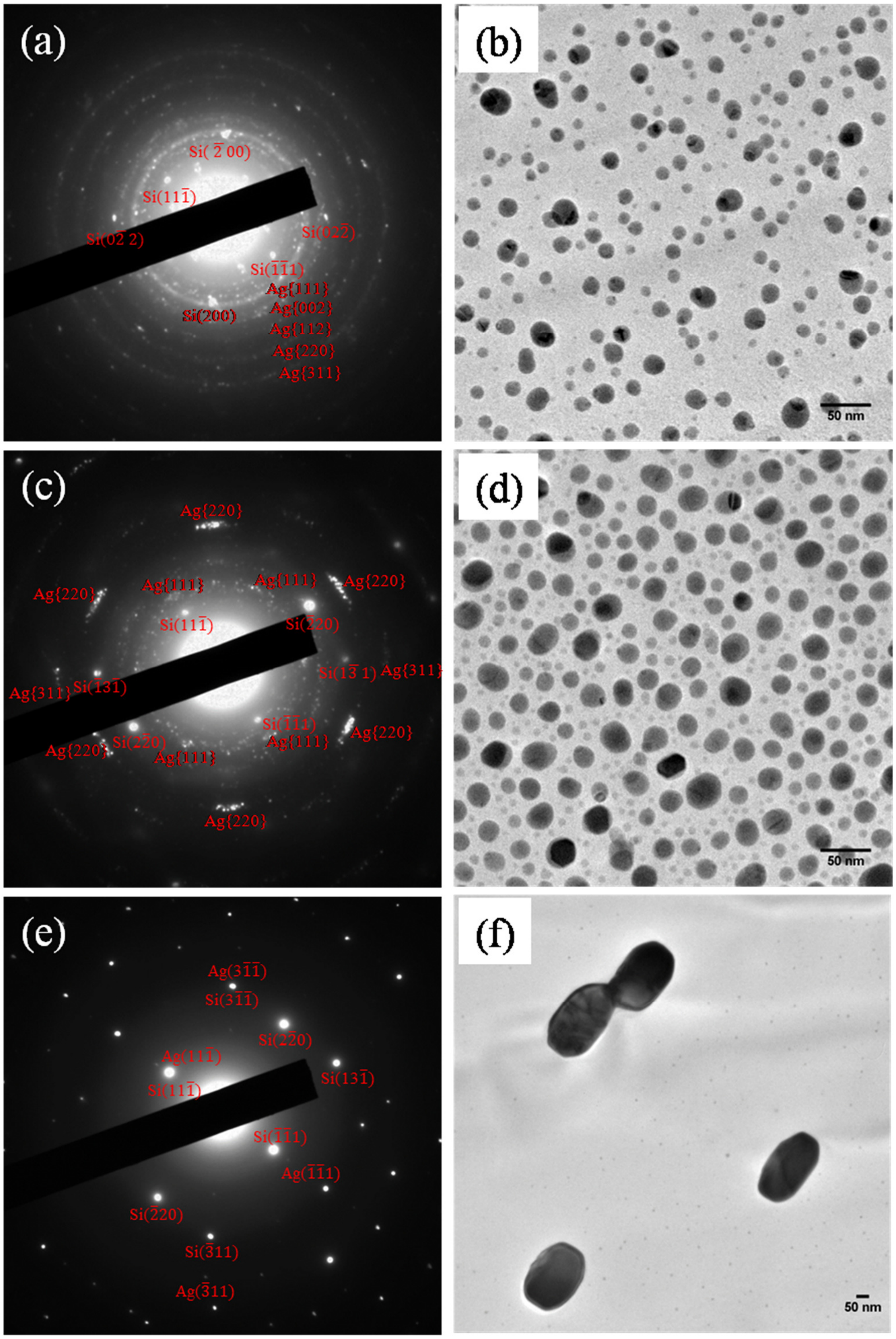

Figure 3.8 Selected area diffraction (SAD) and corresponding bright field TEM image for samples A, B and C: Fig. (a), (c) and (e) show the SAD pattern and Fig.

(b), (d) and (f) show the corresponding bright field images. For these samples, Ag nanostructures are grown by depositing a 3 nm Ag film under MBE conditions, at substrate temperature 400 °C (Sample A: with Native Oxide; Sample B: HF-treated and Sample C: Reconstructed).

In comparison with reconstructed substrate, amorphous oxide layer is acting as barrier for the nanostructures to follow the underlying substrate orientation. Apparently, after removal of native oxide layer using HF treatment, due to in-homogeneity and absence of long range ordering (Fig. 3.5 (a)-(b), 3.6 (b)) on the template, Ag doesn't grow as single crystalline and is followed as textured growth.

In comparison with native oxide covered and HF treated substrate, particle coverage is reduced for reconstructed substrate (as shown in Fig. 3.8 (b), (d), (f)). In case of reconstructed substrate, much bigger nanostructures (~ 250 nm) are observed. Cross-sectional TEM BF images are shown in Fig. 3.9. For Sample A (Fig. 3.9 (a)), the height of the Ag nanostructure is found to be ~ 20 nm for bigger ones and much smaller for the small ones. For the Sample B (Fig. 3.9 (b)), the height of the nanostructures is around 20 nm and the smaller one are not evident compared to Sample A. Fig. 3.9 (c) depicts XTEM BF image for Sample C which shows a typical size of 100 nm as their height. We can infer that bigger nanostructures are formed on reconstructed surface, at the expense of smaller nanostructures, due to smaller surface diffusion barrier compared to other two types of substrate. The inset in Fig. 3.9 (c) shows a crystalline interface between

Ag and Si. For Sample A and Sample B, presence of amorphous oxide layer has been seen. For Sample A, it indicates native oxide layer, whereas for Sample B it is probably partially grown re-oxidized layer due to keeping the HF treated substrate in air.

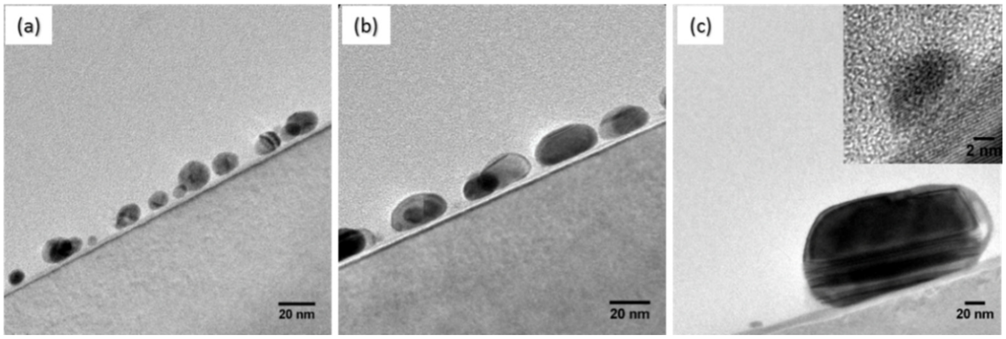

Figure 3.9 Bright field XTEM image for 3 nm Ag deposition on Si(5 5 12), at substrate temperature 400 °C with substrate a) native oxide covered (Sample A) b) HF treated (Sample B) c) reconstructed (Sample C).

3.4.3 Effect of substrate temperature (during Ag growth) on crystalline quality of Ag nanostructures on HF treated template

One of the main aim of this study is to find alternate methods to prepare high quality, highly oriented Ag nanostructures on Si on passivated high index substrates. We have also investigated the influence of substrate temperature on crystalline quality for Ag growth on HF treated substrate. In-situ RHEED studies have been carried out, after the growth of Ag nanostructures (by depositing a ~ 3 nm thin film under MBE conditions) along Si$[66\bar{5}]$ direction, keeping substrate at near RT (Sample D) and 600 °C (Sample E). Formation of Debye-Scherrer rings in RHEED pattern (as shown in Fig. 3.10 (a)) corresponding Ag{311} and Ag{311} reveals, Ag grows as polycrystalline in nature at near RT (Sample D). Whereas, in other case (Sample E), appearance of well ordered, symmetrically arranged diffraction spots (as shown in Fig. 3.10 (b)) and absence of Debye-Scherrer rings indicate grown Ag nanostructures at 600 °C (Sample E) has good crystalline quality. After cooling down to near RT, RHEED observation of Sample E shows same orientation relationship with good crystalline quality persists, similar as growth temperature 600 °C.

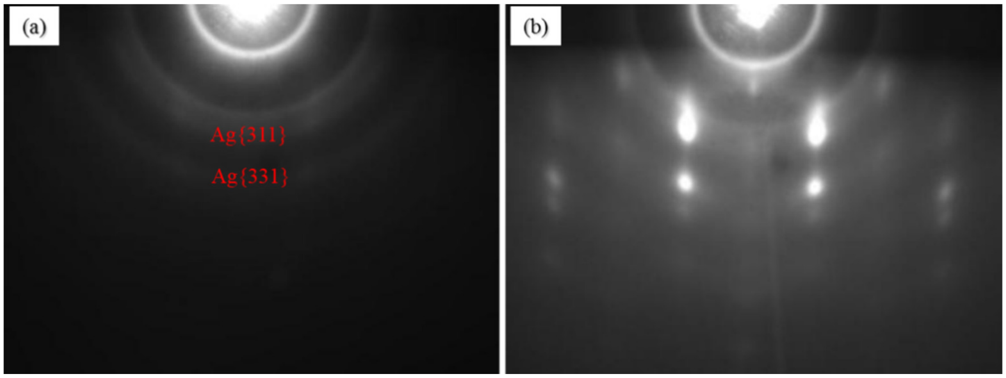

Figure 3.10 RHEED pattern along azimuthal direction Si[66$\bar{5}$], for 3 nm Ag deposition on HF treated substrate, at substrate temperature a) near room temperature (Sample D) b) 600 °C (Sample E).

3.4.4 Effect of Ag thickness on morphology for Ag growth on HF treated template

We have also investigated morphological evolution of the grown Ag nanostructures for growth on HF treated Si(5 5 12) surface at substrate temperature 400 °C, with variation of Ag thickness. SEM micrographs for growth of Ag with its thickness 1.0 nm, 1.6 nm and 3.0 nm are shown in Fig. 3.11 (a), (b) and (c) respectively. Evolution of probability distribution of particle size and 'mean size' of the particle with the Ag thickness are presented in Fig. 3.12 (a) and (b) respectively. Mean particle size of the nanostructures for 1.0 nm Ag growth is found as 56.61±5.97 nm^2. As the Ag thickness is increased to 1.6 nm, along with smaller size particles, larger particles start to grow (Fig. 3.11 (b)). It consequences slightly larger broadening of probability distribution of the particle size for 1.6 nm Ag growth than its lower thickness 1.0 nm (Fig. 3.12 (a)). In this case mean size of the particles becomes 160.37±11.75 nm^2. With further increase of Ag thickness to 3.0 nm, growth of quite larger sized nanostructures is evidenced (Fig. 3.11 (c)). In comparison with the growths with lower Ag thicknesses, in this case probability distribution of size of the grown nanostructures becomes relatively more diverge (Fig. 3.12 (a)). Indeed, 3.0 nm Ag growth consequences mean size of the particle as 348.35±38.15 nm^2. Therefore for Ag growth on HF treated Si(5 5 12) substrate at substrate temperature 400 °C, mean size of the particles is gradually increased in accordance with Ag thickness (Fig. 3.12 (b)).

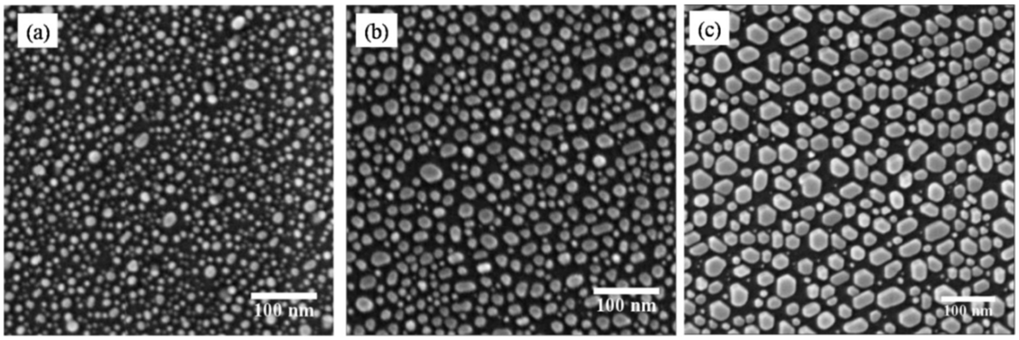

Figure 3.11 SEM micrographs for growth of Ag on HF treated Si(5 5 12) surface at substrate temperature 400 °C with various Ag thickness: a) 1.0 nm, b) 1.6 nm and c) 3.0 nm.

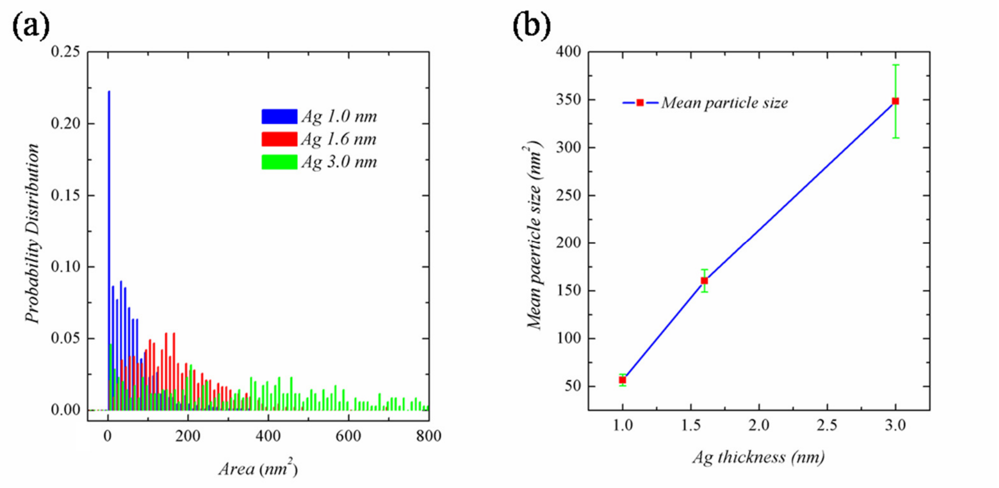

Figure 3.12 Ag growth on HF treated Si(5 5 12) substrate; a) Probability distribution of particle size for various Ag thickness and b) Plot of mean particle size as a function of Ag thickness.

3.5 Conclusions

We have presented the results to show a possibility of partial cleaning (*i.e.* removal of native oxide layer) of high-index silicon substrate at low-temperature using H-passivation through HF treatment. Usually, clean surfaces are obtained by removing native oxide layer by flashing the substrates to high temperature under UHV conditions. Our observations explore that the crystalline nature of Ag nanostructures grown on high index surface of silicon substrates [viz., on Si (5 5 12)] can be controlled by varying the composition of oxide layer at the interface of Ag and Si. Polycrystalline, textured or highly oriented Ag nanostructures are grown using a native oxide covered, HF-treated and reconstructed surface, respectively. Transmission electron microscopy and RHEED measurements have revealed that the textured grains are highly oriented in nature. We have shown that the crystalline quality of Ag nanostructures on HF-treated substrate is improved with increase in substrate temperature during growth. Ag growth on HF-treated substrate at elevated substrate temperature 400 °C explores gradual enhancement of particle size with increase of Ag thickness.

References

[1] A. A. Baski, L. J. Whitman, S. C. Erwin, *Science* **269**, 1556 (1995).

[2] A. A. Baski, K. M. Saoud, K. M. Jones, *Appl. Surf. Sci.* **182**, 216 (2001).

[3] R. A. Zhachuk, S. A. Teys, A. E. Dolbak, B. Z. Olshanetsky, *Surf. Sci.* **565**, 37 (2004).

[4] H. Omi, T. Ogino, *Phys. Rev. B* **59**, 7521 (1999).

[5] H. Kim, H. Li, J. M. Seo, *Surf. Sci.* **602**, 2563 (2008).

[6] K. Ohmori, Y. L. Foo, S. Hong , J. G. Wen, J. E. Greene., I. Petrov, *Nano Lett.* **5**, 369 (2005).

[7] M. Kumar, Govind, V. K. Paliwal, A. G. Vedeshwar, S. M. Shivaprasad, *J. Nanosci. Nanotechnol.* **7**, 1841 (2007).

[8] M. Hanbucken, B. Rottger, H. Neddermeyer, *Appl. Surf. Sci.* **164**, 91 (2000).

[9] H. H. Song, K.M. Jones, A. A. Baski, *J. Vac. Sci. Technol., A***17**, 1696 (1999).

[10] K. M. Jones, H. H. Song, A. A. Baski, *J. Cluster Sci.* **10**, 573 (1999).

[11] T. Nakahara, S. Ohkura, F. Shoji, T. Hanawa, K. Oura, *Nucl. Instrum. Methods Phys. Res., Sect. B* **45**, 467 (1990).

[12] K. Sekar, P. V. Satyam, G. Kuri, D. P. Mahapatra, B. N. Dev, *Nucl. Instrum. Methods Phys. Res., Sect. B* **71**, 308 (1992).

[13] R. Naik , C. Kota, B.U. M. Rao, G. W. Auner, *J. Vac. Sci. Technol., A* **12**, 1832 (1994).

[14] B. Sundaravel, A. K. Das, S. K. Ghose, K. Sekar, B. N. Dev, *Appl. Surf. Sci.* **137**, 11 (1999).

[15] A. Roy, K. Bhattacharjee, J. K. Dash, B. N. Dev, *Thin Solid Films* **520**, 853 (2011).

[16] A. Roy, K. Bhattacharjee, J. K. Dash, B. N. Dev, *Appl. Surf. Sci.* **256**, 361 (2009).

[17] A. Roy, K. Bhattacharjee, J. Ghatak, B. N. Dev, *Appl. Surf. Sci.* **258**, 2255 (2012).

[18] T. Wadayama, M. Takada, A. Hatta, *Appl. Phys. A* **80**, 615 (2005).

[19] Y. Chen, C. Wang, H. Liu, J. Qiu, X. Bao, *Chem. Commun.* **42**, 5298 (2005).

[20] R.R. Juluri, A. Ghosh, A. Bhukta, R. Sathyavathi, P. V. Satyam, *Thin Solid Films* **586**, 88 (2015).

[21] R. R. Juluri, A. Rath, A. Ghosh, A. Bhukta, R. Sathyavathi, D. N. Rao, K. Muller, M. Schowalter, K. Frank, T. Grieb, F. Krause, A. Rosenauer, P. V. Satyam, *Sci. Rep.* **4**, 4633 (2014) *(Nature publishing group).*

[22] D. K. Goswami, B. Satpati, P. V. Satyam, B. N. Dev, *Curr. Sci. (India)* **84**, 903 (2003).

[23] C. W. Jones, *Applications of Hydrogen Peroxide and Derivatives*, Royal Society of Chemistry, Cambridge UK, 1999.

[24] T. Suzuki, H. Minoda, Y. Tanishiro and K. Yagi, *Surf. Sci.* **348**, 335 (1996).

[25] J. K. Dash, T. Bagarti, A. Rath, R. R. Juluri and P. V. Satyam, *EPL* **99**, 66004 (2012).

[26] A. Bhukta, P. Guha, A. Ghosh, P. Maiti, P. V. Satyam, *Appl. Phys. A* **122**, 356 (2016).

[27] A. A. Baski, S. C. Erwin, L. J. Whitman, *Surf. Sci.* **392**, 69 (1997).

Chapter 4

Ag Induced Bimetallic (Au-Ag) Nanowires on High Index Si(5 5 12) Substrate

4.1 Introduction

To achieve superior performance than the conventional metal nanoparticle, a lot of research works have been dedicated to prepare bimetallic nanoparticle (BMNP) with their different configurations as core-shell [1-3], alloy [4, 5] or hetero-junction [6, 8]. Successful implication of grown BMNPs explores their better performance in the field of catalysis [9, 10], electrochemistry [11, 12] than their monometallic counterparts. As a result of nearly equal lattice constant with FCC structure, comparable surface free energy and isoelectronic property Au-Ag binary system comprise remarkable miscibility [13]. Therefore it is considered as an ideal bimetallic system to comprehend various properties of BMNPs. In comparison with its monometallic counterparts, Au-Ag BMNPs exhibit better catalytic property for oxidation of carbon monoxide (CO) [14] and hydrogenation of dimethyl oxalate to methyl glycolate [15]. Systematic variation of Au:Ag composition ratio of the Au-Ag BMNPs consequences proficient tailoring of its surface plasmon resonance property [4] and work function [16].

In the present chapter, we discuss about the role of a sub-monolayer deposition of Ag on a one-dimensional template (achieved through the reconstruction of Si(5 5 12) surface) under ultra-high vacuum (UHV) conditions, energetically favoring the formation of AuAg bimetallic nanowires with *tunable aspect ratio.* Kinematic Monte Carlo (KMC) simulations with solid on solid model system, considering anisotropic diffusion across the steps with the inputs on the ratio of binding energies taken from density functional theory (DFT) calculations, show a favorable mixing of AuAg bimetallic nanowires along with the qualitative agreement on the variation of the aspect ratio of AuAg nanowires.

4.2 Experimental Methods

Reconstructed Si(5 5 12) surface is prepared by repetitive flashing at 1200 °C for 60 seconds, using direct current (DC) heating method. Au and Ag are deposited by using Knudsen cells in a custom designed molecular beam epitaxy (MBE) chamber [17]. The base pressure in the growth chamber is ~ 2.0×10^{-10} mbar and it rises to ~ 1.0×10^{-9} mbar during growth of the metals. For both the metals, thickness is represented in a monolayer (ML) unit where 1 ML = 1.0×10^{15} atoms/cm^2. Substrate temperature is measured using a Type K thermocouple attached to the substrate. In-situ scanning tunneling microscopy (STM) measurements have been carried out using the variable temperature STM (VTSTM) which is coupled with MBE chamber [17]. Post-annealing has been performed inside the MBE chamber using resistive heating method. Followed by the growth and in-situ STM measurements, samples are brought out from the

MBE chamber and imaging is performed with 20 keV electrons by employing field emission gun based scanning electron microscopy (FEGSEM). Further 300 keV scanning transmission electron microscopy (STEM) is utilized to accomplish high angle annular dark field (HAADF) imaging and compositional analysis using energy dispersive X-ray spectroscopy (EDS) mapping.

4.3 Theoretical Modeling

4.3.1 Description of DFT model and outcomes

The electronic structure of layered silicon has been calculated within a plane wave pseudo potential implementation of density functional theory using VASP [18] code. In the calculation 8 layers of Si, a vacuum of 15 Å has been inserted between 8 successive Si layers to minimize interactions between images in the periodic supercell method that we use.

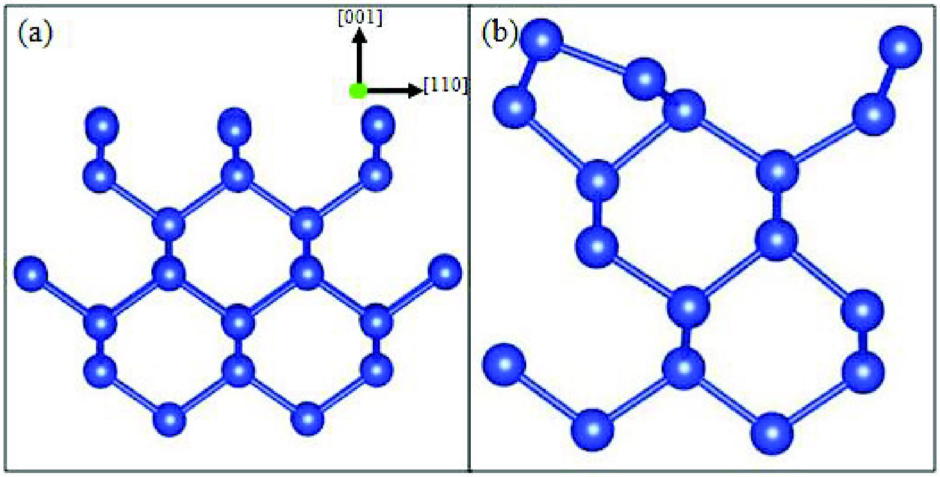

Figure 4.1 Schematic diagram of configuration of substrate Si atoms a) before and b) after the reconstruction. Si atoms are indicated as Blue color. Orientations of the substrate planes are indicated inside of Fig. 4.1 (a).

Projected augmented wave [19, 20] potentials have been used to solve the electronic structure self consistently using a k-points mesh of 12 × 12 × 1, and plane wave with kinetic energy 410 eV. PBE [21] potentials have been used for the exchange correlation. Focused on dimer rows of surface Si atoms of reconstructed surface, dependence of binding energies of Au-Ag binary system on Au:Ag concentration ratio has been systematically investigated. In our present model, reconstruction of surface Si atoms for the stable low index plane of Si *i.e.* Si(001) has been considered. The last layer of Si and the passivated H atoms are kept fixed in order to mimic the bulk like structure, and the remaining layers are allowed to relax. It consequences formation of stable template consisting of dimer rows on top of the Si surface (Fig. 4.1) which is further employed as a reference to determine the binding energy of the Au-Ag binary system.

In the Au-dimer calculations, we first assume the various probable configurations of dimers as shown in Fig. 4.2. Among them, Conf-C comprises highest stability which consistently follows the previously reported results [22]. Similarly, for Ag-dimer and Au-Ag dimer the Conf-C remains the most stable configuration. The binding energy of the dimer is calculated as $E_{BE(dimer)} = E_{Si} + E_{dimer} - E_{dimer\text{-}Si}$, where $E_{BE(dimer)}$ is binding energy of Au-Au, Ag-Ag or Au-Ag dimers, $E_{dimer\text{-}Si}$ is the total energy of the dimer over the 8-Si layers, E_{Si} is the total energy of the 8-Si layers and E_{dimer} is the total energy of the dimers in a vacuum of 15Å × 15Å × 15Å. The binding energies obtained from the calculations are $E_{BE(Ag\text{-}Ag)} = 3.37$ eV, $E_{BE(Au\text{-}Ag)} = 3.85$ eV and $E_{BE(Au\text{-}Au)} = 4.56$ eV. Thereafter, we have also investigated the binding energies of various trimers with varying Au:Ag concentration ratio on such template (Fig. 4.3). Since from the dimer calculations we get Conf-C as the most stable, so we continue to add another atom in that configuration, for the trimer calculations. The binding energy values for the trimers are $E_{BE(Ag3)} = 5.19$ eV, $E_{BE(Au-Ag2)} = 5.71$ eV, $E_{BE(Au2-Ag)} = 6.19$ eV and $E_{BE(Au3)} = 6.89$ eV.

Therefore, our investigation on both dimer and trimer configurations reveal binding energy of Au-Ag binary system is systematically enhanced with gradual increase of Au:Ag concentration ratio. Such correlation has also been reported by Q. Deng *et al.* with consideration Au32-nAgn (n = 1-31) binary clusters [23].

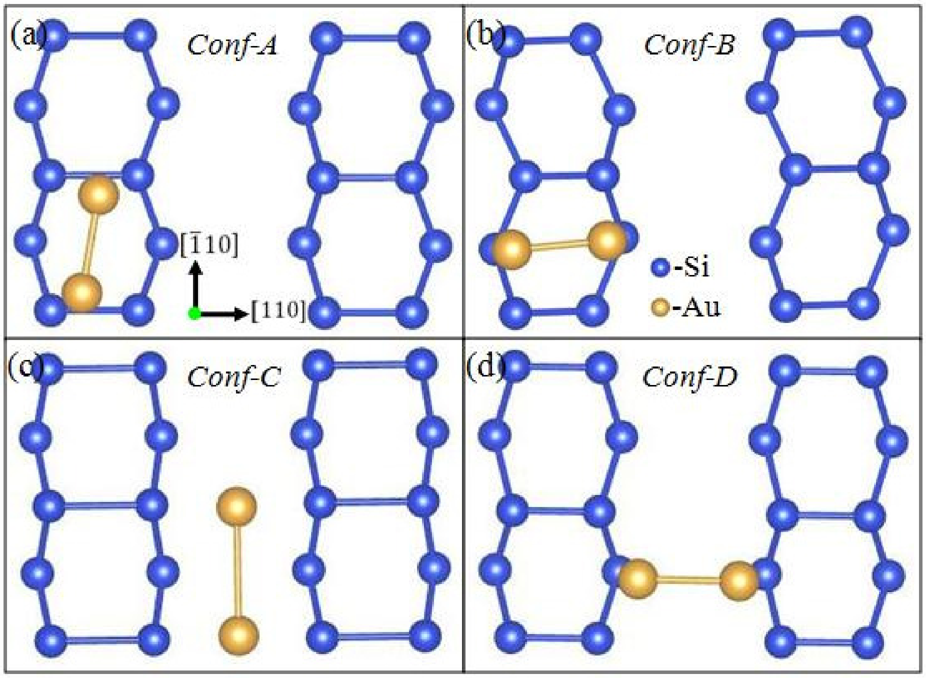

Figure 4.2 Schematic diagram of Au dimer over Si layer with four different configurations (a)-(d). Au and Si atoms are indicated as yellow and blue color respectively. Orientations of the substrate planes are indicated inside of Fig. 4.2(a).

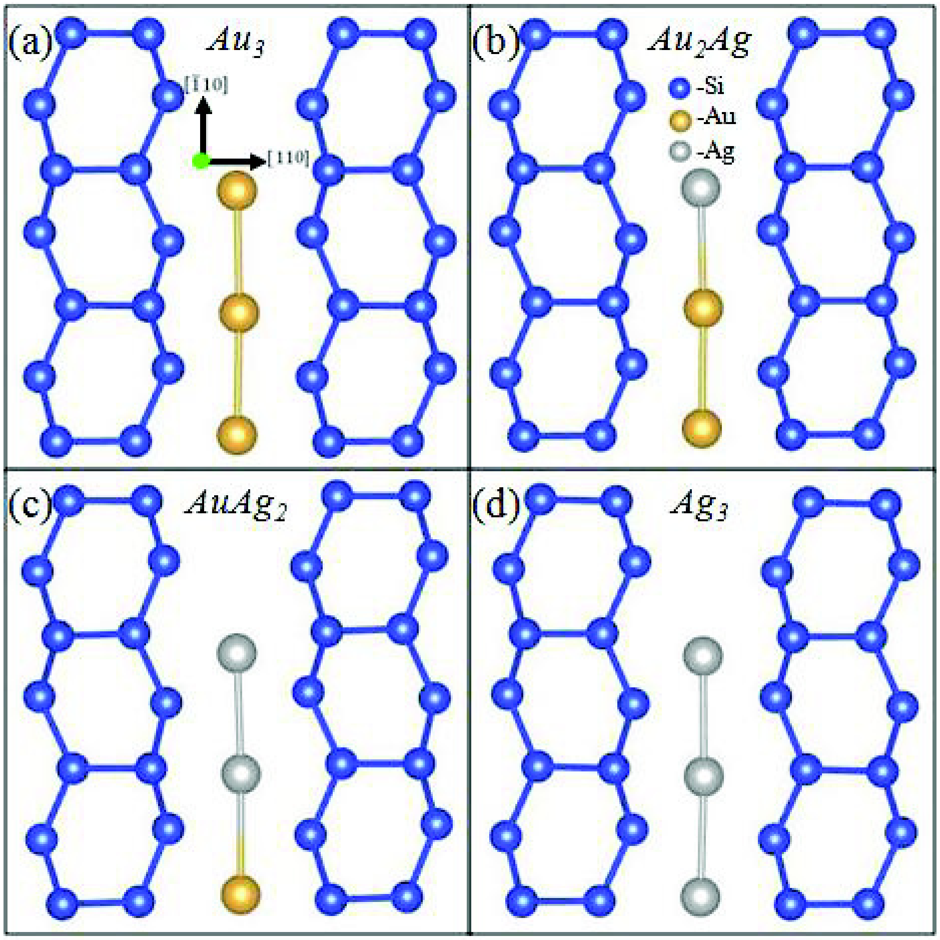

Figure 4.3 Schematic diagram of Au-Ag trimer over Si layer with substrate configuration Conf-C (as mentioned in Fig. 4.2) for a) Au_3, b) Au_2Ag, c) $AuAg_2$ and d) Ag_3. Here, Si, Au and Ag atoms are indicated by blue, yellow and grey color respectively. Orientations of the substrate planes are indicated inside of Fig. 4.3(a).

4.3.2 Description of KMC model

Remarkable influence of Ag on the morphology of Au-Ag bimetallic growth has been explained by using a simple solid-on-solid KMC model which approximately incorporates the symmetries of reconstructed Si(5 5 12) surface. In the model, a periodic variation of the diffusion barrier along the y-axis (*i.e.* Si$\langle 66\bar{5}\rangle$) and constant along the x-axis (*i.e.* Si$\langle 1\bar{1}0\rangle$) has been considered. The deposition proceeds in two steps, *i.e.* first Ag is deposited followed by Au with the same rate. The thermally activated hopping rate (P) is given by

$$P = \gamma_d \exp^{-\left(E/k_B T\right)} \tag{4.1}$$

where, E is the activation energy, k_B is the Boltzman constant, T is the temperature and γ_d is the attempt frequency with typically values of ~ 10^{13} s^{-1}. The energy $E = E_1 + E_2 + E_d + V$ where, $E_1 = nE_{Ag\text{-}Ag} + mE_{Ag\text{-}Au}$, for the Ag hopping atom and $E_1 = nE_{Au\text{-}Au} + mE_{Ag\text{-}Au}$ for Au, $E_2 = n'E'_{Ag\text{-}Ag} + m'E'_{Ag\text{-}Au}$ for the Ag atom and $E_2 = n'E'_{Au\text{-}Au} + m'E'_{Ag\text{-}Au}$ for Au, are the nearest neighbor and the next nearest neighbor binding energies with n(n') and m(m') denoting the number of bonds, E_d is the diffusion barrier, V(x, y) is potential that adds a periodic modulation to the diffusion barrier. Nearest neighbor hopping is allowed with probability 1 if the site is empty and does not form overhang. Hopping over a step edge is allowed with a probability $\exp(-E_{ES}/k_B T)$ where E_{ES} is the Elrich-Schboebel barrier. For simulation, we use an algorithm similar to the one used in [24, 25]. Since energy scales with temperature, we set $k_B T = 1$ in our present KMC model. Based on our DFT results (as discussed in preceding subsection

4.3.1) which reveals the binding energy of Au-Ag binary system is gradually increased in accordance to Au:Ag concentration ratio, we have chosen nearest neighbor binding energies as $E_{Ag\text{-}Ag} = 1.0$, $E_{Ag\text{-}Au} = 1.25$, $E_{Au\text{-}Au} = 1.5$. Next nearest neighbor binding energies are considered as $E'_{Ag\text{-}Ag} = 0.025$, $E'_{Ag\text{-}Au} = E'_{Au\text{-}Au} = 0.0375$. At elevated substrate temperature, larger and isotropic interaction of Au than Ag with surface atoms on reconstructed Si(5 5 12) surface [26] is rationalized by us with relative strength of E_d and V for Au and Ag. The anisotropic diffusion barrier is $E_d = 0.75$ for Au and $E_d = 0.5$ for Ag. The potential $V(x, y) = 0.75$ if $0 < y \bmod L < L_1$ and 0.15 otherwise for Ag, and $V(x, y) = 1.0$ if $0 < y \bmod L < L_1$ and 0.4 otherwise for Au, where $L = L_1 + L_2$ is the periodicity of the potential. We have taken $L_1 = 5$ and $L_2 = 30$ in units of lattice constant. The periodic characteristic of V(x, y) along y-axis is analogous to the periodic reactivity of reconstructed Si(5 5 12) surface with adatoms along Si$\langle 66\bar{5} \rangle$ [27]. For the KMC simulation we have used lattice size N = 400 and coverages $\Theta_{Ag} = 0.0,\ldots,0.7$ ML for fixed value of $\Theta_{Au} = 1.0$ ML.

4.4 Results and discussions

4.4.1 Modification of ultra-clean reconstructed Si(5 5 12) substrate by sub monolayer Ag

Fig. 4.4(a) shows the unmodified, ultra-clean reconstructed Si(5 5 12) surface exploring its characteristic periodicity ~ 5.30 nm along $<66\bar{5}>$ and atomic rows along $<1\bar{1}0>$, respectively [28-30]. When it is modified with a sub-monolayer (0.50 ML) Ag deposition at room temperature (RT) and subsequent annealing at

300 °C, oriented Ag strips along atomic row direction are formed [Fig. 4.4(b)] in agreement of the H. H. Song *et al.* [27]. Atomic rows of reconstructed Si surface are still locally evident as it is not completely terminated by such Ag strips. The dimension of these Ag strips along step edge direction *i.e.* <1$\bar{1}$0> is much larger than its perpendicular direction and this is evident by imaging over a larger area (40 nm × 40 nm) [Fig. 4.4(c)]. Locally, well ordered growth of Ag strips is also disrupted by agglomeration of the Ag atoms. Line profile over a unit cell along <66$\bar{5}$> reveals underlying periodicity which has three subunits *i.e.* (225), (337) and (225) plane of Si, is not significantly modified due to partial disappearance of reconstructed surface by the Ag strips [Fig. 4.4(d)].

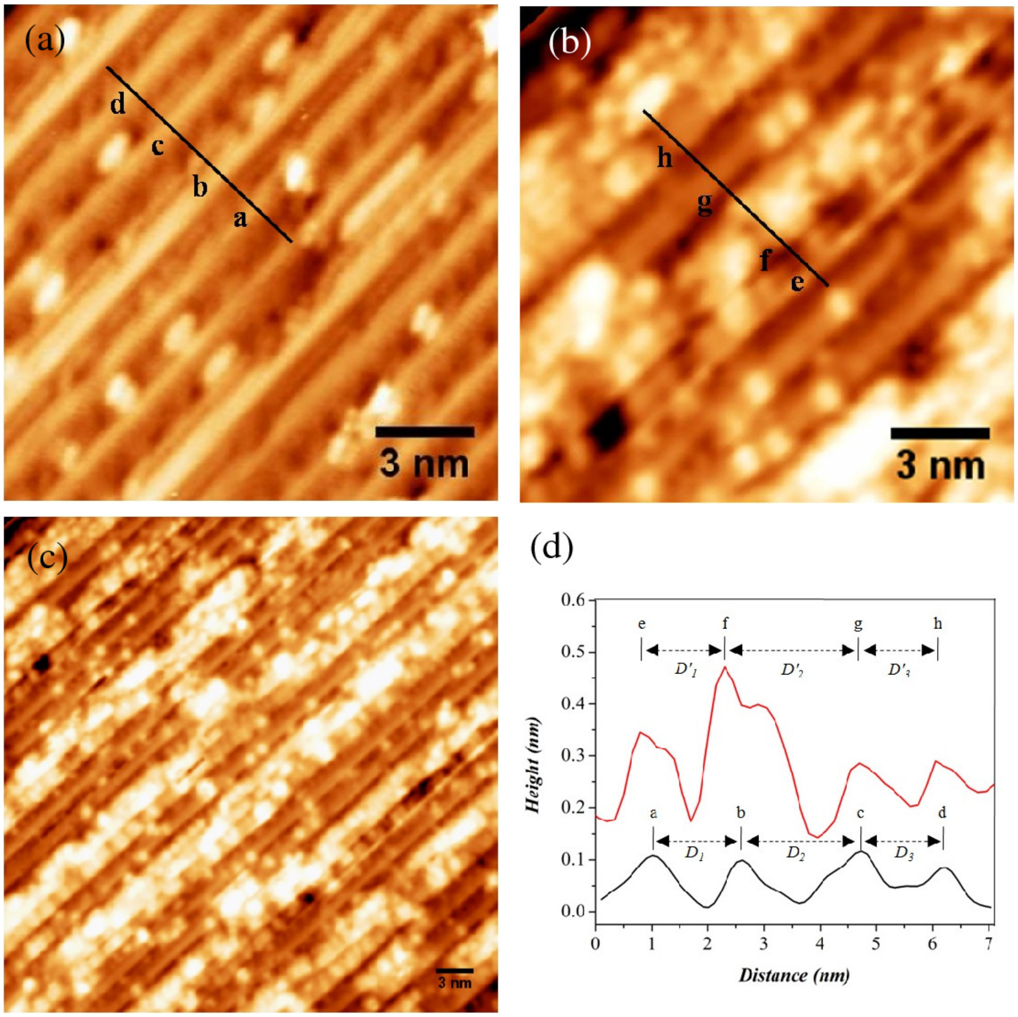

Figure 4.4 STM topographic image of a) reconstructed Si(5 5 12), b) and c) after modification of reconstructed Si(5 5 12) surface with 0.50 ML Ag and subsequent annealing at 300 ºC for one hour over a smaller and larger area of the surface respectively. d) Line profile along Si$[66\bar{5}]$ as marked on reconstructed surface (black line) and Ag modified surface (red line) as shown in Fig. 4.4(a) and Fig. 4.4(b) respectively. Three subunits of unit cell *i.e.* Si(225), Si(337) and Si(225) planes are represented as D_1(1.65±0.43 nm), D_2(1.99±0.42 nm) and D_3(1.54±0.38 nm) on reconstructed surface and as D_1'(1.34±0.52 nm), D_2'(2.55±0.53 nm) and D_3'(1.36±0.59 nm) on Ag modified surface.

4.4.2 Morphological evolution of Au-Ag bimetallic growth with variation of Ag thickness: *experimental outcomes*

Our investigations are focused to understand the influence of a sub-monolayer deposition of Ag on ultraclean reconstructed surface on the over-layer growth of Au at elevated growth temperature (300 °C). Reconstructed Si(5 5 12) is modified by growing Ag (Ag:Si(5 5 12)), with different thickness and subsequent annealing at 300 °C for one hour. For preparing different Ag:Si(5 5 12) systems, Ag thickness (Θ_{Ag}) is varied as 0.0 ML, 0.10 ML, 0.25 ML, 0.50 ML and 1.00 ML. Au with thickness 1.50 ML is grown by keeping different Ag:Si(5 512) at 300 °C. Following the Au growth, Au/Ag:Si(5 5 12) system is post annealed at 300 °C for 30 Minutes in UHV. Each Ag thickness and fixed Au thickness is considered as one system. Fig. 4.5(a)-(e) show the topographical image of different Au/Ag:Si(5 5 12) systems with varying Θ_{Ag} and the corresponding mean aspect ratio is presented in Fig. 4.10. In-situ (UHV) STM topographic image for Au growth with 0.0 ML Ag (*i.e.* ultra-clean reconstructed surface) is presented in Fig. 4.5(a) which shows formation of elliptical shaped Au nanostructures with slight elongation along the step edge direction $\langle 1\bar{1}0 \rangle$reflecting the anisotropic growth of adatoms [26, 31, 32]. With increase of Θ_{Ag} (prior deposition of Ag with coverage Θ_{Ag}) to 0.10 ML, no significant change in morphology of elliptical nanostructures is observed compared to no prior Ag deposition (Θ_{Ag} = 0 ML). Effect of pre-deposition by Ag on growth of Au is noticeable, when Θ_{Ag} is increased to 0.25 ML [Fig. 4.5(c)]. Here, along the elliptical shaped nanostructures, rectangular shaped nanowires with higher aspect ratio have started to grow. On further increasing of Ag to 0.50 ML, formation probability of rectangular wire shaped nanostructures is enhanced relative to 0.25ML. Hence, pre-deposition of ultraclean reconstructed substrate with Ag coverage lower than 0.25 ML, does not influence substantial modification of morphology of the Au-Ag bimetallic growth. It is found that Ag initiates decisive role to govern morphology after Au growth for Θ_{Ag} larger than 0.25 ML. With further enhancement of Θ_{Ag}, in the ~ 0.25-0.60 ML regime, mean aspect ratio is steadily increased with much faster rate than the lower regime ($\Theta_{Ag}< 0.25$ ML). Thereafter, up to maximum a value (of our consideration) of $\Theta_{Ag} = 1.00$ ML, both elliptical shaped nanostructures with smaller aspect ratio and rectangular shaped nanowire with higher aspect ratio co-exist. In this regime, gradual addition of Ag although consequences enhancement of width and length of the nanostructures, mean aspect ratio is not altered considerably. Indeed, modification of ultraclean surface with $\Theta_{Ag} = 1.0$ ML remarkably enhance the aspect ratio of a few nanowires by nearly five times than the Au growth. In the efficient influencing region of Θ_{Ag} *i.e.* 0.25-1.0 ML, substantial formation of nanowires with aspect ratio much larger than its mean value is quite evidenced. Probability distribution of the aspect ratio reveals that with respect to Θ_{Ag} equals to 0.0 ML, mean aspect ratio is enhanced nearly 1.70 times [Fig. 4.5(f)] for increase of Θ_{Ag} to 1.0 ML. Indeed influence of Ag makes the probability distribution more broadened towards its tail due to substantial formation of nanostuctures with larger aspect ratio than its mean value.

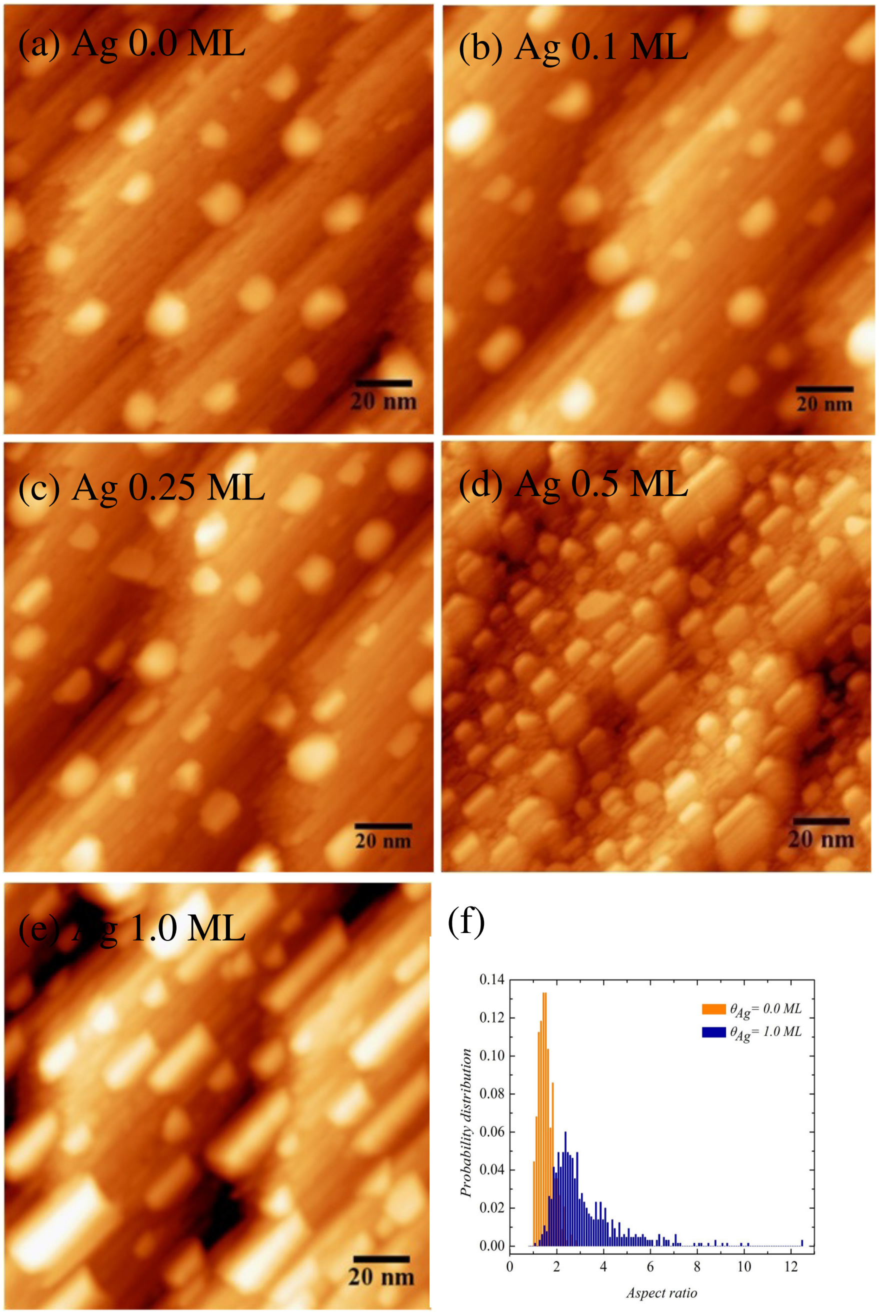

Figure 4.5 STM topographic image after 1.5 ML Au growth on Ag:Si(5 5 12) at 300 ℃ substrate temperature with Θ_{Ag} as a) 0.0 ML, b) 0.10 ML, c) 0.25 ML, d) 0.50 ML and e) 1.00 ML. f) Probability distribution of aspect ratio of grown nanostructures for Θ_{Au} = 1.5 ML with Θ_{Ag} = 0.0 ML (orange) and Θ_{Ag} = 1.0 ML (blue) as shown in Fig. 4.5(a) and 4.5(e) respectively.

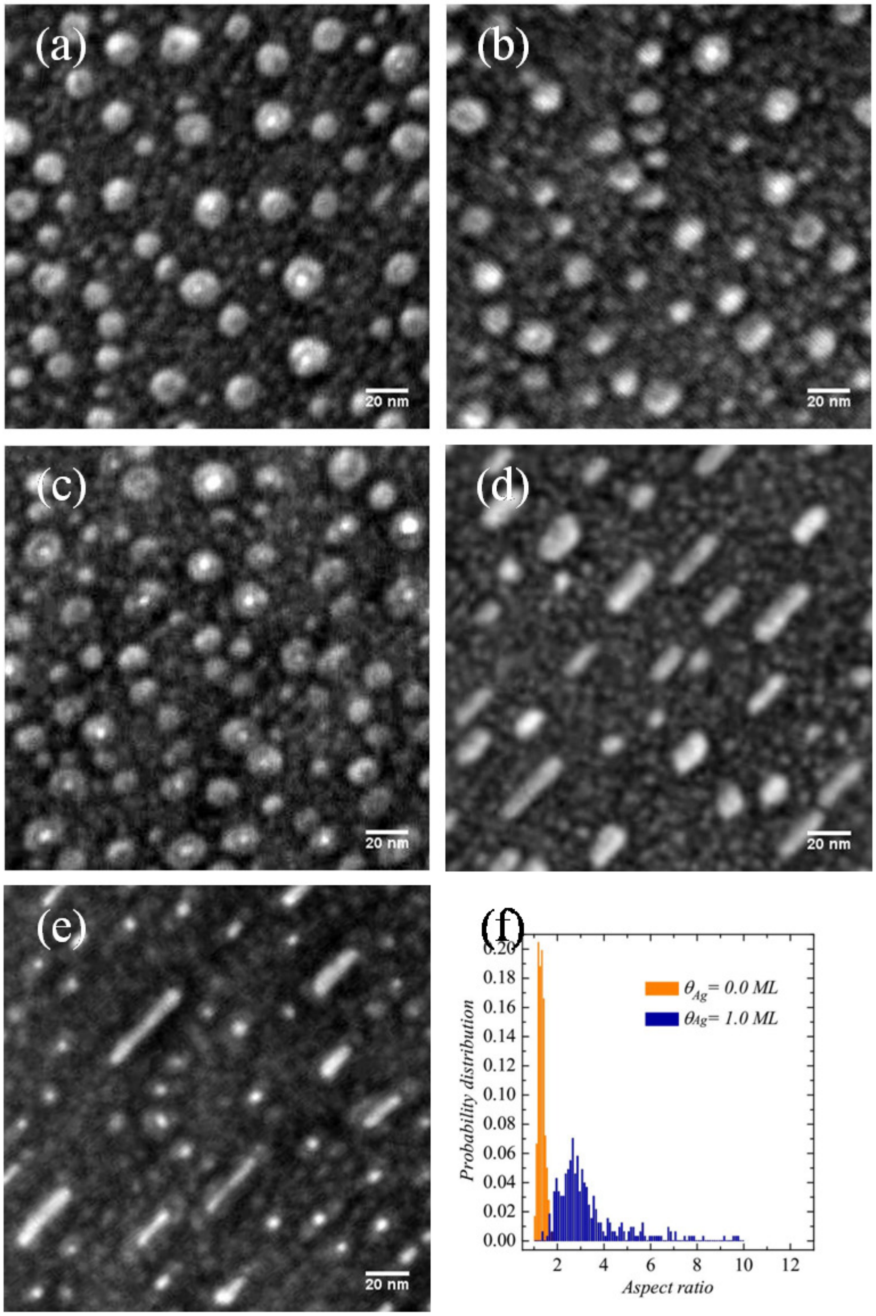

Figure 4.6 SEM image after 1.5 ML Au growth on Ag:Si(5 5 12) at 300 ºC substrate temperature with Θ_{Ag} as a) 0.0 ML, b) 0.10 ML, c) 0.25 ML, d) 0.50 ML, e) 1.00 ML. f) Probability distribution of aspect ratio of grown nanostructures for Θ_{Au} = 1.5 ML with Θ_{Ag} 0.0 ML (orange) and Θ_{Ag} 1.0 ML (blue) as shown in Fig. 4.6(a) and 4.6(e) respectively.

After bringing out these samples exterior of the growth chamber, we have carried out ex-situ scanning electron microscopy (SEM) measurements to study these morphological aspects (Fig. 4.6). General characteristics of morphological evolution from both methods (*i.e.* SEM and STM) show quite resemblance with slight variation of mean aspect ratio of the nanostructures.

4.4.3 Morphological evolution of Au-Ag bimetallic growth with variation of Ag thickness: *KMC simulation outcomes*

Nucleation

Fig. 4.7 represents 3D imaging of the nanoislands as observed in KMC simulation at various stages of Au-Ag bimetallic growth. We observe that when Ag atoms are deposited on the anisotropic template, elongated Ag islands are grown along the preferential direction *i.e.* x-axis (Fig. 4.7(a)). Thereafter as the Au atoms are deposited they are nucleated towards the Ag islands and also the uncovered region (*i.e.* Ag free region) of the surface (Fig. 4.7 (b)). Before Au deposition, a few of the Ag atoms are observed on the template, which are not incorporated in the 3D Ag islands. Such Ag atoms are also acting as the nucleation center for the incoming Au adatoms.

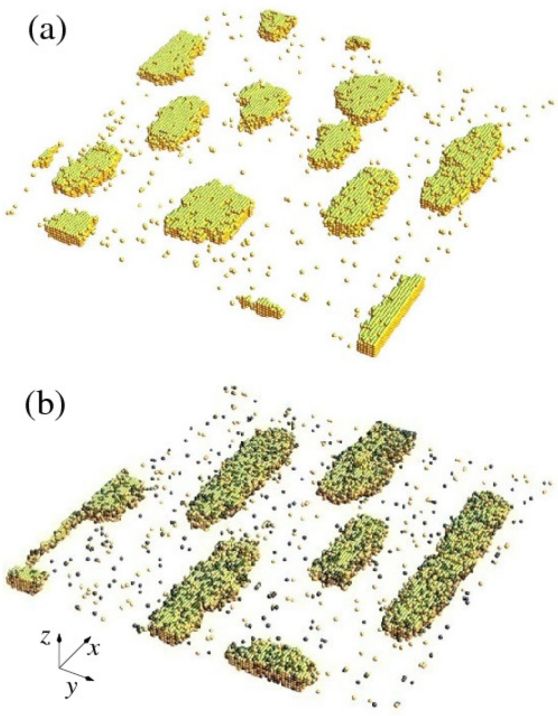

Figure 4.7 Three dimensional (3D) KMC simulation image over 400×400 square lattice in X-Y plane, for growth of a) 0.40 ML Ag and b) 1.0 ML Au followed by the Ag growth as shown in Fig. 4.7(a).

Morphology

Fig. 4.8(a)-(h) represents the Au-Ag bimetal island growth with systematic variation of Θ_{Ag} and corresponding mean aspect ratios are shown in Fig. 4.10. For Θ_{Ag} equals to 0.0 ML, elongated Au islands are grown along the preferential growth direction of adatoms *i.e.* x-axis. Au-Ag morphology is not influenced significantly with small increase of Θ_{Ag} to 0.10 ML and the mean aspect ratio remains nearly invariant. Substantial influence of Ag is starts to exhibit when Θ_{Ag} becomes ~ 0.30 ML. In the regime of Ag coverage ~ 0.20-0.40 ML, islands gradually become more elongated along x-axis and the mean aspect ratio is rapidly increased. Such steady enhancement of mean aspect ratio is interrupted as Θ_{Ag} is increased further. In the higher regime of Θ_{Ag} *i.e.* ~ 0.40-0.70 ML although length and width of the islands are changed, mean aspect ratio remains almost invariant. It should be noted that, a small number of island coalesce with neighboring islands at higher coverage ($\Theta_{Ag} > 0.40$ ML).

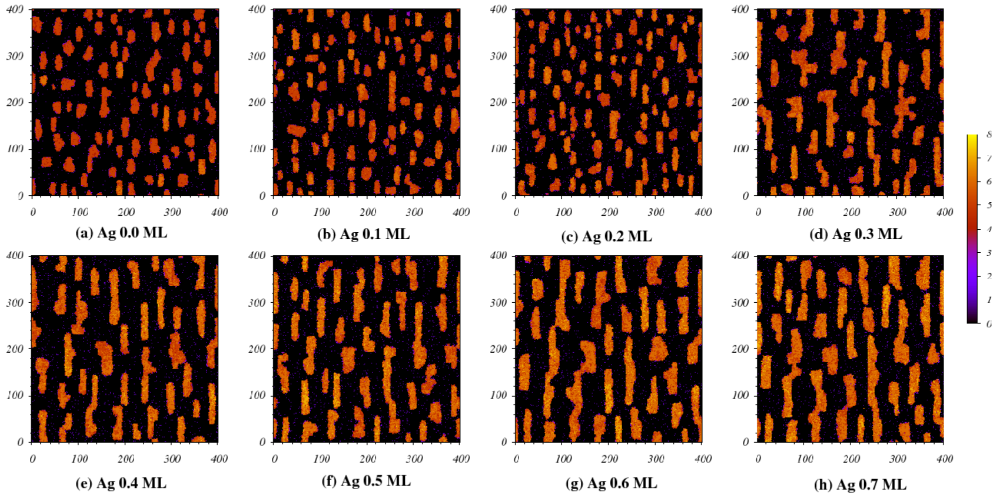

(a) Ag 0.0 ML (b) Ag 0.1 ML (c) Ag 0.2 ML (d) Ag 0.3 ML

(e) Ag 0.4 ML (f) Ag 0.5 ML (g) Ag 0.6 ML (h) Ag 0.7 ML

Figure 4.8 KMC growths of Au-Ag bimetallic islands with Θ_{Au} 1.0 ML and varying Θ_{Ag} as a) 0.0 ML, b) 0.1 ML, c) 0.2 ML, d) 0.3 ML, e) 0.4 ML, f) 0.5 ML, g) 0.60 ML and h) 0.70 ML.

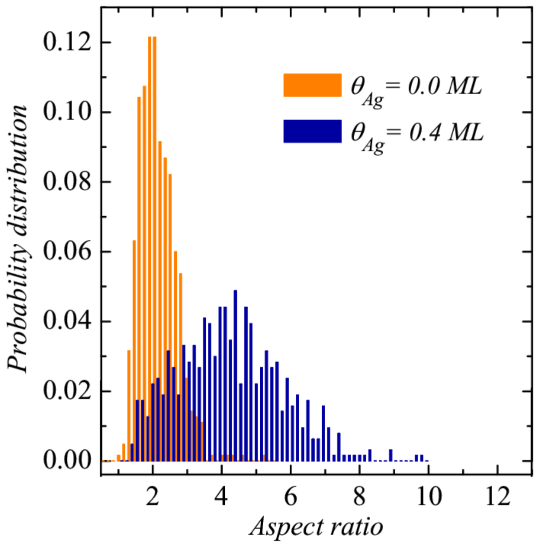

Figure 4.9 Probability distribution of aspect ratio of grown nanoislands in KMC simulation for Θ_{Au} = 1.0 ML with Θ_{Ag} = 0.0 ML (orange) and Θ_{Ag} = 0.4 ML (blue).

4.4.4 Comparison of experimental and KMC simulation outcomes

The fitted solid curve in Fig. 4.10 is $R(\Theta) = a + b\tanh(c(\Theta - \Theta_0))$, where Θ is the Ag coverage, which saturates for large value of Ag coverage to a value $R(\Theta)$ = a + b. Θ_0 is the Ag coverage where R = a and aspect ratio grows with Θ at a rate b×c. It roughly gives an estimate of the threshold Ag coverage beyond which aspect ratio begins to saturate. The obtained parameters are a = 2.09±0.01, b = 0.54±0.15, c = 11.5±2.3 and Θ_0 = 0.231±0.006 for experiment and a = 3.24±0.04, b = 1.0±0.05, c = 15.4±4.6 and Θ_0 = 0.30±0.01 for simulation. Although the numerical values are slightly different, general features of evolution of Au-Ag morphology (in terms of mean aspect ratio) by influence of Ag coverage are analogously supported by our experimental measurements and KMC simulation.

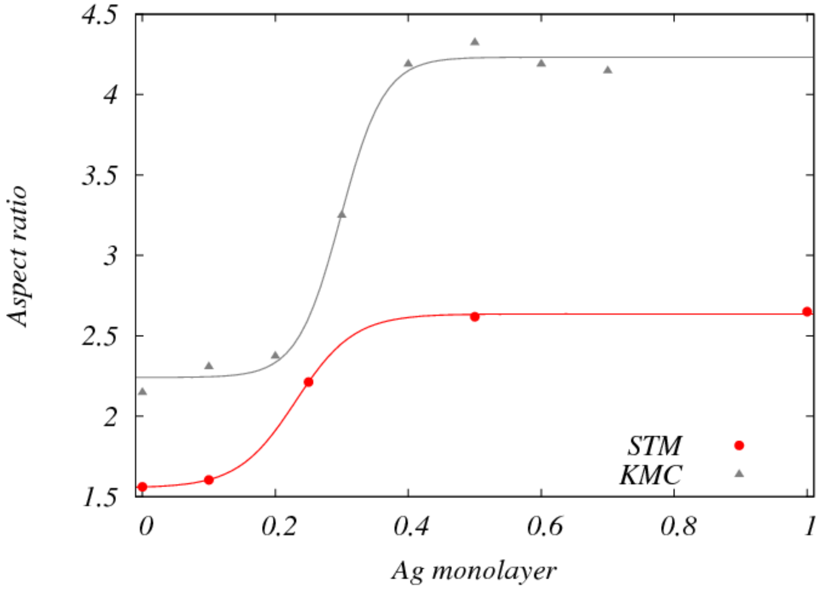

Figure 4.10 Plot of mean aspect ratio of the nanostructures as a function of Ag coverage as obtained from experiment (red) with Θ_{Au} = 1.50 ML and KMC simulation (grey) with Θ_{Au} = 1.00 ML. Fitted curves are represented by the corresponding solid lines.

4.4.5 Structural aspects of grown Au-Ag bimetallic nanostructures *from STEM*

Fig. 4.11 (a) indicates the cross section STEM micrograph, where brighter regions indicate higher Z value due to 'Z contrast' among the dissimilar elements of the nanostructure and the substrate. EDS Line profile using cross section STEM method indicates that grown nanostructures are composed of both the constituent metal Au and Ag [Fig. 4.11 (b)]. Within a single nanostructure, core shell structure of constituent atoms or bimetallic heterojunction, is not observed.

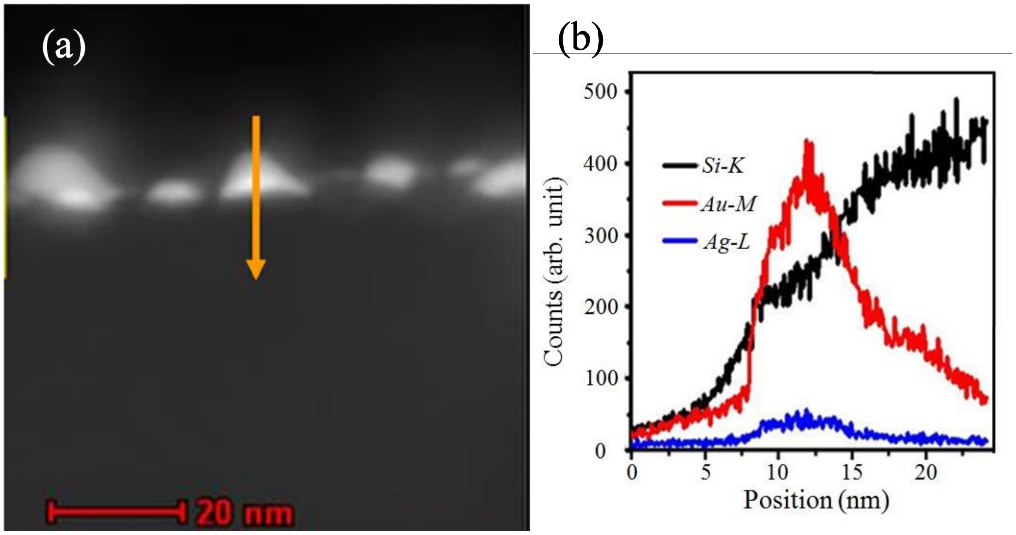

Figure 4.11 STEM study with cross sectional view a) image showing the interface of nanostructure and substrate and b) EDS line profile over a region as shown in Fig. 4.11(a).

Indeed, Au and Ag are uniformly distributed over the entire regions of the nanostructures and consequence homogeneous bimetallic mixing. Dominating the possibility of inter-diffusion of Au and Ag atoms inside the Si matrix, they are preferably intermixed on top of the Si surface.

from KMC simulation

We have also investigated the composition of the grown Au-Ag islands in KMC simulations. In Fig. 4.12, individual position of Au and Ag atoms at a particular layer of grown Au-Ag nanoisland is shown. It reveals that within the grown 3D islands Au-Ag bimetallic intermixing occurs in accordance with our STEM-EDS measurements.

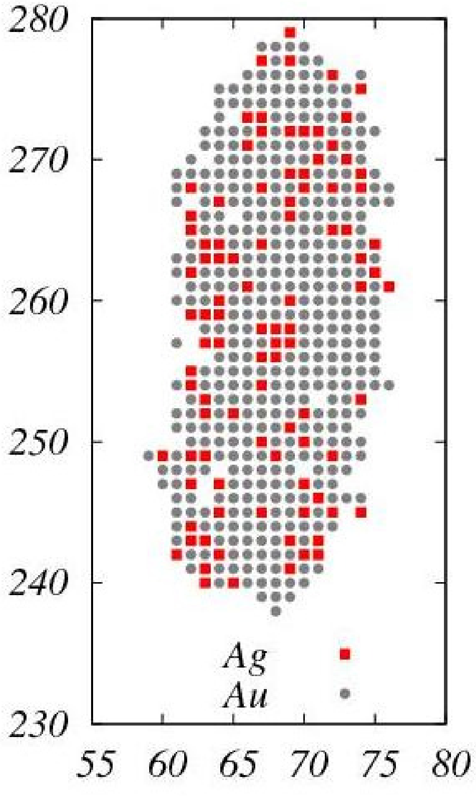

Figure 4.12 Elemental mapping of constituent atoms in a particular layer of grown Au-Ag nanostructure in KMC simulation for Θ_{Au} = 1.0 ML and Θ_{Ag} = 0.40 ML. Dimensions of the selected rectangular region are represented in unit of lattice constant.

The role of prior deposition of Ag is discussed in the following:

The Ag adatoms are preferentially nucleated on the tetramer rows which comprise preferential reactivity than the other atomic rows on the ultra-clean reconstructed Si(5 5 12) surface [27, 31]. Followed by the nucleation process, Ag adatoms exhibit favored mobility along dimer rows compared to its perpendicular direction. As a consequence of such preferential reactivity of the surface and anisotropic growth, Ag strips are formed along the atomic row direction. The Ag strips (for $\Theta_{Ag} > 0.25$ ML) that are formed before growth of Au appears to act as seed layer of nucleation centre for Au adatoms due to highly probable Au-Ag intermixing and subsequently Au mobility is hindered. Bimetallic intermixing on the surface and near surface regions, becomes anisotropic in accordance with the anisotropic mobility of Au and Ag adatoms on reconstructed Si(5 5 12) surface. Hence, two simultaneous processes i) acting of one dimensional Ag strips as the nucleation centre due to strong Au-Ag bonding and ii) anisotropic bimetallic intermixing onnear surface region, consequence growth of one dimensional Au-Ag intermixed nanostructures. Compared to these reasons, anisotropic mobility of Au adatoms on the ultraclean reconstructed surface causes smaller degree of anisotropy on the morphology in terms of mean aspect ratio. For Θ_{Ag} less than 0.25 ML, acting of Ag as seed is not prominent as it is expected that for formation of 1D Ag strip and appreciable intermixing with Au, a least amount of Ag is essential. Whereas for Θ_{Ag} 0.25-0.60 ML, gradual increase of Ag amount results in enhancement of aspect ratio of Ag strips, due preferential accumulation of Ag atoms along step edge direction [27] and mean aspect ratio of Au-Ag nanostructures is also increased accordingly. Gradual accumulation of Ag adatoms over the step edge direction along Si$\langle 66\bar{5}\rangle$ starts to take place when Θ_{Ag} becomes nearly to 0.60 ML. Thereafter accumulation of growth species (Au adatoms) towards the nucleation centre (Ag strips) and mobile surface Ag atoms, become comparable along both Si$\langle 1\bar{1}0\rangle$ and Si$\langle 66\bar{5}\rangle$ direction. Plausibly these processes restrain mean aspect ratio from further considerable enhancement with large coverage of Ag. For Θ_{Ag} 0.25-1.00 ML, where Ag significantly modify morphology of Au-Ag bimetallic growth, formation of longer bimetallic nanowire with much larger aspect ratio than its mean value is attributed as coalescence of multiple smaller nanowires.

4.5 Conclusion

In conclusion, we report a simple method for fabricating Au-Ag bimetallic intermixed nanowires on reconstructed Si(5 5 12) surface. Morphology of the grown nanowires is crucially dependent on the *'amount of Ag'* which has been utilized for the modification of ultraclean reconstructed surface, prior to Au growth. To interpret these experimental outcomes we have proposed a KMC model. Using the simulation parameters analogous to the experimental conditions, proposed theoretical model qualitatively explains the experimental findings. For the formation of such nanowires simultaneous fulfillment of three growth conditions are essential: i) formation of one dimensional template, ii) adequate mobility of the adatoms and iii) high miscibility of corresponding binary system. On one dimensional templates like reconstructed vicinal Si surfaces or Si(110) surface, the evaporated adatoms comprise of anisotropic surface mobility. For appreciable binary intermixing, both kinds of adatoms should comprise adequate mobility *i.e.* kinetic energy. Therefore, although we report growth of Au-Ag bimetallic nanowires on reconstructed Si(5 5 12) surface in our present work, we believe the mechanism could lead formation of binary nanowires on anisotropic surface where the aforementioned growth conditions are satisfied.

References

[1] C. J. Serpell, J. Cookson, D. Ozkaya, and P. D. Beer, *Nat. Chem.* **3**, 478 (2011).

[2] F. Tao, M. E. Grass, Y. Zhang, D. R. Butcher, J. R. Renzas, Z. Liu, J. Y. Chung, B. S. Mun, M. Salmeron and G. A. Somorjai, *Science* **322**, 932 (2008).

[3] D. Ferrer, A. Torres-Castro, X. Gao, S. Sepu´lveda-Guzma´n, U. Ortiz-Me´ndez and M. Jose´-Yacama´n, *Nano Lett.* **7**, 1701 (2007).

[4] M. P. Mallin and C. J. Murphy, *Nano Lett.* **2**, 1235 (2002).

[5] L. Sun , W. Luan and Y. J. Shan, *Nanoscale Res. Lett.* **7**, 225 (2012).

[6] S. R. Nicewarner-Pena, R. G. Freeman, B. D. Reiss, L. He, D.J. Pena, I.D. Walton, R. Cromer, C. D. Keating, M. J. Natan, *Science* **294**, 137 (2001).

[7] S. E. Habas, H. Lee, V. Radmilovic, G. A. Somorjai and P. Yang, *Nat. Mater.* **6**, 692 (2007).

[8] D. Seo, C. II Yoo, J. Jung and H. Song, *J. Am. Chem. Soc.* **130**, 2940 (2008).

[9] E. Iglesia, S.L. Soled, R.A. Fiato and G.H. Via, *J. Catal.* **143**, 345 (1993).

[10] Y. Mizukoshi, T. Fujimoto, Y. Nagata, R. Oshima, Y. Maeda, *J. Phys. Chem. B* **104**, 6028 (2000).

[11] X. Li, J. Yao, F. Liu, H. He, M. Zhou, N. Mao, P. Xiao, Y. Zhang, *Sens. Actuator B-Chem.* **181**, 501 (2013).

[12] J. Liu, H. Zhou, Q. Wang, F. Zeng, Y. Kuang, *J. Mater. Sci.***47**, 2188 (2012).

[13] H. Okamoto, T. B. Massalski, *Bull. Alloy Phase Diagra.* **4**, 30 (1983).

[14] J. H. Liu, A. Q. Wang, Y.S. Chi, H. P. Lin,C. Y. Mou, *J. Phys. Chem. B* **109**, 40 (2005).

[15] J. Zheng, H. Lin, Y. Wang, X. Zheng, X. Duan, Y. Yuan, *J. Catal.* **297**, 110 (2013).

[16] S. C. Fain, Jr. and J. M. McDavid, *Phys. Rev. B* **9**, 5099 (1974).

[17] D.K. Goswami, B. Satpati, P.V. Satyam, B.N. Dev, *Curr. Sci. (India)* **84**, 903 (2003).

[18] G. Kresse, J. Furthmüller, *Phys. Rev. B* **54**, 11169 (1996).

[19] G. Kresse, D. Joubert, *Phys. Rev. B* 59, 1758 (1999).

[20] P. E. Blochl, *Phys. Rev. B* **50**, 17953 (1994).

[21] J. Paier, R. Hirschl, M. Marsman, G. Kresse, *J. Chem. Phys.* **122**, 234102 (2005).

[22] C. Niu, J. Wang, *Solid State Commun.* **151**, 655 (2011).

[23] Q. Deng, L. Zhao, X. Feng, M. Zhang, W. Zhang, B. Fang, *Comp. Theor. Chem.* **976**, 183 (2011).

[24] S. Pal, D. P. Landau, *Phys. Rev. B* **49**, 10597 (1994).

[25] A. Lo, R. T. Skodje, *J. Chem. Phys.* **112**, 1996 (2000).

[26] A. A. Baski, K. M. Saoud, K.M. Jones, *Appl. Surf. Sci.* **182**, 216 (2001).

[27] H. H. Song, K. M. Jones, A. A. Baski, *J. Vac. Sci. Technol., A***17**, 1696 (1999).

[28] A. A. Baski, L.J. Whitman, S. C. Erwin, *Science* **269**, 1556 (1995).

[29] H. Kim, H. Li, Y. Zhu, J.R. Hahn, J. M. Seo, *Surf. Sci.* **601**, 1831 (2007).

[30] T. Suzuki, H. Minoda, Y. Tanishiro, K. Yagi, *Surf. Sci.* **348**, 335 (1996).

[31] A. A. Baski, K. M. Jones, K. M. Saoud, *Ultramicroscopy* **86**, 23 (2001).

[32] J. W. Dickinson, J. C. Moore, A. A. Baski, *Surf. Sci.* **561**, 193 (2004).

[33] D. B. Williams, & C. B. Carter, *Transmission Electron Microscopy: A Textbook for Materials Science (Springer, 1996).*

Chapter 5

Growth of Au-Ag bimetallic nanowires on reconstructed Si(5 5 12) substrate under various MBE conditions

5.1 Introduction

'Quantum size effect' of metal particles due to reduction of their sizes to nanoscale (<100 nm) and control over their shapes, emerge many advantageous physical properties [1, 2]. Implementations of these properties in modern technology explore proficient utility of metal nanoparticles in the field of biomedicine [3, 4], catalysis [5], nonlinear optics [6, 7], electronics etc. Comparing with the conventional size and shape manipulation of monometallic nanoparticles (MMNP), bimetallic nanoparticles (BMNP) withstand 'tuning of its composition' which is an extremely important aspect of modern nanotechnology. Coexistence of two dissimilar metals within each BMNP consequences numerous superior synergic properties *e.g.* catalysis [8, 9], electrochemistry [10, 11], than their monometallic counterparts. Among the different binary combinations of

BMNP, Au-Ag binary system has caught intense attention of the researchers due to their complete miscibility with any desired composition ratio (Au:Ag) [12-14]. Catalytic property of Au-Ag BMNP for oxidation of carbon monoxide (CO) excels than its complementary metallic parts [15]. Similarly its efficient catalytic property is also observed for hydrogenation of dimethyl oxalate to methyl glycolate [16]. Non linear optical property of Au-Ag bimetallic nanoparticles reveals that absorption frequency of surface plasmon resonance (SPR) could be successfully tuned in the UV and visible regime of electromagnetic spectrum, with systemic variation of the Au:Ag composition ratio [17]. Along with these aspects, Au-Ag bimetallic alloyed structure holds possibility to be considered as a suitable candidate for gate electrode in MOSFET devices [18], because the work function of the Au-Ag bimetallic alloy system is tuned with gradual change of Au:Ag composition ratio [19].

Growth of nanostructures on reconstructed surface in ‘self-assembly’ method provides a better control of morphology and composition than the other kinds of growth methods. Detailed understanding of nucleation process, ad-atom mobility and substrate-thin film interfacial interaction provides potential control to achieve desired morphology and composition. On reconstructed vicinal Si surfaces which are tilted from stable low index plane such as Si(001) and Si(111), preferred mobility of metal ad-atoms along step edge directions (*i.e.* Si$\langle 1\bar{1}0\rangle$) consequences to one dimensional (1D) growth of nanostructures [20-22]. In the midst of various vicinal Si surfaces, Si(5 5 12) is particularly important due to its very large (5.35 nm × 0.77 nm), stable and single-domain reconstruction [23-25], followed by the removal of native SiO_x layer (~ 2 nm). Several groups have focused on monometallic growth of Au or Ag on reconstructed Si(5 5 12) surfaces at various experimental conditions. Depositions of Au of low coverage (0.25-1.5 ML) and annealing at elevated temperatures (500-900 °C) show the formation of facet planes of numerous orientations which lie within approximately ±5° with (5 512) orientation [26-28]. These Au induced surfaces consist of (113), (225), (337), (5511) and (7715) facet planes and over-layer grown periodic 1D nanostructures. Similarly, growth of sub monolayer Ag and subsequent annealing at elevated temperature results in formation extremely large aspect ratio over-layer nanowires. Median average aspect ratio of these Ag nanowires has been found to increase with Ag coverage in the regime 0.10-0.80 ML [27-29].

In the earlier chapter, we have reported sub monolayer Ag deposition prior to Au growth on Si(5 5 12) surface at substrate temperature 300 °C, remarkably modifies the post-growth morphology of Au thin film and indeed consequences formation Au-Ag bimetallic intermixed nanowires [30]. Dependence of Au-Ag bimetallic morphology on Ag thickness explore that efficient enhancement of mean aspect ratio of the nanostructures takes place for Ag thickness 0.25-1.0 ML and substrate temperature 300 °C. However, in preceding chapter, dependence of Au-Ag growth with other important growth parameters *i.e.* Au thickness and substrate temperature (during Au growth) have not been explored [30]. Dependence of Au-Ag bimetallic morphology on Ag thickness explore that efficient enhancement of mean aspect ratio of the nanostructures takes place for Ag thickness 0.25-1.0 ML and substrate temperature 300 °C. Such phenomenon has been explained in the light of kinetic Monte Carlo (KMC) simulations and density functional theory (DFT). Therefore, in our present chapter, we have investigated effect of Au thickness variation and substrate temperature on Au-Ag bimetallic growth on Ag:Si(5 5 12) (for 0.50 ML Ag). Our investigations reveal morphology of Au-Ag bimetallic growth could be proficiently tailored with systematic variation of these growth parameters. Growth of 3.0 ML Au on Ag:Si(5 5 12) substrate at substrate temperature 300 °C is found as the optimum growth condition to achieve maximum enhancement of aspect ratio (~ 3.12) of the AuAg bimetallic intermixed nanostructures.

5.2 Experimental methods

Reconstructed surface is prepared using n-type Si(5 5 12) (resistivity 1-20 Ω-cm) in two steps: a) Si wafer is degassed at 600 °C for 12-15 hours, b) top native silicon oxide layer is removed by repetitive flashing at 1200 °C for 60 seconds using direct current (DC) heating method. Base pressure in MBE chamber is ~ 2.0×10^{-10} mbar which rises to ~ 1.0×10^{-9} mbar during deposition [31]. For growth of Au and Ag, alumina and pyrolytic boron nitride crucible is used respectively. Thickness is measured using quartz microbalance, which has been calibrated using Rutherford backscattering spectrometry (RBS) technique. For both materials Au and Ag, we have considered 1 ML = 1.0×10^{15} atoms/cm^2. Ag and Au is grown in thermal evaporation method, with flux rate 0.33 ML/min and 0.5 ML/min respectively. Substrate temperature is measured using a Type K thermocouple. For in-situ scanning tunneling microscopy (STM) measurements, an omicron variable temperature STM (VTSTM) is utilized which is coupled with MBE growth chamber. All the STM measurements are done in constant current mode using a tungsten tip, keeping the samples at room temperature (RT). Transmission electron microscopy (TEM) specimen is prepared by mechanical polishing and low energy Ar^+ ion milling. TEM measurements are done using JEOL-2010 with 200 keV electrons (URP pole pieces). Further 300 keV scanning transmission electron microscopy (STEM) is also employed for imaging and energy dispersive X-ray spectroscopy (EDS) measurements. Planar STEM EDS measurements have been also carried out with 200 keV electrons using a Talos F200 at Indian Institute of Science, Bangalore, India. For RBS measurements, we have used He+ ions having energy 2.0 MeV generated from 3.0 MV Pelletron accelerator (NEC, USA) at Institute of Physics, Bhubaneswar, India. Compositional depth profile analysis from RBS spectrum has been carried out by SIMNRA simulation package [32].

5.3 Results and discussions

5.3.1 Effect of *Au thickness* on Au-Ag bimetallic growth at substrate temperature 300 °C (during Au growth)

Morphology

Growth of bimetallic intermixed nanostructures with enhanced aspect ratio is noticeably evident when substrate temperature during Au growth is kept at 300 °C

[30]. Therefore at this substrate temperature, morphological evolution of the Au-Ag bimetallic intermixed nanostructures, with variation of Au thickness is studied. Fig. 5.1(a)-(f) represents the topographic STM image for growth of Au with various thickness on Ag:Si(5 5 12) substrate at substrate temperature 300 °C. Ag:Si(5 5 12) substrate has been prepared by deposition of 0.50 ML Ag at RT on ultra-clean reconstructed Si(5 5 12) substrate and subsequent annealing at 300 °C for one hour. For Au growth on Ag:Si(5 5 12), Au thickness is considered as 0.50 ML, 1.33 ML, 1.50 ML, 2.2 ML, 3.0 ML and 5.0 ML. Followed by the Au growth, Au/Ag:Si(5 5 12) system has been annealed at 300 °C for 30 minutes. For growth of sub monolayer Au on Ag:Si(5 512), discontinuous, non uniform thin film is formed (Fig. 5.1 (a)). Higher magnification image (as shown in inset of Fig. 5.1 (a)) explores grown Au-Ag thin film indeed comprises of elongated strip like structures along the row direction of the underlying reconstructed substrate. Prior to Au growth, we had observed on Ag:Si(5 5 12) substrate, formation of Ag strips partially covers the reconstructed Si(5 5 12) surface and atomic rows of surface Si atoms are visible (Fig. 4.4 (b)-(c)) [30]. Due to Au growth on such template although the strip like structures persist, atomic rows of reconstructed substrate are not visible. In some regions, typical width of such Au-Ag strip like structure is found ~ 5.30 nm, in accordance to the periodicity of the ultra-clean reconstructed Si(5 5 12) surface along Si$\langle 66\bar{5}\rangle$. Predominantly, surface is covered by such strip like structures and formation of 3 dimensional (3D) nanostructures rarely takes place (Fig. 5.1 (a)) indicating early stage of growth of 3D nanostructures. Following the formation of wetting layer, growth of such 3D

islands is quite evidenced for increase of Au thickness to 1.33 ML (Fig. 5.1 (b)). For Au thickness ~1.33-5.0 ML, strip like structures are not formed and elongated Au-Ag nanostructures are grown along dimer row direction (*i.e.* $\mathrm{Si}\langle 1\bar{1}0\rangle$) of the reconstructed substrate. For growth of 1.33 ML Au, grown nanostructures comprise mean aspect ratio 2.2±0.2 with mean size 22.9±1.6 nm^2. As the growth of Au with larger thickness 2.2 ML takes place on Ag:Si(5 5 12), nanowires are grown with quite large aspect ratio and their mean size is also increased. Such elongated nanowires have mean aspect ratio 2.7±0.2 and size 63.5±5.0 nm^2 (Fig. 5.1 (d)). In our previous work, we had presented these morphological aspects of Au growth on Ag:Si(5 5 12) substrate at 300 °C, with Au thickness 1.50 ML and 3.00 ML [30]. In case of 1.50 ML Au growth mean aspect ratio and mean size have been found as 2.6±0.2 and 48.9±2.5 nm^2 respectively (Fig. 5.1 (c)). While, for 3.0 ML Au we have observed mean aspect ratio and mean size of the grown nanostructures as 3.1±0.2 and 147.0±12.0 nm^2 respectively (Fig. 5.1 (e)). With gradual increase of Au thickness from sub monolayer to 3.0 ML, grown 3D islands are remained isolated from each other. But above this thickness, smaller sized 3D nanostructures show a tendency to coalescence with each other (Fig. 5.1 (f)).

In some regions, coalescence process consequences formation of non-uniform thin film. Size of the isolated 3D nanostructure also becomes larger due to coalescence of multiple smaller sized nanostructures. Such isolated 3D nanostructures are considered by us to explore their morphological aspects. For growth of 5.0 ML Au, grown nanostructures are found elongated along

Si$\langle 1\bar{1}0 \rangle$with mean aspect ratio 2.5±0.2. In this case, mean size of the nanostructures becomes 664.5±32.4 nm^2 which is larger than the growth of Au with smaller thicknesses. Plot of mean size and mean aspect ratio of the grown nanostructures as a function of Au thickness has been presented in Fig. 5.2 (a) and Fig. 5.2 (b) respectively. It explores, in the entire regime of variation of Au thickness *i.e.* 1.33-5.0 ML, mean size of the particle is gradually increased in accordance with Au thickness. Similarly, systematic enhancement of Au thickness explores, mean aspect ratio is steadily increased up to 3.0 ML.

Interestingly above this intermediate value of Au thickness ~ 3.0 ML, steady enhancement of mean aspect ratio is disrupted and its dependence on Au thickness evolves in reverse manner. In contrast with lower regime (*i.e.* Au thickness $\leq$ 3.0 ML), mean aspect ratio of the nanostructures is gradually deceased as a function of Au thickness.

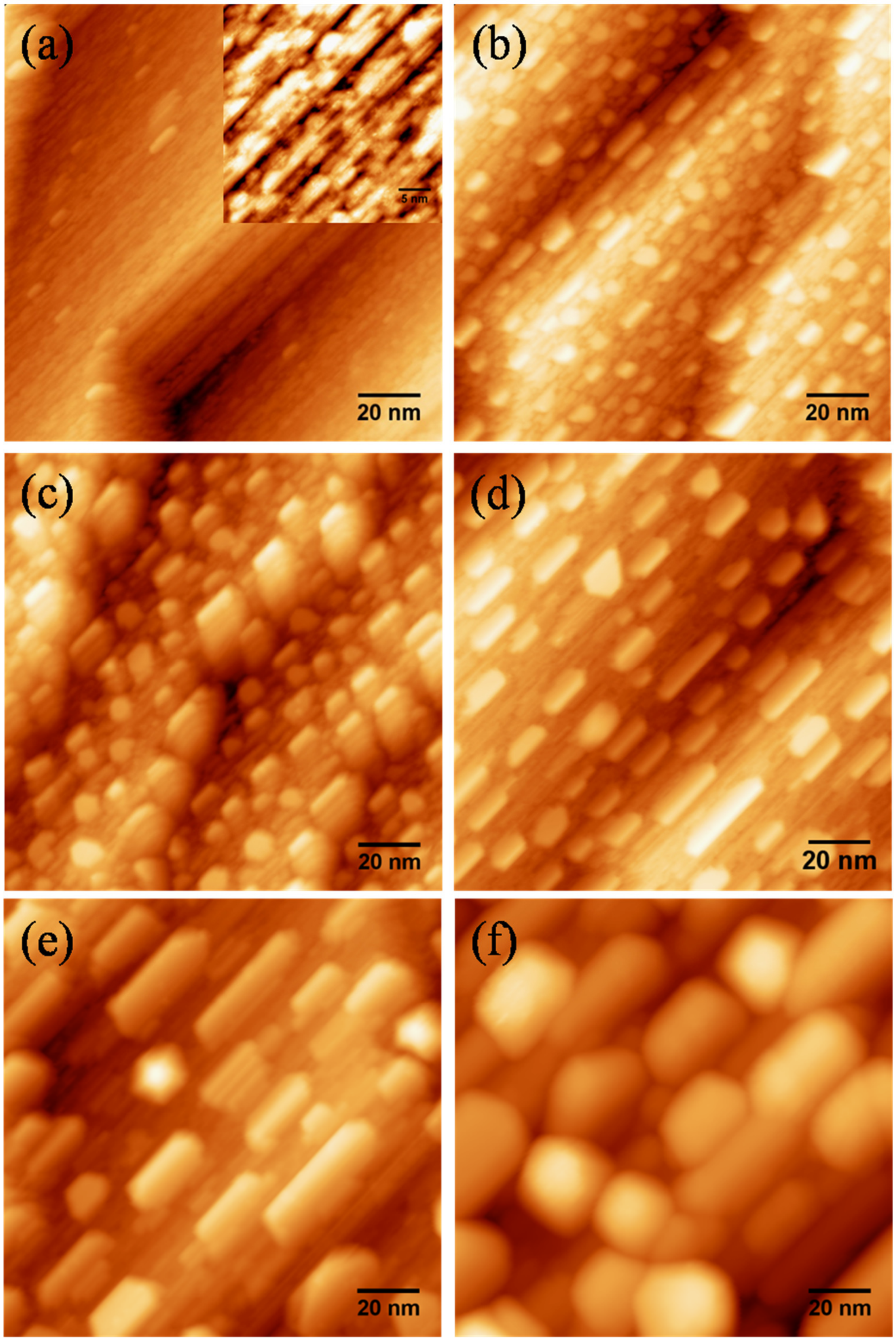

Fig. 5.1 Topographic STM image for growth of Au on Ag:Si(5 5 12) at growth temperature 300 ℃ with varying Au thickness a) 0.50 ML, b) 1.33 ML, c) 1.50 ML, d) 2.20 ML, e) 3.00 ML and f) 5.00 ML.

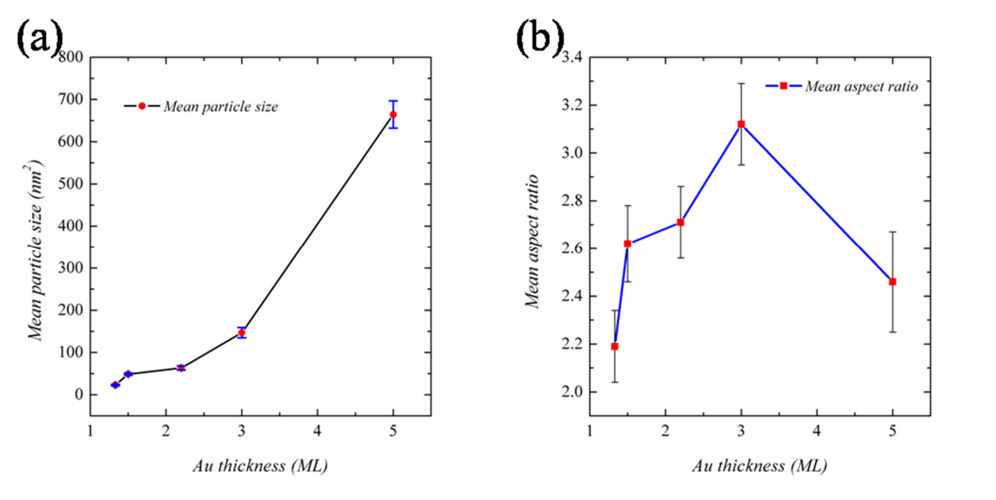

Figure 5.2 Plot of a) mean particle size and b) mean aspect ratio of the grown nanostructures as a function of Au thickness.

Structural aspects of grown Au-Ag bimetallic nanostructures

RBS

Following the in-situ investigations of morphological evolution using STM, all the samples are brought outside of the growth chamber and characterized by ex-situ RBS method at RT. Thickness variation of Au thickness is evidenced from gradual increase of 'area under the Au peak' which reflects amount of Au on the substrate (Fig. 5.3 (a)). Fig. 5.3 (b) represents the RBS spectrum for growth of 3.0 ML Au on Ag:Si(5 5 12) substrate at room temperature (during Au growth). In comparison with growth of Au on Ag:Si(5 5 12) at RT, shift of Au peak towards lower backscattered energy side doesn't take place and lower energy edge of Au peak also remains unchanged as compared RT growth (Fig. 5.3 (b)). Therefore it reflects absence of detectable inter diffusion of Au inside Si matrix.

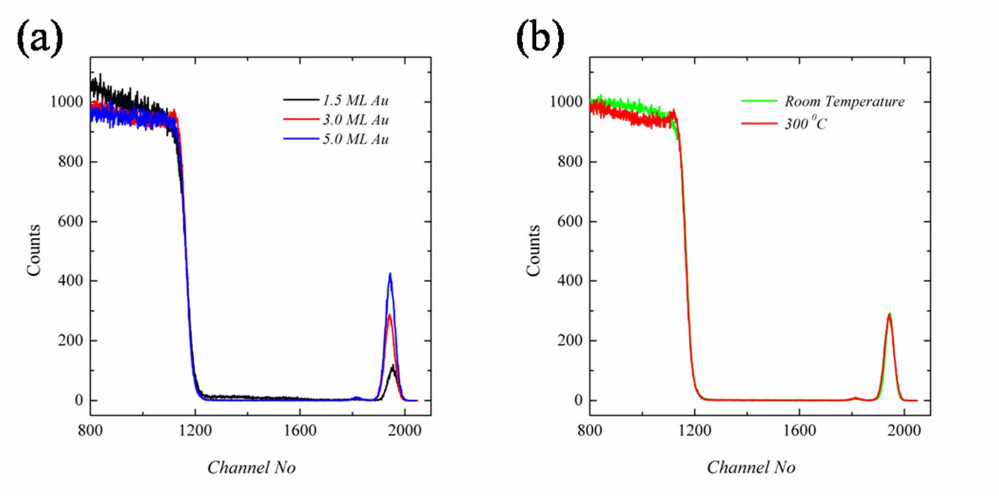

Figure 5.3 a) Comparative RBS spectrum for growth of Au on Ag:Si(5 5 12) substrate at substrate temperature 300 ºC with Au thickness 1.5 ML (black line), 3.0 ML (red line) and 5.0 ML (blue line). b) Comparative RBS spectrum for growth of 3.0 ML Au on Ag:Si(5 5 12) substrate at room temperature (green line) and 300 °C (red line) substrate temperature.

STEM

To achieve better insight about spatially resolved composition, we have carried out STEM measurements on grown Au-Ag bimetallic nanostructures. Fig. 5.4 represents the planar STEM study for bimetallic Au-Ag growth on reconstructed Si(5 5 12) surface at substrate temperature 300 °C. Along with the smaller sized nanostructures, formation of much bigger nanostructures is explored from the dark field image (Fig. 5.4 (a)). Indeed, aspect ratio of the smaller sized nanostructures is much smaller than the bigger structures.

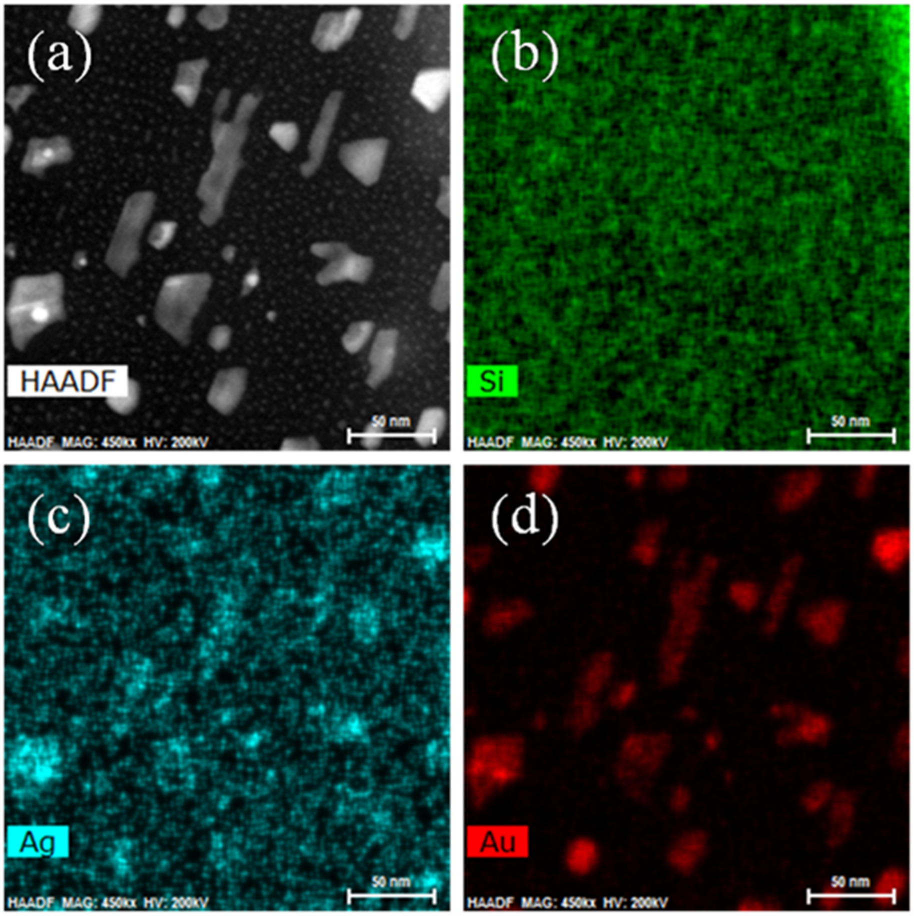

Figure 5.4 STEM EDS study with planar view for growth of Au on Ag:Si(5 5 12) at substrate temperature 300 ℃ with planar view: a) bright field image, EDS Mapping of b) Si, c) Ag, d) Au. These measurements have been done with Talos F200.

EDS elemental mapping over this selected region of the sample reveals both metals *i.e.* Au and Ag, are present within each nanostructures (Fig. 5.4 (b)-(d)). EDS line profile over the nanostructure-substrate interface in cross sectional view of STEM study (Fig. 5.5 (b)) explores that, grown nanostructures are composed of uniform Au-Ag bimetallic intermixing. Incorporation of very small amount of Ag compared to Au inside the individual nanostructure is also reflected from the intensity of the EDS line profile. Other plausible configurations of bimetallic nanostructures such as core-shell, hetero junction is not observed. It also exhibits, both the metal are not detectably inter diffused inside Si matrix and consistently supports our RBS measurements (Fig. 5.3 (a)).

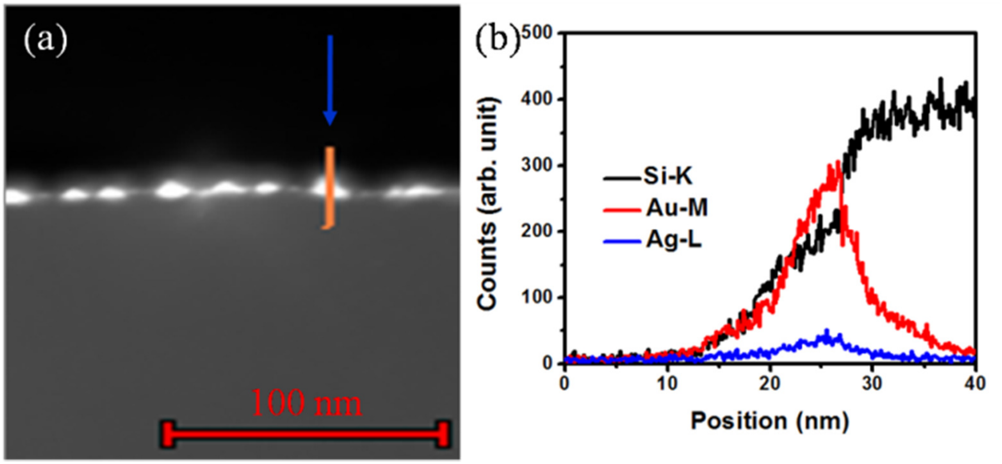

Fig. 5.5 STEM study with cross sectional view for growth of Au on Ag:Si(5 5 12) at substrate temperature 300 °C: a) HAADF image indicating the nanostructure-substrate interface, b) EDS line profile over a region as shown in Fig. 5.5 (a).

Evolution of mean size and mean aspect ratio of grown Au-Ag nanostructures as a function of Au thickness (as shown in Fig. 5.2(a) and (b)) is explained as following:

When a 0.50 ML Ag is deposited on ultra-clean reconstructed Si(5 5 12) surface at RT and annealed subsequently, elongated Ag strips are grown because of preferential reactivity of tetramer rows on reconstructed Si(5 5 12) surface and anisotropic surface mobility of Ag [27, 29]. Thereafter as the Au is deposited on

Ag:Si(5 5 12) surface at substrate temperature 300 °C and subsequently annealed, high miscibility of Au-Ag binary system consequences bimetallic Au-Ag intermixing. Such intermixing process becomes anisotropic following the grown one dimensional Ag strips. After reaching to the Ag:Si(5 5 12) substrate, Au ad-atoms are nucleated towards Ag strips and uncovered region (where Ag is not present) of template. However, the nucleation of Au atoms is also governed by the smaller Ag clusters which are not incorporated into the grown Ag strips. When 0.50 ML Au is deposited on Ag:Si(5 512) substrate, morphology of the grown Au-Ag thin film comprises one dimensional strip like nature following the morphology of Ag:Si(5 5 12) substrate. Hence, for sub monolayer growth of Au, morphology of Au-Ag growth is predominantly influenced by nucleation process. As the Au thickness is increased to nearly one monolayer, following the nucleation process gradual accumulation of Au adatoms takes place to form 3D nanostructures. Therefore mean size of the Au-Ag bimetallic nanostructures is systematically enhanced in accordance with Au thickness. Due to one dimensionality of nucleation centers on Ag:Si(5 5 12) substrate for incoming Au adatoms and higher surface mobility along Si$\langle 1\bar{1}0 \rangle$ direction, Au adatoms preferentially accumulated along the following direction to form a 3D nanostructure. It causes, in the regime of Au thickness ~ 1.33-3.0 ML, mean aspect ratio of the Au-Ag nanostructures is gradually increased as a function of Au thickness. When amount of Au is further increased, following the preferential nucleation and initial accumulation process along Si$\langle 1\bar{1}0 \rangle$ direction, excess Au adatoms also begin to accumulate along the Si$\langle 66\bar{5} \rangle$ direction. It causes coalescence of multiple smaller nanostructures to grow larger and reduction of mean aspect ratio of the nanostructures.

Nanostructure-substrate interface

We have also carried out detailed investigations on the crystalline nanostructure-substrate interface using HRTEM method. Fig. 5.6 (b) represents a HRTEM image for a grown nanostructures followed by Au growth on Ag:Si(5 5 12) at 300 °C. It depicts the formation periodic dislocations at the nanostructure-substrate interface. Interior to the substrate, inter planar spacing 0.32±0.04 nm (d') indicates the Si(111) plane. While, measured inter-planar spacing within a crystalline region (as shown in Fig. 5.6 (b)) is 0.24±0.04 nm (d''), which closely corresponds to Ag(111) or Au(111) plane. Therefore minimization of interfacial strain energy, due to very close lattice matching as 3×d' ~ 4×d'' results in formation of periodic dislocation at the interface. At the interface, Moiré fringes with spacing 0.94±0.05 nm are also observed. Spacing in Moiré fringe (d_m) can be found from the relationship $d_m = d_1 d_2/[(d_1-d_2)^2+\beta^2 d_1 d_2]^{1/2}$, where d_1, d_2 lattice spacing of the planes constituting the Moiré fringe and β is the angle (in radian) between these two planes [33]. Using the experimentally measured value of Si(111) (as d_1), Au(111) (as d_2) and β equals to zero, we have found d_m is 0.99 nm. It closely matches with our experimental results.

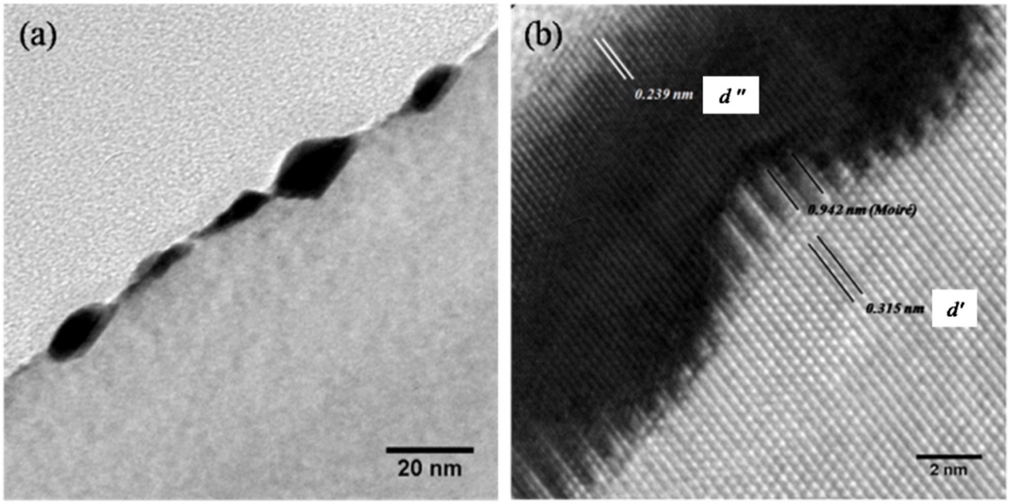

Figure 5.6 a) Bright field cross sectional TEM study for growth of Au on Ag:Si(5 5 12) at substrate temperature 300 ºC b) corresponding high resolution image for a single nanostructure.

5.3.2 Effect of *substrate temperature* (during Au growth) on Au-Ag bimetallic growth with Au thickness 3.0 ML

Morphology

Ag modified ultra-clean reconstructed Si(5 5 12) surface, with Θ_{Ag} 0.50 ML which resides in the effective regime of Θ_{Ag} (*i.e.* 0.25-1.0 ML) that substantially influences Au-Ag morphology (Fig. 4.5) has been considered for temperature dependence study [30]. After modification of reconstructed Si(5 5 12) with 0.50 ML Ag at RT, growth template Ag:Si(5 5 12) is kept at different substrate temperature (RT to 400 °C) during Au deposition (~ 3.0 ML) and subsequent post-annealing process. Fig. 5.7 depicts STM images for a system 3.0 ML Au/0.5 ML Ag/Si(5 5 12) at various temperatures. For all the samples, after Au deposition, Au/Ag:Si(5 5 12) system is post annealed at corresponding growth temperature for 30 minutes. For growth at RT, nanostructures are not formed, rather inhomogeneous thin film is evidenced (Fig. 5.7 (a)). As the substrate temperature is increased to 200 °C, anisotropic nanostructures start to grow along atomic row direction Si$\langle 1\bar{1}0\rangle$ (Fig. 5.7 (b)). Above 200 °C, morphologies of such anisotropic nanostructures are significantly influenced by the variation of substrate temperature. For growth at 300 °C, coexistence of rectangular shaped nanostructures with higher aspect ratio along elliptical shaped nanostructures with lower aspect ratio is evidenced in Fig. 5.7 (c).

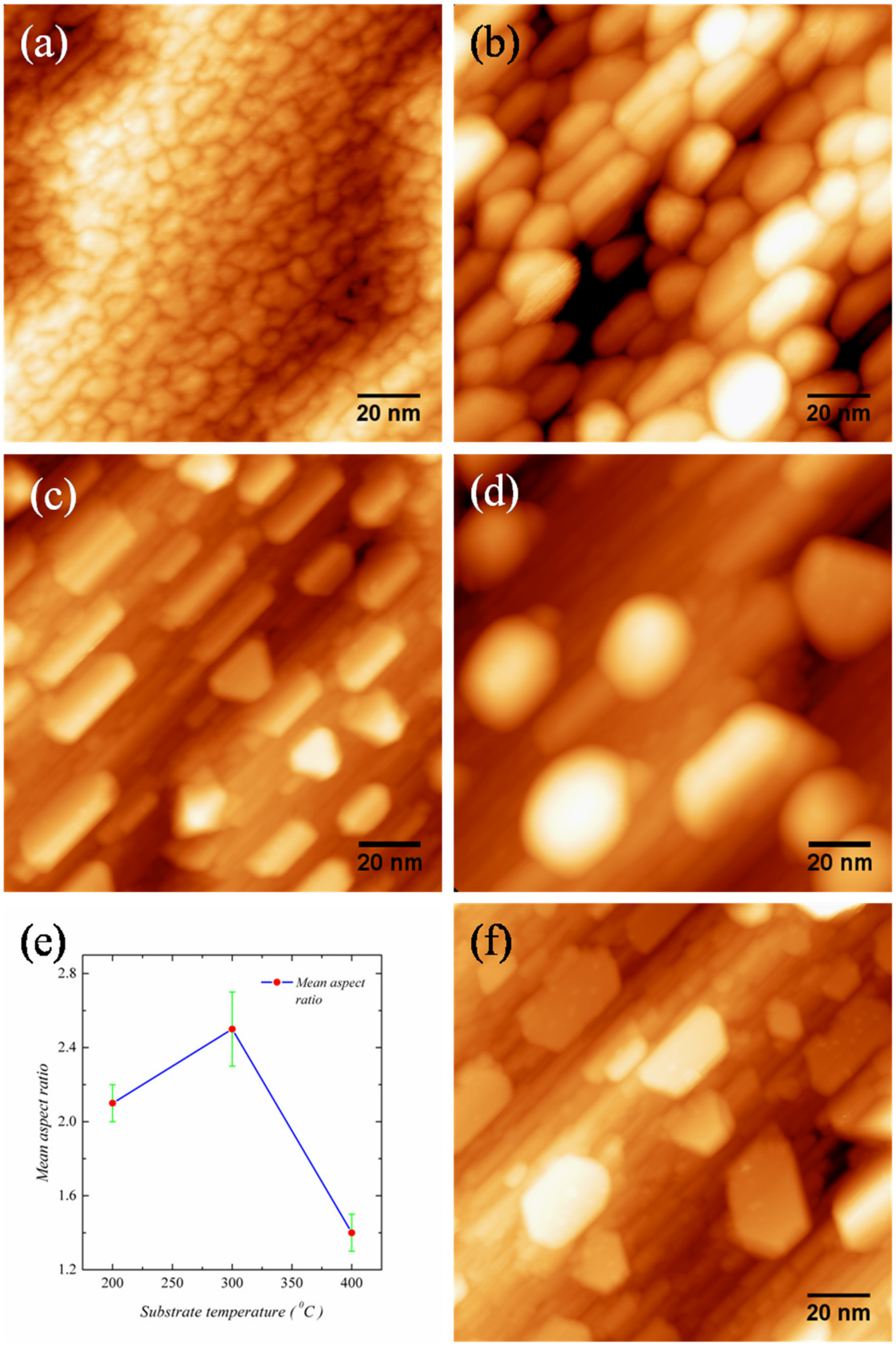

Figure 5.7 Topographic STM image for growth of 3.0 ML Au on Ag:Si(5 5 12) at substrate temperature (during Au growth) a) RT, b) 200 °C, c) 300 °C and d) 400 °C. e) Plot of mean aspect ratio of the grown nanostructures as a function of substrate temperature. f) 3.0 ML Au growth on Ag:Si(5 5 12) at RT (during Au growth) and then annealed at 300 °C.

But as the Au growth takes place at higher temperature 400 °C, rectangular shaped nanostructures with higher aspect ratio rarely grow (Fig. 5.7 (d)). Mean aspect ratio of the grown Au-Ag bimetallic nanostructures is found as 2.1±0.1, 2.50±0.2, and 1.4±0.1 for growth temperature 200 °C, 300 °C and 400 °C respectively and its variation has been plotted in Fig. 5.7 (e). Following the STM measurement after Au growth at RT on Ag:Si(5 5 12) surface as shown in Fig. 5.7 (a), we have performed in-situ annealing at 300 °C for 30 minutes under UHV. Due to annealing, grown thin film is dewetted to form three dimensional, anisotropic nanoislands (Fig. 5.7 (f)). Morphology of the grown nanostructures in this case is quite different from the Au growth on Ag:Si(5 5 12) at 300 °C (as shown in Fig. 5.7 (c)) where enhancement of aspect ratio ~ 4.0 of individual nanostructure has been observed. It reflects, mobility of Ag adatoms during Au deposition is playing an essential role to determine the post-growth morphology of the Au/Ag:Si(5 5 12) system.

Structural aspects from RBS

Followed by the study of morphological aspects using in-situ STM method, structural aspects have been investigated using ex-situ RBS method at RT (Fig. 5.8 (a)). It is interesting to note that no appreciable shift of Au peak position for the growth at 200-400 °C occurs, in comparison with RT growth. This shows that there is no detectable diffusion of Au into Silicon in all the Ag pre-deposited systems. In the entire regime of substrate temperatures, very small amount of Ag with sub monolayer thickness is present (Fig. 5.8 (b)). It is quite interesting that, although Ag is present during Au growth at 400 °C, the effect of Ag on Au-Ag morphology is not prominent. Indeed, morphology of bimetallic Au-Ag growth for 400 °C (Fig. 5.7 (d)) is quite similar as monometallic Au growth (Fig. 4.5 (a)). In both cases, small aspect ratio elliptical shaped nanostructures are grown, but the formation of large aspect ratio (~ 4.0) nanowires is not observed. However, inefficacy of Ag may be governed by its probable diffusion inside Si matrix prior to Au growth at 400 °C. Such inter diffusion of Ag is not detectable from these RBS spectrums (Fig. 5.8) due to small amount of Ag. Therefore, to explore this aspect using RBS method, we have considered growth of larger Ag thickness *i.e.* 4.1 ML. We have prepared three samples : i) Ag growth at RT, ii) Ag growth at RT and post annealed at 300 °C for 60 minutes and iii) Ag growth at RT and post annealed at 400 °C for 60 minutes.

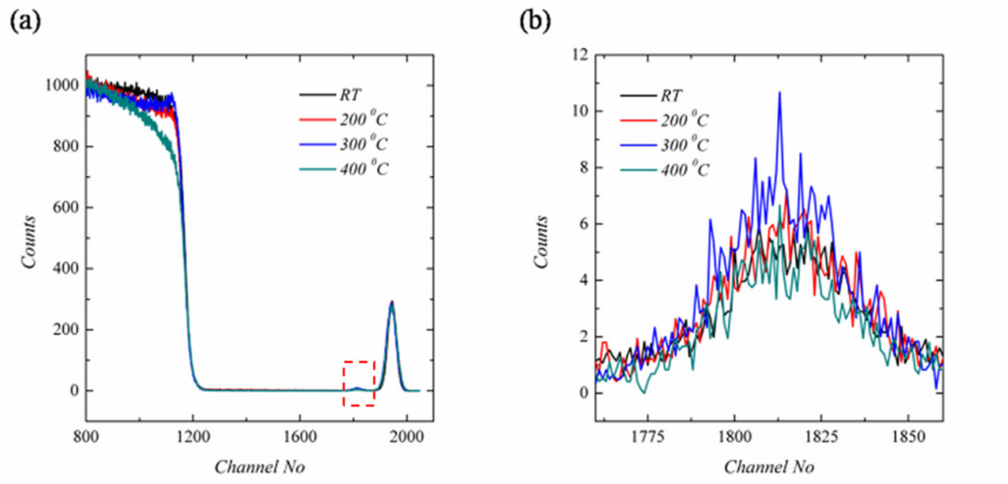

Figure 5.8 Comparative RBS spectrum (random) for growth of 3.0 ML Au on Ag:Si(5 5 12) at various substrate temperature (during Au growth): a) RT (black), 200 °C (red), 300 °C (blue) and 400 °C (green) b) enlarged portion of Ag (shown as rectangular dotted box in Fig. 5.8 (a)) .

The experimental RBS spectrums and fitted parameters using SIMNRA software package and have been presented in Fig. 5.9 and Table 5.1. It explores, in comparison with Ag growth at RT, annealed sample at 300 °C, show small inter diffusion of Ag inside Si matrix. But, inter diffusion becomes very prominent for the annealed sample at 400 °C. Therefore, we infer that due inter diffusion of 0.50 ML Ag which has been utilized for modification of ultraclean Si(5 5 12) substrate, Ag atoms become immobile during Au growth at 400 °C and Ag doesn’t have any substantial influence on the Au-Ag morphology. Interestingly, pre-deposition of Ag, before Au growth on Si(5 5 12) surface consequences inhibiting of inter diffusion of Au inside Si at 400 °C. Followed by the inter diffusion of Ag inside Si matrix at 400 °C, when Au is deposited and subsequently annealed, Au is probably intermixed with Ag and Si in the Ag-Si inter diffused region due to strong Au-Ag affinity. Within the inter-diffused region, outward diffusion of Ag and Si for intermixing with Au is also possible.

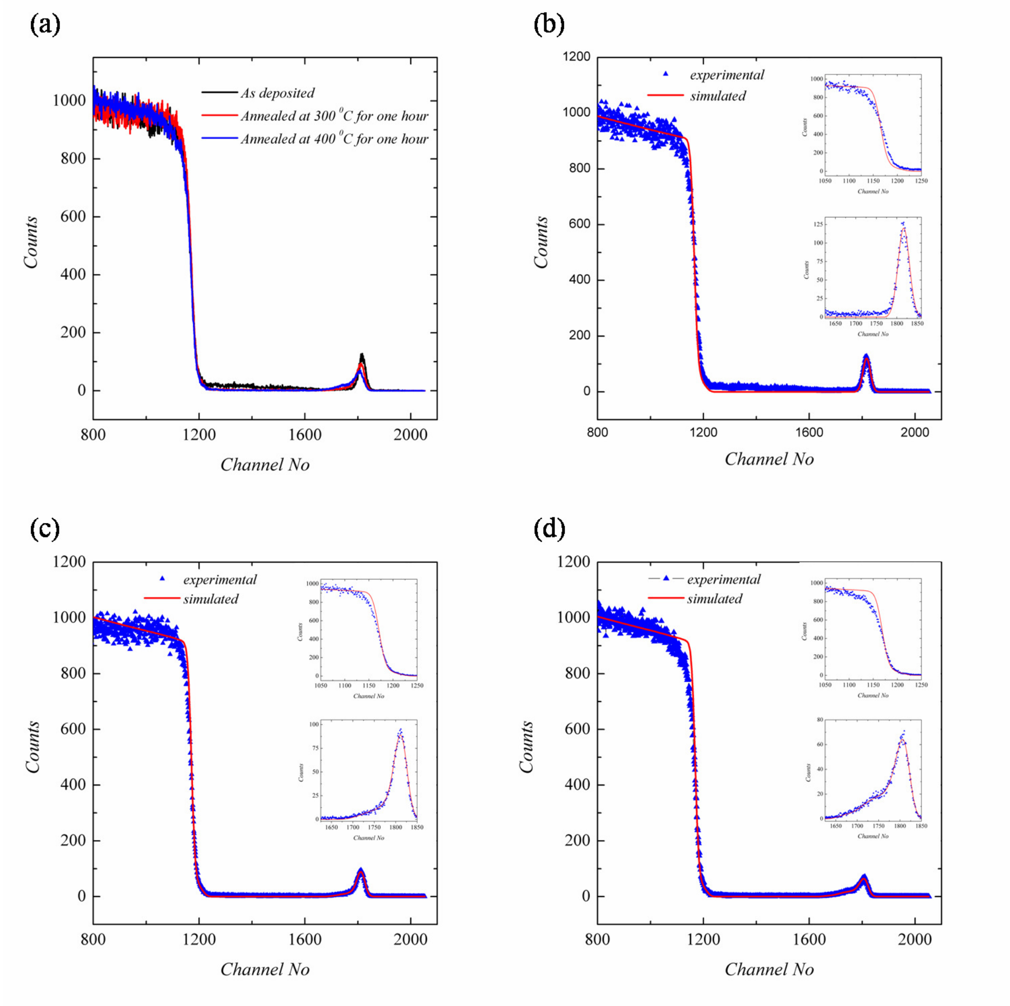

Figure 5.9 RBS study (random) to understand substrate temperature dependent inter diffusion of Ag inside Si matrix for 4.1 ML Ag/Si(5 5 12). a) experimental spectrum for as-deposited, post annealing at 300 °C and 400 °C. Experimental along with simulated spectrum for b) as-deposited, c) post annealing at 300 °C and d) post annealing at 400 °C. In Fig. 5.9 (b), (c) and (d), insets show enlarged portion of Si (top-right) and Ag (bottom-right).

Table 5.1 Obtained parameters after fitting RBS spectrums (random) to understand substrate temperature dependent inter diffusion of Ag for 4.1 ML Ag/Si(5 5 12) using SIMNRA code.

As deposited			
Layer	Ag	Si	Thickness
Layer 1	1	0	4.1
Layer 2	0	1	Bulk
Post annealed at 300 °C for one hour			
Layer 1	0.01400	0.98600	100
Layer 2	0.01350	0.98650	100
Layer 3	0.00400	0.99600	125
Layer 4	0.00180	0.99820	200
Layer 5	0.00100	0.99900	300
Layer 6	0.00060	0.99940	200
Layer 7	0.00025	0.99975	200
Layer 8	0	1	Bulk
Post annealed at 400 °C for one hour			
Layer 1	0.0100	0.9900	150
Layer 2	0.0057	0.9943	100
Layer 3	0.0042	0.9958	125
Layer 4	0.0020	0.998	250
Layer 5	0.0018	0.9982	150
Layer 6	0.0015	0.9985	150
Layer 7	0.0011	0.9989	200
Layer 8	0.0004	0.9996	400
Layer 9	0	1	Bulk

5.4 Conclusions

Our observations explore at substrate temperature 300 °C, Au growth followed by pre modification of reconstructed Si(5 5 12) surface with sub monolayer (~ 0.50 ML) Ag, exhibits formation of well oriented, parallel array of Au-Ag bimetallic intermixed nanowires. Morphology of the Au-Ag bimetallic growth could be successfully tailored with systematic variation of Au thickness in its regime 0.50-5.0 ML. In the entire regime of Au thickness, mean size of the nanostructures is gradually increased in accordance with Au thickness. But the mean aspect ratio of the nanostructures is increased as a function of Au thickness up to its intermediate value ~ 3.0 ML and thereafter it is reduced. It is attributed that following the nucleation process, at low coverage of Au (≤ 3.0 ML) preferential accumulation of Au atoms along Si$\langle 1\bar{1}0 \rangle$ consequences steady enhancement of mean aspect ratio, and at higher coverage of Au (>3.0 ML) accumulation of Au atoms along both direction *i.e.* Si$\langle 1\bar{1}0 \rangle$ and Si$\langle 66\bar{5} \rangle$ consequence reduction of mean aspect ratio. 3.0 ML Au/Ag:Si(5 5 12) system explores formation of thin film for Au growth at room temperature due to low mobility of both metal adatoms (Au, Ag) and disappearing role of Ag on the Au-Ag morphology at 400 °C caused by appreciable inter diffusion of Ag atoms inside Si matrix.

References

[1] Y. Volokitin, J. Sinzig, L. J. De Jongh, G. Schmid, M. N. Vargaftik , I. I. Moiseevi, *Nature* **384,** 621(1996).

[2] P. J. Feibelmen, *Phys. Rev. B* **27**, 1991 (1983).

[3] A. Nel, T. Xia, L. Mädler, N. Li, *Science* **311**, 622 (2006).

[4] Q. A. Pankhurst, J. Connolly, S. K. Jones, J. Dobson, *J. Phys. D : Appl. Phys.* **36**, 167 (2003).

[5] K. R. Gopidas, J. K. Whitecell, M. A. Fox, *Nano Lett.* **3,** 1757 (2003).

[6] W. L. Barnes, Alain Dereux, T. W. Ebbesen, *Nature* **424**, 824 (2003).

[7] K. L. Kelly, E. Coronado, L. L. Zhao, G. C. Schatz, *J. Phys. Chem. B* **107**, 668 (2003).

[8] E. Iglesia, S. L. Soled, R. A. Fiato, G. H. Via, *J. Catal.* **143**, 345 (1993).

[9] Y. Mizukoshi, T. Fujimoto, Y. Nagata, R. Oshima, Y. Maeda, *J. Phys. Chem. B* **104**, 6028 (2000).

[10] X. Li, J. Yao, F. Liu, H. He, M. Zhou, N. Mao, P. Xiao, Y. Zhang, *Sens. Actuator B-Chem.* **181**, 501 (2013).

[11] J. Liu, H. Zhou, Q. Wang, F. Zeng, Y. Kuang, *J. Mater. Sci.* **47**, 2188 (2012).

[12] H. Okamoto and T. B. Massalski, *Bull. Alloy Phase Diagra.* **4**, 30 (1983).

[13] J. L. White, R. L. Orr, R. Hultgren, *Acta Metall.* **5**, 747 (1957).

[14] W. C. Mallard, A. B. Gardner, R. F. Bass, L. M. Slifkin, *Phys. Rev.***129**, 617 (1963).

[15] J. H. Liu, A. Q. Wang, Y.S. Chi, H. P. Lin, C. Y. Mou, *J. Phys. Chem.* **109**, 40 (2005).

[16] J. Zheng, H. Lin, Y. Wang, X. Zheng, X. Duan, Y. Yuan, *J. Catal.* **297,** 110 (2013).

[17] M. P. Mallin, C. J. Murphy, *Nano Lett.* **2,** 1235 (2002).

[18] H. R. Gong, *Solid State Commun.* **149**, 2143 (2009).

[19] S. C. Fain, Jr. , J. M. McDavid, *Phys. Rev. B* **9,** 5099 (1974).

[20] R.A. Zhachuk, S.A. Teys, A.E. Dolbak, B. Olshanetsky, *Surf. Sci.* **565**, 37 (2004).

[21] H. Omi, T. Ogino, *Appl. Phys. Lett.* **71**, 2163 (1997).

[22] H. Omi, T. Ogino ,*Phys. Rev. B* **59**, 7521 (1999).

[23] H. Kim, H. Li, Y. Zhu, J. R. Hahn, J. M. Seo, *Surf. Sci.* **601**, 1831 (2007).

[24] A. A. Baski, S.C. Erwin, L.J. Whitman, *Science* **269**, 1556 (1995).

[25] T. Suzuki, H. Minoda, Y. Tanishiro, K. Yagi, *Surf. Sci.* **348**, 335 (1996).

[26] J. W. Dickinson, J. C. Moore, A. A. Baski *Surf. Sci.* **561**, 193 (2004).

[27] A. A. Baski, K. M. Jones, K. M. Saoud, *Ultramicroscopy* **86**, 23 (2001).

[28] A. A. Baski, K. M. Saoud, K. M. Jones, *Appl. Surf. Sci.***182**, 216 (2001).

[29] H. H. Song, K. M. Jones, A. A. Baski,*J. Vac. Sci. Technol., A* **17,** 1696 (1999).

[30] A. Bhukta, T. Bagarti, P. Guha, B. Satpati, B. Rakshit, P. Maiti, P. V. Satyam *(submitted in J. Appl. Phys.).*

[31] D. K. Goswami, B. Satpati, P. V. Satyam, B. N. Dev, *Current Science (India)* **84**, 903 (2003).

[32] M. Mayer, *Nucl. Instrum. Methods Phys. Res., Sect. B* **194**, 177 (2002).

[33] D. B. Williams, & C. B. Carter, *Transmission Electron Microscopy: A Textbook for Materials Science (Springer, 1996).*

Chapter 6

Ag induced growth of large aspect ratio Au-Ag bimetallic intermixed nanowires on Si(110) substrate

6.1 Introduction

In the diverge fields of nanotechnology, nanowires (NWs) are extremely important because of their implication as nanoscale interconnects [1, 2], mesoscopic devices [3], laser [4], nanoscale optical waveguide [5] etc. Due to reduction of the dimension of metal particle to its electron scattering wavelength, many interesting, advantageous physical properties (plasmonic [6], magnetic [7], Catalysis [8, 9] etc.) are explored that are absent in their bulk counterpart. Metal NWs which comprise anisotropic electronic states along its one dimension than the other two orthogonal dimensions [10, 11], play a crucial role in modern nanotechnology. NW found applications in versatile areas, such as, Hydrogen gas sensing by Pd NWs [12], field emission from cobalt NWs [13], glucose bio sensing using Au NWs [14] etc. In contrast with spherical shaped Au and Ag nanoparticles, one dimensionality of confinement of electron clouds results in two distinct plasmon frequencies (known as longitudinal and transverse) for Au and Ag nanowire (NW) [15, 16].

Combining two dissimilar metals at nanoscale in various methods give rise to formation of bimetallic nanoparticles (BMNPs) that can have many synergic effects. In many cases, such synergic effects become more advantageous than their monometallic counterparts such as catalysis [17, 18], electrochemistry [19, 20] etc. Among the different bimetallic pairs, Au-Ag combination shows remarkable miscibility in the entire window of variation of composition (Au:Ag ratio) [21, 22, 23] due to their isoelectronic configurations, nearly similar lattice constant with FCC structure and comparable surface energy. Indeed, Au-Ag bimetallic alloy nanostructures have superior catalytic activity for oxidation of CO in fuel cells [24] and hydrogenation of dimethyl oxalate to methyl glycolate at low temperature as 418 Kelvin [25] than its monometallic counterparts. Using Au-Ag composite BMNPs in enzyme electrode, current response is largely enhanced in the β-D-Glucose and significant biosensing of glucose is achieved [26]. Surface plasmon resonance (SPR) property of Au-Ag alloy nanostructures is successfully tuned with gradual enhancement of Au:Ag concentration ratio [27]. Surface enhanced Raman spectroscopy studies based on the SPR properties of Au-Ag bimetallic system, have been successfully implemented for substantial detection of 4-mer-captobezoic acid (4-MBA) [28] and Rhodamine 6G molecules [29]. Therefore, fabrication of Au-Ag bimetallic NWs on one dimensional template of clean Si surface could lead a step forward for advancement of application of metallic NWs in Si based technology, coupled with numerous synergic effects of BMNPs.

In this chapter, Au growth at substrate temperature 300 °C on Ag:Si(110) is reported. It is found that a well aligned array of large aspect ratio Au-Ag bimetallic intermixed nanowires. We have also tailored the morphology of Au-Ag bimetallic growth with variation of growth parameters *i.e.* substrate temperature (during Au growth) and Au thickness.

6.2 Experimental Methods

We have used commercially available phosphorous doped Si(110) wafer with resistivity 1-30 Ω-cm for growth of metal thin film. As a first step of preparing clean surface (*i.e.* native oxide free), sample is degassed at temperature 600 °C for 12-15 hours under ultra high vacuum (UHV). Then naturally grown native silicon oxide (SiO_X) layer (~ 2 nm) from the top of Si(110) surface is removed using direct current (DC) heating method by repetitive flashing at 1200 °C for one minute. Then it is slowly cooled down to desired temperature to carry out further experiments. Ag:Si(110) surface is prepared by deposition of 0.50 monolayer (ML) Ag on clean Si(110) surface at room temperature (RT). The base pressure inside the MBE chamber is routinely maintained ~ 2.0×10^{-10} mbar [30]. However, the pressure rises to ~ 1.0×10^{-9} mbar during *'flashing'* process while removing the native oxide layer and during the thin film deposition. In Knudsen cell (K-cell), alumina and pyrolytic boron nitride crucible are used for evaporation of Au and Ag respectively. Thickness of the metal thin films is measured using a quartz crystal microbalance which has been calibrated for all the K-cells using Rutherford backscattering spectrometry (RBS) method. Au and Ag is evaporated with flux rate as 0.50 ML/minute and 0.33 ML/minute, respectively. Substrate temperature is measured using a type K thermocouple which is attached in the backside of the manipulator. After the preparation of the sample it is brought in the ambient condition and morphology of the grown thin film (and nanostructures) is investigated utilizing field emission gun based scanning electron microscope (FEGSEM). Further imaging and energy dispersive X-ray spectroscopy (EDS) analysis have been carried out using a 300 keV scanning transmission electron microscopy (STEM). Further details of these experimental methods have been described in Chapter 2.

6.3 Results and Discussions

6.3.1 Comparison between monometallic Au and bimetallic Au-Ag growth

Fig. 6.1 (a) shows SEM micrographs for growth of 3.0 ML Au on ultra-clean Si(110) substrate at substrate temperature 300 °C. Followed by the Au growth, Au/Si(110) system is annealed at 300 °C for 30 minutes. It depicts the formation of aligned array of elongated nanostructures reflecting the preferred anisotropic growth of nanostructures along Si$\langle 1\bar{1}0 \rangle$ on ultraclean Si(110) substrate. Following this, Au growth has been also performed on Ag pre-modified Si(110) substrate. Pre-modification of ultra-clean Si(110) substrate is done by deposition of 0.50 ML on ultra-clean Si(110) substrate at RT (Ag:Si(110)). In this case, a 3.0

ML Au is deposited on Ag:Si(110) substrate at substrate temperature 300 °C. Followed by the Au growth, Au/Ag:Si(110) system is annealed at 300 °C for 30 minutes. SEM micrographs for such Au-Ag growth on Si(110) substrate has been represented in Fig. 6.1 (b) indicating formation of aligned array of elongated nanostructures. In this case, along with formation of smaller aspect ratio nanostructures, extremely large aspect ratio, as large as ~ 20.0 can be seen.

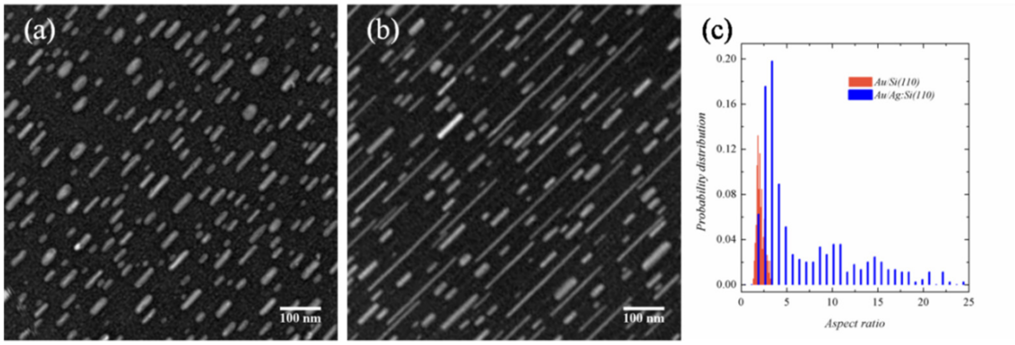

Figure 6.1 SEM micrograph for growth of 3.0 ML Au at substrate temperature 300 °C, on a) reconstructed Si(110) surface and b) Ag:Si(110) surface. c) Probability distribution of aspect ratio of the nanostructures for growth of 3.0 ML Au at substrate temperature 300 °C on ultraclean Si(110) surface (shown as orange colored) and Ag:Si(110) surface (shown as blue colored).

Fig. 6.1 (c) represents the probability distribution of aspect ratio of the nanostructures: for a 3.0 ML Au deposited only on reconstructed Si(110) surface (Fig. 6.1(c) orange color) and on pre-deposited Ag on Si(110) substrate (Fig. 6.1(c) blue color). Comparison of these two systems indicates that, in terms of aspect ratio of the nanostructures, monometallic Au growth is relatively uniform.

But, for Au-Ag growth, histogram of probability distribution becomes prominently broadened towards its tail with large magnitude of aspect ratio. Mean aspect ratio of the nanostructures for Au growth is found 2.1±0.1 and is enhanced to 7.2±0.8 for Au-Ag growth.

6.3.2 Composition for grown Au-Ag bimetallic nanostructures at substrate temperature 300 °C

Fig. 6.2 (a) shows *bright field* STEM micrograph for growth of 3.0 ML Au on Ag:Si(110) surface at substrate temperature 300 °C. Small aspect ratio nanostructures are coexisting with large aspect ratio nanowires as consistent with SEM micrograph (Fig. 6.1 (b)). In this case, darker contrast indicates the higher Z value (as the micrograph is a bright field STEM) (*i.e.* Au and Ag) and thickness of the constituent material on the sample. Crystalline nature of the grown nanowires with large aspect ratio is evidenced from a higher resolution image over an edge of the nanowires (Fig. 6.2 (b)). In Fig. 6.2 (c), we have presented a selected region (as shown in Fig. 6.2 (a)) containing an elongated nanowire with aspect ratio, as large as, ~ 44.5. This particular nanowire (Fig. 6.2 (c)), shows an intermediate stage before accumulation with other small aspect ratio nanostructures with nearly equal width. It is noteworthy to mention that, high resolution image in STEM (as shown in Fig. 6.2 (c)) micrograph indicates formation of smaller size nanostructures (less than ~ 30 nm^2) that have not been considered for analysis of aspect ratio of the nanostructures at various experimental conditions. Such smaller sized nanostructures are not well resolved by SEM as well.

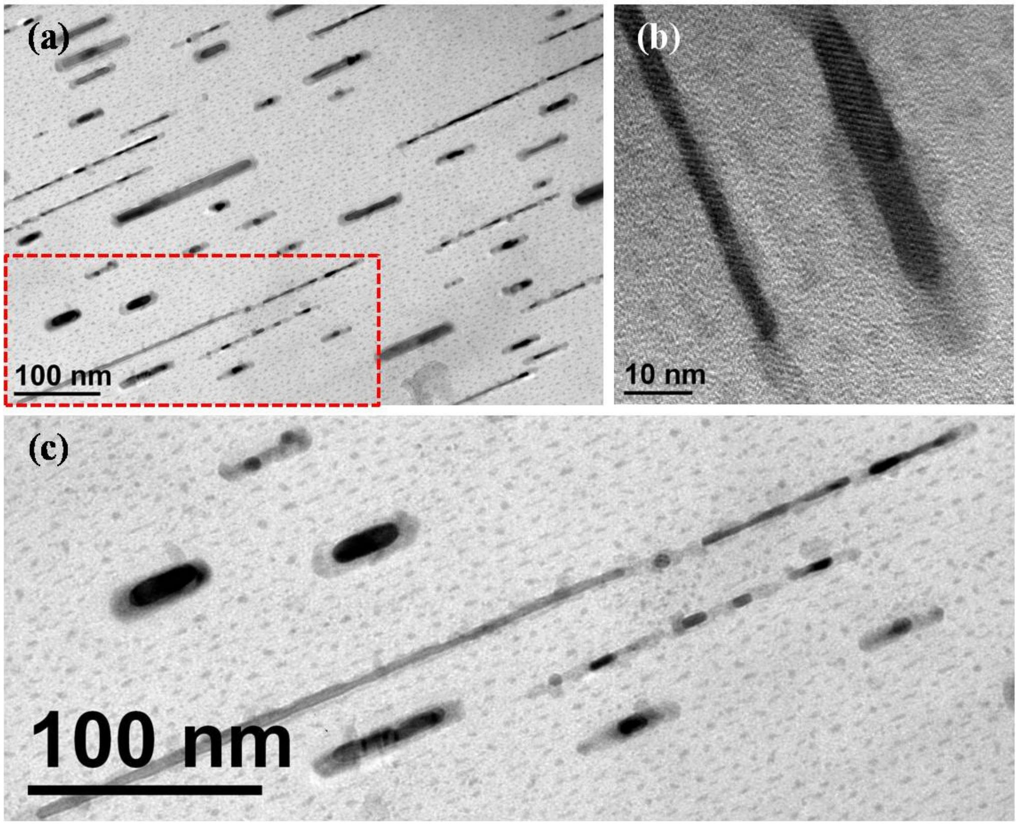

Figure6.2 Bright field STEM micrograph for growth of 3.0 ML Au on Ag:Si(110) at substrate temperature 300 °C with a) Low magnification and b) high magnification. c) Zoomed view of selected region (marked as rectangle with dotted red line) in Fig. 6.2 (a) to show a nanowire with aspect ratio ~ 44.5.

On this sample, we have also carried out dark field imaging in STEM method where brighter contrast depicts higher Z value and thickness of the constituent element in the sample (Fig. 6.3 (a)). We have studied elemental mapping using Si-Kα, Ag-Kα, Au-Mα and Au-Lα X-ray signals to identify constituents of the grown elongated nanowires. It explores both the smaller aspect ratio nanostructures and larger aspect ratio nanostructures are composed of Au and Ag.

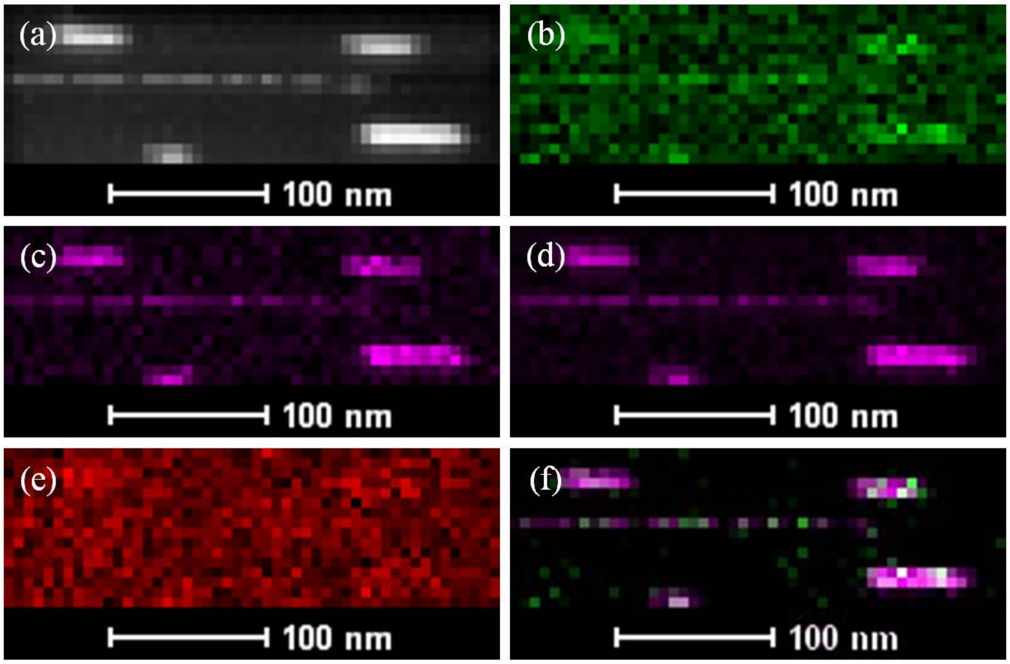

Figure 6.3 STEM study with planar view for growth of 3.0 ML Au on Ag:Si(110) at substrate temperature 300 °C a) HAADF image, EDS elemental map of b) Ag Lα, c) Au Lα, d) Au Mα, e) O Kα and f) their overlap.

Considering an elongated single nanostructure, we have investigated energy dispersive spectroscopy (EDS) analysis with Si-Kα, Ag-Lα and Au-Lα X-ray signals (Fig. 6.4). EDS line profile is consistent with the elemental mapping. Intensity of the X-ray signals indicates that, compared to Ag, amount of Au is much larger within such Au-Ag bimetallic nanostructures. Followed by the EDS analysis in planar view, we have also studied these aspects from a cross sectional view (Fig. 6.5). Over a selected region of the sample (Fig. 6.5 (a)), EDS elemental mapping for Ag-Lα and Au-Lα are shown in Fig. 6.5 (b) and 6.5 (c) respectively. In this case X-ray signals from the corresponding metal is shown as brighter contrast (Fig. 6.5 (b) and (c)). Both kinds of metals are present within each nanostructure with their uniform distributions.

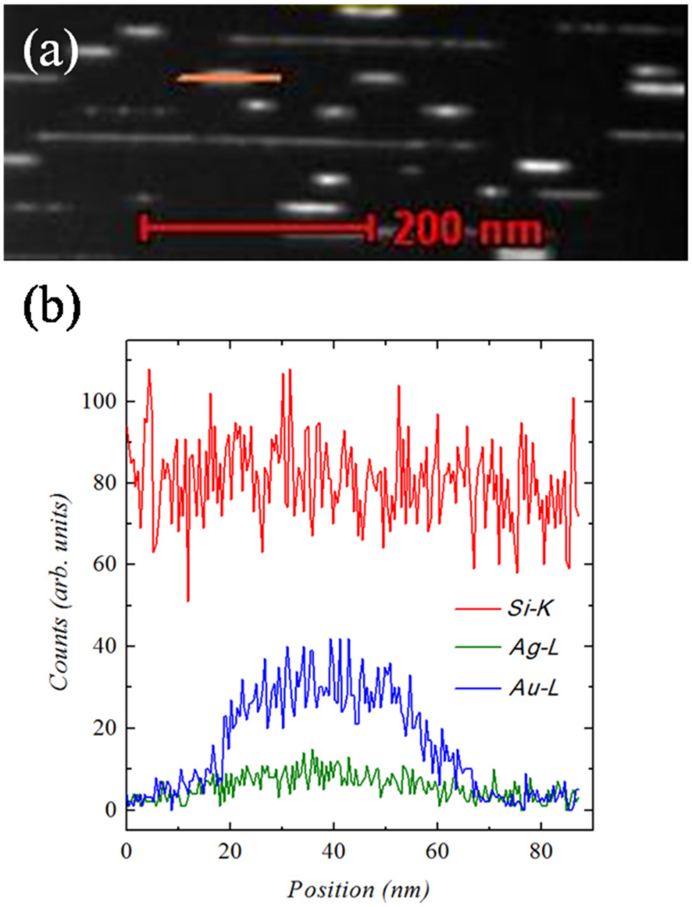

Figure 6.4 STEM study with planar view for growth of 3.0 ML Au on Ag:Si(110) surface at substrate temperature 300 °C a) HAADF image and b) EDS line profile over a selected region in Fig. 6.4 (a) as marked by orange colored line showing Si Kα (red line), Ag Lα (green line) and Au Lα (blue line) signal.

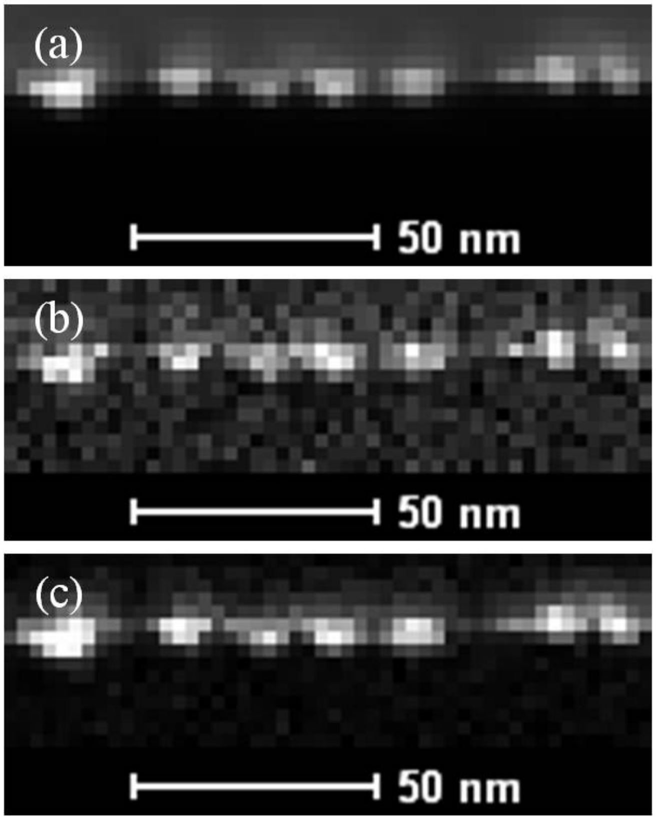

Figure 6.5 STEM study with cross sectional view for growth of 3.0 ML Au on Ag:Si(110) surface at substrate temperature 300 °C a) HAADF image, EDS elemental mapping of b) Ag Lα and c) Au Lα.

As mentioned earlier, upon the growth of 0.5 ML of Ag on reconstructed Si(110), it is expected that one dimensional Ag stripes are formed. Due to preferential ad-atom mobility along the $\langle 1\bar{1}0\rangle$ direction in comparison with the $\langle 001\rangle$ direction, the Ag stripes are expected to grow along $\langle 1\bar{1}0\rangle$ direction. In our previous work, we have also shown that such Ag stripes are formed on reconstructed vicinal Si(5 5 12) surface along its step edge direction $\langle 1\bar{1}0\rangle$ (Fig. 4.4 (b), (c)). Followed by the formation of Ag stripes when Au is deposited on Ag:Si(110), due strong affinity of the Au-Ag system, Ag stripes act as the efficient nucleation center for the incoming Au ad-atoms. Along with this, Au ad-atoms are expected to nucleate on the clean Si(110) surface where Ag is absent. Followed by the nucleation of Au ad-atoms towards the Ag atoms, further intermixing of Au-Ag atoms also takes place as the mobile Au and Ag atoms are reached to the intermixed nucleated regions. Therefore the combined effect of acting of Ag layer as nucleation center and anisotropic bimetallic Au-Ag admixing results in larger anisotropy (in terms of mean aspect ratio) than anisotropic mobility of Au atoms on ultra-clean Si(110) surface.

6.3.3 Morphological evolution of Au-Ag bimetallic growth for Au thickness 3.0 ML with variation of *substrate temperature*

To explore dependence of Au-Ag bimetallic morphology on substrate temperature, we have considered growth of 3.0 ML Au on Ag:Si(110) substrate at different substrate temperature. Starting from room temperature (RT), we have studied the growth at elevated temperature 200 °C, 270 °C, 300 °C, 330 °C and 400 °C. For all these cases, Au/Ag:Si(110) system has been post annealed at corresponding substrate temperature for 30 minutes. When Au is grown on Ag:Si(110) keeping the substrate at RT, formation of nanostructures doesn’t take place (Fig. 6.6 (a)). From the SEM micrograph, it appears formation of non uniform thin film. Growth of well ordered, elongated nanostructures is observable when we grow Au on Ag:Si(110) at growth temperature 200 ºC (Fig. 6.6 (b)). They comprise mean aspect ratio as 3.5±0.2 with elongation along Si$\langle 1\bar{1}0 \rangle$. Formation of elongated nanostructures is evident up to 400 ºC, which is maximum temperature of our investigation. Probability distribution of the aspect ratio with variation of the growth temperature has been presented in Fig. 6.7. Mean aspect ratio of the nanostructures at each growth temperature (as shown by representative SEM micrographs in Fig. 6.1 (b) and Fig. 6.7 (a)-(d)) has been measured and plotted in Fig. 6.8 as a function of growth temperature. In comparison with 200 ºC, when the substrate temperature is increased to 270 ºC, mean aspect ratio becomes 5.7±0.7 which is ~1.6 times larger than its value at 200 ºC. With increase of substrate temperature, probability distribution of aspect ratio becomes more non-uniform with broadening towards its tail (Fig. 6.7 (a) and 6.7 (b)). With further increase of substrate temperature to 330 °C, mean aspect is also enhanced to 7.3±0.9 exploring that in the temperature regime 200-330 °C, the mean aspect ratio is gradually increased (Fig. 6.8). From the corresponding SEM micrographs (Fig. 6.6 (b) and 6.6 (c)), we have found at 270-330 °C formation of nanostructures with much larger length and aspect ratio than its mean value is quite noticeable. As the temperature is further increased to 400 °C, mean aspect ratio becomes 3.7±0.2 indicating its reduction by ~ 0.5 times with respect to growth at 330 °C (Fig. 6.7 (c)). At 400 °C, probability distribution of aspect ratio (Fig. 6.7 (d)) becomes more uniform about its mean value. In this case, formation of nanostructures with much larger aspect ratio than its mean value is rarely observed. Such uniform distribution of aspect ratio shows well resemblance with the monometallic Au growth on ultraclean Si(110) (Fig. 6.1 (c)). From the SEM micrographs (Fig. 6.6) it is also evident that, formation of very large aspect ratio nanostructures which have been noticeably observed at substrate temperature 270-330 °C, rarely takes place at 400 °C.

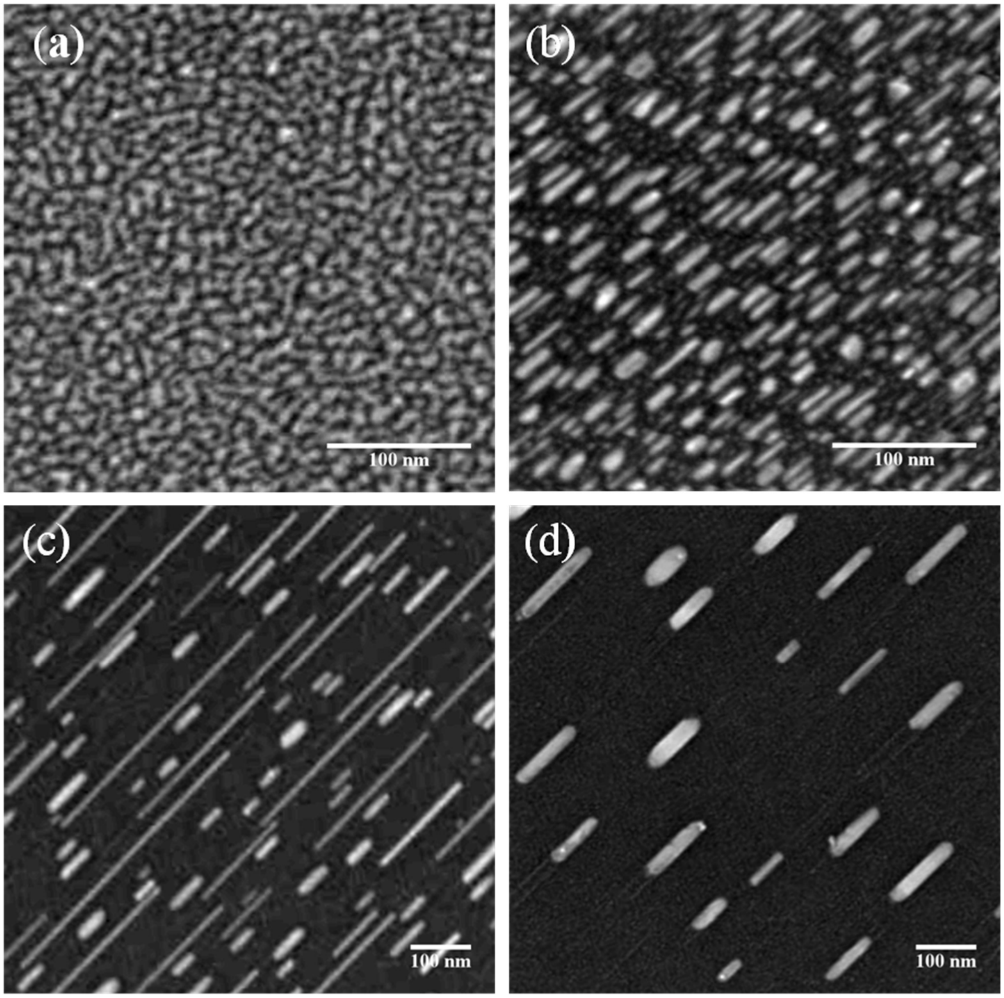

Figure 6.6 SEM micrographs for growth of 3.0 ML Au on Ag:Si(110) surface at various substrate temperature a) room temperature, b) 200 °C, c) 330 °C and d) 400 °C.

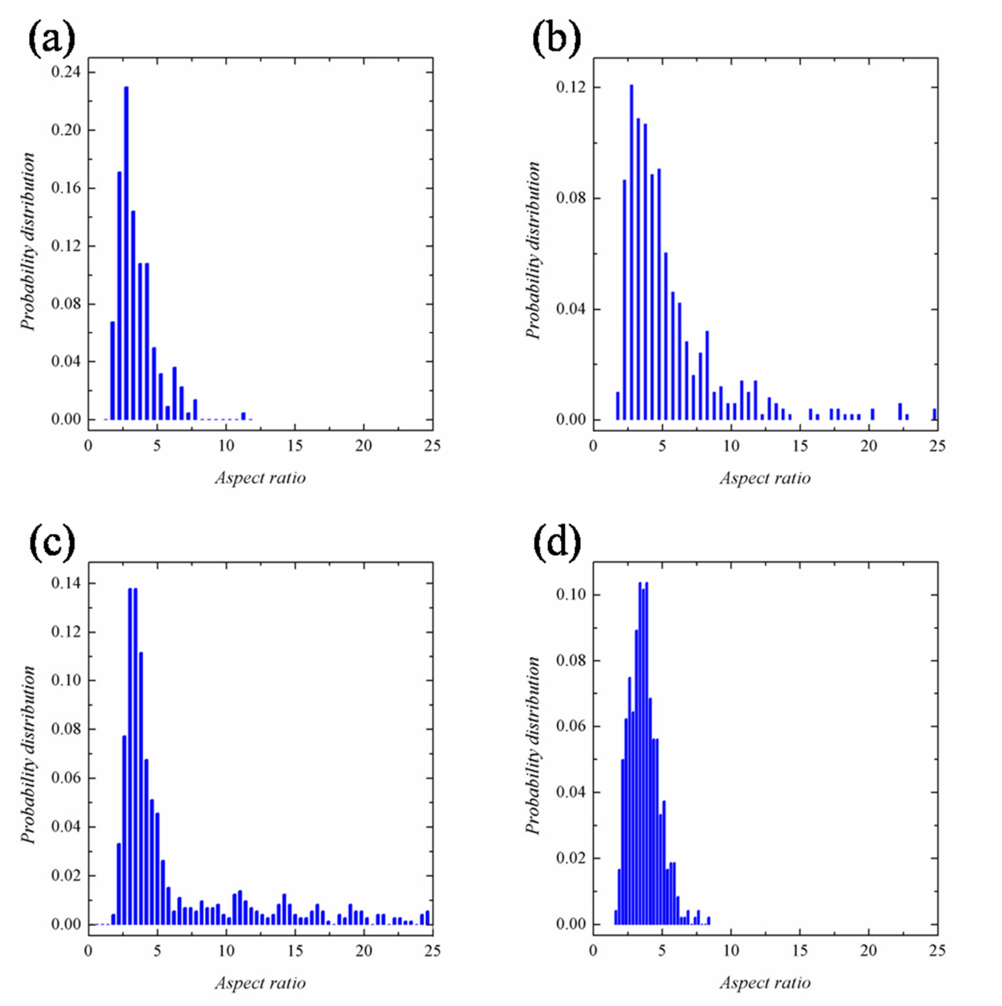

Figure 6.7 Probability distribution of aspect ratio of the nanostructures for growth of 3.0 ML Au on Ag:Si(110) surface at various substrate temperature a) 200 °C, b) 270 °C, c) 330 °C and d) 400 °C.

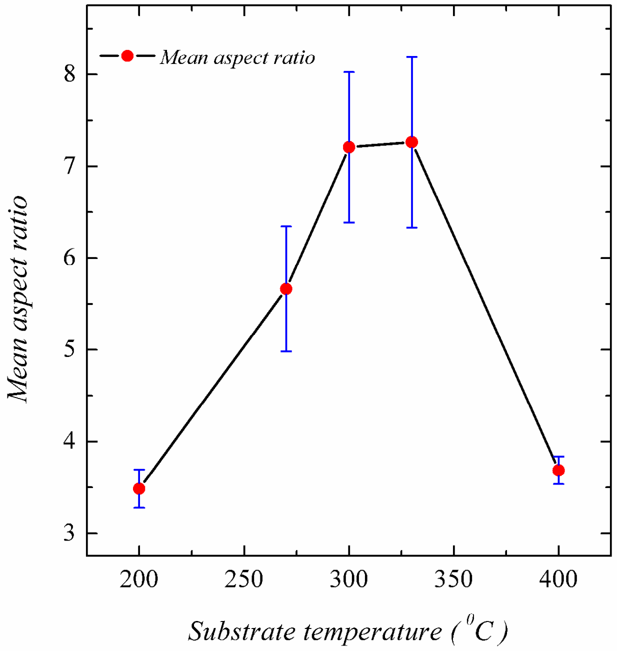

Figure 6.8 Plot of mean aspect ratio of the grown nanostructures as a function of substrate temperature for growth of 3.0 ML Au on Ag:Si(110).

At RT after Au growth on Ag:Si(110), formation of non-uniform thin film indicates that both the Au and Ag adatoms are not provided enough external thermal energy to diffuse on the template. As the substrate temperature is increased to 200 °C, the Au and Ag atoms become enough mobile to form well ordered nanostructures. At ~ 270 °C, enhancement of mean aspect ratio indicates effect of the Ag stripes as the nucleation center for Au growth becomes more prominent. As the temperature increased in the regime 270-330 °C, Au and Ag ad-atoms become more mobile on the surface and probability of Au-Ag binary intermixing is increased. As the substrate temperature is increased further to 400

°C, morphology of the grown nanostructures become quite similar as the monometallic Au growth. Probably, at this temperature Ag ad-atoms that have been deposited before Au growth are inter- diffused inside the Si matrix. In our previous work, we have shown that, Ag is largely inter diffused inside the Si matrix of Si(5 5 12) substrate (Fig. 5.9). As the Ag is inter-diffused, presence of mobile Ag atoms during Au growth becomes very rare and Ag doesn't exhibit any prominent influence on post grown Au-Ag morphology. Although at 400 °C the probability distribution of aspect ratio of Au/Ag:Si(110) is quite uniform like Au/Si(110) at 300 ºC, among these two cases Au/Ag:Si(110) system comprises higher mean aspect ratio.

6.3.4 Morphological evolution of Au-Ag bimetallic growth at substrate temperature 300 °C with variation of *Au thickness*

In the following section, we have presented the morphological evolution of the Au-Ag bimetallic growth on Ag:Si(110) surface with systematic variation of the thickness of Au. To understand this aspect, we have considered growth of Au with varying thickness 1.5-6.0 ML, on Ag:Si(110) at substrate temperature ~ 300 °C. Followed by the growth, morphology of the grown nanostructures is studied by SEM and the images are shown in Fig. 6.9. In all cases, after the growth of Au, Au/Ag:Si(110) system has been annealed at 300 °C for 30 minutes.

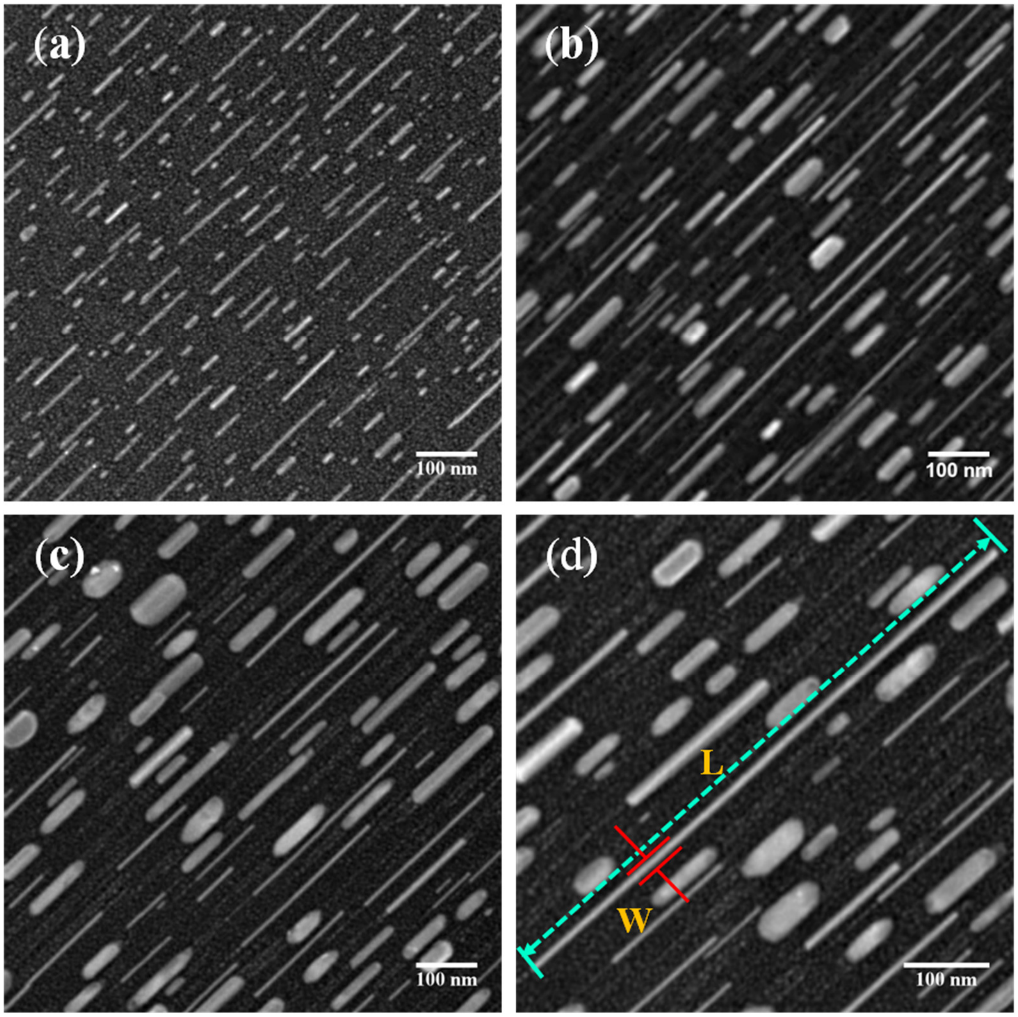

Figure 6.9 SEM micrographs for growth of Au on Ag:Si(110) surface at substrate temperature 300 °C with varying Au thickness as a) 1.5 ML, b) 5.0 ML and c) 6.0 ML. d) Higher magnification image of Fig. 6.9 (c) to show the formation of single nanowire with aspect ratio (L:W) ~ 45.0 and length (L) ~ 731 nm.

For growth of 1.5 ML Au, we have observed formation of elongated nanowire with mean aspect ratio 4.0±0.6 (Fig. 6.9 (a)). With respect to the condition 1.50 ML, for increase of Au to 3.0 ML, the mean aspect ratio is increased by ~ 1.8

times and becomes 7.2±0.8. As the Au thickness is increased further to 5.0 ML, a slight decrease of mean aspect ratio is observed in comparison with Au 3.0 ML. In this case grown nanostructures comprise mean aspect ratio as 6.7±0.6.

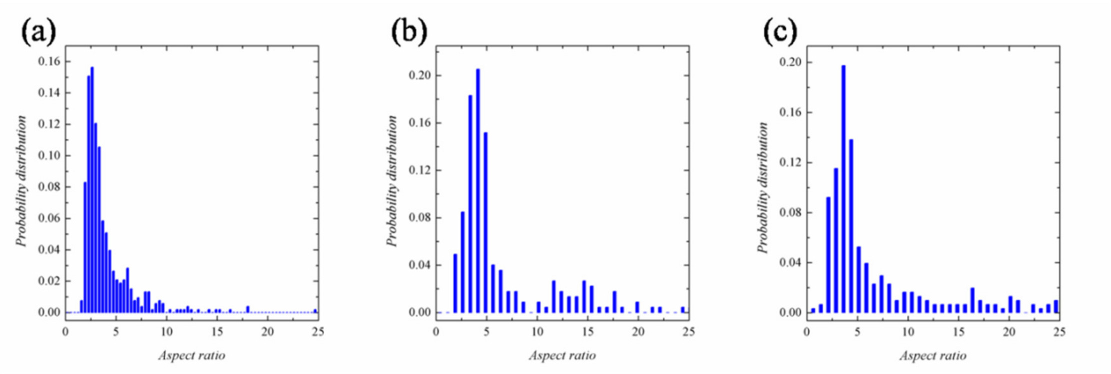

Figure 6.10 Probability distribution of aspect ratio of the nanostructures for growth of Au on Ag:Si(110) surface at substrate temperature 300 °C with varying Au thickness as a) 1.5 ML, b) 5.0 ML and c) 6.0 ML.

In a similar manner, mean aspect ratio is also decreased for enhancement of Au thickness to 6.0 ML. For growth of 6.0 ML Au, mean aspect ratio is obtained as 5.9±0.8. It consequences that steady enhancement of mean aspect ratio is restrained for Au thickness above 3.0 ML. It is noteworthy to mention that for growth 5.0 ML Au, we have observed a single nanowire with aspect ratio as ~ 45, with its length ~ 731 nm (Fig. 6.9 (d)). Steady enhancement of mean aspect ratio for Au up to 3.0 ML, indicates that followed by the nucleation of Au adatoms, accumulation and incorporation of the mobile ad atoms (both Au and Ag) preferentially takes place along $\mathrm{Si}\langle 1\bar{1}0\rangle$ compared to $\mathrm{Si}\langle 001\rangle$ direction. It is plausibly occurs due to one dimensionality of nucleation center *i.e.* Ag stripes and the anisotropic intermixing of the metal adatoms. But as the Au thickness is increased to 5.0 ML, the appreciable effect of the Ag stripes on the morphology becomes weaker. Plausibly, followed by the early nucleation process and Au-Ag intermixing towards pre-grown one dimensional Ag stripes, excess Au adatoms also begin to accumulate along Si⟨001⟩. So the incorporation of Au adatoms along Si⟨001⟩ to grow a larger nanostructure, becomes more probable for Au thickness larger than 3.0 ML and mean aspect ratio of the nanostructures is gradually decreased.

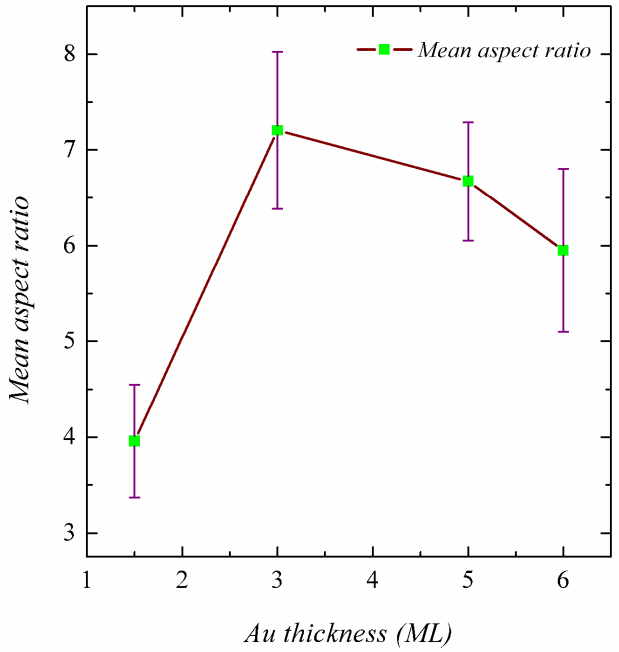

Figure 6.11 Plot of mean aspect ratio of the nanostructures as a function of Au thickness, for growth of Au on Ag:Si(110) surface at substrate temperature 300 °C.

6.4 Conclusions

We report on the post growth morphology of Au-Ag bimetallic system on ultra-clean Si(110) surface and show that the morphology is very much dependent on growth parameters: substrate temperature and Au thickness. In the regime of substrate temperature 270-330 ºC, presence of Ag layer, prior to Au growth efficiently acts as preferential nucleation center and consequences to large aspect ratio nanowires. At higher temperature 400 ºC, role of Ag to influence the morphology of Au-Ag bimetallic growth becomes less significant. In other scenario, for very low temperature such as room temperature, they form non-uniform thin film. At an optimum substrate temperature 300 ºC, variation of Au thickness up to 3.0 ML reveals gradual enhancement of the mean aspect ratio of the nanowires. Above 3.0 ML, mean aspect ratio of the nanowires is reduced, indicating the appreciable mobility of ad atoms along Si$\langle 001 \rangle$ on the surface takes place. For growth at 300 ºC, grown nanowires are found as comprised of uniform mixing of Au and Ag.

References

[1] G. S Snider, R Stanley Williams, *Nanotechnology* **18**, 035204 (2007).

[2] L. Dong, J. Bush, V. Chirayos, R. Solanki, J. Jiao, *Nano Lett.*, **5**, 2112 (2005).

[3] J. Xiang, A. Vidan, M. Tinkham, R. M. Westervelt, C. M. Lieber, *Nat. Nanotechnol.* **1**, 208 (2006).

[4]X. Duan, Y. Huang, R. Agarwal, C. M. Lieber *Nature* **421**, 241 (2003).

[5] A. L. Pyayt, B. Wiley, Y. Xia, A. Chen, L. Dalton, *Nat. Nanotechnol.* **3**, 660 (2008).

[6] K. L. Kelly, E. Coronado, L. L. Zhao, G. C. Schatz, *J. Phys. Chem. B* **107**, 668 (2003).

[7] A. Lu, E. L. Salabas, F. Schüth, *Angewandte Chemie International Edition* **46**, 1222 (2007).

[8] B. R. Cuenya, *Thin Solid Films* **518**, 3127 (2010).

[9] B. Hvolbæk, Ton V. W. Janssens, B. S. Clausen, H. Falsig, C. H. Christensen, J. K. Nørskov, *Nanotoday* **2**, 14 (2007).

[10] N. Oncel, A. van Houselt, J. Huijben, A. Hallba¨ck, O. Gurlu, H. J. W. Zandvliet, B. Poelsema, *Phys. Rev. Lett.* **95,** 116801 (2005).

[11] S Noor Mohammad, *J. Phys. Condens. Matter* **26**, 423202 (2014).

[12] F. Favier, E. C. Walter, M. P. Zach, T. Benter, R. M. Penner, *Science* **293**, 2227 (2001).

[13] L. Vila, P. Vincent, L. D. Pra, G. Pirio, E. Minoux, L. Gangloff, S. Demoustier-Champagne, N. Sarazin, E. Ferain, R. Legras, L. Piraux, P. Legagneux, *Nano Lett.* **4**, 521 (2004).

[14] Q. Wang, F. Min, J. Zhu, *Mater. Lett.* **91**, 9 (2013).

[15] M. N'Gom, J. Ringnalda, J. F. Mansfield, A. Agarwal and N. Kotov, N. J. Zaluzec, T. B. Norris, *Nano Lett.* **8**, 3200 (2008).

[16] S. Link, M. A. El-Sayed, *J. Phys. Chem. B* **103**, 8410 (1999).

[17] Y. Mizukoshi, T. Fujimoto, Y. Nagata, R. Oshima, Y. Maeda, *J. Phys. Chem. B* **104,** 6028(2000).

[18]E. Iglesia, S. L. Soled, R. A. Fiato, G. H. Via, *J. Catal.* **143**, 345 (1993).

[19] J. Liu, H. Zhou, Q. Wang, F. Zeng,Y. Kuang, *J. Mater. Sci.* **47**, 2188 (2012)

[20] X. Li, J. Yao, F. Liu, H. He, M. Zhou, N. Mao, P. Xiao, Y. Zhang, *Sens. Actuator B- Chem.***181**, 501 (2013).

[21] H. Okamoto and T. B. Massalski, *Bull. Alloy Phase Diagram.* **4**, 30 (1983).

[22] W. C. Mallard, A. B. Gardner, R. F. Bass, L. M. Slifkin, *Phys. Rev.* **129**, 617 (1963).

[23] J. L. White, R. L. Orr, R. Hultgren, *Acta Metall.* **5**, 747 (1957).

[24] J. H. Liu, A. Q. Wang, Y.S. Chi, H. P. Lin, C. Y. Mou, *J. Phys. Chem. B* **109**, 40 (2005).

[25] J. Zheng, H. Lin, Y. Wang, X. Zheng, X. Duan, Y. Yuan, *J. Catal.* **297**, 110 (2013).

[26] X. Ren, X. Meng, F. Tang, *Sens. Actuators B* **110**, 358 (2005).

[27] M. P. Mallin, C. J. Murphy, *Nano Lett.* **2**, 1235 (2002).

[28] S. Xu, B. Zhao, W. Xu, Y. Fan, *Colloids Surf.,A: Physicochem. Eng. Aspects* **257-258**, 313 (2005).

[29] Y. Yang, J. Shi, G. Kawamurab and M. Nogami, *Scr. Mater.* **58**, 862 (2008).

[30] D. K. Goswami, B. Satpati, P.V. Satyam, B. N. Dev *Curr. Sci.* (*India*) **84**, 903 (2003).

Chapter 7

Substrate orientation dependence of Au-Ag bimetallic growth on clean Si substrates

7.1 Introduction

Growth of parallel array of metal nanowires, oriented along single direction with large density is important due its implication as interconnect in Si-based nano electronics [1, 2], laser [3], mesoscopic devices [4] and to understand many other fundamental aspects of one dimensional electron system [5, 6]. In comparison with other growth methods, fabrication of metal nanostructures on reconstructed Si(hkl) substrates under MBE conditions withstands advantages of tailoring of its morphology, composition, crystalline quality etc. [7] For example, over-layer metal growth on reconstructed Si(111) surface results information of hexagonal and triangular shaped nanostructures [8, 9] and formation of square and rectangular shaped nanostructures on Si(001) surface [10]. These growth patterns appear to follow the substrate symmetry. But reconstructed Si(001) surface with of ‘2×1’ unit cell is comprised of two orthogonal domains and therefore grown nanowires become elongated along two orthogonal directions [11-13]. Such limitation could be overcome by employing reconstructed Si(110) [14, 15] and vicinal Si(hkl) surfaces [16-18] for fabrication of nanostructures.

In search of efficient next generation nano materials for technological application as magnetic material [19, 20], catalyst [21-23], non linear optics [24] with chemical stability, a lot of research work have been devoted to understand bimetallic nanoparticle, in the last two decades. Implementation of bimetallic nanoparticle for such application has been proven technologically more advantageous than its monometallic counterpart. In particular, Au-Ag nano alloy system becomes very fascinating compared to other binary systems for its remarkable electrochemical [25-27] and optical property [28] in visible range of electromagnetic spectrum. $Au^{\delta-}$-$Ag^{\delta+}$ bond is formed as Au has higher electronegativity 1.92 than Ag 1.87 (in Pauling scale) and electronic structure [29] Au: $(5d)^{10}(6s)^{1}$ and $Ag(4d)^{10}(5s)^{1}$. Au and Ag comprise FCC lattice structure with lattice constant 4.0788 Å and 4.0862 Å respectively. Because of these characteristics, Au-Ag binary system shows completely miscibility with any desired composition ratio (Au:Ag) [30-32]. Alloying with controlled composition ratio (Au:Ag), turns out to be an extra tuning parameter like size, shape, dielectric constant of the nanostructures, to achieve desired surface plasmon resonance (SPR) wavelength in the visible range [33]. Efficient tuning of SPR absorption peak causes Au-Ag binary nano alloy system as an ideal candidate for application of optical sensors [34] and light stable color filtering [35]. Catalytic performance of Au-Ag alloy nanoparticles is significantly better than the counterpart monometallic nanoparticles, for oxidation of CO [36]. Such oxidation process is very crucial to generate CO free Hydrogen steam for superior performance of fuel cells at low temperature [37]. Improved catalytic property of Au-Ag bimetallic nanoparticle than the monometallic (Au, Ag) nanoparticle is also observed for hydrogenation of dimethyl oxalate to methyl glycolate at low temperature as 418 Kelvin [38]. Alloying with Au makes possible to improve stability and inhibit oxidation of Ag nanoparticles in ambient condition [39, 40].

Preparation of Au-Ag bimetallic parallel array of intermixed nanowires on reconstructed Si(hkl) surfaces explores a possibility of combined advantage of metal nanowire on Si substrate and synergic effects of bimetallic nanoparticle. In our present study, we have considered Au growth at elevated substrate temperature 300 °C, on two kinds of growth template: (i) reconstructed Si(hkl) and (ii) Ag modified reconstructed Ag:Si(hkl), substrate. Morphological aspects of monometallic (Au/Si(hkl)) and bimetallic growth (Au/Ag:Si(hkl)), depending upon the variation of (hkl) plane have been understood. Observed morphology for Au/Si(111) and Au/Ag:Si(111) in our experiments show quite similarity with reported results obtained by A. Endo [41]. Thereafter, we have investigated morphological and structural aspects of bimetallic Au-Ag growth and monometallic Au growth on reconstructed Si(001) substrate. With reference to this observation, we have studied bimetallic (Au-Ag) growth, on one dimensional template viz. low index Si(110) and high index Si(553) and Si(5 5 12) substrate. For all the Si(hkl) substrates, Au-Ag growth consequences higher particle density than the Au growth. Bimetallic growth results in formation Au-Ag bimetallic intermixed nanowires having two orthogonal orientations on Si(001) surface and parallel array on Si(110), Si(5 5 12) and Si(553) surfaces. Thereafter, we have presented a comparative study of variations of dimensions of the nanostructures as a function of its size for various orientations of the substrate. Substantial effect of pre-modification of Ag on such morphological aspect of grown nanostructures has been also investigated.

7.2 Experimental Methods

For growth of Au and Ag under MBE conditions, reconstructed single crystal Si surfaces with various (hkl) orientations are considered. It includes low index plane of Si surfaces: reconstructed Si(111), S(001) and Si(110). For comparative studies, we have also considered other kinds of one dimensional template (high index plane) *i.e.* reconstructed Si(553) and Si(5 5 12) surface. Top native oxide layer from the Si(111) surface is removed by repetitive flash heating at 1200 °C for one minute by usual direct current (DC) heating method, followed by the degassing at 600 °C for 12-15 hours. This Si(111) wafer is commercially available with Ph doping and resistivity 1-20 Ω-cm. The Si(110) surface is also cleaned (removal of native oxide layer) under similar procedure, which is Ph doped with resistivity 1-30 Ω-cm. Repetitive flash heating at 1200 °C for one minute, is also employed to clean the high index Si surfaces. During degassing and flashing process, direct current is passed along the Si$\langle 1\bar{1}0\rangle$ of the sample and it is quenched to low temperature ~ 700 °C after flashing, to avoid step bunching on the high index surfaces. Wafer is cut in small pieces in rectangular shape with dimensions 3 mm × 10 mm. During DC heating, magnitude of the current passing through the sample is controlled according the size of the sample and resistivity, to achieve the desired substrate temperature. An external optical pyrometer and a thermocouple (TC) attached with the manipulator, is utilized to measure the substrate temperature. Base pressure of the molecular beam epitaxy (MBE) growth chamber is ~ 2.0×10^{-10} mbar which is increased to ~ 1.0×10^{-9} mbar during deposition and flashing process [42]. Thickness of the thin film is determined using quartz crystal microbalance which is pre-calibrated using Rutherford backscattering spectrometry technique. Here, we have presented the thin film thickness in monolayer (ML) unit which indicates 1 ML = 1.0×10^{15} atoms/cm^2 for both kinds of material *i.e.* Au and Ag. Au and Ag are grown with flux rate ~ 0.50 ML/minute and ~ 0.33 ML/minute respectively. Evaporation temperature of growth materials (Au and Ag) is measured using a type C TC, which is coupled with a PID controller. At different stage of sample preparation, in-situ imaging has been carried using a variable temperature scanning tunneling microscopy (VTSTM) which is attached with MBE growth chamber. All the STM measurements, as described in the present Chapter, have been performed in constant current mode at room temperature (RT). Followed by the acquisition of the images in STM, further analysis of the images to understand different morphological aspects has been carried out using ImageJ software package. To perform scanning transmission electron microscopy (STEM) measurements, specimens are prepared by mechanical polishing and low energy Ar^+ ion milling. High angle annular dark field (HAADF) imaging and energy dispersive X-ray spectroscopy (EDS) measurements in STEM method have been carried out using 300 keV electron beam. Some of the EDS measurements have been also performed using Talos F200 with 200 keV electrons in IISc Bangalore, India.

7.3 Results and Discussion

Followed by the removal of native SiOx layer by ‘flashing’ at 1200 °C, ultra-clean Si(hkl) substrates are brought to RT and thereafter 0.50 ML Ag is deposited on it (Ag:Si(hkl)). After such modification of ultra-clean Si(hkl) substrates with Ag, they are brought to 300 °C and subsequently annealed for one hour prior to Au growth.

7.3.1 Morphological evolution of Au/Si(hkl) monometallic and Au/Ag:Si(hkl) bimetallic growth for various (hkl) orientation

Fig. 7.1 (a) and (b) represents the topographic STM image for growth of 1.50 ML Au at substrate temperature 300 °C, on reconstructed Si(111) and Ag:Si(111) surface respectively. In both cases, followed by the Au growth, grown thin films are post annealed at 300 °C for 30 minutes. For both the systems (*i.e.* Au/Si(111) and Au/Ag:Si(111)), in some regions, nanostructures are grown as hexagonal shaped following the three fold symmetry of the substrate. With respect to monometallic Au growth, bimetallic Au-Ag growth consequences much smaller sized particles. In case of Au/Si(111) growth particle density is found as ~

0.50×10^3 /μm^2. While it becomes ~ $3.02\times10^3/\mu m^2$ for Au/Ag:Si(111) growth, depicting the enhancement of particle density by ~ 6.0 times.

Morphology for 1.50 ML Au growth on reconstructed Si(001) surface and Ag:Si(001) surface have been presented in Fig. 7.1 (c) and (d) respectively. In both cases, followed by the Au growth, samples have been annealed at 300 °C for 30 minutes. In case of Au/Si(001) system, well ordered growth of square shaped nanostructures are observed following the fourfold symmetry of the crystal lattice of the substrate. Along with the grown square shaped nanostructures, slightly elongated rectangular shaped nanostructures are also formed with elongation towards two orthogonal directions of the substrate. In this case mean aspect ratio of the grown nanostructures is found as 1.23±0.03. Quite interesting morphology is observed for Au/Ag:Si(001) system (Fig. 7.1 (d)), which explores that with small aspect ratio, nearly square shaped nanostructures, formation of extremely large aspect ratio nanowires. Growth of nanowires with their elongations along two orthogonal directions of the substrate having aspect ratio as large as ~ 5.5 is also observed. It consequences, with pre modification of ultraclean Si(001) substrate with 0.50 ML Ag, grown nanostructures comprise mean aspect ratio as 2.3±0.1 which is 1.8±0.1 times larger than monometallic Au growth. Particle density for growth of monometallic Au growth is found ~ $1.47\times10^3/\mu m^2$. Compared to monometallic Au growth, bimetallic Au-Ag growth results in enhancement of particle density. Grown Au-Ag nanostructures comprise particle density ~ $2.66\times10^3/\mu m^2$ which is nearly 1.81 times larger the monometallic Au growth.

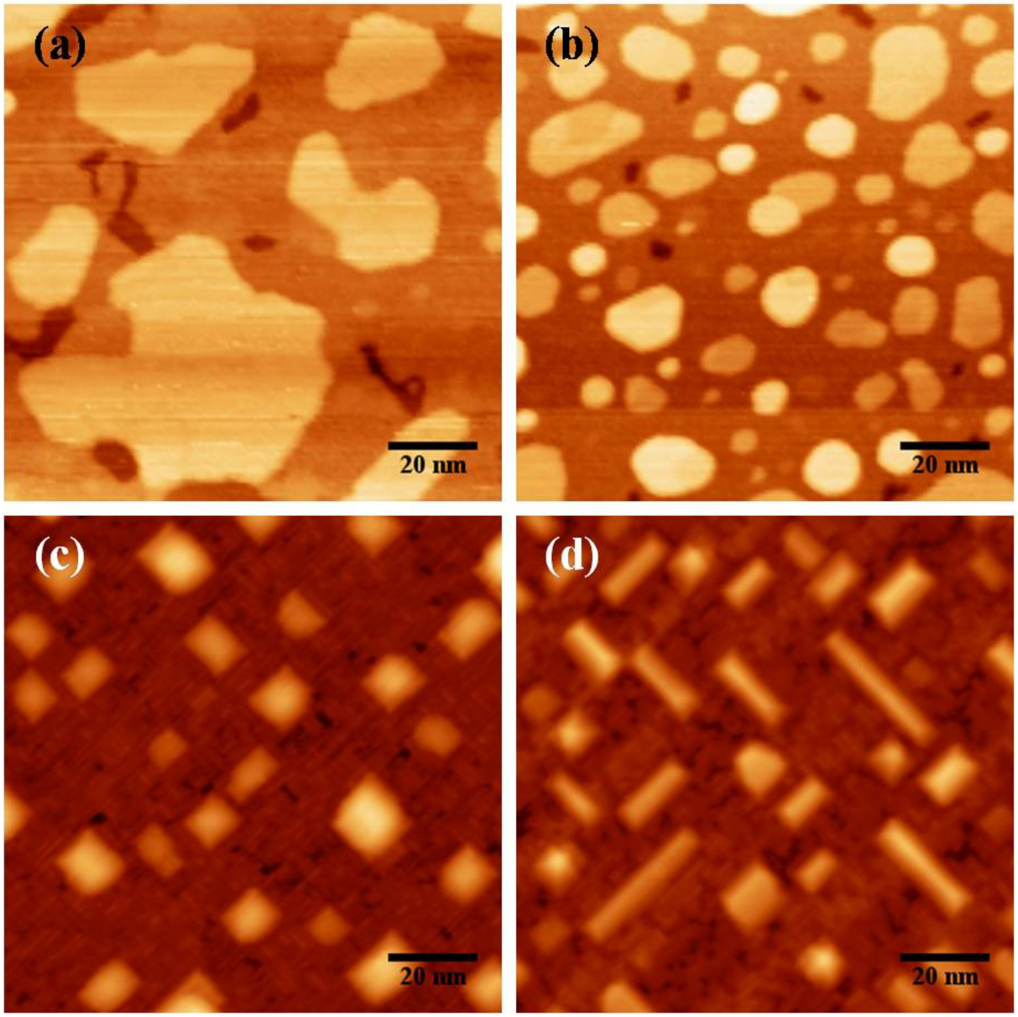

Figure 7.1 STM topographic image for 1.50 ML Au growth at substrate temperature 300 °C on a) reconstructed Si(111), b) Ag:Si(111), c) reconstructed Si(001) and d) Ag:Si(001), surface.

Following this we have investigated morphologies of Au/Si(110) and Au/Ag:Si(110) system. In case of Au/Si(110) system we observe formation rectangular shaped nanostructures with mean aspect ratio 2.1±0.1 and particle density ~ $1.05\times10^3/\mu m^2$ (Fig. 7.2 (a)). Whereas when Au grows on Ag:Si(110), mean aspect ratio and particle density becomes as 3.4±0.2 and ~ $2.26\times10^3/\mu m^2$ respectively (Fig. 7.2 (b)). Comparing these two systems, due to pre modification by Ag relative enhancement of mean aspect ratio and particle density becomes 1.6±0.2 and ~ 2.15 times respectively. Similar effect of Ag on the Au-Ag growth has been also observed (as shown in Fig. 7.2 (c) and (d)) on high index reconstructed Si(5 5 12) surface. Monometallic growth of Au on ultra-clean Si(5 5 12) surface results in formation of small aspect ratio nanostructures with mean aspect ratio 1.56±0.01 and particle density ~ $1.35\times10^3/\mu m^2$ (as shown in Fig.7.2 (c)). Due to modification of ultraclean substrate prior to Au growth, formation of elongated nanowires with much larger aspect ratio as large as ~ 6.0 is quite evidenced (Fig. 7.2 (d)). Indeed, such bimetallic Au-Ag nanostructures comprise mean aspect ratio 2.6±0.1 and particle density ~ $3.6\times10^3/\mu m^2$. It explores that enhancement of mean aspect ratio and particle density of the Au-Ag nanostructures is 1.7±0.10 times and ~ 2.67 times respectively, than the monometallic Au nanostructures. Following this, we have also investigated growth of monometallic Au and bimetallic Au-Ag on reconstructed Si(553) surface. Morphologies of the grown nanostructures are quite analogous to growth on reconstructed Si(110) and Si(5 5 12) surfaces. Grown nanostructures for Au/Si(553) system are comprised of mean aspect ratio 1.77±0.05 with elongation along step edge direction (Fig. 7.2 (e)). While in other scenario, for Au/Ag:Si(553) growth nanostructures have much larger aspect ratio. Indeed, Au-Ag bimetallic nanowire with aspect ratio as large as ~ 5.0 is also observed. Grown Au-Ag bimetallic nanostructures comprise mean aspect ratio 2.99±0.18 (Fig. 7.2

(f)) which is 1.68±0.15 times larger than the monometallic Au growth. Particle density for the Au/Si(553) growth is obtained as $1.08\times10^3/\mu m^2$ and becomes $3.36\times10^3/\mu m^2$ for Au/Ag:Si(553) growth indicating ~ 3.11 times enhancement due to pre modification by Ag.

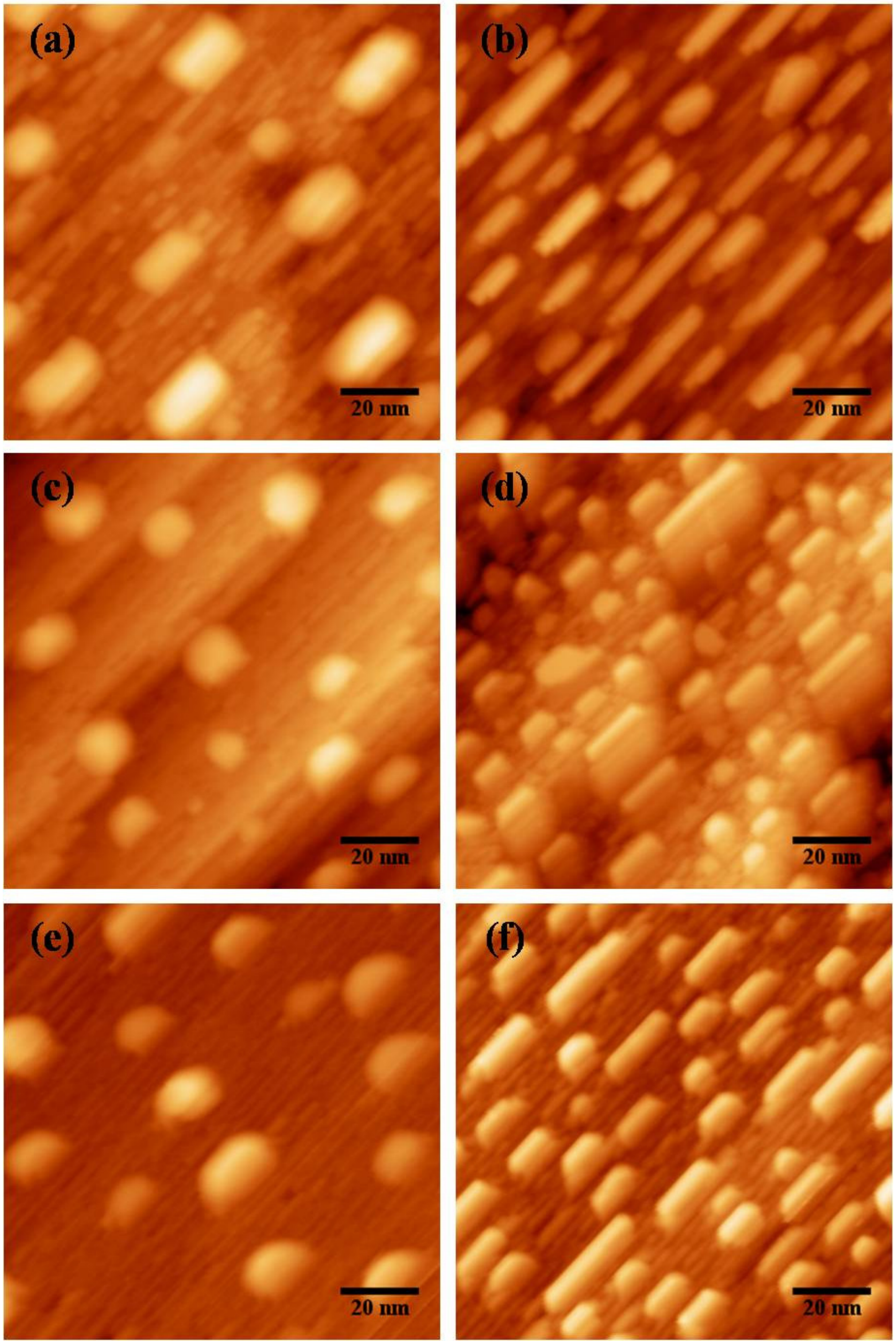

Figure 7.2 STM topographic image for 1.50 ML Au growth at substrate temperature 300 °C on a) reconstructed Si(110), b) Ag:Si(110), c) reconstructed Si(5 5 12), d) Ag:Si(5 5 12), e) reconstructed Si(553) and f) Ag:Si(553) surface.

Probability distribution of aspect ratio of the grown nanostructures

For Au growth on reconstructed Si(001) substrate and Ag:Si(001) substrate, probability distribution of aspect ratio of the nanostructures have been presented in Fig. 7.3 (a). Similarly probability distribution for Si(110), Si(5 5 12) and Si(553) substrate has been shown in Fig. 7.3 (b), (c) and (d) respectively. From the probability distribution of aspect ratio of the nanostructures, Au/Si(001) growth is found quite uniform in terms of aspect ratio (Fig. 7.3 (a)). It becomes non-uniform for Au/Ag:Si(001) growth as reflected from the broadening of probability distribution of aspect ratio towards its tail. It explores, in contrast with monometallic Au growth, bimetallic Au-Ag growth results in formation of elongated nanowires with their aspect ratio much larger than mean value. For other substrates, although the peak position of the probability distribution is different from the Si(001) surface, general characteristic of influence of Ag on probability distribution of aspect ratio is quite similar.

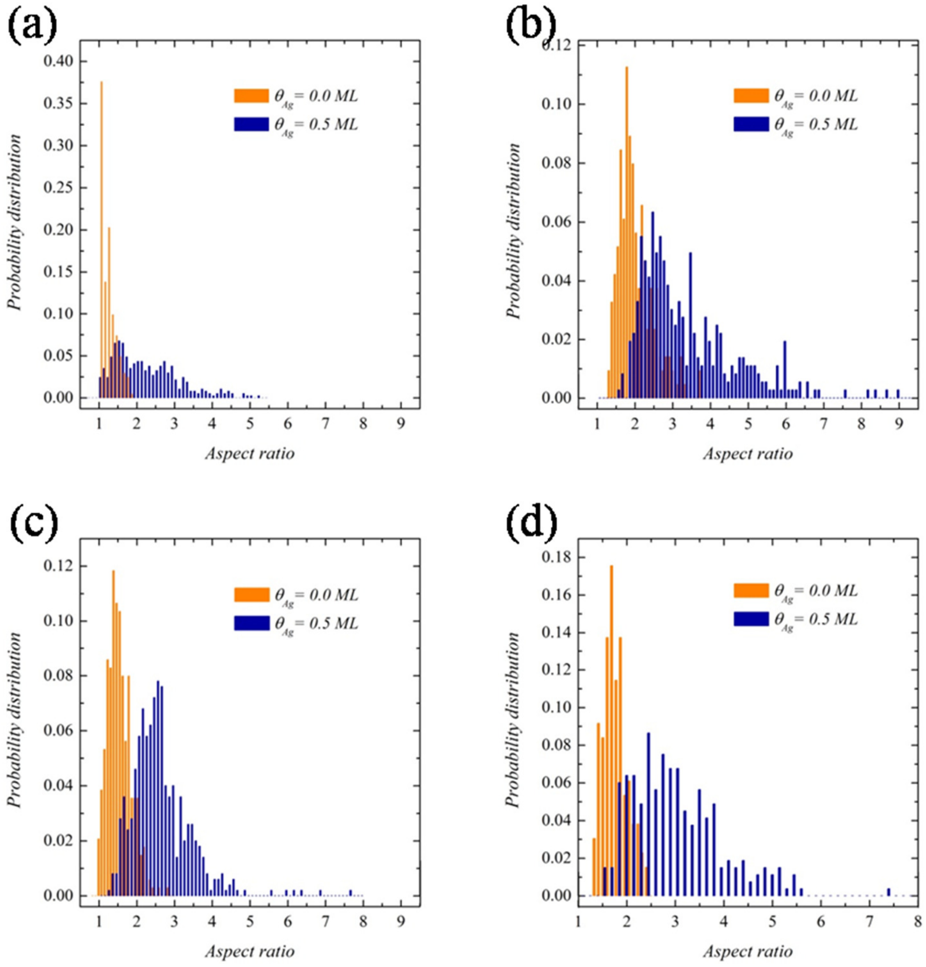

Figure 7.3 Probability distribution of mean aspect ratio of grown nanostructures for growth on a) Si(001), b) on Si(110), c) Si(5 5 12) and d) Si(553). In Fig. 7.3 (a)-(d), probability distribution of aspect ratio of the nanostructures among monometallic Au growth (orange colored) and bimetallic Au-Ag growth (blue colored) is compared.

7.3.2 Composition of grown Au-Ag bimetallic nanostructures

EDS study in STEM method for grown sample with Au growth on Ag:Si(001) at 300 °C explores the coexistence of both kinds metal (Au and Ag) within each nanostructures (Fig. 7.4). Figure 7.5 represents the elemental mapping in cross section view (using STEM) of the nanostructures for growth of Au growth on Ag:Si(001) surface. Within each nanostructure both metals Au and Ag are present with their uniform intermixing. Bimetallic intermixing among Au and Ag occurs on the top of the surface and their inter diffusion inside Si matrix is quite small. Indeed, outer diffusion of Si is also not prominent. We have also carried out elemental mapping of the nanostructures for growth of Au on Ag:Si(553) surface in cross section view (using STEM) (as shown in Fig. 7.6). It also explores uniform Au-Ag bimetallic intermixing and negligible inter-diffusion of metals inside the Si matrix. Similar structural aspects have been observed by us for Au growth on Ag:Si(5 5 12) and Ag:Si(110) surface and presented in earlier chapters.

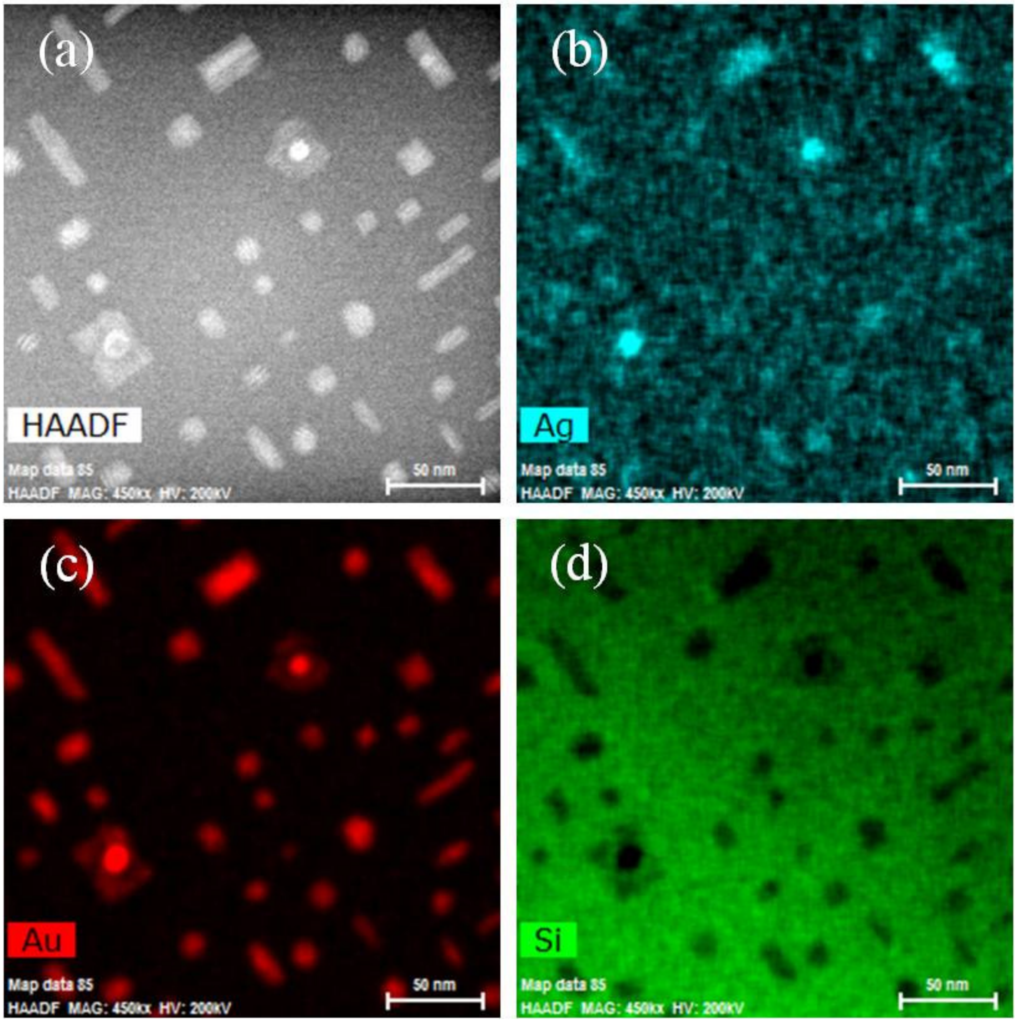

Figure 7.4 STEM study with planar view for growth of Au on Ag:Si(001) surface at substrate temperature 300 °C as: a) HAADF image and EDS mapping for b) Ag, c) Au and d) Si.

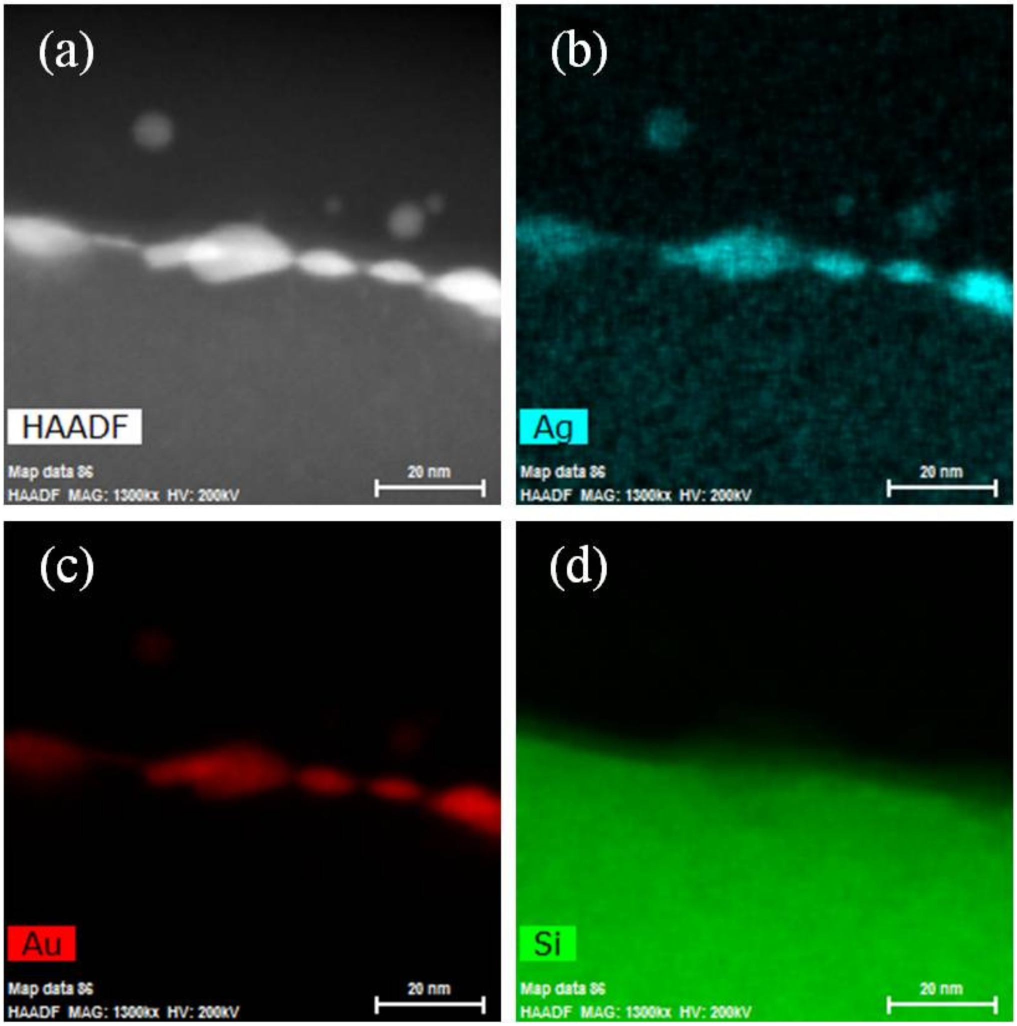

Figure 7.5 Cross-sectional STEM study for growth of Au growth on Ag:Si(001) surface as: a) HAADF image, EDS mapping for b) Ag, c) Au and d) Si.

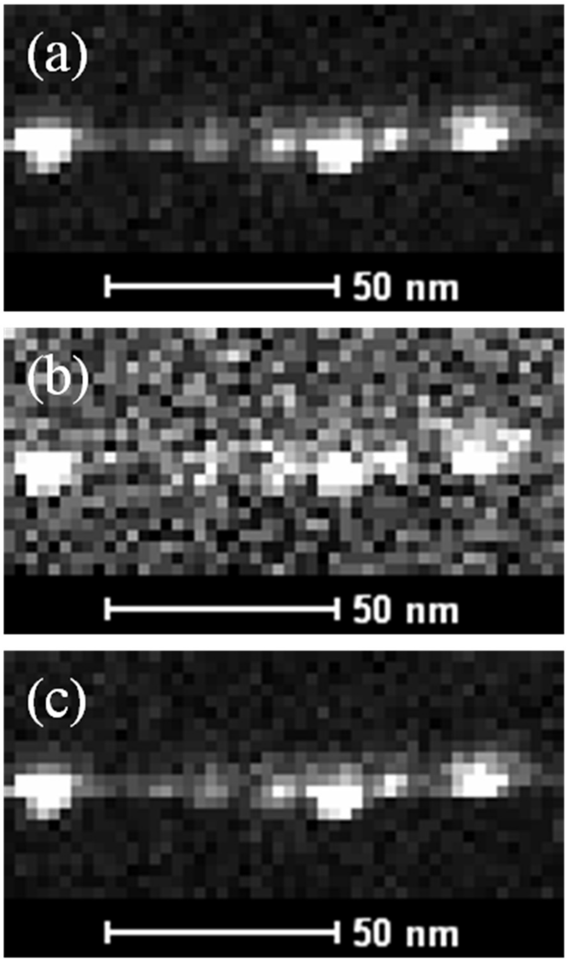

Figure 7.6 Cross-sectional STEM study for growth of Au growth on Ag:Si(553) surface: a) HAADF image and EDS mapping for b) Ag and c) Au.

7.3.3 Variation of width and length of nanostructures with its size for different Si(hkl) substrate

In the present subsection, we report our observations for variation of dimensions of the nanostructures *i.e.* width and length, with respect to its size, for different experimental conditions.

For monometallic Au growth on reconstructed Si(001) surface, length of the nanostructures is steadily increased in accordance with the its size (Fig. 7.7 (a)). Similarly other dimension of the nanostructure *i.e.* width is also gradually increased with its size. It explores, in the entire regime of size variation, size of the nanostructures is gradually increased with enhancement of the both dimensions. In other scenario, when Au is grown Ag:Si(001) surface, length of the nanostructures is systematically enhanced with its size (Fig. 7.7 (b)). It should be noted that, variation of length in accordance with the size for Au-Ag growth comprises quite resemblance with the variation of length and width with size for Au growth on ultraclean Si(001) surface. With respect to these variations, width of Au-Ag nanostructures explores a prominent dissimilar behavior (Fig. 7.7 (b)). It reveals that, as the size of nanostructures start to increase from its lowest value, width is steadily enhanced. Such steady enhancement is interrupted after reaching an intermediate size. Above this size, width becomes a slowly varying dimension as a function of size of the nanostructure. Below this intermediate size, nanostructures become larger in comparable effects of the enhancement of its both dimensions. While above this size, enhancement of the size of the nanostructure is predominantly influenced by the increase of the length.

Thereafter, we have investigated these aspects of morphology on other anisotropic surfaces: Si(110) (as shown in Fig. 7.7 (c) and (d)), Si(5 5 12) (as shown in Fig. 7.7 (e) and (f)) and Si(553) (as shown in Fig. 7.7 (g) and (h)). Due to consideration of different (hkl) orientations, extent of variation of dimensions (*i.e.* length and width) and their dependence (in terms of rapidity) on size are also different. But, overall general characteristic of such variation on these surfaces are quite similar as Si(001) surface.

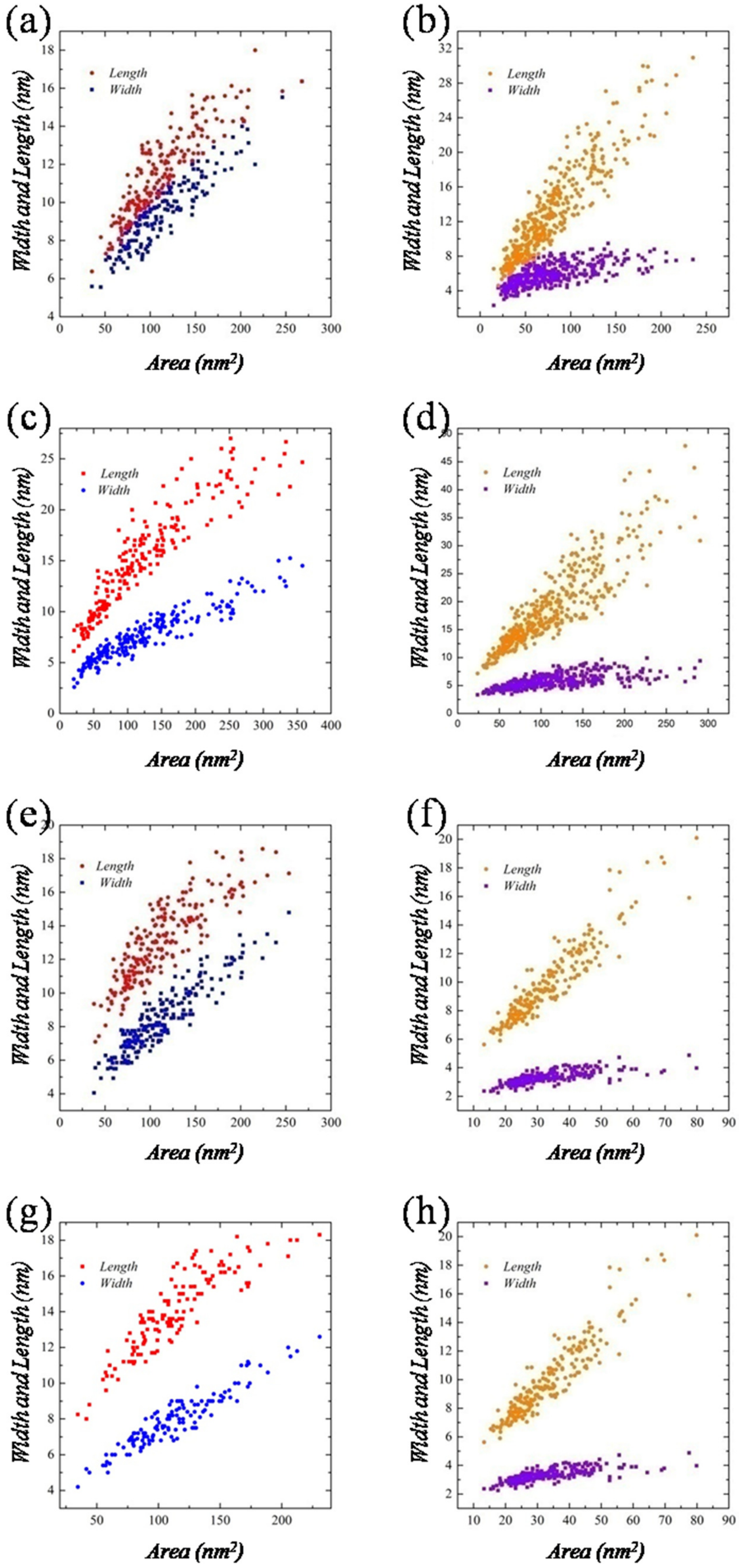
(a)
(b)
(c)
(d)
(e)
(f)
(g)
(h)
Length
Width
Width and Length (nm)
Area (nm²)
0
50
100
150
200
250
300
350
400
4
6
8
10
12
14
16
18
20
24
28
32
5
15
25
30
35
40
45
50
2
60
70
80
90

Figure 7.7 Variation of width and length of the grown nanostructures with area (size) on a) reconstructed Si(001), b) Ag:Si(001), c) reconstructed Si(110), d) Ag:Si(110), e) reconstructed Si(5 5 12), f) Ag:Si(5 5 12), g) reconstructed Si(553) and h) Ag:Si(553), surface. In Fig. 7.7 (a), (c), (e) and (g) width and length is denoted by filled blue colored square box and red colored circle respectively. In Fig. 7.7 (b), (d), (f) and (h) width and length is denoted by filled violet colored square box and orange colored circle respectively.

7.3.4 Variation of width and length of nanostructures with its size for Au/Ag:Si(5 5 12) for different Ag thickness

In the present subsection, the ***influence of Ag modification*** of ultra-clean Si(hkl) substrate on the variation of width and length of the nanostructures with its size is discussed. We have explored this aspect in the light of our previously reported results (Fig. 4.5) where morphological evolution of Au-Ag bimetallic growth at substrate temperature 300 °C with variation of Ag thickness has been discussed.

At growth temperature 300 ºC, deposition of 1.50 ML Au on Ag:Si(5 512) with varying Ag thickness have been investigated using in-situ STM. These results have been represented in Fig. 4.5 (a)-(e). When Au is deposited on reconstructed Si(5 5 12) surface, elongated nanostructures along step edge direction Si$\langle 1\bar{1}0\rangle$ are formed, reflecting the preferential mobility of the Au adatoms in this direction. Quite similar morphology is also observed for the case of Ag thickness equals to 0.10 ML. Pre modification of reconstructed surface with Ag starts to influence the morphology after Au growth, when Ag thickness is increased to 0.25 ML. For this case, with compact shaped elongated nanostructures (as observed for Ag thickness equals to 0.0 ML), slightly more elongated nanostructures start to grow. The elongation of the nanostructures become more prominent as the amount of Ag is increased to 0.50 ML and the mean aspect ratio of the nanostructures is gradually increased. Here, formation of elongated nanostructures with aspect ratio larger than its mean value becomes more evident. With further increase of Ag thickness to 1.0 ML, modification of the ultraclean template with Ag results in formation of very large aspect ratio nanostructures. It is noteworthy to mention that, in case of Ag thickness 1.0 ML, elongated nanostructures with the aspect ratio as large as ~ 7.5 are also grown.

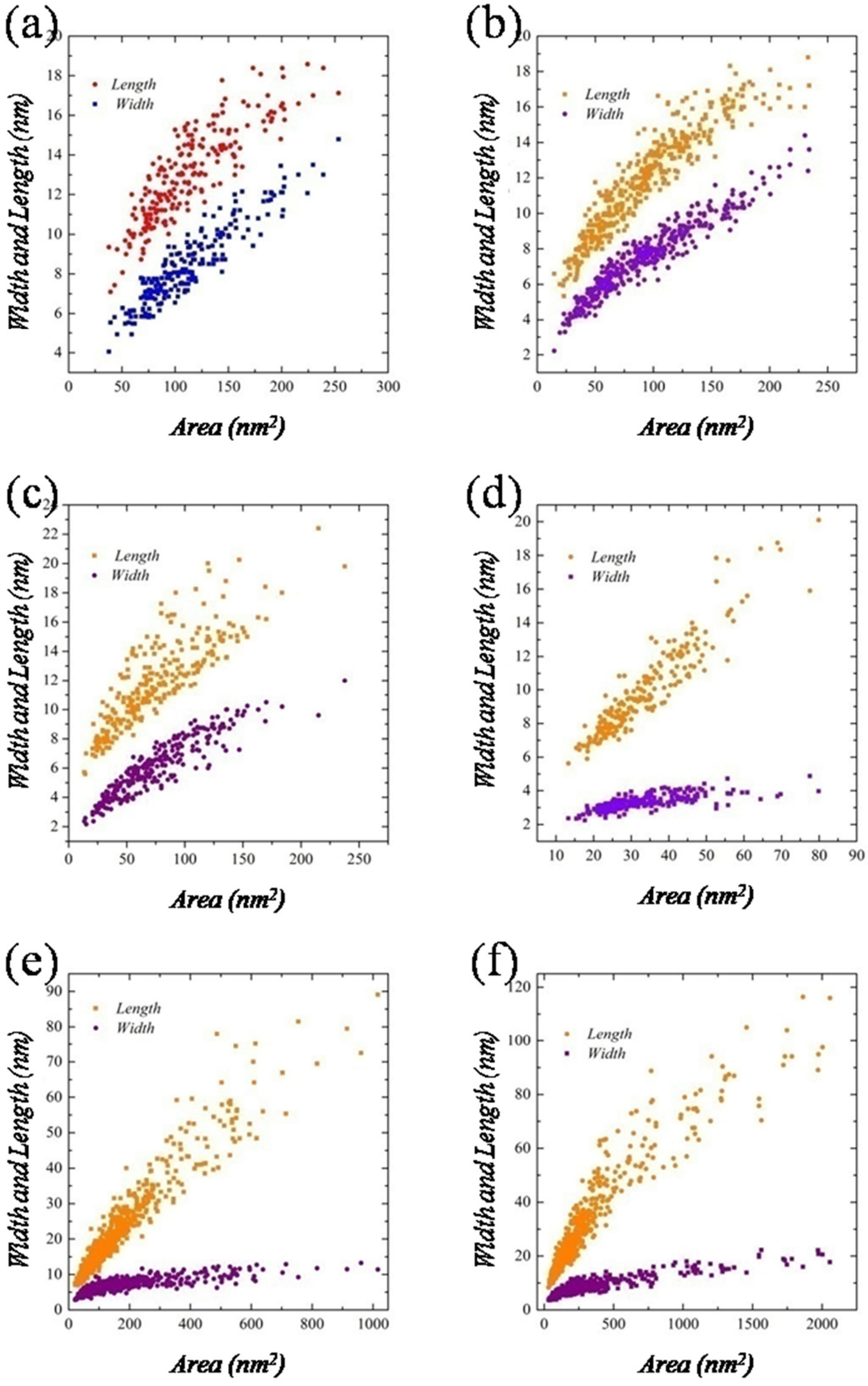

Figure 7.8 Variation of width and length of the grown nanostructures with area (size) on a) Au growth on reconstructed Si(5 5 12), Au growth on Ag:Si(5 5 12)

surface with varying Ag thickness as b) 0.10 ML, c) 0.25 ML, d) 0.50 ML, e) 1.00 ML and f) 1.25 ML. In Fig. 7.8 (a), width and length is denoted by filled blue colored square box and red colored circle respectively. In Fig. 7.8 (b)-(f) width and length is denoted by filled violet colored square box and orange colored circle respectively.

First let us consider the growth of Au on ultraclean reconstructed Si(5 5 12) surface without any modification with Ag. In this case, dependence of the length and width with the size of the nanostructures, are plotted in Fig. 7.8 (a). It depicts, both dimensions length and width of the grown nanostructures are increased in magnitude steadily with their sizes. Further when we consider these morphological aspects for Au growth with pre modification of reconstructed substrate by Ag thickness 0.10 ML, these growth aspects are found quite analogous as reconstructed surface (Fig. 7.8 (b)). Following this, as the reconstructed surface is modified with small increase of Ag thickness to 0.25 ML, these growth aspects becomes dissimilar (as shown in Fig. 7.8 (c)) and its unusual characteristics become more prominent for enhancement of Ag thickness to 0.50 ML (Fig. 7.8 (d)). For the case with Ag thickness 0.50 ML, length of the nanostructures is varied uniformly with its size. In contrast, width of the nanostructure is not uniformly varied with its size, over the entire region of its size distribution. An intermediate size is found which distinguishes the different rapidity of variation of width with size of the nanostructures. From the beginning of smallest value of the size up to this intermediate size, width is steadily increased with size. Such steady enhancement is interrupted after reaching this intermediate region. Above this intermediate size, rapidity of variation of width with size becomes much smaller. Successively, Au growth on Ag:Si(5 5 12) template, with larger Ag thickness up to 1.25 ML, reveals in every cases, an intermediate size of the nanostructures exist as a crossover for two kinds of distinguishable one-dimensional growth (Fig. 7.8 (e) and (f)).

Reconstructed Si(5 5 12) surface consists of atomic arrangement of surface atoms with long range ordering of '2×1' unit cell. Along the dimer row directions (*i.e.* Si$\langle 1\bar{1}0\rangle$), the surface Si atoms have the uniform reactivity with the ad atoms. But along its perpendicular direction Si$\langle 66\bar{5}\rangle$, reactivity of the adatoms with surface atoms is not uniform and the tetramer rows are found most reactive for the Au and Ag adatoms. Therefore mobile adatoms experience a periodic potential along the direction Si$\langle 66\bar{5}\rangle$. When very small amount of adatoms (like Au or Ag) with sub-monolayer thickness is deposited on reconstructed Si(5 5 12) surface they can easily hop along Si$\langle 1\bar{1}0\rangle$. But due to periodic potential and formation of atomic steps along the Si$\langle 66\bar{5}\rangle$, their hopping is perturbed. Hence, for very small amount (sub monolayer) of adatoms, width of the grown nanostructures along Si$\langle 66\bar{5}\rangle$ becomes constrained. As the ultra-clean Si(5 5 12) surface is modified with 0.50 ML Ag, mobility of the adatoms is followed according to surface atomic arrangement of the reconstructed surface. Hence ultra-clean template is partially covered by Ag and very high aspect ratio Ag strips are formed (Fig. 4.4 (b), (c)). Although, length distribution of the grown Ag strips becomes non uniform and diverse, width distribution becomes constrained.

The periodic potential of mobility is experienced by the adatoms, for very low coverage *i.e.* sub monolayer thickness. As the thickness is increased approximately one monolayer or above, influence of periodic potential on adatoms becomes weaker. Then, the hopping the adatoms takes place over the atomic rows. However, overall anisotropic nature of mobility of the adatoms still persists and elongated nanostructures are grown for growth of 1.50 ML Au on ultraclean reconstructed Si(5 5 12) surface.

As 1.50 ML Au is deposited on Ag:Si(5 5 12), a fraction of Au atoms is bonded to the Ag strips due to adequately large Au-Ag binding energy. Rest of incoming Au atoms are bonded with surface Si atoms, where the Ag strips are not formed. However after nucleation in both regions, incorporation of both types of adatoms (Au and Ag) towards the nucleated region is also possible. When the Au adatoms are bonded with the one dimensional Ag strips and intermixed, width of the Au-Ag bimetallic nanostructures are also constrained following by the width of initial Ag strips. It expected that the widths of the Au-Ag bimetallic nanostructures have the larger width than the initial Ag strips which has acted as nucleation centre during nucleation process. As the lengths of the initial Ag strips are not constrained, the length distribution of the Au-Ag bimetallic nanostructures also becomes more diverge.

When the Au-Ag intermixing takes place below the size of the *critical width*, incorporation of adatoms (Au and Ag) takes place in both the direction: along the length and along the width. Hence in this regime, both dimensions: length and width are increased. But as the gradual incorporation and intermixing is continued, these processes become limited along the width but continued along the length. It cause, although the length variation with the size is not perturbed, but width variation with size becomes constrained and width becomes a slowly varying dimension. Such processes are possibly playing the decisive role for characteristic behavior of variation of width and length of the nanostructure with its size for other substrates also (*i.e.* for Si(001), Si(110) and Si(5 5 3)). Due to formation of two domains orthogonal to each other on '2×1' reconstructed Si(001) surface, growth of Ag nanoislands along two orthogonal directions has been observed. Such growth of Ag nanoislands and their performance as nucleation center for incoming Au atoms is attributed for formation of nanowires along two orthogonal directions in our present case.

7.4 Conclusions

Our observations show reconstructed Si(hkl) substrates with different (hkl) orientation can be successfully implemented for growth of differently shaped bimetallic (Au-Ag) intermixed nanostructures. For instance, hexagonal shaped on Si(111), and rectangular shaped on Si(001), Si(110), Si(553) and Si(5 5 12) bimetallic intermixed nanostructures are grown. Generalized aspects of the comparative growth between Au/Si(hkl) and Au/Ag:Si(hkl) are found as (i) increase of particle density and (ii) nearly equal relative enhancement of aspect ratio, for bimetallic (Au-Ag) growth than monometallic (Au) growth. We have also investigated effect of Ag modification of ultraclean Si(001), Si(110), Si(5 5 12) and Si(553) surfaces, on the variation of width and length of the nanostructures with their sizes. It reveals width and length on ultraclean Si(hkl) surface and length on Ag:Si(hkl) surfaces is steadily increased with its size. But an intermediate size exists for growth on Ag:Si(hkl) substrates, above which width becomes a slowly varying function of its size. Focused on Ag:Si(5 5 12) surface, such behavior of width of the nanostructure is found for Ag coverage 0.25 ML to 1.25 ML (maximum Ag thickness of our consideration).

References

[1] G. S. Snider, R. S. Williams, *Nanotechnology* **18**, 035204 (2007).

[2] L. Dong, J. Bush, V. Chirayos, R. Solanki, J. Jiao, *Nano Lett.* **5**, 2112 (2005).

[3]X. Duan, Y. Huang, R. Agarwal, C. M. Lieber**,** *Nature* **421**, 241 (2003).

[4] J. Xiang, A. Vidan, M. Tinkham, R. M. Westervelt, C. M. Lieber, *Nat. Nanotechnol.* **1,** 208 (2006).

[5] H. S. Park, K. Gall, J. A. Zimmerman, *Phys. Rev. Lett.* **95**, 255504 (2005).

[6] I. K. Yanson, O. I. Shklyarevskii, Sz. Csonka, H. van Kempen, S. Speller, A. I. Yanson, J. M. van Ruitenbeek, *Phys. Rev. Lett.* **95**, 256806 (2005).

[7] J. R. Arthur, *Surf. Sci.* **500**, 189 (2002).

[8] J. M. MacLeod, J. A. Lipton-Duffin, U. Lanke, S. G. Urquhart, F. Rosei, *Appl. Phys. Lett.* **94**, 103109 (2009).

[9] R. J. Hamers. U. K. Kohler, J. E. Demuth, *Ultramicroscopy* **31**, 11 (1989).

[10] A. Rath, J. K. Dash, R. R. Juluri, A. Rosenauer, P. V. Satyam, *J. Phys. D: Appl. Phys.* **44,** 115301 (2011).

[11] Y. Gangfeng, A. C. Martin, J. Nogami, *J. Appl. Phys.* **105,** 104304 (2009).

[12] J. Nogami, B. Z. Liu, M. V. Katkov, C. Ohbuchi, *Phys. Rev. B* **63**, 233305 (2001).

[13] Y. Chen, A. Douglas, A. Ohlberg, R. S. Williams, *J. Appl. Phys.* **91,** 3213 (2000).

[14] I.-H. Hong, S.-C. Yen, F.-S. Lin, *Small* **5**, 1855 (2009).

[15] I. Hong, Y. Tsai, T. Ming Chen, *Appl. Phys. Lett.* **98,** 193118 (2011).

[16] B. Z. Liu, J. Nogami, *Nanotechnology* **14,** 873 (2003).

[17] J. N. Crain, J. L. McChesney, F. Zheng, M. C. Gallagher, P. C. Snijders, M. Bissen, C. Gundelach, S. C. Erwin, F. J. Himpsel, *Phys. Rev. B* **69**, 125401 (2004).

[18] H. H. Song, K. M. Jones, A. A. Baski, *J. Vac. Sci. Technol., A* **17,** 1696 (1999).

[19] B. Bian, Y. Hirotsu, K. Sato, T. Ohkubo, A. Makino, *J. Electron Microsc.* **48,** 753 (1999).

[20] S. Sun, C. B. Murry, D. Weller, L. Folks, A. Moser, *Science*, **287**, 1989 (2000).

[21] N. Toshima, T. Yonezawa, K. Kushihashi, *J. Chem. Soc. Faraday Trans.* **89**, 2537 (1993).

[22] M. Harada, K. Asakura, Y. Ueki, N. Toshima, *J. Phys. Chem.* **97**, 5103 (1993).

[23] Y. Wang, N. Toshima, *J. Phys. Chem. B* **101**, 5301 (1997).

[24] T. Ung, L.M. Liz-Marzan, P. Mulvaney, *J. Phys. Chem. B* **105,** 3441 (2001).

[25] R. G. Freeman, M. B. Hommer, K. C. Grabar, M. A. Jackson, M. J. Natan, *J. Phys. Chem.* **100**, 718 (1996).

[26] P. Mulvaney, M. Giersig, A. Henglein, *J. Phys. Chem.* **97**, 7061 (1993).

[27] J. Rivory, *Opt. Commun.***1**, 53 (1969).

[28] S. Link, Z. L. Wang, M. A. El-Sayed, *J. Phys. Chem. B*, **103**, 3529 (1999).

[29] L. Pauling, *J. Am. Chem. Soc.* **54**, 3570 (1932).

[30] H. Okamoto, T. B. Massalski, *Bull. Alloy Phase Diagra.* **4**, 30 (1983).

[31] W. C. Mallard, A. B. Gardner, R. F. Bass, L. M. Slifkin, *Phys. Rev.* **129**, 617 (1963).

[32] J. L. White, R. L. Orr, R. Hultgren, *Acta Metall.* **5**, 747 (1957).

[33]D. –H. Chen, *J. Mater. Chem.***12**, 1557 (2002).

[34] R. D. Harris, J. S. Wilkinson, *Sens. Actuators, B* **29**, 261 (1995).

[35]A. G. de Leon, *Appl. Opt.* **39**, 4847 (2001).

[36] J.H. Liu, *J. Phys. Chem. B*, **109**, 40 (2005).

[37] J.N. Armor, *Appl. Catal., A: General* **176,** 159 (1999).

[38] J. Zheng, *J. Catal.* **297,** 110 (2013).

[39] L. Wang, *Opt. Express* **19**, 10640 (2011).

[40] M. Mcmahon, *Appl. Phys. B* **80**, 915 (2005).

[41] A. Endo, *Surf. Sci.* **297**, 71 (1993).

[42] D. K. Goswami, B. Satpati, P.V. Satyam, B. N. Dev, *Curr. Sci. (India)* **84**, 903 (2003).

Chapter 8
Summary

The thesis focuses on the combination of self-assembly on “natural” patterned surfaces (*i.e.* on reconstructed surfaces with periodic arrangements) and novel nanostructures growth under ultra-clean conditions, such as, molecular beam epitaxy under ultra-high vacuum conditions, to achieve tailored fabrication of self assembled AuAg bimetallic nanostructures on Si substrates. The thesis presents a simple idea of adding a sub-monolayer of Ag prior to Au growth on the reconstructed Si surfaces and resulting in formation of high aspect ratio of AuAg bimetallic nanostructures. Various growth parameters, such as, thickness of pre-deposited Ag layer or post-deposited Au layers, substrate temperature, substrate orientation, etc., have been worked in detail to find optimum conditions for growing AuAg bimetallic nanostructures.

A brief introduction to the area of nanoscience and nanotechnology and the usefulness and need of bimetallic nanostructures, in particular, AuAg nanostructures has been dealt in Chapter 1. A large number experimental method have been used: Molecular Beam Epitaxy under UHV conditions, Scanning Tunneling Microscopy (in-situ), Scanning Electron Microscopy, (Scanning) transmission electron microscopy (STEM), high resolution TEM and Rutherford backscattering spectrometry (RBS). A brief detail about these experimental methods has been discussed in Chapter 2. Experimental results, theoretical calculations using density functional theory (DFT), and kinematic Monte Carlo (KMC) simulations, discussion on experimental results with proposed growth mechanisms have been presented in Chapter 3 - 7. Thereafter the present thesis work has been summarized in this Chapter (chapter 8).

Among the different orientations of the Si surfaces, focusing on the Si(5 5 12) surface role of pre-modification by ultrathin Ag layer on morphology and composition of the on Au-Ag bimetallic nanostructures, have been studied in detail. These experimental outcomes have been explained in the light of the solid on solid model KMC simulation and DFT modeling. Along with this, morphological and structural aspects of the Au-Ag bimetallic growth with variation of substrate orientation, thickness of the metal thin films (Au, Ag) have been also explored.

At the beginning, we have presented our results based on the insight that effect of different types of surface treatments of the Silicon surface on the crystalline quality and the morphology of the metal nanostructures. Considering the growth of Ag thin film on a important vicinal surface of Si *i.e.* Si(5 5 12), we have found that, to achieve very good crystalline quality and surface oriented growth of Ag, appropriate preparation of surface (such as, reconstructed surface) is found be essential. In comparison with reconstructed surface, crystalline quality is found to be of poor quality for Hydrofluoric acid (HF) treated and native oxide covered Si surfaces. Indeed, the crystallographic relationship of grown Ag nanostructures on HF treated and native oxide covered surface reveal textured and polycrystalline nature, respectively. Morphology of Ag nanostructures grown on reconstructed

Si(5 5 12) surfaces exhibit formation of oriented array of the nanostructures with elongation along Si$\langle 1\bar{1}0 \rangle$. For HF treated surface, only a small fraction of the Ag nanostructures are oriented along Si$\langle 1\bar{1}0 \rangle$. Whereas, on native oxide covered surface non-oriented and irregular shaped nanostructures were formed. From the surface sensitive RHHED and STM measurements, we have found that the reconstructed Si(5 5 12) surface consists of very well ordered arrangement of surface atoms. Although the native oxide layer is removed from top of the surface using HF treatment, surface atoms are not at all reconstructed. The robust property of HF to etch out the native silicon oxide layer results in formation inhomogeneous growth template with rms roughness ~ 0.255 nm. Indeed HF treatment in ambient condition results in partial re oxidation of the surface. We attribute that formation of inhomogeneous template for Ag growth and partial re-oxidation inhibits epitaxial and morphologically oriented growth of Ag. Therefore, it follows fractionally orientation relationship of Ag nanostructures with the substrate. In contrast, native silicon oxide layer on the Si(5 5 12) surface, acts as barrier for substantial influence of the substrate on the Ag growth. Therefore Ag crystallites having all possible low index (hkl) orientation are formed without any preferred orientation caused by the influence of the substrate orientation. In contrast, with the HF treated and native oxide covered surface, formation of bigger nanostructures is more evident on reconstructed surface. This is followed by the fact that, Ag atoms have higher mobility on ordered reconstructed surface than the o non uniform surfaces.

On reconstructed Si(5 5 12) surface, when a ~ 1.50 ML Au is deposited (1 ML=1.0×10^{15} atoms/cm^2), at growth temperature of 300 °C and further annealed for 30 minutes, formation of ordered nanostructures took place. These are elongated along the step edge direction of the reconstructed surface and have a mean aspect ratio ~1.6. Such monometallic Au growth is compared with bimetallic Au-Ag growth on reconstructed surface. We have prepared other kind of template for Au growth by depositing of 0.50 ML Ag on reconstructed Si(5 5 12) (Ag:Si(5 5 12)) at RT. Thereafter, as the Au is grown with similar thickness, growth temperature and post growth annealing condition, much more elongated nanostructures with mean aspect ratio ~ 2.6 are grown. Structural and compositional analysis explores that, these elongated nanostructures on Ag:Si(5 5 12) are found to have uniform mixture of Au and Ag.

In-situ STM measurements revealed that Ag:Si(5 5 12) surface is consisted with one dimensional Ag stripes along the step edge direction. In comparison with ultraclean reconstructed surface, when Au is growing on Ag:Si(5 5 12), such Ag stripes are acting as nucleation centers for Au atoms and mobility of the Au atoms is reduced. Following the nucleation process, both the mobile Au and Ag ad-atoms are incorporated to the nucleated region to grow further with larger volume. Therefore Ag:Si(5 5 12) templates induce higher mean aspect ratio for Au-Ag bimetallic growth in comparison with monometallic Au growth.

The thesis work also focused on understanding the plausible mechanism in the light of proposed model based on the solid on solid KMC simulation method. In this model, we have considered, Au growth followed by the Ag growth on two dimensional square lattices. On the template, we have considered periodic and uniform potential barrier along two orthogonal directions. Among the two different adatoms Au and Ag, Ag adatoms have consigned with higher diffusivity. Using a DFT model based on the dimer calculation on reconstructed Si surface, we have calculated the binding energy of different binary pairs like Ag-Ag, Ag-Au and Au-Au. Based on the outcomes from DFT calculations that explore binding energy of Au-Ag binary system is gradually increased in accordance with the Au:Ag ratio, we have carried out the KMC simulation. The results of the simulation works reveal that, presence of Ag before Au growth enhance the aspect ratio of the nanostructures, compared to monometallic Au growth. Considering different layers of a single nanostructure, identification of the metal atoms (Au, Ag) indicates Au and Ag are intermixed in throughout the entire region. We conclude, theoretical outcomes are qualitatively in good agreement with the experimental observations.

To achieve a better understanding on the point *'influence of Ag on the post-grown morphology of the Au-Ag bimetallic nanostructures'*, we have studied the morphology of the Au-Ag nanostructures for varying Ag coverage 0.0-1.25 ML with a fixed Au thickness of 1.50 ML and growth temperature of 300 °C. It shows morphologies of the Au-Ag bimetallic nanostructures is crucially dependent on the initial Ag coverage. In terms of aspect ratio, Ag does not influence significantly for its coverage below 0.25 ML. For Ag coverage $\geq$ 0.25 ML and it influence the growth to enhance the aspect ratio of the nanostructures. Aspect ratio of the nanostructures is gradually increased up to 0.60 ML of pre-deposited

Ag thickness, following the enhancement of the Ag coverage. In this range 0.25-0.60 ML, the mean aspect ratio is steadily increased. But above Ag coverage of 0.60 ML, variation of the aspect ratio becomes slower. For Ag coverage of 0.25-1.00 ML, the appreciable effects of Ag on the morphology of the Au-Ag bimetallic growth is noticeable, we have observed several elongated nanowires which comprise aspect ratio and the length much larger than the corresponding to mean values. In the light of our proposed model, we have studied this aspect considering constant Au thickness (1.0 ML) and varying Ag thickness 0.0-0.7 ML. With this consideration, we have found that the effect of Ag on the Au-Ag post grown morphology is negligible for its thickness up to ~ 0.20 ML. Thereafter, Ag influence to enhance the aspect ratio of the Au-Ag nanostructures up to Ag coverage 0.4 ML. But for Ag coverage above this value, the mean aspect ratio is not varied appreciably. Although the numerical values of the metal coverage, mean aspect ratio are not matched in good agreement, overall general characteristic of *'mean aspect ratio variation with Ag coverage'* is followed analogously in the experiment and simulation.

To understand effects of other growth parameters, like Au thickness and growth temperature on the post growth morphology of Au-Ag bimetallic growth on Si(5 5 12), we have considered an intermediate Ag coverage (0.5 ML) to modify ultraclean reconstructed Si(5 5 12) surface. Considering the growth of 3.0ML Au on Ag:Si(5 5 12) for 0.50 ML Ag, we have found that growth temperature plays a crucial role to determine the Au-Ag post growth morphology. When the growth takes place keeping the template Ag:Si(5 5 12) at room temperature, no formation of any nanostructures is observed. Elongated nanostructures start to appear when the growth temperature is increased to 200 °C. Increase of growth temperature up to 400 °C, results is formation of such aligned nanostructures with elongation along the step edge direction. When the growth temperature is increased from 200°C to 300 °C, the mean aspect ratio is increased by ~1.3 times. Interestingly, as the growth temperature is further increased to 400°C, average aspect ratio of the nano structures is reduced to ~ 0.58 times with respect to 300 °C. After deposition of Au on Ag:Si(5 5 12) for 0.50 ML, when we anneal the Au/Ag/Si(5 5 12) at 300°C, elongated nanostructures are formed. But in this case, the aspect ratio becomes ~ 1.4, which is quite similar to the corresponding value for Au growth on ultraclean reconstructed surface. Further metal inter-diffusion study indicates that Ag is largely inter-diffused inside Si matrix for growth temperature 400°C in comparison with 300 °C. Therefore, at 400 °C, during Au deposition as the Au atoms reach to the substrate amount of mobile Ag atoms on the surface becomes very small. Therefore, in terms of aspect ratio, Ag doesn't have much significant influence on the Au-Ag post growth morphology. For annealing the Au/Ag/Si system at 300 °C, although Au-Ag intermixing takes place but one dimensional Ag stripes are not formed before the Au growth. So annealing in this process doesn't influence the Au-Ag bimetallic growth to enhance the average aspect ratio in comparison with the Au growth on ultraclean reconstructed surface.

Following this, we have also investigated morphological aspects of Au-Ag bimetallic growth with varying Au thickness 0.50-5.0 ML, at a growth temperature 300°C on Ag:Si(5 5 12) for 0.50 ML Ag. For very low coverage of Au ~ 0.50 ML, deposited Au is found to form non uniform thin film and 3D islands are rarely observed. After deposition of Au, in some regions of the thin film, stripe like structures are grown whose width closely match with the unit cell dimension (~ 5.30 nm) of reconstructed Si(5 5 12) surface. Such stripe like structures are expected due acting of one dimensional Ag seed layer as the preferential nucleation centre for Au. On top of this thin film, elongated nanostructures start to develop as the Au thickness is increased to ~ 1.0 ML and above. The mean aspect ratio is gradually increased with increase of Au thickness up to ~ 2.2 ML and thereafter it reduces. It indicates, role of Ag stripes to hinder the mobility of Au adatoms along Si$\langle 66\bar{5} \rangle$ becomes very less for Au thickness above 2.2 ML and mean aspect ratio is gradually reduced.

Comparative RBS studies with variation of growth temperature (RT-400°C) indicates that significant inter diffusion of the deposited material (Au and Ag) inside the Si matrix does not take place, until at about 400 °C.

Thereafter, we have studied effects of growth parameters *i.e.* substrate temperature (during Au growth) and Au thickness on the morphological evolution of Au-Ag bimetallic growth on ultra-clean Si(110) substrate. Prior to Au growth, ultra-clean Si(110) substrate is modified with deposition of 0.50 ML Ag at RT. When Au with its thickness ~ 3.0 ML is deposited on Ag modified Si(110) substrate at RT, formation of Au-Ag thin film takes place. While growth of Au occurs at substrate temperature 200-300 °C, formation of parallel array of nanowires becomes quite evident. With gradual increase of substrate temperature, mean aspect ratio of the grown nanostructures is systematically increased. Indeed, for growths with substrate temperature 270-330 °C, nanowires with aspect ratio (20:1) which is quite larger than its mean value of aspect ratio, are formed. We have found that, growth of such extremely large aspect ratio nanowires are evident in the temperature regime ~ 270-330 °C. As the substrate temperature is further increased to 400 °C, in terms of aspect ratio, morphology of the grown nanostructure becomes comparatively more uniform. Extremely large aspect ratio (20:1) nanowires which have been observed a lower temperature are not formed at 400 °C and mean aspect ratio is also reduced compared to 330 °C. Comparing the morphology of bimetallic Au-Ag growth with monometallic Au growth we have found that pre-deposition of Ag doesn't have any significant effect on Au-Ag morphology at 400 °C. From STEM EDS measurements, grown nanowires at 300 °C are found composed of uniform Au-Ag bimetallic intermixing. Within each nanostructure, amount of Au is quite larger than other monometallic counterpart Ag.

Thereafter at substrate temperature 300 °C where extremely large aspect ratio nanowires are grown, we have studied Au-Ag bimetallic morphological evolution with systematic variation of Au thickness. In this scenario, mean aspect ratio of the elongated nanostructures is gradually increased in accordance with Au thickness up to ~ 3.0 ML. With increase of Au thickness to ~ 3.0 ML, steady enhancement of mean aspect ratio is disrupted and further increase of Au thickness consequences reduction of mean aspect ratio. For ultra-clean Si(5 5 12) and Si(110) substrates, magnitude of mean aspect ratio with similar experimental conditions are obtained different from each other. But general characteristics of morphological evolution of bimetallic Au-Ag growth (in terms of mean aspect ratio) with variation of substrate temperature and Au thickness is quite similar to each other for two different substrates (*i.e.* Si(5 5 12) and Si(110) surfaces).Following this, our investigations evolved to comprehend the role of orientation of the Si surface on the morphology of the Au-Ag bimetallic growth. After modification of the reconstructed Si surface with various orientation like (553), (5 5 12), (110), (001) and (111) by 0.50 ML Ag, we have deposited 1.50 ML Au at growth temperature 300 °C. When Au is grown on Ag:Si(111), hexagonal shaped nanostructures are grown similar as the ultra-clean surface. In contrast to the (111) orientation, when we come across of the other orientation, we have found one dimensional bimetallic nano wires are formed.

For different orientation of the surface like (110), (553) and (5 5 12) both the Au and Ag adatoms have the preferential mobility alone the Si$\langle 1\bar{1}0 \rangle$ direction. It causes the formation one dimensional Ag nucleation layer before Au growth. Following the Au growth, as the incorporation Au and Ag ad-atoms is driven by the mobility, therefore growing of the bimetallic nanostructures is also become anisotropic. It reveals that for the formation of one dimensional bimetallic nanowires, orthogonal anisotropy of the ad-atom mobility is essential. On reconstructed Si(5 5 12) surface for 1.50 ML Au growth, in comparison with monometallic Au growth, bimetallic Au-Ag growth (*i.e.* Au deposition followed by 0.50 ML Ag deposition) consequences enhancement of mean aspect ratio of the nanostructures by 1.68±0.10 times. Detailed studies on other anisotropic substrate *i.e.* Si(110) and Si(553), magnitude of such enhancement factor is nearly similar with variation ± 3%. From the length and width vs size plot, we have found that on Ag modified one dimensional template (*i.e.* Ag:Si(110), Ag:Si(5 5 12) and Ag:Si(553)) and Ag:Si(001) surface, length of nanostructures is monotonously increased with size. But width of the nanostructures is rapidly increased with its size from minimum to an intermediate value. With respect to this, above the intermediate value, the increase of width with size becomes much slower. In contrast to Ag:Si(hkl) surface, on ultraclean reconstructed Si(hkl) surface both the length and width of the nanostructures is monotonously increased with size.

In the conclusion, the present thesis work dealt with a very detailed study on the dependence of Ag, Au, substrate orientation, growth temperatures for growing large aspect ratio Au-Ag bimetallic intermixed nanostructures on ultra-clean Si substrates and carried out theoretical investigations to arrive at a plausible growth mechanism.